3   EXPERIMENTAL EQUIPMENT FOR THE 12 GeV UPGRADE

The equipment planned for the Upgrade project takes full advantage of apparatus developed for the present program. In each of the existing halls, new spectrometers are added and/or present equipment upgraded to meet the demands of the 12 GeV program. Then a new hall, Hall D, will be added to support the meson spectroscopy program.

In Hall A, the Upgrade will add a large angular- and momentum-acceptance, moderate-resolution magnetic spectrometer (to be called the Medium-Acceptance Device, or MAD) and a high-resolution electromagnetic calorimeter. The spectrometer will provide a tool for high-luminosity, high-x studies of the properties of nucleons with an 11 GeV beam, and will also be used for selected investigations of the GPD's, where high luminosity and good resolution are needed. Details are provided in Section 3.A below. In Hall B, the CEBAF Large Acceptance Spectrometer (CLAS), which was designed to study multi-particle, exclusive reactions with its combination of large acceptance and moderate momentum resolution, will be upgraded to CLAS^{++} and optimized for studying exclusive reactions (emphasizing the investigation of the GPD's) at high energy. It will also be used for selected valence quark structure studies involving neutron "tagging" or polarized targets capable of supporting only very low beam current. Most importantly, the maximum luminosity will be upgraded from 10^{34} to 10^{35} cm^{-2} s^{-1}. The present toroidal magnet, time-of-flight counters, Čerenkov detectors, and shower counter will be retained, but the tracking system and other details of the central region of the detector will be changed to match the new physics goals. Details are provided in Section 3.B. In Hall C a new, high-momentum spectrometer (the SHMS, Super-High-Momentum Spectrometer) will be constructed to support high-luminosity experiments detecting reaction products with momenta up to the full 11 GeV beam energy. This feature is essential for studies such as the pion form factor, color transparency, duality, and high-Q^2 N^* form factors. The spectrometer will be usable at very small scattering angles. See Section 3.C for details. In the new hall, Hall D, a tagged coherent bremsstrahlung beam and solenoidal detector will be constructed in support of a program of gluonic spectroscopy aimed at testing experimentally our current understanding that quark confinement arises from the formation of QCD flux tubes. This apparatus is described in detail in Section 3.D. Finally, we describe in Section 3.E the apparatus required for the Primakoff effect experiments that will investigate the properties of light pseudoscalar mesons. This apparatus builds on experience being gained in a related experiment now underway in Hall B.

3.A   Hall A and the Medium Acceptance Device (MAD)

With the Jefferson Lab 12 GeV upgrade a large kinematics domain becomes accessible in deep inelastic scattering. The high luminosity and high polarization of beam and targets allow a unique contribution to the understanding of nucleon and nuclear structure, and the strong interaction in the high x region (which is dominated by the valence quarks). To fully utilize the high luminosity

Table 15: The design characteristics of the MAD spectrometer shown along with the HRS performance.

Parameter	MAD design	HRS performance
Central momentum range	0.4 - 7.5 GeV/c	0.2 - 4.3 GeV/c
Scattering angle range	$6°$ - $130°$	$6°$ - $150°$
Momentum acceptance	$\pm 15\%$	$\pm 5\%$
Momentum resolution	0.1%	0.02%
Angular acceptance	28 msr ($\geq 35°$)	6 msr (standard)
	4-6 msr ($5° - 12°$)	12 msr (forward)
Angular resolution (hor)	1 mrad	0.5 mrad
Angular resolution (ver)	1 mrad	1 mrad
Target length acceptance ($90°$)	50 cm	10 cm
Vertex resolution	0.5 cm	0.1 cm
Maximum DAQ rate	20 kHz	5 kHz
e/h Discrimination	0.5×10^5 at 98%	1×10^5 at 98%
π/K Discrimination	1000 at 95%	1000 at 95%

available at CEBAF (up to 10^{39} e $\cdot$ nucleons/cm^2/s), a well-matched spectrometer, given the name Medium-Acceptance Device (MAD), has been designed as the instrumental upgrade for Hall A.

The design of the MAD spectrometer has resulted in a versatile instrument. The main components are two warm-bore combined-function (dipole and quadrupole) superconducting magnets. Its maximum central momentum is 7.5 GeV/c with a momentum acceptance of $\pm$ 15% which makes it possible to accept particles with momenta above 8.5 GeV/c. It is expected that even higher momenta can be accommodated for specific experiments by decreasing the deflection of the second magnet. MAD has a momentum resolution of better than 10^{-3} and an angular resolution of better than 1 mrad. A pointing accuracy of better than 0.5 mrad, required for an accurate L/T separation, can be obtained. The angular acceptance is 28 msr at angles larger than $35°$ and decreases linearly to 6 msr at an angle of $12°$. An angle as small as $5°$ can be reached by using one of the existing septum magnets. This design has resulted in the characteristics shown in Table 15.

A detector package has been designed for the detection of electrons and hadrons. The standard electron detection system consists of four planes of scintillators for triggering, two drift chambers and a multi-wire proportional chamber for tracking and a gas Čerenkov counter and an electromagnetic calorimeter for particle-identification purposes. For hadron detection two aerogel Čerenkov counters or a focal plane polarimeter are additionally available. Both packages provide excellent ($e^\pm, \pi^\pm, K^\pm$ and p) identification over the full momentum range. Pion rejection as good as a few times 10^{-5} will be provided. The data acquisition system is designed with a new generation of pipeline digitizing front-end electronics to be able to handle event rates up to 20 kHz.

In combination with the MAD spectrometer, a 100 msr lead-glass calorimeter is available for studies of nucleon form factors and of Real Compton Scattering. A large acceptance, high granularity calorimeter with 1296 element array of PbF$_2$ crystals is proposed to optimally study

Generalized Parton Distributions through Deep Virtual Compton Scattering. It will also benefit other experiments, such as photo-production of neutral mesons at large transverse momenta.

With the cross section dropping rapidly with increasing Q^2, both a high luminosity and a large acceptance spectrometer are crucial for precision measurements. In combination with the existing HRS in Hall A MAD will open up a window to a rich program, including measurements of:

- Polarized and unpolarized quark distributions up to large x, using polarized proton and ^3He targets. Values of x larger than 0.8 can be probed once spin duality has been established.

- Semi-inclusive $\pi^\pm$ and $K^\pm$ electroproduction in order to separate the spin and flavor components of the sea quark distributions up to $x \approx 0.65$,

- Nucleon form factors to significantly larger Q^2-values, over 5 $(\text{GeV/c})^2$ for G_E^n and over 14 $(\text{GeV/c})^2$ for G_E^p,

- Real Compton Scattering up to $s \approx 20$ $(\text{GeV/c})^2$ and $|t| \approx 15$ $(\text{GeV/c})^2$ and Deep Virtual Compton Scattering up to $Q^2 \approx 7$ $(\text{GeV/c})^2$ and $x \approx 0.5$,

- Deuteron photo-disintegration up to photon energies of 7 GeV over a large range of CM angles, with recoil polarization up to a photon energy of 4 GeV,

- Few-body elastic form factors to Q^2-values of over 10 $(\text{GeV/c})^2$,

- Parity violation in deep inelastic scattering with very high accuracy to probe possible extensions of the Standard Model,

- Threshold ψ photoproduction to study the color Van der Waals-type component of the NN force.

3.A.1   Design Characteristics of the MAD Spectrometer

In order to perform the experimental program, the Medium Acceptance Device (MAD) spectrometer has been designed. MAD is a 7.5 GeV/c super-conducting spectrometer with a moderately large acceptance of up to 30 msr. This device consists of two 4 m long super-conducting combined-function magnets, each with a 120 cm warm bore. These magnets and the shield house are supported by a welded steel structure with steel drive wheels. The shield house is a composite of concrete, steel, and lead. The cryogenics are proven systems using standard JLab components. A schematic drawing of the MAD spectrometer is shown in Fig. 142.

The MAD spectrometer requires two similar combined-function super-conducting magnets. The first magnet, MAD-1, simultaneously produces a 1.9 T dipole field and a 4.2 T/m quadrupole field while the second magnet, MAD-2, simultaneously produces a 3.7 T dipole field and a 3.3 T/m
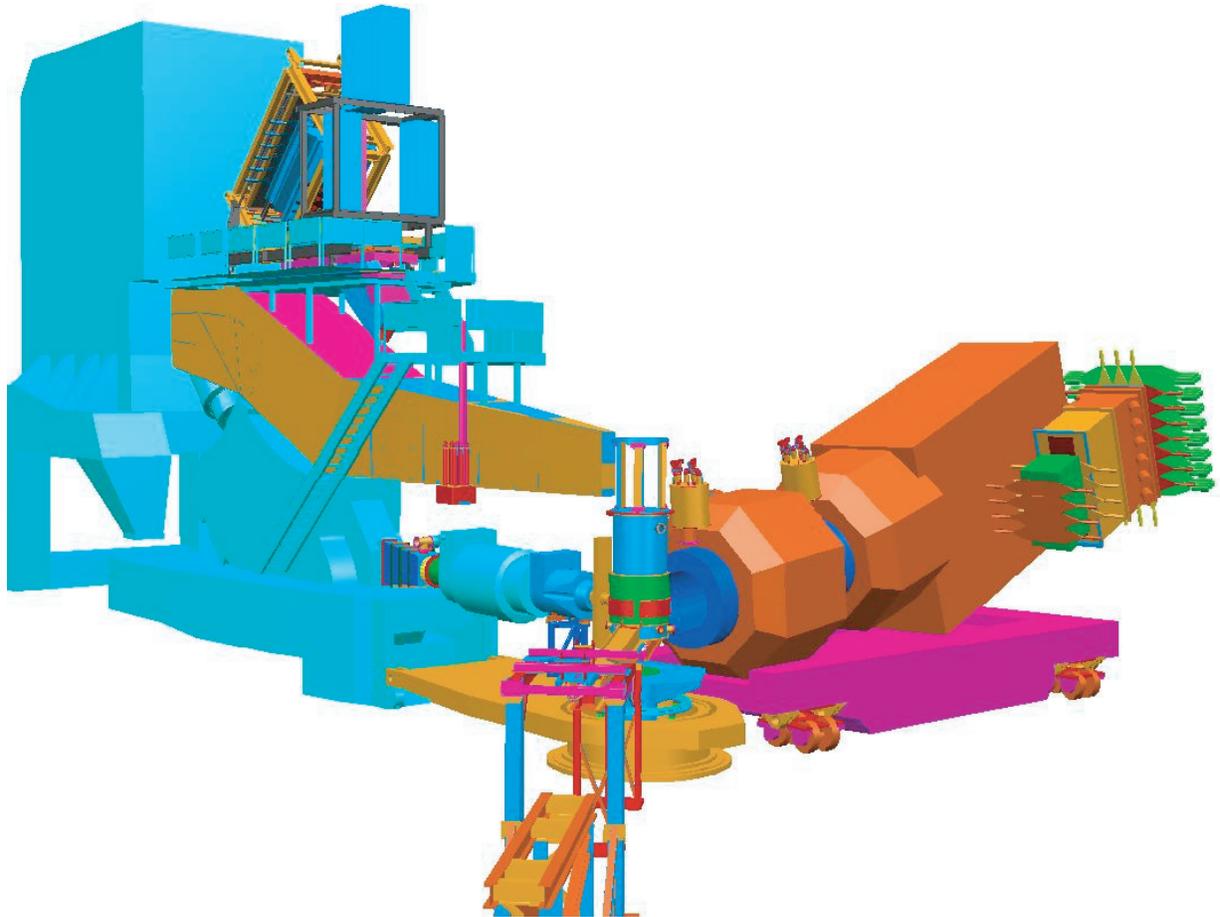
Figure 142: Three-dimensional CAD drawing of Hall A showing the MAD Spectrometer on the right along with one of the present high resolution spectrometers on the left.

quadrupole field. A magnetic design using TOSCA-3D has been performed to establish the basic magnetic requirements, provide 3D field maps for optics analysis and produce basic engineering information. A two-sector nested $\cos\theta/\cos2\theta$ design with low current-density coils ($5140/5750$ A/cm^2 for MAD-1 and $5125/5250$ A/cm^2 for MAD-2), warm bore and warm iron has been selected and analyzed. These low current densities are within the limits for a cryostable winding. Coils of this type are the most conservative that can be built and the large size and modest field-quality requirements ($\delta\text{B}/\text{B} = 3 \times 10^{-3}$) insure that construction tolerances (1-2 mm) are easily achievable. Other relevant parameters of the magnets are listed in Tables 16 and 17.

The magnetic design uses TOSCA-generated $\cos\theta$ type coils with "constant perimeter" ends. These coils closely approximate the ideal cosine geometry that is well established as a "perfect" generator of high purity fields. Practical considerations, finite current distributions, and a limited number of sectors all contribute to higher-order field errors in the design. The yoke is modeled with the nominal properties of 1010 steel. This steel is a commonly available alloy with properties suitable for the simple return-yoke function of a cosine style magnet. The present design yoke has an elliptical outside shape to permit a closer approach to the beam line and a circular inner shape to fit the cryostat. Table 17 contains the designed yoke dimensions. Modifying the yoke shape to improve the smallest angles attainable by MAD does not have a significant effect on field quality, rather the effect is felt most in the integral strength. The MAD magnets have significant stability margins so small increases in current to make up for iron that is removed to provide access to small scattering angles can be easily accommodated without sacrificing reliability.

The combined-function magnets produce peak fields of 5.6 T in the warm bore of MAD-1 and of 6.4 T in the windings of MAD-2. These fields are comparable to those achieved in large-bore magnets produced 20 years ago for MHD research, although the stored energy and average forces of the present magnets are typically less, even though the field volumes are comparable. This is due to the fact that the superposed quadrupole field produces significantly less stored energy for a given maximum field. The combined fields also produce a very asymmetric field and force distribution. The fields add on the bottom of the magnet and subtract on the top, so that the fields across the bore range from -0.6 T to 4.4 T for MAD-1. Similarly, the fields in the windings are highest where the fields add giving 6.5 T winding fields and nearly -2 T where they subtract. The MAD magnets must operate in both relative polarities so the magnets must be designed accordingly. The peak linear force densities are 23,000 N/m for MAD-1 and 33,600 N/m for MAD-2.

The cryogenics for the MAD combined-function magnets are based on the successful thermal syphon cooling that has been incorporated in nearly all the SC magnets at JLab. The high (100 g/s) internal flow rates and simple reservoir level control insure reliable operation with simple controls. These magnets have approximately 100 liters of helium in a reservoir over the magnet coils and thus are capable of about 1 hour of isolated operation during a refrigerator shutdown.

Internally the magnets will have thermal syphon circulation from helium and nitrogen reservoirs. The magnets will have liquid level control and valves to permit independent warm up or cool

down using a local heat exchanger. The cryogenic supply will use the existing Hall A transfer lines, septum adapter box, vacuum jacketed return lines, flex gas lines, and cool-down heat exchanger. The MAD cryogenic system requires a new cryogenic distribution box that rides on the back of MAD and a flexible transfer line similar to that constructed for the G0 experiment. The magnets will be connected by JLab standard u-tubes similar to those used on HMS/HRS quads. A set of gas manifolds installed on the back of the MAD will collect and return cryogenic gases to the existing Hall A gas system. A stand to hold the new equipment and a platform are required for support and personnel access. The system is completed by automated cool down valves and actuators identical to those used on HMS.

The heart of this system is a somewhat complex control reservoir that contains JT valves, bayonet connections, phase-separating reservoirs, current leads, relief valves and instrumentation including level sensors. There are six of these control reservoirs at JLab and one more being delivered. The standardization of design and function and use of standardized components insures compatibility, reliability, and cost and operational savings. The control reservoir will be mounted on the downstream ends of the MAD magnets and will be located on the side to keep the overall profile of the MAD magnets low enough to fit through the truck access door. The cryogenic valving allows for top and bottom fill of helium and nitrogen for level operation and cool down, respectively. There will also be a separate valve for variable temperature cool down gas made in a LN2 to He gas heat exchanger (also standard design). This will be used to minimize thermal stresses and increase the overall efficiency of cryogenic operations during cool down and warm up of the MAD magnets.

During normal operation and liquid level control the MAD magnets are fed helium gas at 4.5 K and 3 atm. This gas is JT expanded at each magnet by a valve that is controlled by the MAD magnets control system to maintain liquid level. Boil-off gas and JT flash are returned to the local refrigerator cold at 1.2 atm and 4.2 K. Nitrogen is fed to the MAD at 85 K and 4 atm where it is expanded into the N2 reservoir by a local valve under local control. Boil-off N2 is vented outside. Vapor-cooled current leads are controlled by local valves that servo on current in the MAD magnet and adjust the helium gas flow accordingly. No burnout current leads are specified. The helium gas from the vapor cooled leads (VCL's) is returned warm to the ESR compressor suction. The cool down gas return and N2 gas return lines are vacuum jacketed to prevent ice and water from accumulating near the magnets.

Separate flow control and measurement for each current lead is a normal part of this design. Finally, the reservoirs contain dual relief devices, an ASME coded mechanical relief and a rupture disc, set at a 25% higher pressure. Exhaust lines for relief separate from cool down lines are used so that there is no chance of a contamination blockage in these all important pressure relief paths. The reservoirs contain temperature sensors, liquid level sensors and voltage taps. Generally all internal instrumentation is routed to the reservoir to a set of vacuum feed-throughs. Strain gauges in the cold to warm support system will be essential due to the force between yoke and coil, especially considering the asymmetry of these forces. Vacuum gauging and system pressure sensors will also

be located in the control reservoir. JLab owns the design for the installed and to be delivered control reservoirs, all of which were built commercially.

The MAD magnets will have a control system that is self-contained and able to be operated by an EPICS control screen. The internal controls will take care of interlocks, operating valves by PID, and processing information from the magnet. The EPICS system will allow user operation from GUI screens, archival data logging, and graphic display. A dual processor PLC of a type produced by Mitsubishi for critical fail safe process control will be used. These dual processor PLCs can switch the process control from primary to secondary in 50 ms in the event that the primary processor fails. These processors can also be switched manually or by software for routine software maintenance. Liquid-level control is by commercial AMI units and cryogenic thermometry is by commercial Lakeshore electronics modules. Readouts of magnet voltages, pressures, strain gauges, and valve position LVDTs is by standard PLC plug-ins. These systems are in wide use and all PLCs support them.

The DC power for the MAD magnets will be provided by four independent power supplies. These supplies will be 12 pulse SCR supplies with a final stage transistor regulator and stability of 10 ppm. These devices are readily available from Danfysik and others. The power supplies will provide 10 V for ramp up or down, have polarity switches and the possibility of NMR control for the dipole coils. The energy dump systems will consist of a 10 V ramp down, a slow dump and a fast dump resistor. The fast dump will apply a voltage of 150 V to the dipole coils and 250 V to the quad coils to reduce the current to zero in 150 s. These voltages may increase as the design progresses to maintain a reasonable final coil temperature near 80 K. The dipoles and quadrupoles have dump resistances such that the time constants are equal so that both coils discharge equally. The design of the MAD magnets is such that in the event of a discharge of one coil the second coil will see a voltage which will mimic a quench and a discharge of the second coil will be initiated.

The very large cold mass and low current density insure that sufficient material is available in the cold mass to absorb a large fraction of the stored energy at a low temperature during a quench discharge resulting in a safer overall magnet. Cryostable magnets are in general extremely safe and reliable but the presence of liquid helium in the windings is essential. The open windings characteristic of a cryostable coil exposes the coil to the risk of high temperature during a quench if the windings are uncovered due to the small residual heat conduction through the insulated spacers. The MAD coils would not be self-protecting and therefore a reliable fast discharge system is essential. Twelve of the thirteen large super-conducting magnets presently at JLab are cryostable. These systems all have dual quench detection systems and fail-safe energy dump switches.

The graphs in Fig. 143 display the field vs. current for the MAD-1 (top) and MAD-2 (bottom) combined-function magnets. The dashed curves display the short sample critical currents and the solid lines are the load line curves for the magnets where the B used is the maximum B found in the coil. The load line curves measure the current and field margins and the margin along the load line of the respective coil relative to the short sample curve at the operating temperature (4.4 K
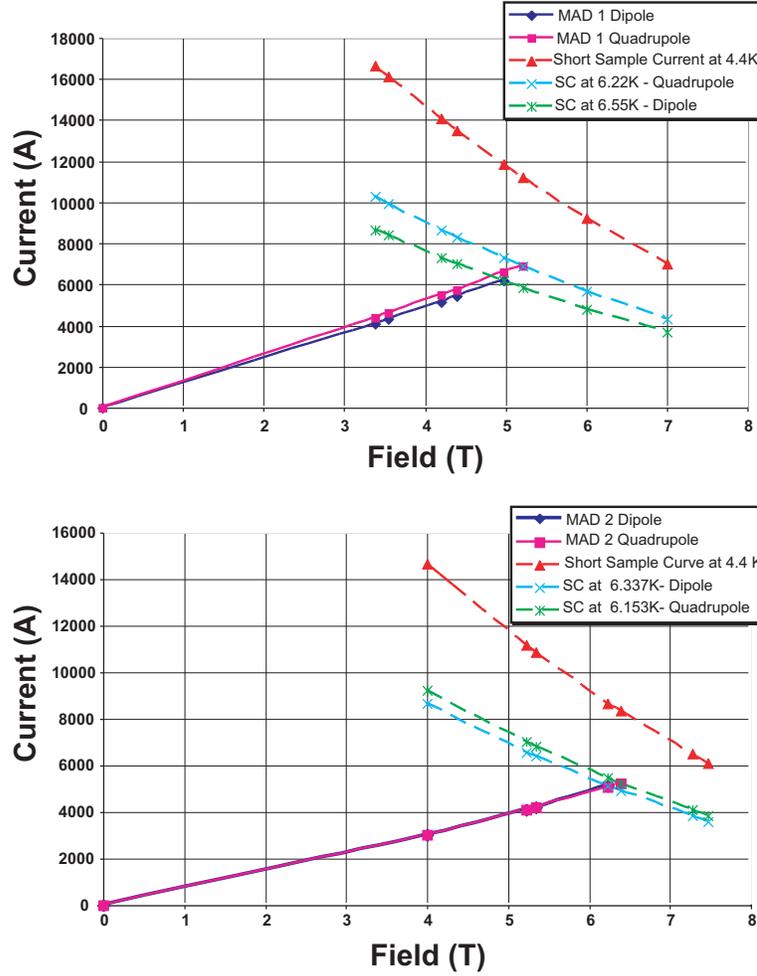
Figure 143: The field vs. current for the MAD-1 (top) and MAD-2 (bottom) combined-function magnets

dashed curve). The two intersecting dashed SC curves show the behavior in the MAD dipole and quadrupole at their respective critical temperatures. These curves measure the critical temperature margin ($\sim$2 K) relative to the operating temperature of 4.4 K.

Table 16 lists the parameters of the evaluation of the Steckly criteria (α) for cryogenic stability where α is the ratio of Joule heating in an adiabatic unit length of conductor to the heat removed by surface conduction from the same unit length:

$$\alpha = I^2 \times \rho/(area \times perimeter \times \Gamma \times (T_c - T_o) \times H_c). \tag{70}$$

The condition of stability ($\alpha < 1$) means that the velocity of spread of the normal zone is negative, therefore a normal zone will always shrink. This evaluation of α ignores heat that is conducted along the conductor so this criteria is satisfied by an arbitrary length of conductor as long as the surface is wetted by liquid helium. Thus the magnets must be protected from operation when the helium liquid level is low and there is risk of exposed (non-wetted) coils. Therefore, in addition to
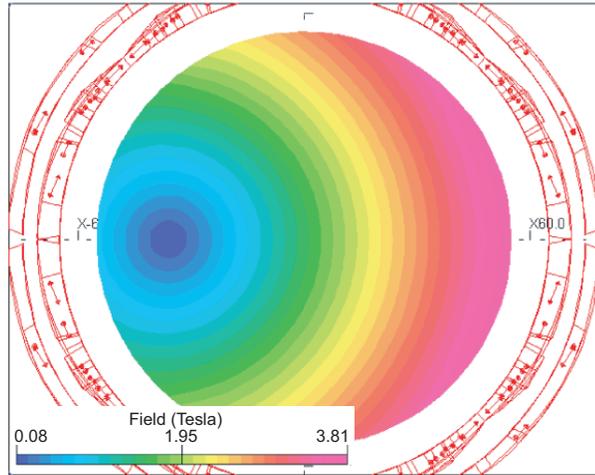
Figure 144: A TOSCA plot of the magnitude of the magnetic field in the warm bore of the combined-function MAD magnet. The bullseye pattern is typical of the superimposed quadrupole and dipole fields.
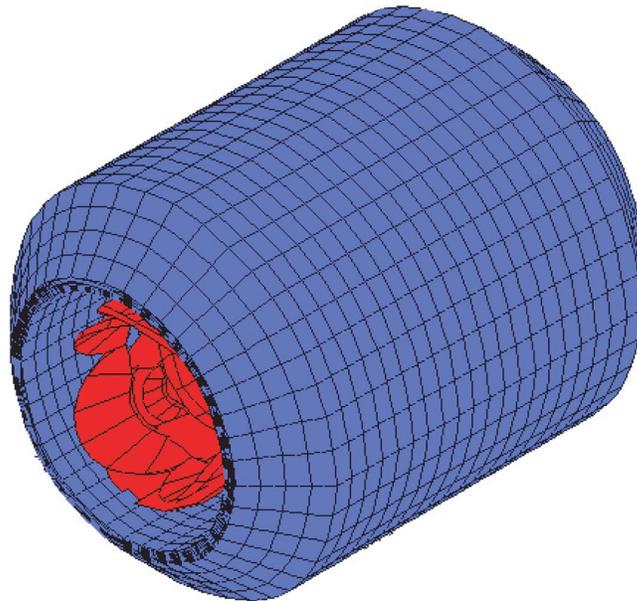

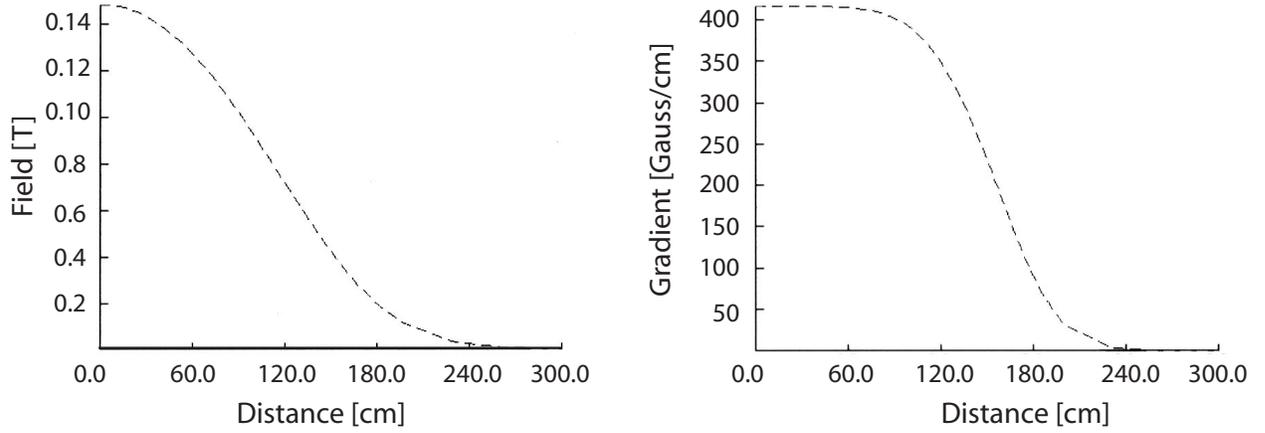Figure 145: Exterior view of one of MAD's combined function magnets.

Figure 146: Plot of the dipole component (B_y) and of the field gradient of the MAD-1 magnet along the centerline from the magnet center to 300 cm along the axis.

Table 16: The parameters necessary to evaluate the cryogenic stability by the Steckly criteria are listed. B_{max} is the maximum conduction field, area the conductor cross section, perimeter the fraction exposed to helium, Γ the percent of the perimeter that is covered with liquid helium, ρ the resistivity corrected for the magnetic field via the Kohler Plot, H_c the surface nucleate boiling heat transfer, $(T_c - T_o)$ the temperature difference between the current sharing and the operating temperature, and I_{max} the maximum design operating current.

	MAD-1 Dipole	MAD-1 Quadrupole	MAD-2 Dipole	MAD-2 Quadrupole
B_{max}	4.2 T	4.4 T	6.24 T	6.39 T
area	1 cm^2	1 cm^2	1 cm^2	1 cm^2
perimeter	5 cm	5 cm	5 cm	5 cm
Γ	0.6	0.6	0.6	0.6
$\rho(273)$	1.60×10^{-6} Ω cm	1.60×10^{-6} Ω cm	1.60×10^{-8} Ω cm	1.60×10^{-6} Ω cm
$\rho(4.4K)$	8.00×10^{-9} Ω cm	8.00×10^{-9} Ω cm	8.00×10^{-8} Ω cm	8.00×10^{-9} Ω cm
$\rho(5T,4.4K)$	2.82×10^{-8} Ω cm	2.91×10^{-8} Ω cm	3.87×10^{-8} Ω cm	3.87×10^{-8} Ω cm
H_c	0.21^2	0.21^2	0.21^2	0.21 W/cm^2
T_c	7.39 K	7.10 K	6.33 K	6.15 K
T_o	4.42 K	4.42 K	4.42 K	4.42 K
$I_c(B, 4.2K)$	14739 A	14115 A	9087 A	8722 A
$I_c(B, 4.4K)$	14078 A	13481 A	8671 A	8331 A
I_{max}	5140 A	5750 A	5125 A	5250 A
α	0.40	0.57	0.83	0.98

Table 17: Properties of the large-acceptance spectrometer magnets.

MAD-1	Combined-function quadrupole-dipole
Nominal Bend	10 °
Aperture	120 cm warm bore
NI dipole	2.33×10^6 A turns, 5140 A/cm^2, 2 sector - $\cos\theta$
NI quad	4.92×10^6 A turns, 5750 A/cm^2, 2 sector - $\cos2\theta$
Bend strength,Bo,EFL	4.46 Tm, central field 1.87 T, effective length dipole 2.4 m
Quad strength,Go,EFL	12.8 (T/m)m, gradient 4.19 T/m, effective length quad 3.07 m
Field Homogenity	3×10^{-3}
Length	4.0 m
Yoke	1010 steel 140 ton warm iron, 3.2 m OD, 2.0 m ID, 3.0 m long
Coil and cryostat	28 ton stainless steel, 1.99 m OD, 1.20 m ID, 4.0 m long
Stored Energy	16.9 MJ
Peak linear force density dipole coil	21,600 N/m
Peak linear force density quad coil	23,000 N/m

MAD-2	Combined-function quadrupole-dipole
Nominal Bend	22 °
Aperture	120 cm warm bore
NI dipole	5.89×10^6 A turns, 5125 A/cm^2, 2 sector - $\cos\theta$
NI quad	4.08×10^6 A turns, 5250 A/cm^2, 2 sector - $\cos2\theta$
Bend strength	10.2 Tm central field, 3.66 T, effective length dipole 2.78 m
Quad strength	9.79 (T/m)m gradient, 3.30 T/m, effective length quad 2.96 m
Field Homogenity	3×10^{-3}
Length	4.0 m
Yoke	1010 steel 205 ton warm iron, 4.0 m OD, 2.0 m ID, 3.2 m long
Coil and cryostat	28 ton stainless steel, 1.99 m OD, 1.20 m ID, 4.0 m long
Stored Energy	44.9 MJ
Peak linear force density dipole coil	32,000 N/m
Peak linear force density quad coil	33,600 N/m

quench voltage detection, a low liquid level condition is also cause for a fast discharge.

The MAD support structure is a welded steel frame riding on steel wheels. It will be fabricated from pre-fabricated sections that must be welded together in the Hall. The steel structure will have a main beam section that will carry the entire spectrometer. The steel fabrications will be hollow welded structures similar to ship hull sections. As such they will have internal access to permit complete welding of all seams and joints. The entire beam and spectrometer will ride on large steerable steel wheel bogies that permit radial motion and scattering angle changes. The wheel sections will be driven by motors and reducers with variable frequency drives. The wheels are planned to be flat cylindrical wheels that are steered while in motion to control the radius of rotation.

The MAD rotates and translates as a free body, without pivot connection. The wheels can be steered over 90° and then used to position the spectrometer radially for the lower acceptance small angle regime (12°-35°), the regime with a septum magnet (6°-12°), and the large acceptance (greater than 35°) regime. Pointing is achieved by slewing the front wheels relative to the rear

wheels and using a laser retro-reflector system to achieve the desired pointing accuracy. The retro-reflector is mounted on a reference circular stage on the scattering chamber. The distance off the pivot is determined by the same system.

The motion of the MAD spectrometer is coordinated by a stand-alone PLC that integrates the drive wheel motion, laser system read-back, proximity sensors and the laser scan (light curtain) obstacle detection. The rotation motion is limited to a preprogrammed range set in EPROM in the PLC and by the proximity detection. The slew drive system is a maximum $\pm$ 1 cm and a minimum $\pm$ 1 mm jog type system that acts on the front drive wheels only. Shaft encoders on the drive wheels are used to control the motion. A scale etched into the floor at the radius of the rear drive wheels and viewed by a video camera with a graticule lens is used to confirm the scattering angle setting. A sieve slit will provide angular calibrations of better than 0.5 mrad. Pointing accuracy is confirmed by the laser retro-reflector system with the spectrometer at rest. The final distance off the pivot is measured when all angle adjustments have been made.

The MAD spectrometer shield house is a reinforced cast-concrete structure that is built on the steel carriage. The concrete is confined by a steel housing that is up to 10 cm thick. The concrete thickness varies to optimize the shielding in all directions. The concrete is 80 cm thick in the sides towards the beam, back, and bottom. The sides away from the beam and the top are 40 cm thick and the front toward the target is 70 cm thick. The concrete is formed and poured in place including the two door sections. The concrete is a conventional mix with borate added to absorb thermal neutrons. The interior walls, floor, and ceiling will have a minimum 1 inch thick lead lining except for the front wall which has 3 inches of lead. The MAD detectors will be mounted on a transverse rail system so that the detectors may be moved sideways for servicing and relocated accurately. The shield house will be accessed by doors that are hinged to open outward on the side away from the beam.

The MAD spectrometer has three vacuum systems dedicated to the operation of the magnets, the MAD spectrometer vacuum, and the Čerenkov detector. The MAD cryogenic system is presumed to be leak-tight and cryo-pumping so a dedicated vacuum system is not included. The magnets are also assumed to be leak-tight but a vacuum system tailored to leak testing, commissioning, and bi-annual vacuum servicing is included as a dedicated vacuum system. This system can be used to commission and service the cryogenic system as needed. This system is assumed to be portable, self-contained, and fully instrumented. The spectrometer vacuum system and the Čerenkov vacuum systems are dedicated to these two systems and are permanently installed on the MAD.

3.A.2   Optical Characteristics of the MAD Spectrometer

The quadrupole components of the MAD provide the focusing necessary to achieve the desired solid angle while the dipole components provide the dispersion needed for momentum resolution. The

Table 18: The table shows the estimated performance parameters based on TRANSPORT calculations of the optical properties. The error estimates assume a 0.5 mrad angle determination and 100 μm position determination.

Configuration	35°	20°	12°	6°
Central Momentum	7.5 GeV/c	7.5 GeV/c	7.5 GeV/c	7.5 GeV/c
$\Delta p/p_0$	± 15%	± 15%	± 15%	± 15%
y_0	±25 cm	±25 cm	±25 cm	±25 cm
θ_0	± 198 mrad	± 138 mrad	± 68 mrad	± 50 mrad
ϕ_0	± 35 mrad	± 32 mrad	± 23 mrad	± 20 mrad
$\Delta\Omega$	∼ 28 msr	∼ 18 msr	∼ 6 msr	∼ 4.5 msr
δy_0	2.6 mm	3.6 mm	4.6 mm	4.6 mm
$\delta\theta_0$	1.9 mrad	1.3 mrad	0.6 mrad	0.6 mrad
$\delta\phi_0$	0.5 mrad	0.5 mrad	0.5 mrad	0.5 mrad
$\delta\sigma$	1.3×10^{-3}	1.0×10^{-3}	0.7×10^{-3}	0.7×10^{-3}

maximum central momentum is 7.5 GeV/c. The total bend angle is 32° with a 10° bend in the first magnet and a 22° bend in the second. The larger bend in the second magnet was chosen to prevent direct line of sight between the target and the detectors while keeping the dispersion reasonably small thereby reducing the size requirements on the detector package. Extra versatility can be achieved by varying the drift distance to the first magnet. Larger drift distances allow smaller scattering angles at the cost of reduced acceptance. Depending on the details of the detector package, scattering angles as small as 12° are possible, which can be extended to 6° with a septum magnet. The overall performance expected of the spectrometer is summarized in Table 18.

The optics is very much that of a quadrupole pair. The large acceptance is achieved by keeping the magnets as short as possible and as close together as possible. The first-order transfer matrices for the 35° and 20° configurations are shown in Table 19. In both cases $< x|\delta\theta >\sim 17$, which drives the expected momentum resolution at $\delta\pm$ 15%. The first-order transfer matrix for the 12° configuration is also shown in Table 19; in this case, $< x|\delta\theta >\sim 25$. The extreme particle trajectories for the MAD optics are shown in Fig. 147.

A working model of MAD was developed using the ray-tracing code SNAKE. The magnetic fields in the magnets were based on TOSCA-generated maps. Two maps were created by running TOSCA with only the quadrupole coil energized and with only the dipole element energized; these maps were then added with scale factors to simulate tuning the various elements. Once the first-order properties expected from the TRANSPORT studies were obtained, a large number (appr. 2000) of random trajectories spanning the full acceptance of the spectrometer were traced through the spectrometer using SNAKE. These trajectories were then used as input to a fitting program (MUDIFI) that determines the best-fit polynomials reconstructing the target parameters (δ, θ_0, y_0, and ϕ_0) of the trajectories based on their positions and angles (x_f, y_f, θ_f, and ϕ_f) in the detectors. The sensitivity to measurement errors in the detectors can then be explored in a Monte-Carlo
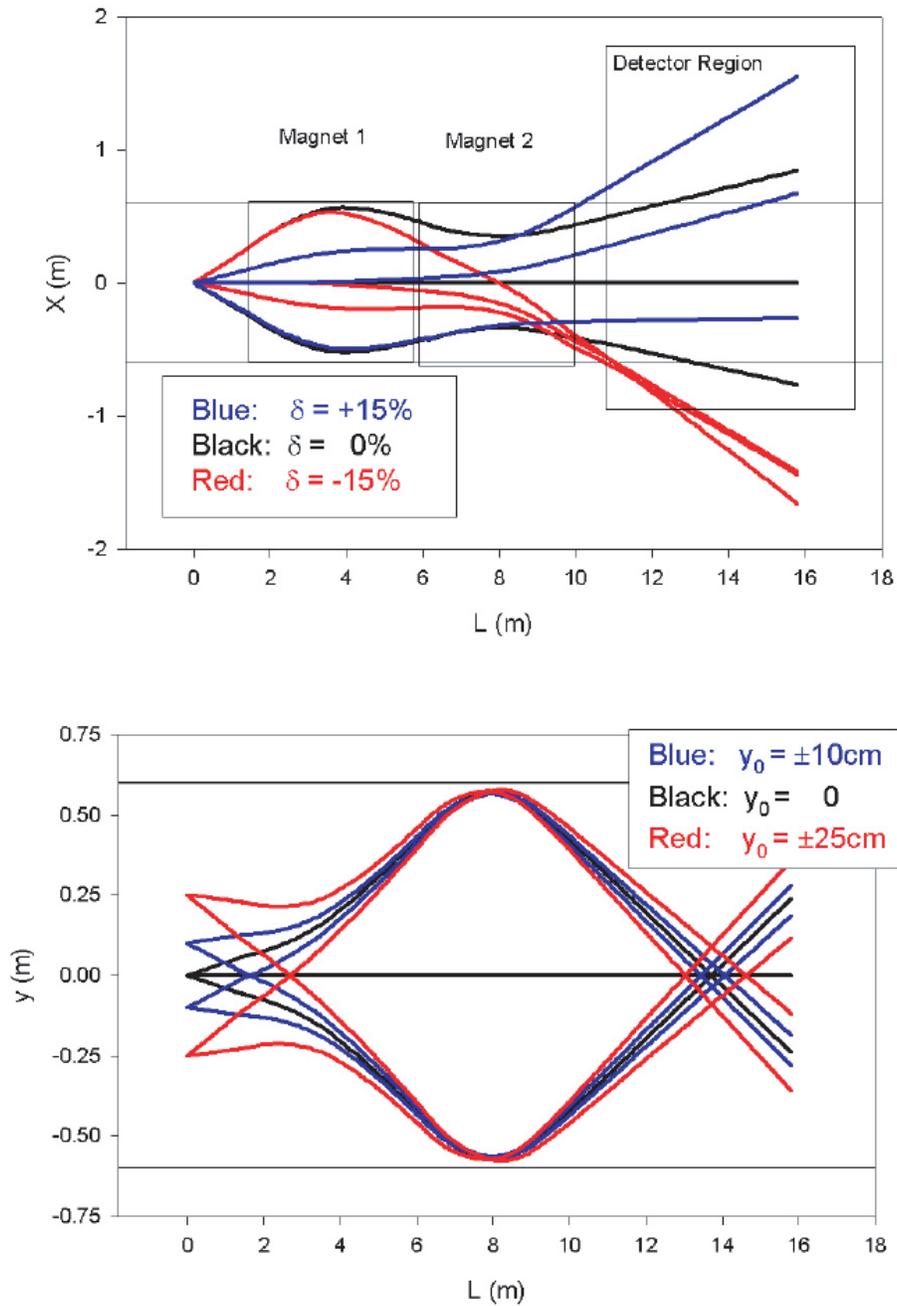
Figure 147: The top plot shows the distribution of extreme trajectories in the bend plane for δ of +15%, 0%, and -15%. The bottom plot shows the distribution of the extreme transverse rays at $\delta=0$ for different values of y_0.

Table 19: The first-order TRANSPORT matrices in natural units (m) for various configurations of the MAD spectrometer

For the 35 degree configuration:

$$
\begin{bmatrix} x_{fp} \\ \theta_{fp} \\ y_{fp} \\ \phi_{fp} \\ \delta_{fp} \end{bmatrix} = \begin{bmatrix} -3.72 & 0.00 & 0.00 & 0.00 & 3.54 \\ -1.03 & -0.27 & 0.00 & 0.00 & 103.0 \\ 0.00 & 0.00 & 1.00 & 5.15 & 0.00 \\ 0.00 & 0.00 & -1.05 & -4.43 & 0.00 \\ 0.00 & 0.00 & 0.00 & 0.00 & 1.00 \end{bmatrix} \begin{bmatrix} x_{tg} \\ \theta_{tg} \\ y_{tg} \\ \phi_{tg} \\ \delta \end{bmatrix} \tag{71}
$$

For the 20 degree configuration:

$$
\begin{bmatrix} x_{fp} \\ \theta_{fp} \\ y_{fp} \\ \phi_{fp} \\ \delta_{fp} \end{bmatrix} = \begin{bmatrix} -2.51 & 0.00 & 0.00 & 0.00 & 3.29 \\ -0.70 & -0.40 & 0.00 & 0.00 & 90.2 \\ 0.00 & 0.00 & 1.00 & 7.10 & 0.00 \\ 0.00 & 0.00 & -0.79 & -4.58 & 0.00 \\ 0.00 & 0.00 & 0.00 & 0.00 & 1.00 \end{bmatrix} \begin{bmatrix} x_{tg} \\ \theta_{tg} \\ y_{tg} \\ \phi_{tg} \\ \delta \end{bmatrix} \tag{72}
$$

For the 12 degree configuration:

$$
\begin{bmatrix} x_{fp} \\ \theta_{fp} \\ y_{fp} \\ \phi_{fp} \\ \delta_{fp} \end{bmatrix} = \begin{bmatrix} -1.22 & 0.00 & 0.00 & 0.00 & 3.29 \\ -0.37 & -0.82 & 0.00 & 0.00 & 90.2 \\ 0.00 & 0.00 & 1.00 & 12.4 & 0.00 \\ 0.00 & 0.00 & -0.53 & -5.51 & 0.00 \\ 0.00 & 0.00 & 0.00 & 0.00 & 1.00 \end{bmatrix} \begin{bmatrix} x_{tg} \\ \theta_{tg} \\ y_{tg} \\ \phi_{tg} \\ \delta \end{bmatrix} \tag{73}
$$

fashion using a new set of trajectories generated in the same manner as those used in the fitting. Figs. 148a)-d) show the resolutions δ, θ_0, y_0, and ϕ_0 generated in the Monte Carlo analysis. There is a reasonable match between the Monte-Carlo analysis and the TRANSPORT based predictions, with some degradation particularly at large positive δ's. This is most likely a consequence of higher order aberrations not accounted for in the TRANSPORT analysis.

The overall performance shown is for a generic tune that roughly meets the needs of the proposed experiments. Alternate tunes are possible. Better momentum resolution in the positive delta region could be achieved at the cost of momentum resolution in the negative delta region, and trade-offs sacrificing acceptance for resolution, in momentum and angles, are possible.

3.A.3 Simulations of the MAD Spectrometer

Three different software packages were used to simulate the MAD spectrometer. The first two, MCEEP and SIMC, were employed mainly to simulate physics results such as counting rates and distributions. Results of these simulations can be found in the various physics sections of this document. The third software package, GEANT, was used to simulate the spectrometer performance in terms of backgrounds and resolution. Results of the GEANT simulations are given below.

MCEEP [Ulpc] and SIMC [Abpc] are standard simulation programs for the existing pair of Hall A high resolution spectrometers. They are designed to simulate (e,e'X) experiments by averag-
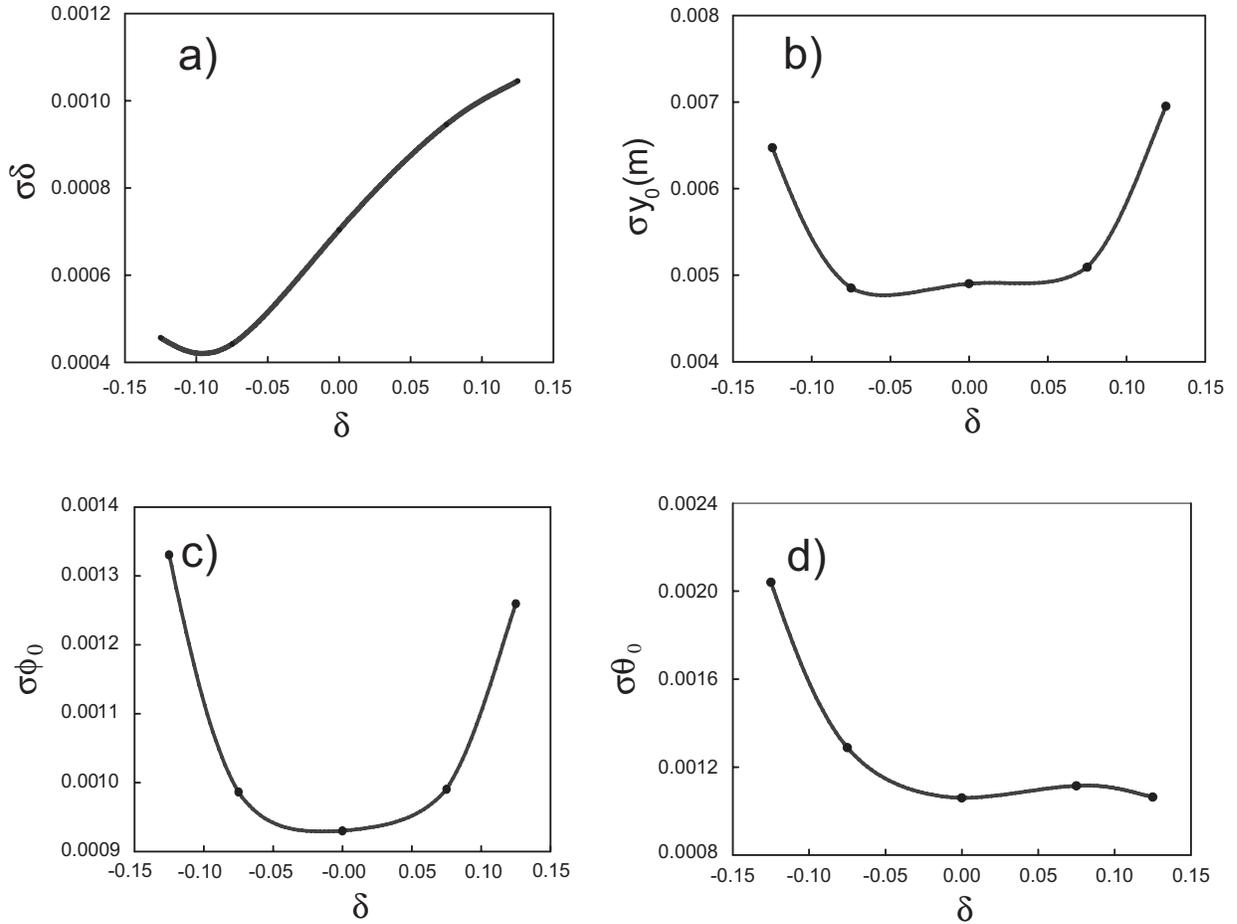
Figure 148: The MAD spectrometer's a) momentum, b) y_0, c) θ, and d) ϕ resolution. The calculations include the effects of multiple scattering in a polarized ^{3}He target and a 10 m helium bag, and the effects of the intrinsic resolution of the detectors.

ing theoretical models over an experimental acceptance. The current version includes cross-section models for the proton, deuteron, triton, ^{3}He, ^{4}He, ^{12}C, ^{56}Fe, ^{197}Au and ^{208}Pb. Single-arm experiments can also be simulated. Internal and external radiative effects and multiple scattering can be simulated. Spin transport and precession inside magnetic elements of the spectrometer can be taken into account. MAD is described within MCEEP and SIMC via a set of transfer functions, which are essentially TRANSPORT matrices generalized to higher orders. Both forward and reverse functions have been incorporated in MCEEP. Coefficients up to 5th order and sometimes higher were included.

A thorough simulation of the expected backgrounds in MAD detectors is particularly important because of its large aperture and momentum acceptance. A simulation was used to optimize the optics and collimators in order to reduce the backgrounds. The background consists of high-energy particles, like electrons from DIS and pions from photoproduction by quasi-real photons, as well as a low-energy photon background stemming from cascades of electromagnetic interactions of electrons in the target and windows. The latter background was simulated using GEANT 3.21. The geometry used included the target vacuum chamber with all relevant details of the construction, the windows and the target cell, as well as the MAD geometry including the distribution of the materials and magnetic field maps. The beam interaction with the material on its way and the interactions of the secondary particles was done with GEANT, which includes the most important electromagnetic reactions, such as Møller scattering, bremsstrahlung, Compton scattering, etc. The main source of background is a cascade of processes involving low energy photons going inside the spectrometer aperture, scattering (via Compton scattering) one or more times on the walls of the spectrometer chamber, and finally impacting on the detector. There are several ways to reduce this background:

a) *Increase the bending angle of the spectrometer.* It turns out that increasing the bending angle from 20° to 32° reduces the background by a factor of 5.

b) *Place collimators inside the spectrometer in its focal areas.* The spectrometer optics accepts particles crossing the entrance to the first magnet of MAD in a relatively narrow vertical band. A collimator (COL1) with a rectangular opening 30 cm wide and 100 cm high does not affect the acceptance while reducing the background. Additionally, a collimator (COL3) close to the target chamber and leaving only the particles coming directly from the target, helps. In the vertical projection, MAD focuses the particles at about the center of the second magnet. A collimator (COL2) 30 cm upstream of the center of the second magnet with a hole about 30 cm high and as wide as the magnet bore helps to reduce the background. All three collimators reduce the soft photon background by a factor of 3.

c) *Trap the photons on a special profile of the spectrometer chamber surface.* The hole in COL2 is in the direct line of sight from the target. Nearly half of the background left is formed by photons passing directly from the target through this hole and rescattering on the bottom side of the magnet chamber behind the collimator. A periodic structure on the surface of the chamber can reduce the background by a factor of about 1.5.

Table 20: MAD detector parameters

	Scintillators	Drift Chamber	Gas Čerenkov	Calorimeter
sensitive area	$0.5(0.6) \times 2.0(2.5)$ m^2	0.5×2.5 m^2	0.6×2.5 m^2	1.0×3.0 m^2
depth used	10, 10, 20 cm	100 cm	250 cm	100 cm
segmentation	16 paddles, 4 planes	1200	12 PMTs	192 PMTs
resolution	0.15 ns	75 μm	> 7.5 ph.electrons	$10\%/\sqrt{E}$

With MAD positioned at $25°$, with a 50 μA beam impinging on a 15 cm liquid hydrogen target the calculated photon flux in the detector area is about 100 MHz with an average energy of $\sim$0.7 MeV. The photon energy spectrum is well described by the function $\frac{dN}{dE} \propto e^{-\alpha \cdot E}$, where α=1.5 MeV^{-1}. This flux was taken into account in the detector design.

3.A.4   MAD Spectrometer Detector Systems

With a maximum central momentum of 7.5 GeV/c for the spectrometer and a momentum bite of $\pm 15\%$ a wide range of momenta (0.4-9 GeV/c) must be considered in the design of the detector package. The proposed detector package for the spectrometer has three major functions: triggering, tracking, and particle identification. These are accomplished by using scintillator counters, multi-wire drift chambers (MWDC), gas and aerogel Čerenkov counters, and an electromagnetic calorimeter. Figure 149 shows the side view of the detector package in the configurations for electron and for hadron detection. The trigger will be formed from the signals of scintillators, Čerenkov counters, and the electromagnetic calorimeter. Two MWDCs separated by 100 cm will provide tracking information for momentum and angle reconstruction. A multi-wire proportional chamber (MWPC), installed between MWDCs, will improve the high-rate capability of the tracking system. The main parameters of the detector package are presented in Table 20 (without aerogel Čerenkov counters and Focal Plane Polarimeter).

Particle identification in the electron configuration utilizes the gas Čerenkov counter and the electromagnetic calorimeter. A variable refraction index is achieved by using a mixture of helium and nitrogen. The required pion rejection factor is dictated by the π/e ratio in inclusive electron scattering, which varies from less then 10^3 at high momentum up to 10^5 at low momentum and forward angles. The pion rejection factor, the product of rejection by the electromagnetic calorimeter (100) and gas Čerenkov counter (200), is sufficient to reduce the pion contamination to the 1% level in inclusive electron scattering experiments. A higher rejection factor, required at lower momentum settings, will be achieved by using gas with a higher index of refraction.

Two aerogel Čerenkov counters and a short (100 cm), high-index, gas Čerenkov counter will be used in the hadron configuration. The Čerenkov counters for the hadron configuration will use the same space as the low-index gas Čerenkov counter in the electron configuration. Expected rates in the spectrometer are shown in Table 21. They were calculated for a beam energy of 11 GeV and a

Table 21: Single rates in MAD detector (kHz) with $E_{beam} = 11$ GeV , $I_{beam} = 70$ μA, and a 15 cm long liquid hydrogen target.

p(GeV/c)	$\theta = 15°$				$\theta = 25°$				$\theta = 35°$			
	e	π^-	π^+	p	e	π^-	π^+	p	e	π^-	π^+	p
1.5	1	780	830	360	500	290	300	290	0.1	21	120	330
3.0	3	90	90	170	0.4	5	100	270	0.02	0.04	130	270
4.5	4	9	70	170	0.1	0.03	30	280	—	—	—	—

beam current of 70 μA on a 15 cm liquid hydrogen target (the luminosity is 2.5×10^{38} Hz/cm^2).

The following paragraphs present the details of proposed detectors and their expected performance. The detector package does not need to be moved when the magnets are moved away from the interaction point to accommodate more forward scattering angles.

Scintillators The trigger package for the MAD detector system consists of four segmented planes of scintillators, designated S_0, S_1, $S_2.V$, and $S_2.H$. The S_0 and S_1 planes are located immediately before and after the drift chambers, respectively. The S_2 package will consist of two planes ($S_2.V$ and $S_2.H$), oriented orthogonal to each other in a hodoscope configuration, and located just before the electromagnetic calorimeter. The primary DAQ trigger is formed by a coincidence between the S_1 and S_2 planes, with timing set by $S_2.V$. The S_0 plane will be used primarily for trigger efficiency studies and can be removed when multiple scattering degrades the angular resolution of the spectrometer. Each plane will be segmented into 16 elements to keep the total rate in a given paddle at an acceptable level.

Based on GEANT simulations, the background rate due to low-energy photons will be approximately 10^8 Hz under typical running conditions. The fraction of these photons that interact is 4% in S_0 and S_1, and 30% in each plane of S_2. Using discriminator thresholds of 0.5 MeV for S_0 and S_1, and 5 MeV for S_2 provides high efficiency for electron detection while reducing the background singles rate per paddle to approximately 50 kHz in S_0 and S_1, and 100 Hz in each plane of S_2. Requiring a coincidence between S_1 and one of the S_2 planes yields a background trigger rate of approximately 10 Hz. Requiring S_1 and both planes of S_2 in coincidence makes the background trigger rate negligible.

The scintillator elements in the S_0 and S_1 planes will be stacked horizontally (segmentation in the dispersive direction). The thickness of each element is 0.5 cm for S_0 and S_1, with a 1 cm overlap between adjacent elements. Each of the S_2 planes will contain 16 scintillator elements, with one plane oriented vertically and the other horizontally. The scintillator elements in S_2 are 5 cm thick to provide good timing resolution ($\sigma < 150$ ps). Approximate geometrical dimensions for each element are given in Table 22.
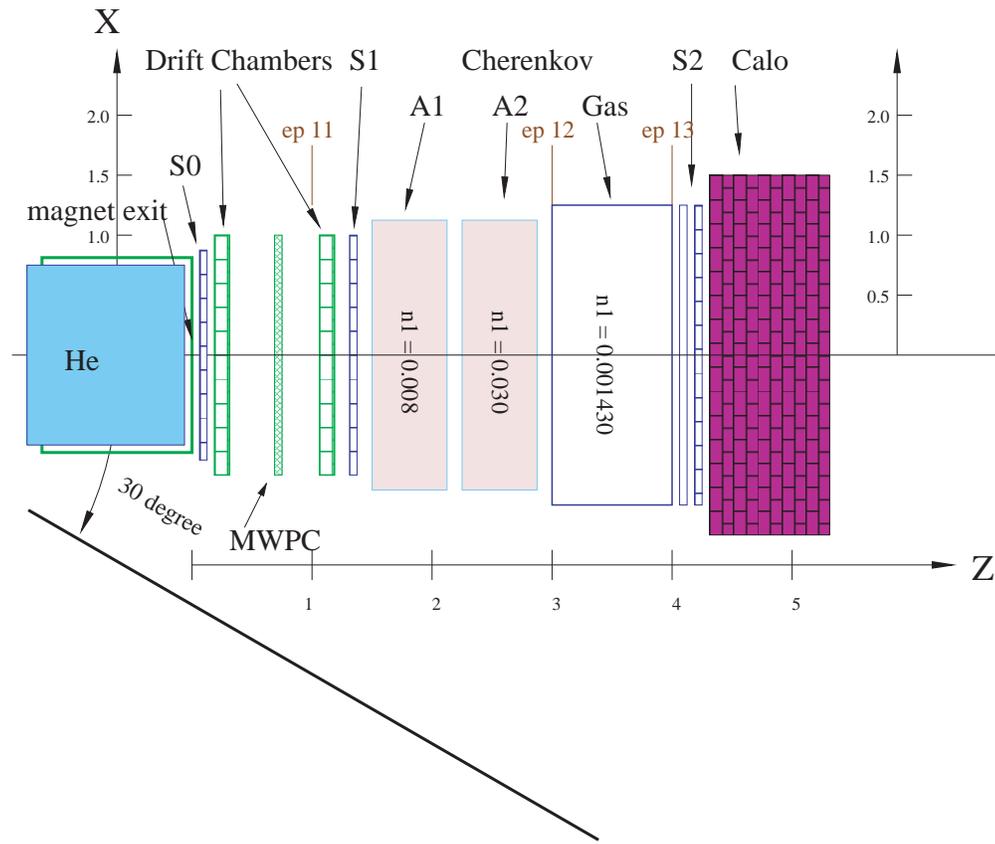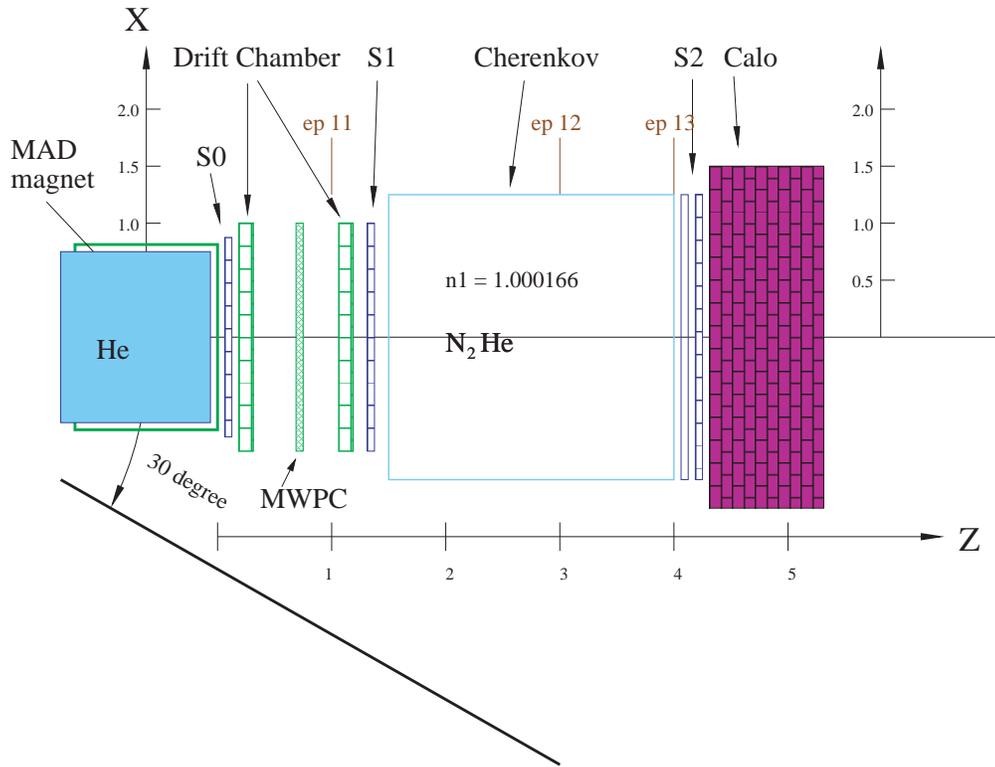
Figure 149: Configuration of the detector package for electrons (top) and hadrons (bottom).

Table 22: Geometrical specifications for scintillator planes.

Plane	Location (z)	Active Area (H x V)	Number of Elements	Element Dimensions, cm (L x W x T)
S_0	0.0-0.1 m	0.50 m x 2.0 m	16	50 x 13.5 x 0.5
S_1	1.3-1.4 m	0.50 m x 2.0 m	16	50 x 13.5 x 0.5
$S_2.V$	4.1-4.2 m	0.60 m x 2.5 m	16	60 x 16 x 5
$S_2.H$	4.2-4.3 m	0.64 m x 2.5 m	16	4 x 250 x 5

The detectors will be built of Bicron BC-408 or Eljen Technologies EJ-200 with a typical pulse width of FWHM $\sim$ 2.5 ns and long attenuation lengths. Each scintillator will have light guides attached to both ends which will channel the light onto 2 inch diameter photomultiplier tubes (PMTs). For S_0 and S_1, a high gain PMT such as the Photonis XP2262 is appropriate. For S_2, the light output is expected to be high and a fast, 8-stage tube such as the Photonis XP2282B is suitable.

Drift Chambers A system of two drift chambers and a multi-wire proportional chamber is proposed to instrument the MAD focal plane. The first drift chamber is located at 0.1 m from the exit of the last MAD magnet, the second drift chamber 1 m further down-stream. The MWPC will be located at the mid-point between the chambers. Simulations of particle tracks through the MAD spectrometer indicate that the active area of the second chamber needs to be only about 20% larger than the active area of the first chamber. Design and construction considerations make it more cost-effective and convenient to make all three chambers with the same dimensions, 0.6 m $\times$2.5 m. The two drift chambers are proposed to have identical design, each with three groups of wire planes with wires oriented at +45° (u) , -45° (v) ,and +90° (x). Each group of wire planes consists of four planes separated by 1 cm each. The four planes in each direction are essential to reconstruct good tracks in a high-rate environment. Furthermore, the four planes provide high resolution and high efficiency: single-wire plane resolutions of roughly $100 - 150$ μm have been achieved in the past, having four planes will improve this resolution to the required 75 μm value. In case of inefficiencies, at least two wire planes in the same direction are required to resolve the left-right ambiguity of drift times. With the single-wire inefficiency for a drift chamber usually very low ($< 3\%$), the inefficiency for a chamber with four planes, resulting from the absence of two out of four planes, is extremely small. The low-energy photon background at the MAD focus is estimated to be 100 MHz. Assuming a conversion efficiency of 0.1% we can estimate a low-energy electron rate of 0.1 MHz at the drift chambers. Some of these electrons will give random hits in the wire planes while others will make tracks through one or both drift chambers. The dead-time per drift cell, mainly arising from the drift of positive ions away from the region around the sense wire, electronic dead-time and pulse-widths, is usually limited to several hundred ns. As a result, the soft-photon background results in a negligible dead-time. Furthermore, four wire planes are combined in each direction and hence, the high timing resolution of the drift chamber can be used to suppress hits and tracks from

background electrons. The per-wire position resolution of roughly 100 μm corresponds to a timing resolution of about 2 ns. Thus a comfortable 5σ track reconstruction window of 10 ns can be used to select good tracks. This will easily separate the real track that registered the scintillator trigger from background tracks. The extra group of planes (x) enhances high-rate operation and further improves resolution. In the rare case where two out of the four planes in a (u), or (v) group fail to fire, the hits on the (x) planes can be used to ensure that the chamber has almost 100% efficiency. A wire spacing of 30 mm between sense wires is proposed to give a drift distance of 15 mm. This drift distance corresponds to a drift time of roughly 300 ns, and an extremely high limit on the rate *per wire* of around 3 MHz. For this inter-wire spacing, each plane will consist of 65 sense wires (about 1600 sense wires for the two chambers). Sensitive planes will contain alternating sense and field wires. Each sensitive plane will be between two field-shaping planes consisting of only field wires separated by 5 mm.

The chamber will be constructed out of planar frames. This design is popular in wire-chamber construction as it allows convenient wire stringing and easy access to each wire plane. The wire-chamber simulation package GARFIELD has been used for a complete simulation of the electric field configurations, drift parameters, and resolutions of the proposed drift chambers.

Gas Čerenkov Counter   The gas Čerenkov counter is ~1.5 m from the exit of the magnet, just after the S_1 scintillator counter. In the electron configuration (Fig. 149) the counter is 2.5 m long. The mixture ratio of two gases (He and N_2) will be used to adjustment the index of refraction, so that the number of photo-electrons is maximized for the given momentum and length of the radiator while keeping the pion speed for the same momentum below the threshold of Čerenkov radiation. Figure 150 shows the parameters of the counter vs. particle momentum. At 6 GeV/c central momentum the fraction of N_2 will be 60% resulting in approximately 8 photo-electrons.

In the hadron configuration the length of the counter will be reduced to 1 m. Here, the counter will be used to reject electrons. Depending on the needs of the particular experiment, the momentum threshold for pions can be adjusted by changing the partial pressure of Freon 114. In the momentum range above 2.7 GeV/c this detector can be used for positive identification of a pion.

The back surface of the Čerenkov counter is covered by 12 mirrors in a 2×6 arrangement. Each mirror is tilted by 15° so that the reflected photons can be collected at the side wall of the chamber. Including the tilt, each mirror measures 62 cm×50 cm. Since we need to allow a small overlap between mirrors, the size of the actual mirror will be a little larger than this, about 63 cm×52 cm, which is still reasonable for manufacturing. Each mirror will have a spherical shape with a radius of 1 m (focal length of 50 cm). Figure 150 also shows the geometry of the Čerenkov counter with schematic diagrams for mirrors and phototubes.

Using the transfer functions of MAD, emission of photons, reflection on the mirror and collec-
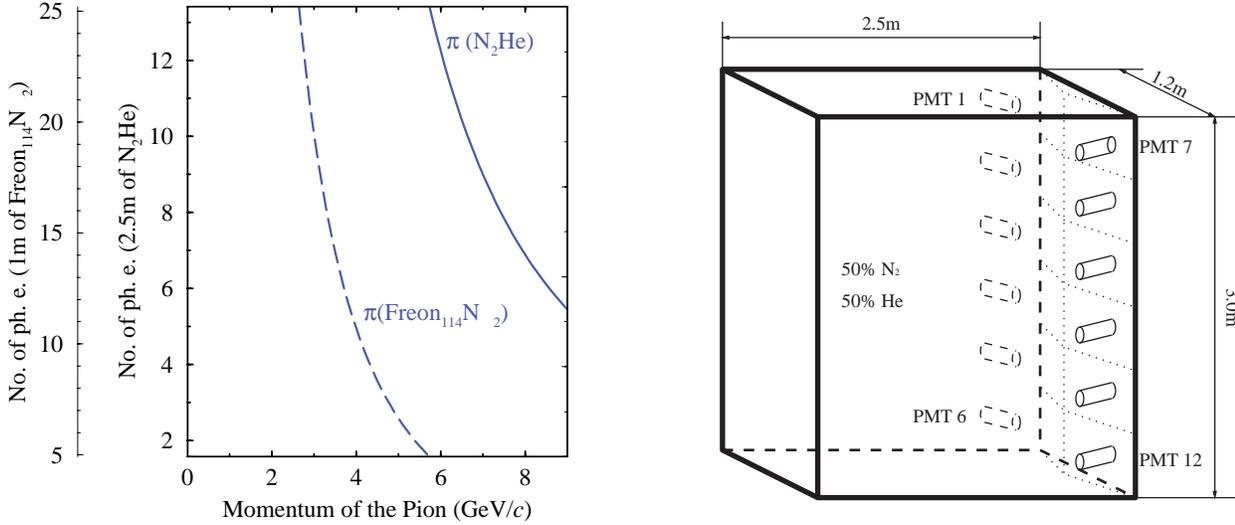
Figure 150: Number of photo-electrons expected for high-energy electrons in the gas Čerenkov counter. The solid line represents the N_2-He mixture and the dashed line the mixture of Freon 114 and N_2. Also shown a schematic diagram of the detector's geometry.

Table 23: Collection efficiency of photons for each phototube.

Tube Number	Efficiency(%)	Tube Number	Efficiency(%)
1	97.6	7	97.6
2	99.7	8	99.4
3	99.9	9	99.9
4	97.3	10	97.4
5	91.4	11	92.4
6	82.5	12	82.6
Average		96.3	

tion in the phototubes have been simulated. Except for the bottom four tubes, almost all of the photons reflected by each mirror will be collected by the 5" phototubes. For the bottom four tubes, "Winston Cones" are used to increase the collection efficiency. The photon collection efficiency has been quantified for each mirror in Table 23 and averages about 96%. With Winston cones, this efficiency will increase slightly.

Aerogel Čerenkov Counters   Hadron identification, mainly π, K, or p, will be accomplished by a combination of time-of-flight measurement and threshold Čerenkov counters. Two aerogel Čerenkov counters, with indices 1.008 and 1.030, are required to cover the full momentum range, as shown in Table 24 and Fig. 151.

A design similar to the current aerogel detectors in Hall A, A1 and A2, will be employed. All the inner surfaces of the detector are covered with millipore paper, including the inactive edge of the PMTs. The detector is constructed out of two separable assemblies for PMTs and aerogel.
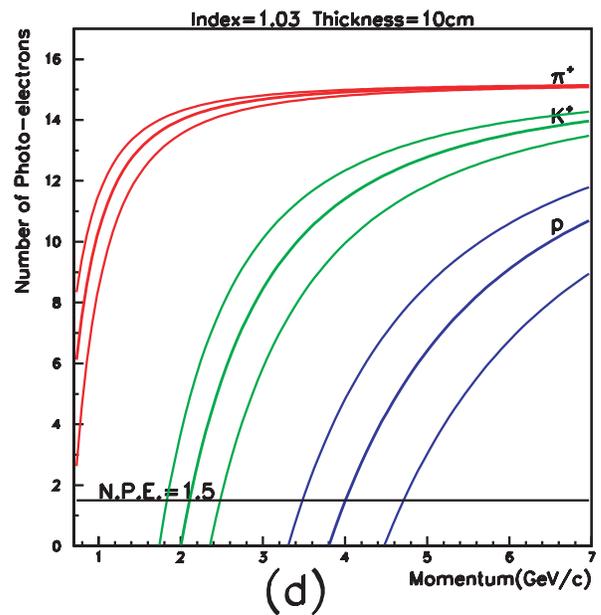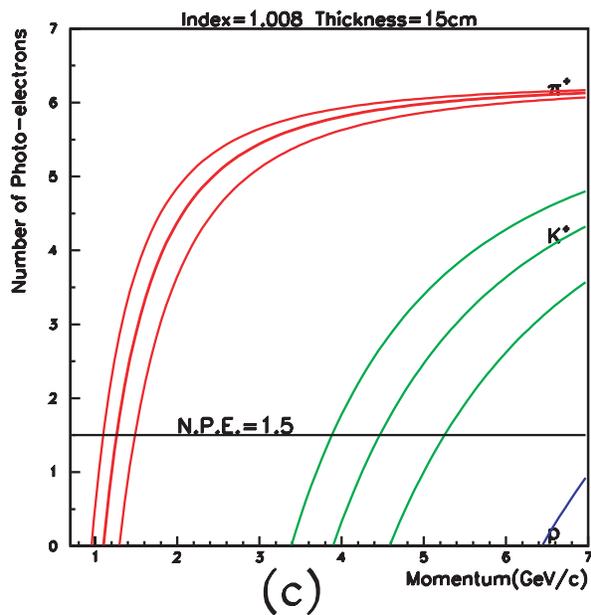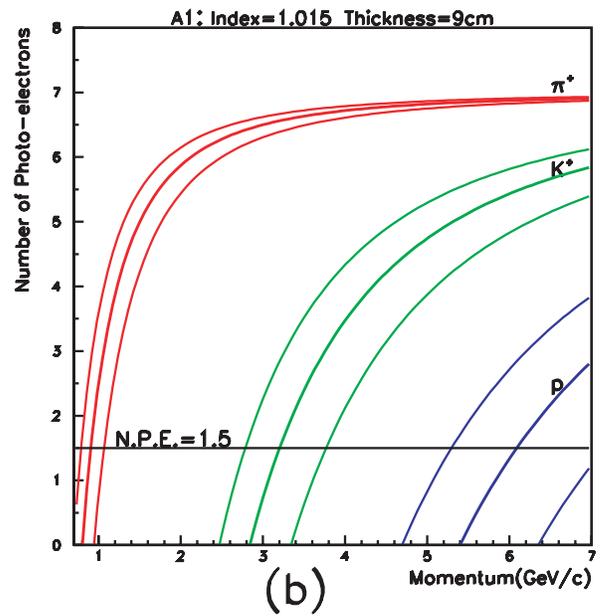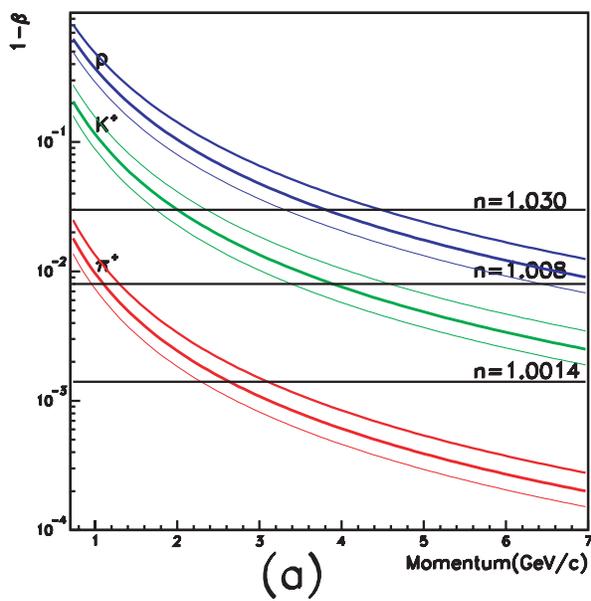
Figure 151: **(a)** The deviation of velocity from 1 vs. momentum for protons, pions and kaons. Dotted lines indicate the momentum bite of the spectrometer. **(b)** A1 performance with index of 1.015 and thickness of 9 cm. **(c)** Estimated number of photo-electrons vs. momentum for index of 1.008 and thickness of 15 cm. **(d)** Estimated number of photo-electrons vs. momentum for index of 1.030 and thickness of 10 cm.

Table 24: The momentum threshold to produce Čerenkov radiation.

Index	p_π (GeV/c)	p_K (GeV/c)	p_p (GeV/c)
1.030	0.58	2.06	3.92
1.008	1.11	3.93	7.46
1.00143	2.61	9.24	17.6

However, some differences do exist:

- Dimensions: The MAD aerogel Čerenkov counters are 0.6 m(H)×2.5 m(V), significantly larger than the dimensions of A1 or of A2. Due to the wider horizontal dimension, the photons will be subject to more diffusion and losses on their way to the PMTs located on the sides of the detector. To compensate for the losses the height of the detector needs to be increased, which requires 2-3 layers of PMTs.

- Magnetic field: A magnetic shield is required as the magnetic field is at the level of 10 G. We will either add an enclosed shield for the whole detector, i.e. to insert an 0.50 mm iron planes before and after the aerogel detector with thicker iron on the sides or add individual shields for each PMT.

- Aerogel thickness: Fewer photo-electrons are expected when the refractive index gets closer to 1, which is nearly proportional to $n - 1$. To get enough photo-electrons, the aerogel thickness must be increased for index n=1.008. The number of photo-electrons will saturate at a thickness of approximately 15 cm due to absorption and scattering in the aerogel.

Based on the performance of A1($n = 1.015$), shown in Fig. 151(b), the number of photo-electrons at different momenta was estimated for indices of 1.008 and 1.030, as shown in Fig. 151(c,d). The value of the rejection factor for a given momentum was estimated to be 30 based on experience with A1.

Electromagnetic Calorimeter   An electromagnetic calorimeter is planned as the most downstream detector in the MAD detector stack. The main purpose of the calorimeter is to separate electrons and charged pions. Electrons, producing showers, have nearly all their energy absorbed in the calorimeter, whereas, only a small fraction of the energy of a hadron will be absorbed. Comparing the energy release in the calorimeter with the momentum of the particle provides pion/electron discrimination.

The size of the calorimeter was selected using the GEANT simulation of MAD at 25° and 35° and at a mean energy of 7.5 GeV. The initial particle was produced in a 10 cm long liquid hydrogen target with uniform angle and momentum distributions over the MAD acceptance. The

results depend considerably on the optics applied, in particular in y-projection (perpendicular to the dispersive direction), since the calorimeter is close to the transverse focus of MAD. Based on the simulation, a lead glass array of 3.2×1.0 m^2 is considered for the present purposes. Since most of the events in MAD will contain only one high-energy particle, only a coarse transverse segmentation of the calorimeter is required.

It is proposed to build a lead-plastic scintillator sandwich calorimeter, about 22 radiation lengths deep, divided along the dispersion direction in 32 bars. Each bar is 10 cm wide and 100 cm long. The bar is divided in three segments along its depth in order to improve the e$^-$/π separation. Since the light attenuation in the scintillator sheets along the bar length of 100 cm is considerable, each segment is read out by two PMTs from both sides of the bar. In total the detector will include 192 PMTs.

A similar design[Am01] is used in the calorimeters in the CLAS detector in Hall B; in this case with three projections read out from triangular-shaped detector modules, employing the same compensation of the attenuation losses. With longitudinal segmentation in two segments an energy resolution of about $\sigma_E/E \sim 0.1\,GeV/\sqrt{E}$ and a e$^-$/π suppression factor of about 100 was obtained. The sandwich contained 2.2 mm lead sheets and 10 mm plastic scintillator sheets. The light was collected with the help of optical fibers. For the design proposed a similar result is expected.

Focal Plane Proton Polarimeter   Conventional polarimeters measure an azimuthal asymmetry from the scattering of the protons in an analyzer to determine the polarization. The incoming trajectory is determined by the focal plane MWDCs, while the outgoing trajectory is determined by tracking chambers specific to the polarimeter. The polarimeter figure of merit, ϵA^2, is enhanced by a large efficiency for detecting scattered protons. This requires both large polarimeter chambers - the existing Hall A polarimeter can measure scatters up to about 70° - and thick analyzers, up to about 1 m, to increase the scattering efficiency. Because thick analyzers also absorb a significant fraction of the protons, up to about 50% at 3 – 4 GeV/c, it is further desirable to segment the polarimeter, alternating layers of analyzer with chambers. A double analyzer, as has been used in the Hall A RCS experiment, is a reasonable compromise between increased costs and increased efficiencies.

Due to the large beam envelope with MAD, an alternate detector stack to the conventional design is desirable. In the experiments considered so far, the only significant background is π^+ mesons, which can be sufficiently reduced through the use of a single Čerenkov detector. Use of smaller tracking detectors further forward in the detector stack reduces the cost of the FPP. The layout of the focal plane polarimeter is shown in Fig. 152. Use of a CH$_2$ analyzer with a density near 1000 kg/m^3 leads to a total analyzer mass of 4500 kg. A carbon analyzer of similar volume would yield a similar figure of merit, with about 60 – 70% greater density. To capture scatterings from the analyzer with a good geometric efficiency, the tracking chambers would need to extend about ± 50 cm beyond the analyzer, leading to active areas near 2.5 m wide by 4 m high. We propose to
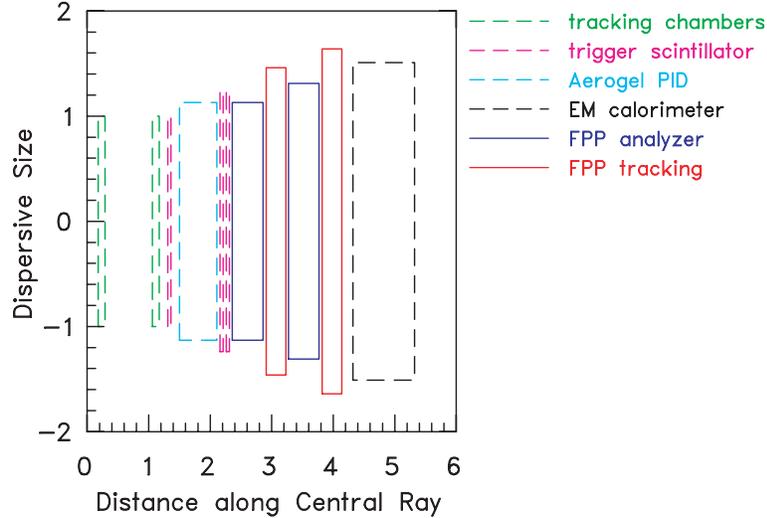
Figure 152: Layout of the MAD focal plane polarimeter.

construct a set of 4 multilayer straw-tube chambers, very similar in design to the existing Hall A FPP, to cover the above active area. With 2 cm drift cell diameter, the number of channels will be about 5000.

Trigger Electronics The proposed trigger electronics system will be built using commercially available components which follow VME, NIM and/or CAMAC standards. The described system will work as well with a DAQ system in a conventional environment or with a DAQ system based on Flash ADCs and Pipelined TDCs. To accomplish high singles rates in some of the detector subsystems, only modules capable of handling rates of 100 MHz or more are acceptable.

As described previously, the detector package of the MAD includes up to four scintillator planes, each made of 16 long scintillator paddles equipped with photo-multiplier tubes (PMTs) on each end. Although the main trigger will usually be formed by the signals of two planes only, all four planes will be built in the same fashion. Then, the trigger definition is very flexible and can be adjusted to the individual needs of each experiment.

The analog signal of each PMT will be split passively on the base of the tube. One signal will be fed into a pipeline Flash ADC, requiring no delay cable. The second signal will be fed into a leading-edge discriminator (e.g. CAEN V895 or C894). The specific modules mentioned parenthetically are examples of presently available off-the-shelf units. The discriminators listed above provide two copies of the logical signal. One will be used for timing purposes and put into a TDC. A programmable delay (e.g. CAEN C211) is used to adjust small timing differences within the different channels. A 16 channel mean-timer (e.g. CAEN C561 or V706) is used to combine the signals of the two PMTs of each scintillator paddle, and make this signal independent of the point of intersection. Finally the logical "or" of the 16 signals is formed in a logic module (e.g. CAEN C561

Table 25: Equipment needed for the triggering system of the MAD detector package

Device	Typical Module	Form Factor	Units (includes spares)
LE Discriminator	Caen C 894	CAMAC	15
Prog. Delay	Caen C 211	CAMAC	10
Mean-timer	Caen C 561	CAMAC	6
Gate and Delay	Caen C 469	CAMAC	4
PLU	Caen C 542	CAMAC	2
ECL-NIM-ECL	Caen C 467/468	CAMAC	6
Fan-Out	Caen C 211	CAMAC	5
Coinc Unit	Caen V 512	VME	4
CAMAC Crates			3
VME Crates			2
VME CPUs			2
CAMAC Controllers			3
Cables			

or V706). This signal is the trigger for each scintillator plane. Using Gate and Delay Generators (GDG, e.g. CAEN 469) and Programmable Logic Units (PLU, e.g. CAEN C542 or V495), the signals from the four scintillator planes can form various triggers, the definition of the trigger can be changed easily and other detectors, for example the Čerenkov detector, can be incorporated if needed. Some additional modules, Fan-in/Fan-Out modules, Level Converters and Coincidence Units, are needed to provide retiming signals, gates for the digitizing modules and scalers.

Data Acquisition   The data acquisition system is built in VME using commercial components like scalers, ADCs, and TDCs where available, plus new custom-built modules that are presently under development by collaborators. The system will have a high performance that will exceed FASTBUS standards. Accommodating the detector design will require approximately 400 ADC channels, 2000 TDC channels, and 400 scaler channels. For the scintillators 60 ps resolution TDCs can be used, while for drift chambers and other detectors a resolution of 0.5 ns is adequate.

A new generation of pipeline digitizing front-end devices can be used for experiments that require speeds in excess of 5 kHz, up to 20 kHz. For pipelined ADCs, there are two foreseeable alternatives. One is a custom-built pipelined Flash ADC being prototyped by Indiana University, which might be manufactured at JLab. In the pipeline approach detector data are continuously digitized and stored in a pipeline, which is a dual-port memory. When a trigger condition is satisfied, the data are extracted from the pipeline and read out on the VME backplane. This scheme has two attractive features: 1) the pipeline approach introduces no deadtime; and 2) delay cables can be avoided. However, a possible disadvantage with respect to ADCs is that if the sampling frequency is not sufficiently high, one may suffer loss of resolution. In tests at Indiana University [IUpc], it was found that with 250 MHz and 8 bits resolution, the Flash ADC samples resulted in an energy resolution much better that the intrinsic resolution of lead glass.

Table 26: Comparison of Pb-Glass, PbF_2, and $PbWO_4$ calorimeter properties.

	Pb-Glass TF-1	PbF_2	$PbWO_4$
Index of Refraction	1.65	1.85	1.85
Radiation Length X_0 (cm)	2.5	0.93	0.89
Moliere Radius r_0 (cm)	3.3	2.2	2.2
Density ρ (g/cm^3)	3.86	7.77	8.28
Photoelectrons/GeV	1100	1600	5000
Critical Energy (MeV)	15	8.6	

A new high-resolution pipelined VME TDC is being designed and prototyped by the Jefferson Lab DAQ group. This TDC has 60 ps resolution with 32 channels on a single slot 6U form factor, or 120 ps for 64 channels. The TDC can either run in a common start mode or a trigger matching mode. In the common start mode, a trigger starts and clears the hit counters, and a subsequent trigger initiates read-out of data since the start time. Of course, this mode will introduce deadtime. In the "trigger matching" or pipelined mode, a trigger is used to define a window in time to pull data out of a hit counter. The hit counter runs continuously even as the desired data is buffered in memory, and therefore produces very little deadtime.

3.A.5   High Performance Calorimeter

High intensity 11 GeV beams in Hall A offer unique possibilities for studying Real and Deep Virtual Compton Scattering (DVCS). These experiments require the construction of a large-acceptance and high-resolution electromagnetic calorimeter, capable of withstanding high levels of background. The photons need to be detected at angles as small as $10°$, with a luminosity of at least 10^{37}. This requires a calorimeter material that is radiation hard. It is also important to have a very fast time response to suppress pile-up and random coincidences.

PbF_2 is an attractive Čerenkov medium for electromagnetic calorimetry. Some basic properties of PbF_2 are listed in Table 26 and compared with Pb-Glass and $PbWO_4$, which are commonly used in electromagnetic calorimeters.

The primary distinction of PbF_2 is its very high Z^2 weighted density, resulting in much smaller individual element sizes. The transverse dimension of each element should be slightly larger than the Moliere radius, to optimize spatial resolution, and the longitudinal dimension should be 20 radiation lengths to fully contain the shower. High density PbF_2 will have lower background from hadrons (including neutrons) than Pb-Glass. The small size of the PbF_2 will also result in very narrow intrinsic time spread (< 0.6 ns r.m.s.) in the collected light [Ap94]. The leading edge time resolution and the total pulse width are both critical parameters for suppression of accidental

coincidences and pile-up rejection. Small blocks make it practical to couple the crystals to very fast photo-tubes.

For radiation doses from 200 Gy (20 kRad) to 1 kGy (100 kRad) the radiation damage to PbF_2 is a factor of 10 less than SF5 Pb-Glass.[Ac98c] Radiation damage reduces the transmittance of the crystals, with the greatest effects at short wavelengths. The transmittance reduced by radiation damage to PbF_2 can be easily annealed with blue light as well as natural light.

Electromagnetic shower energy resolutions of $(3 - 5.6)\%/\sqrt{GeV/E}$ and transverse position resolution of 1 mm$\sqrt{GeV/E}$ were reported for small test arrays for 1 to 6 GeV electrons [Ap94, Ac98c]. The spatial resolution may be degraded slightly with larger crystals, but it is clear that the very high spatial resolution will allow a PbF_2 array to be placed very near the target, without limiting the photon angular resolution.

The optimal angular coverage for DVCS experiments requires a calorimeter with a solid angle of 0.1 sr. To achieve a large solid angle coverage and high angular resolution, we propose a 1296 element array. In DVCS kinematics, with the calorimeter 3 m from the target, the design acceptance of 0.1 sr can be achieved with a photon angular resolution of 0.5 mrad.

Individual crystals will be 26x26x200 mm^3 rectangular blocks coupled to UV transmitting 25 mm fast PMT's. The EMI 9111WB 8-stage photomultiplier is chosen as a baseline solution. With a photo-cathode of 22 mm diameter, the PMT will cover 72% of the surface of the crystal. In addition, the PMT offers high quantum efficiency of about 28% and spectral response down to 180 nm. Simulations suggests light yields with the above solution to be about 2500 pe/GeV. The calorimeter will be arranged in a square matrix of 36x36 elements. However, the array will be flexible in design so that it can be easily reconfigured for a different geometry. A blue laser based light source coupled to each crystal will provide calibration, timing, and gain monitoring signal. Standard integrating ADC's for the readout and programmable high voltage supplies currently used in Hall A will be used.

3.A.6   The Hall A Beam Line

For the 12 GeV upgrade, the basic layout of the Hall A beamline and beamline instrumentation will remain the same. The quality of the beam will be somewhat compromised at the higher energies. Table 1 gives a comparison of the presently achievable beam parameters at 6 GeV and the expected beam parameters at 11 GeV.

No changes are envisaged regarding the primary diagnostic and beamline instrumentation [An03a, HallA]. This includes the present SEE Beam Position Monitors, the Hall A target OTR and the Scanners for beam profile measurements, the two RF cavity monitors (BCMs) and the Unser Monitor for beam current monitoring, the fast-feedback system to maintain the stability of the beam

Table 27: Key parameters of Beam Quality - present and with upgrade

Parameter	Present @6 GeV	With Upgrade @11 GeV
Horizontal emittance ϵ_x	$2.9 * 10^{-7}$ m.rad	$9 * 10^{-6}$ m.rad
Vertical emittance ϵ_y	$2.9 * 10^{-7}$ m.rad	$1.9 * 10^{-6}$ m.rad
Energy spread $\delta p/p$	$1 * 10^{-4}$	$2 * 10^{-4}$

in both position and energy, and the fast rastering system. The installation of a Synchrotron Light Interferometer for beam profile determination and the beam energy width monitoring, and a Silver Calorimeter for beam charge measurement are planned in near future (before the energy upgrade).

The beam optics and layout will also basically remain the same. Most of the modifications involved ensure that the various beam focusing and deflecting elements can reach the requisite higher fields. All the beamline magnets will remain resistive. The present plans for the dipoles (especially in the Hall A Arc section) will be modified from C-type magnets to H-type magnets by adding a return path to the yoke in order to reach the higher fields without saturation. The present beamline quadrupoles have enough margin that they are able to reach 170% of their design current (enough to reach 11 GeV) with acceptable field quality. Higher current power supplies for both will be needed for the upgrade.

The Hall A beam line is equipped with a Møller polarimeter to measure the longitudinal polarization of the electron beam. The analyzing power A depends on the scattering angle in the CM frame θ_{CM} and has its maximum of 7/9 at $\theta_{CM} = 90°$. A ferromagnetic foil, magnetized in an external magnetic field of about 0.03 T is used as the target. Both electrons, scattered close to the horizontal plane, are detected with the help of a spectrometer consisting of three quadrupole magnets, focusing the electrons onto two vertical slits in a dipole magnet, which provides a horizontal field. The dipole magnet deflects the electrons downward, away from the beam line, toward the detector. The beam also passes this dipole magnet, through an area shielded against the magnetic field. The polarimeter can measure the beam polarization in about 30 min with a relative error of about 0.2% statistical and 3% systematic.

Two factors limit the useful beam energy range of the polarimeter: a) the spectrometer acceptance, defined by the positions of the magnets and the available field strength, and also the positions of the collimators; b) the beam deflection in the Møller dipole caused by the residual field in the shielding insertion. At the moment, the first factor gives the lower limit of beam energy 0.8 GeV, the second the upper limit at about 6 GeV. In order to operate at 11 GeV an upgrade of the polarimeter is proposed, keeping the target and the dipole magnet at the same positions along the beam line by reducing the bend angle of the dipole from 11 to 7.3°, thereby reducing the maximum field needed in the dipole, lifting the detector by 10 cm, moving the 1-st quadrupole magnet 40 cm downstream, adding a 4-th quadrupole magnet at 70 cm from the Møller target, and adding a shielding pipe to the magnetic shielding insertion in the dipole magnet.

The four-quadrupole design provides a sufficiently large acceptance on the scattering angle $\Delta\theta_{CM} \approx 20°$. The residual field in the beam area inside the dipole is reduced both by reducing the requirements for the magnetic field strength and by using additional magnetic shielding. The latter was optimized using a TOSCA simulation. The present diameter of the bore in the shielding insertion is 4.0 cm. The diameter of the electron beam line before and after the Møller polarimeter is 2.54 cm. It is possible to increase the attenuation of the shielding insertion by placing a coaxial magnetically isolated pipe with inner/outer diameters of 2.54/3.4 cm, made of magnetic steel AISI-1006, inside the bore. The shielding pipe is centered in the shielding insertion bore with an additional external isolating pipe of a non-magnetic material. The shielding pipe length should be 10 cm longer than the shielding insertion length in order to reduce the influence of the fringe field outside of the shielding insertion. The new design attenuates the dipole magnetic field to an acceptable level up to 14.8 kG, corresponding to a beam energy of 11 GeV and a dipole bending angle of 7.3°. This field can be provided with the power supply currently used for the dipole.

The Hall A Compton polarimeter determines the absolute polarization of the electron beam by measuring the Compton backscattering asymmetry of polarized light from polarized electrons. A detailed description of the existing Compton polarimeter can be found in Ref. [Ba96a]. In brief, the Compton polarimeter consists of a magnetic chicane made of 4 dipole magnets over about 15 m. The chicane displaces the beam downward by 300 mm where it interacts with polarized light confined in a High-Finesse Fabry-Perot cavity. The polarized light is injected from a 1064 nm infrared laser. The backscattered photons and the recoil electrons are detected in a $PbWO_4$ electromagnetic calorimeter and silicon-strip detector, respectively. The Compton polarimeter chicane has been designed to operate up to a maximum beam energy of 8 GeV. This limit is due to the 1 m long dipoles in the chicane which have a maximum pole-tip field of 1.5 T.

To upgrade the maximum beam energy of the chicane to 11 GeV, the chicane displacement will be decreased to 218 mm This requires raising the bottom two dipoles along with the optics cavity and the photon calorimeter by 82 mm.

There are at present two independent devices to measure the absolute energy of the beam in Hall A, the ARC and EP methods. The present EP design enables a measurement of the beam energy to about 6 GeV. A major redesign of the device would be necessary to implement it for energies above 6 GeV. To implement the ARC method at higher energies, the ARC dipoles, modified from C-type magnets to H-type magnets, will have to be remapped. The mapper for the 9th dipole will also have to be modified.
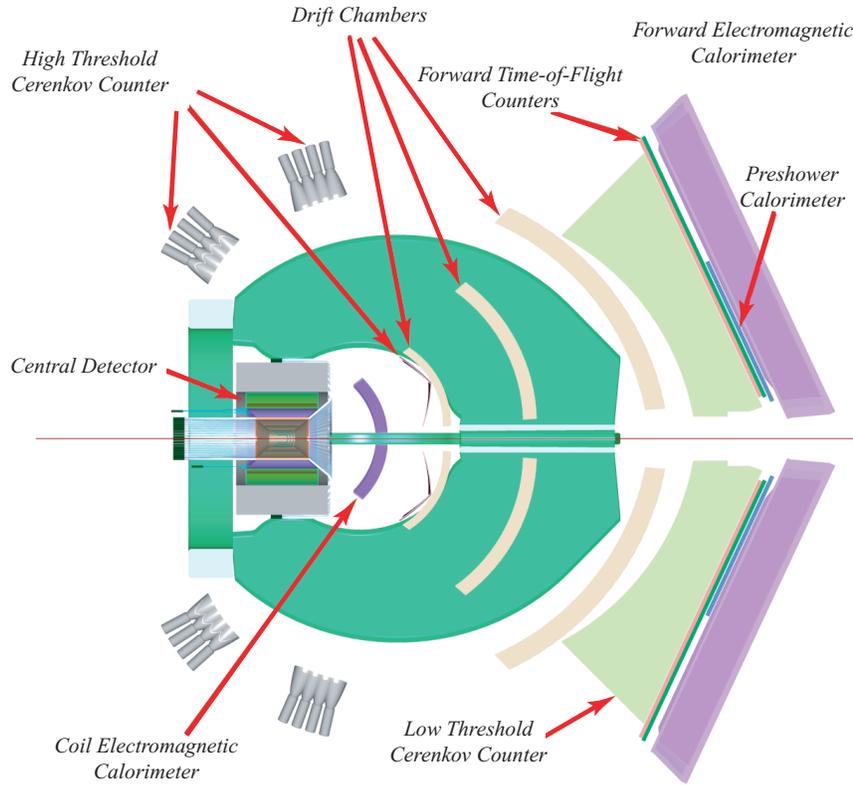
Figure 153: The upgraded CLAS^{++} detector.

3.B   Hall B Upgrade and the CLAS^{++} Detector

3.B.1   Overview

The CLAS^{++} detector is shown in (Fig. 153). It has been designed to meet the basic requirements of the physics program currently anticipated for the 12 GeV Upgrade.

The main features of CLAS^{++} are:

- High operating luminosity of $10^{35} \mathrm{cm}^{-2}\mathrm{s}^{-1}$ for hydrogen targets, a ten-fold increase over current CLAS operating conditions.

- Improved detection capabilities for forward-going high momentum particles. Charged particles that bend outwards in the torus field can be reconstructed for angles as low as 5 degrees. Photon detection will be possible for angles as low as 3 degrees. Acceptances for electrons are momentum-dependent, and range from about 8 degrees to 40 degrees.

- Capability to detect the recoil baryons at large angles.

- Larger momentum range for the separation of electrons, pions, kaons, and protons. This is achieved with better resolution time-of-flight counters, and with the installation of a new gas Čerenkov detector.

- Improved hermeticity for the detection of charged particles and photons in regions where CLAS currently has no detection capabilities, achieved by instrumenting the coil regions and by extending the polar angle range for photon detection to 135 degrees.

CLAS^{++} makes use of many of the components of the current CLAS detector.

- The torus magnet will be re-used in a slightly modified form.

- All large forward calorimeters will be used for electron, photon, and neutron detection.

- All gas Čerenkov counters will be used with adjustments in the optics and replacement of 1/3 of the mirrors.

- The time-of-flight scintillator material will be used to make smaller scintillator slabs for better timing.

- Part of the CLAS drift chamber electronics will be re-used as well.

A major new component in CLAS^{++} is the Central Detector. Its main component is a superconducting solenoid magnet, which has a dual function: It replaces the existing mini-torus for shielding of the Møller electrons, and it provides the magnetic field for the momentum analysis of charged particles at large angles. Time-of-flight scintillators are used to provide particle identification at scattering angles greater than 40 degrees. Due to the limited space available excellent timing resolution is essential. Tracking at large angles is provided by a combination of drift chambers with cathode strip readout and a microstrip detector near the vertex. Since most charged tracks will have momenta of 1 GeV/c or less sufficient momentum resolution can be achieved even in the limited space available for tracking. A compact electromagnetic calorimeter based on tungsten powder and scintillating fiber technology provides photon detection capability for the angle range from 40-135 degree.

Much of the instrumentation of CLAS will be re-used in the CLAS^{++} Forward Detector (FD). However, some modifications and additional detectors are needed in the Forward Detector as well. The main new component is a threshold gas Čerenkov counter for pion detection. The light collection is accomplished using a mirror system that focuses the Čerenkov light onto photomultipliers located sideways of the torus magnet. This area will be accessible after the removal of the CLAS drift chambers. The Čerenkov counter will allow electron and pion identification up to nearly 5 GeV/c. Beyond 5 GeV/c electrons are identified in the forward electromagnetic calorimeter.

There is also additional electromagnetic calorimetry placed in the area of the torus coils for improved hermeticity. Lead-tungstate crystals have emerged as a good choice for this detector.

A pre-shower detector will be inserted in front of the existing CLAS electromagnetic calorimeters. This detector will allow separation of single photons from $\pi^0 \to \gamma\gamma$ events especially needed for deeply virtual Compton scattering.

All drift chambers in CLAS will be replaced by new ones that will cover a smaller angle range with a factor of two smaller cell sizes to reduce the accidental hit occupancy due to photon interactions allowing for a corresponding gain in luminosity.

The existing forward detection system will be modified to extend particle identification and reconstruction to higher momenta. This will be accomplished by several means: The timing resolution of the scintillation counters will be improved by using smaller scintillator slabs, and by adding an additional layer of scintillators, and by replacing the PMTs by new ones with better timing characteristics. This is expected to improve the timing resolution to about 60 psec. The existing gas Čerenkov counter will be modified for improved pion detection capabilities for momenta greater than 2.7 GeV/c. .

With these modifications and additions to the existing CLAS components, CLAS^{++} will be able to carry out the core program for the study of the internal nucleon dynamics and hadronization processes by measuring exclusive, semi-inclusive, and inclusive processes. In the following sections the new components are discussed in some detail.

3.B.2 CLAS Torus Magnet

The CLAS^{++} upgrade is based on using the original CLAS Torus with some modifications. The minimum modification required will be to replace all 72 out-of-plane (OOP) supports. These supports keep the coil centered in the vacuum case and support both magnet and gravitational loads. Experience gained from the original CLAS operation and detailed calculations have shown this to be a requirement for operating a high field solenoid inside the torus at full field. The CLAS Torus will also be modified to allow for the addition of the Central Detector, Solenoid Magnet, and iron flux return. This will require that the backward (upstream) end of the coils are moved out. After all modifications have been completed, the position and geometry will be surveyed, and the magnetic field will be mapped in the region where particle tracking will be done, i.e. up to about 40° in polar angle, and for all six sectors.

3.B.3 Central Detector

CLAS^{++} consists of a forward detector system (FD), which is sensitive to charged and neutral particles emitted at lab angles between 5 and 40 degrees, and a central detector (CD), which covers
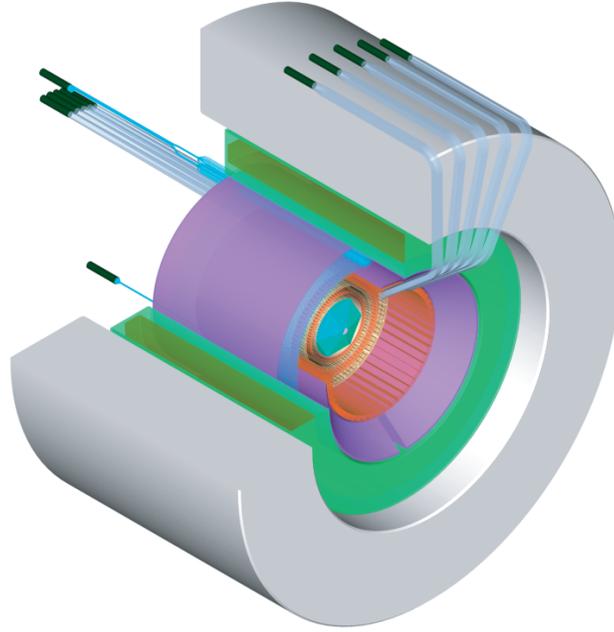
Figure 154: Central detector region showing (from the outside to the inside) the flux return iron, the super-conducting solenoid, and the layout of the central EC and TOF, the central tracker, and the microstrip detector assemblies.

the angular range from approximately 40 to 135 degrees. A layout of the central detector and its solenoid is shown in Fig. 154.

The central detector is located within a superconducting solenoidal magnet which performs a dual function: it curls emitted low-energy Møller electrons into tight spirals which are directed into a cylindrical absorbing tube, and it provides the magnetic field for particle tracking. An iron flux-return surrounding the magnet shields the torus coils from the strong magnetic field of the solenoid.

A major thrust of the experimental program will be measurements of deeply exclusive scattering (DES). DES events are characterized by the presence of the scattered electron and one or two hadrons in the forward spectrometer, and typically one recoil baryon in the central detector. Because we rely on the missing mass technique to identify reactions and to reject background we wish to optimize the missing-mass resolution and to maximize the multi-particle acceptance. This achieved by a combination of tracking devices covering the full angle in azimuth, and the polar angle range from 40° to 135°.

In addition to the tracking devices, the central detector consists of an array of scintillator paddles used to measure time-of-flight (CD-TOF) of the charged particles, and a central electromagnetic calorimeter (CD-EC) use to measure the energy of photons emitted in the central region. With the projected time resolution of 50psec the CD-TOF will be able to separate pions and protons up to 1.2 GeV/c, and kaons from pions up to 0.6 GeV/c. In addition it will be very important

in rejecting the out-of-time hadronic background. This can be accomplished with time resolutions on the order of 1 ns. The CD-EC will complement photon detection in the forward calorimeter, cover the full azimuthal angular range, and the polar angle range from 40° up to 135°. Most of the photons hitting the CD-EC will have energies from 50MeV to up to 1 GeV. The CD-EC has been designed to have sufficient "depth" to fully contain the energy deposition of 1 GeV photons, and allow detection of photons in this energy regime with approximately the same energy resolution as the forward angle calorimeter.

Superconducting Solenoid Magnet At the core of the central detector is a superconducting solenoid to provide a central longitudinal magnetic field of up to 5 Tesla. The solenoid magnet serves the following functions:

- determine particle momenta and charge via tracking in the central tracking devices.

- keep Møller scattered electrons from reaching the detectors by guiding them to a shielding pipe made of heavy metal. The maximum luminosity $CLAS^{++}$ can be operated at is limited by the degree to which tracking chambers are shielded from the Møller electrons and secondary particles. This technique has been used successfully during the CLAS eg1 runs, with the magnetic field provided by the 5 Tesla superconducting Helmholtz magnet that was used with the CLAS polarized target magnet.

- provide the magnetic field for a solid-state dynamically polarized target. This requires a 5 Tesla polarizing magnetic field with an inhomogeneity of $\Delta B/B \leq 5 \times 10^{-4}$ for polarized NH_3 material. The polarized target operation adds homogeneity constraints which will require additional correction coils.

Magnet Design   A magnetic design using $\text{TOSCA}^{(R)}$ 3D has been performed to establish the basic magnetic requirements, provide 3D field maps for Møller background analysis and to produce basic engineering information about the magnet. A single layer, superconducting, warm iron yoke magnet was chosen as the optimal configuration. The field excitation ranges from 2T to 5T. The design constraints were as follows:

- reduce the fringe field in the proximity of the CLAS coils to minimize the CLAS's out of plane forces.

- have a sufficiently large internal radius to house the central detectors, and

- an outer yoke radius to fit within the modified CLAS cryostat

- an opening in the forward region to allow detection of particles from 5° to 40°.
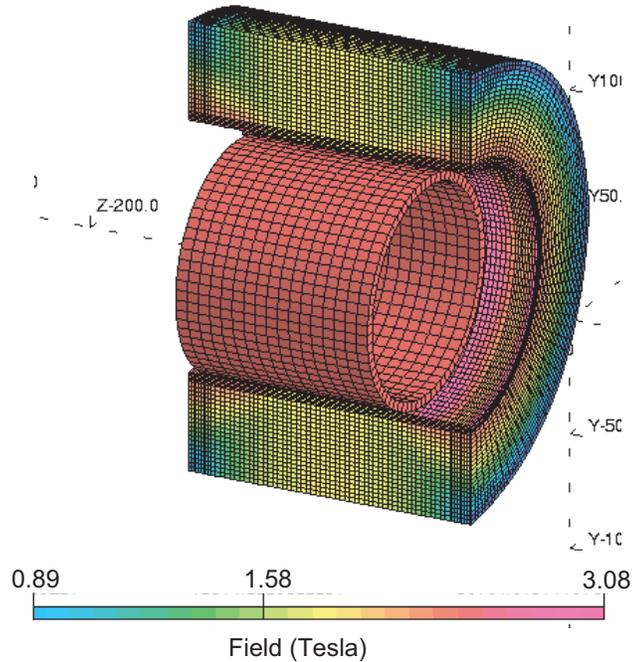
Figure 155: Field distribution in the solenoid magnet and the flux return yoke. The central field is 5 Tesla. The field in the iron yoke is typically less than 2 Tesla. Saturation field levels of up to 3 Tesla occur only in a few localized areas near the edges.

An important aspect of the iron yoke is to avoid magnetic interference with the toroidal magnet which may otherwise produce unacceptably high out-of-plane forces at the torus coils.

The magnetic design uses a TOSCA-generated solenoid coil. The yoke, which is a simple cylinder with an outer diameter of 1.96 m. and an inner diameter of 1.10, was modeled as a nonlinear iron (1006 steel). The length of the yoke is 1.18 m. The Superconducting coil is off centered within the yoke by 0.1252 m. The peak field produced within the yoke is 3.1 Tesla and within the coil windings of 6.4 Tesla. A projected view of the magnet in the cryostat and the flux return yoke is shown in Fig. 154.

The iron flux return reduces the total current required, increases the field homogeneity, and reduces the fringe field. An important aspect of the iron yoke is to avoid magnetic interference with the toroidal magnet which may otherwise produce unacceptably high out-of-plane forces at the torus coils. Since shielding the Møller electrons relies on the fringe field the geometry of the flux return has been optimized to avoid reducing the shielding effect.

Fig. 155 shows the magnetic field density distribution in the magnet bore and the flux return iron. The iron is sized to minimize saturation effects, while keeping its size and weight compatible with installation in the Torus magnet. At the bottom the distribution of the magnetic field density in the r-z plane is shown , where z is the axis along the beam line, and r is the radial distance from the solenoid symmetry axis. The distribution along the beam axis varies rapidly while the

Table 28: Central Electromagnetic Calorimeter parameters

Total Radiation Length	10 -12
Radial Space (radial thickness)	~ 10 cm
Energy Resolution	$\approx 6\%/\sqrt{E}$
Angular Resolution, $\delta\theta = \delta\phi$	$\sim 1^o$
Timing Resolution, δt	few nsec
Energy Threshold, E_γ^{min}	$\leq 50\ MeV$

variation along r is much more uniform. The extended fringe field is important for guiding the Møller electrons far enough away from the interaction region to a shielding pipe (not shown) where they can be absorbed.

Central Electromagnetic Calorimeter

Overview The central electromagnetic calorimeter covers detection angles in the polar range of $40^o \leq \theta \leq 135^o$ and in almost the entire azimuthal range $0^o \leq \phi \leq 360^o$. It is designed for the reconstruction of π^o and η by their neutral decays, therefore, for the detection of multi γ - events . The design parameters are defined to meet an operational luminosity of $L \sim 10^{35}\ cm^{-2} sec^{-1}$. The following sections describe the technical requirements, the detailed concept design and estimates for the calorimeter performance.

Requirements The available radial space for the calorimeter material, inside the magnet, is limited to ~ 10 cm. The calorimeter must provide adequate energy and spatial resolutions to cleanly identify π^o and η . Typical energies of decay photons, produced under large angles ($> 40^o$) at beam energies of 12 GeV, are up to $E_\gamma \sim 1\ GeV$. Reasonable energy resolutions with these size restrictions can only be achieved if very dense materials are used. Table 28 shows the main design parameters of the Central Calorimeter.

Scintillating Fiber/Tungsten Powder Calorimeter Design The overall view and basic dimensions of the central calorimeter mounted inside the solenoid magnet are shown on Fig. 156. Dense Tungsten metal powder is used as shower material. The calorimeter has a cylindrical shape: thin plastic scintillating fibers run in the direction parallel to the beam and are read out from the upstream end, see Fig. 157. Fibers are grouped in sectors of equal size. Each sector combines all fibers covering an azimuthal angle range $\Delta\phi \approx \pm 0.6^o$ to a single photo-multiplier tube readout channel that provides energy, ϕ and timing information. In the radial direction, there are one or two layers of fibers all bent at the same radius with both ends brought out of the sensitive volume. This circular layer of grouped fibers provides independent measurements of the polar angle θ of the
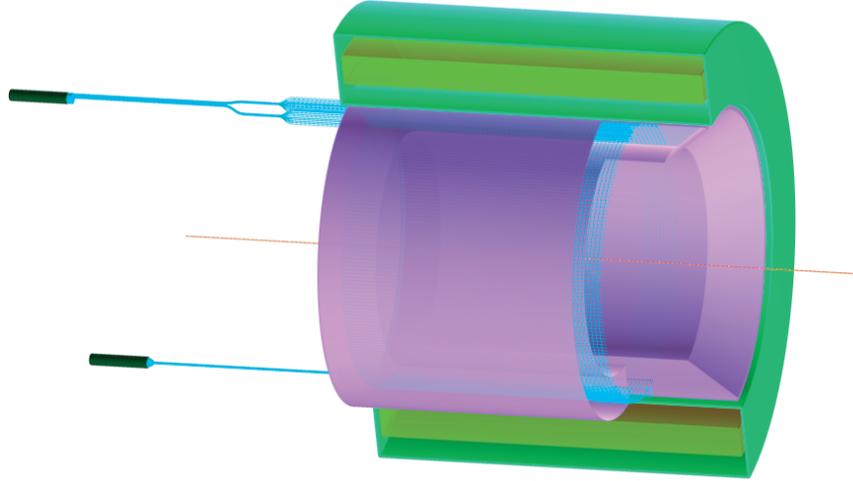
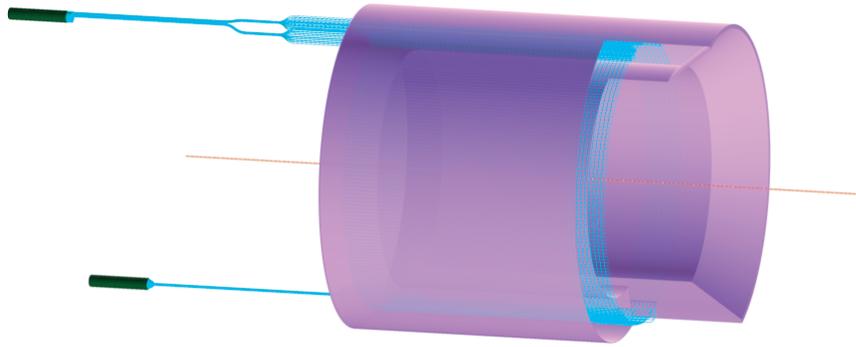Figure 156: Perspective view of the central electromagnetic calorimeter inside the solenoid magnet.

Figure 157: Central calorimeter. The tungsten powder volume and some of the axial readout fibers are shown at the left. Some of the radial fibers are indicated at the right side. The radial fibers are brought to the readout end through a slot at the bottom of the calorimeter.

shower. To have resolutions of $\delta\theta \approx 1^o$ there will be a total of about ~ 50 channels per polar angle measurement.

The implementation of such topology of scintillating fibers within essentially the same sensitive volume is only possible because of the powder technology, the volume is filled by loose tungsten powder. Since the so called "green density" of the Tungsten powder to be used as absorber is of about 12 ± 0.2 g/cm^3, the whole structure becomes very efficient, especially providing high sampling ratios and frequencies with fibers as thin as 0.5 - 0.75 mm or even of smaller diameters. This particular feature allows matching two requirements, i.e. to have sufficient energy resolution and small overall dimensions at the same time.

Expected Performance To estimate the calorimeter response one can use parameterizations based on simulation and previous calorimeter data. We have used parameterizations during

the initial design phase for a fast estimation of the calorimeter basic dimensions and characteristics. The containment of the shower is parameterized using [Fa85]:

$$L(98\%) = 2.5 * [log(\frac{E}{\epsilon}) + 1.2] * X_o (cm)$$

L gives the length in centimeters that contains about 98% of the energy of the shower. E is the energy of the incoming photon, ϵ the critical energy of the material and (X_o) the radiation length of the mix in centimeters . The material in the calorimeter is a mix of tungsten powder and scintillating plastic (Polystyrene) fibers. The radiation length for the mix (X_o) that contains a fraction y of scintillating plastic per volume and a fraction $(1 - y)$ of tungsten powder absorber, is obtained using:

$$\frac{1}{(X_o)} = \frac{y}{X_{Sci}} + \frac{(1 - y)}{X_{Powder}}$$

For the powder with a fraction x of the pure tungsten density the radiation length is

$$X_{Powder} = X_{PureTungsten}/x.$$

The critical energy of the mix is obtained using:

$$\epsilon = y\epsilon_{Sci} + (1 - y)\epsilon_{Powder}$$

The results are shown in Fig. 158. The values of **L** are plotted versus the fraction of scintillating plastic by volume for three values of the powder density: $x= 0.62$ (current loose powder), $x= 0.8$ (cold pressed density currently obtained) and $x= 1.0$, pure tungsten. One can see that if the radial thickness of the calorimeter, using loose powder at $x= 0.62$, is limited by ~ 10 cm, then the fraction of scintillating plastic should not exceed $\sim 35\%$ per volume.

The other important figure-of-merit is provided by the sampling errors (in the energy measurements). For a given material ($x= 0.62$), these sampling errors are a function of the fraction of scintillating plastic in the calorimeter y (sampling fraction), and the diameter of the fibers, ϕ (sampling frequency). The corresponding parameterization for sampling errors are given by [Wi00]:

$$(\frac{\sigma}{E})_{sampling} = 0.02 * \sqrt{\frac{\phi(mm)}{f_{sampl}}}$$

where f_{sampl}, the sampling ratio for minimum ionizing particles (mip) is calculated using:

$$f_{sampl} = \frac{1}{1 + \frac{(1-y)}{y} * x * \frac{dE_W}{dE_{Sci}}}$$

where, dE_W and dE_{Sci} are the energy depositions by minimum ionizing particles in 1cm of tungsten (22.1 MeV/cm) and polystyrene (2.0 MeV/cm), respectively.

Figure 159 shows the sampling errors versus the fraction of scintillating plastic by volume for four different fiber diameters (0.25, 0.5, 0.75 and 1 mm), at a powder density of $x= 0.62$. One
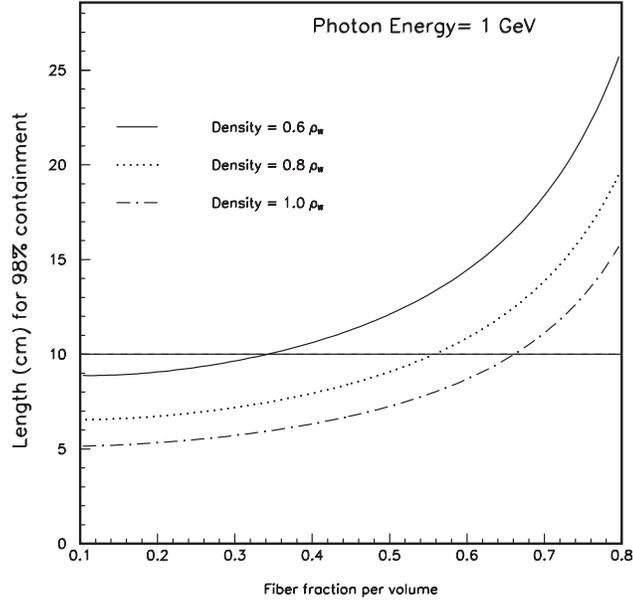
Figure 158: Containment versus fraction of plastic.

can see that for an absorber density of 11.8 g/cm^3 (x= 0.62), a tungsten powder based sampling calorimeter built with fibers of 0.5 mm in diameter and with a fraction of scintillating fibers of 35% per volume can reach energy resolutions better than $\sim$ 6% at 1 GeV energies. These resolutions are similar to the one reached by the KLOE [An96b] and JETSET [He90] calorimeters using larger amount of scintillating fibers. In the same figure also is shown the value obtained by the KLOE collaboration [An96b] with a sampling calorimeter of 23 cm of radial thickness built at y= 0.5, using lead absorber and 1 mm polystyrene fibers.

Prototyping and Simulations The proposed sampling calorimeter will use a new calorimetry construction technology. There are open questions that need to be answered, although some initial tests already have been successful. An important test will be to establish an efficient assembly procedure when fibers having different directions and shapes are installed in the same volume.

A prototype consisting of 12 modules is under construction to examine all basic properties of the calorimeter. The goal is to test the calorimeter in a photon or electron beam in the very near future. The prototype will have 10 cm thickness (12 radiation lengths) with a fraction of plastic of 35% by volume using polystyrene fibers of 0.75 mm in diameter.

Central Time-of-Flight System A conceptual view of the central TOF system is shown Fig. 160. The active scintillator area consists of a cylinder of radius 26 cm and length 50 cm. The thickness of the detector is 2 cm. It is located inside the solenoidal field and must therefore be able to operate in the high magnetic field. The design goal is to achieve timing resolution of σ =50 ps. This timing resolution allows separation of pions from kaons up to 0.64 GeV/c and pions from protons up to
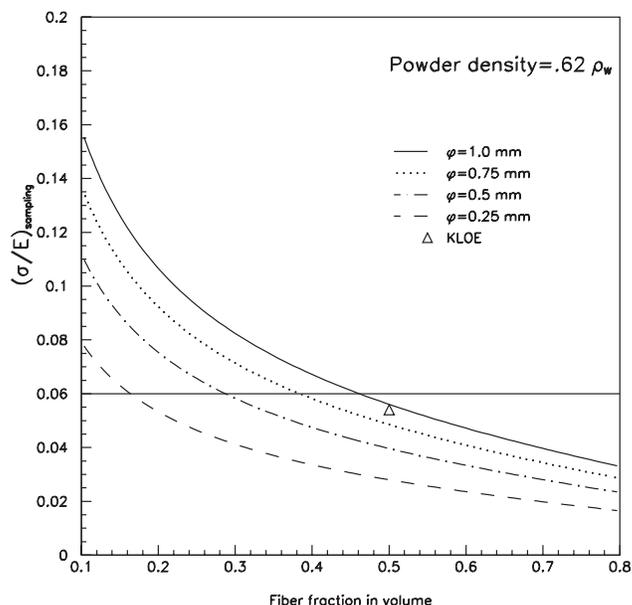
255

Figure 159: Sampling errors versus fraction of plastic.

1.25 GeV/c (Fig. 161). This assumes a "4σ" difference in time between the two particles and allows identification of a signal in the presence of other particles with ten times higher rates.

Expected Rates   The rates in the scintillators for the existing CLAS detector have been studied at two different beam currents and used to predict the counting rates at a luminosity of $10^{35}cm^{-2}s^{-1}$ [Sm02a]. We summarize the results here for both the central and the forward detector systems. The rates are given in Table 3.B.3 at two thresholds. The expected integrated rates for the central and forward detectors are approximately equal. The current threshold setting for the counters is 20 mV, but efficient operation can be achieved at a threshold of 30 mV, which reduces the rate considerably (Fig. 162). The forward detector elements will have a typical rate per counter at 30 mV of about 750 kHz. At this threshold, the central detector has an integrated rate of 40 MHz. In order to keep the rates below one MHz per counter, we require approximately 50 channels of electronics.

Options   The traditional scintillator detector array for TOF measurements in the central detector is challenging due to the magnetic field of the solenoid which may operate at several Tesla. Hybrid photomultipliers such as Hamamatsu R7100U-07 and DEP model PP0350G can operate in magnetic greater than 1.5 Tesla with no reduction in pulse height. The field in the region inside the solenoid near the ends of the scintillator is less than 1 T, so hybrid PMTs are an option for use with short light guides.

A second option is to use light guides to bring the light out of the high magnetic field to the region outside the yoke and use standard PMTs. The field surrounding the yoke is no less than
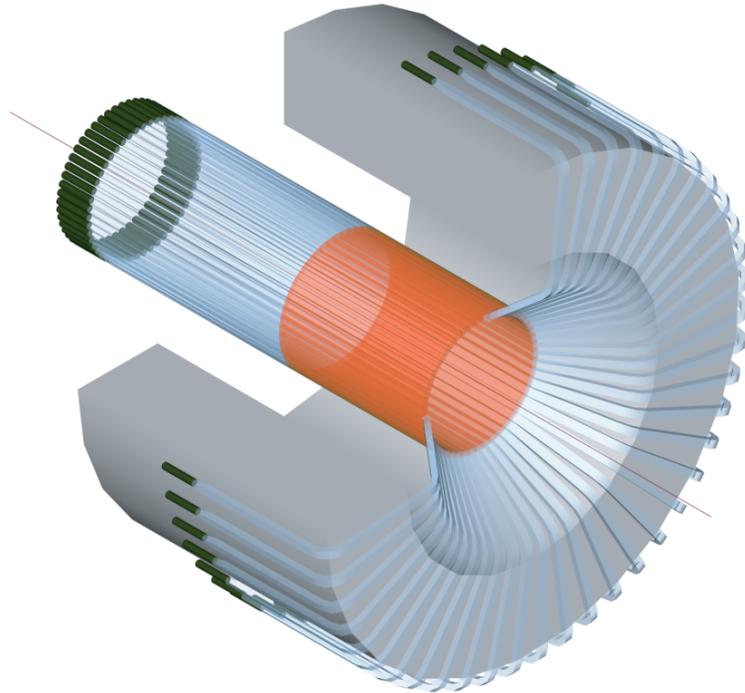
256

Figure 160: Perspective view of the central TOF system. Scintillator material shown in red color. In this option the scintillator light is transported to regions of reduced magnetic field using light guides (shown in translucent light blue color)
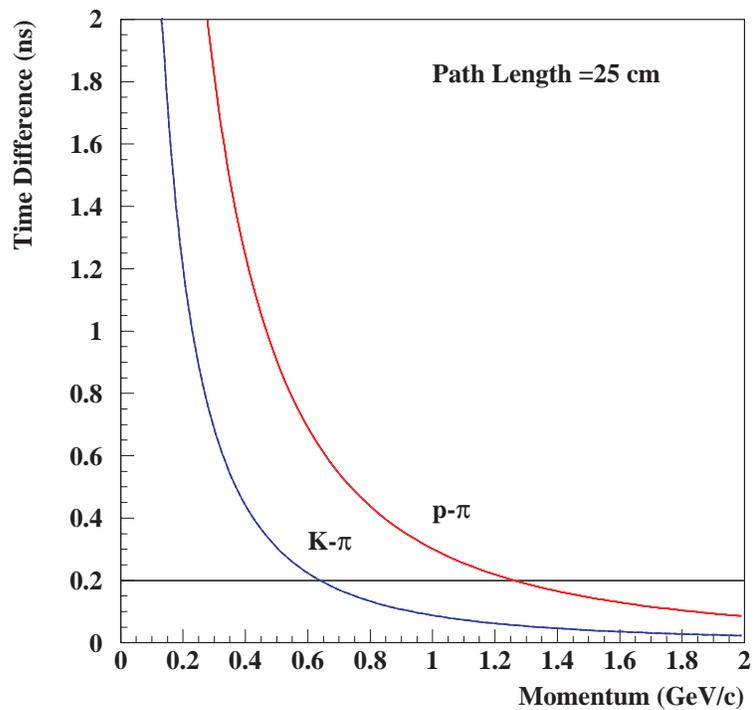

Figure 161: Time differences between protons and pions, and between kaons and pions over the 25 cm path length expected for the outer TOF system.
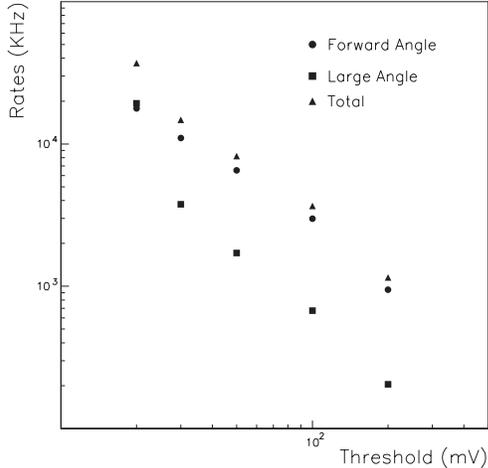
Figure 162: Rates summed over all six sectors as a at a luminosity of $0.9 \times 10^{34} cm^{-2} s^{-1}$. When the threshold is increased by a factor of two the count rates drop by a factor of between two to three.

The scalar rates in the CLAS scintillators extrapolated to a luminosity of $10^{35} \text{cm}^{-2}\text{s}^{-1}$. The rates are summed over all six sectors.

Angular Range	Threshold (mV)	Rate (MHz)
Forward	100	32
Central	100	8
Total	100	42
Forward	20	214
Central	20	243
Total	20	457

70-100 G, where standard magnetic shielding is challenging, though not impossible. We note that in the regions outside the solenoid, the magnetic field of the torus cannot be neglected, although it is not included in the present field tables.

Central Tracker The central tracker is located inside the central solenoid. Fig. 154 shows the layout of the entire area. A gas-filled wire chamber occupies the radial space from 12 to 25 cm. The radial space from 5 to 11.18 cm is occupied by a silicon strip detector.

The wire chamber design is cylindrical with axial anode wires arranged as four, 2-layer (staggered) superlayers with inside, inner and outside cathode foils. Foils reduce the need for additional field wires and lower the wire tension and thus, the thickness of the endplate. The endplates are angled such that the wires all subtend approximately the same range in scattered angle, from 40 to 135 degrees in the laboratory frame. A perspective view is shown in Fig. 163.

There are a total 2 super-layers, 2 layers each, 80 anode wires and 80 field wires per layer, with the drift distance varying from 0.22 to 0.91 cm. The anode wires provide the electric field to produce the avalanches and resulting gas gain. The anode wires will be read out to provide a precise time measurement as well as a phi measurement by converting the drift time into a drift distance. The z-position-sensitive readout is primarily via cathode pads; a drift-time measurement gives a measure of the azimuth, phi, while a charge measurement of several cathode pads gives theta information. When the anode avalanche multiplicity is one, the anode time information will be used for the phi measurement. In case of higher multiplicity on one anode wire, the time information will come from the cathode strips.
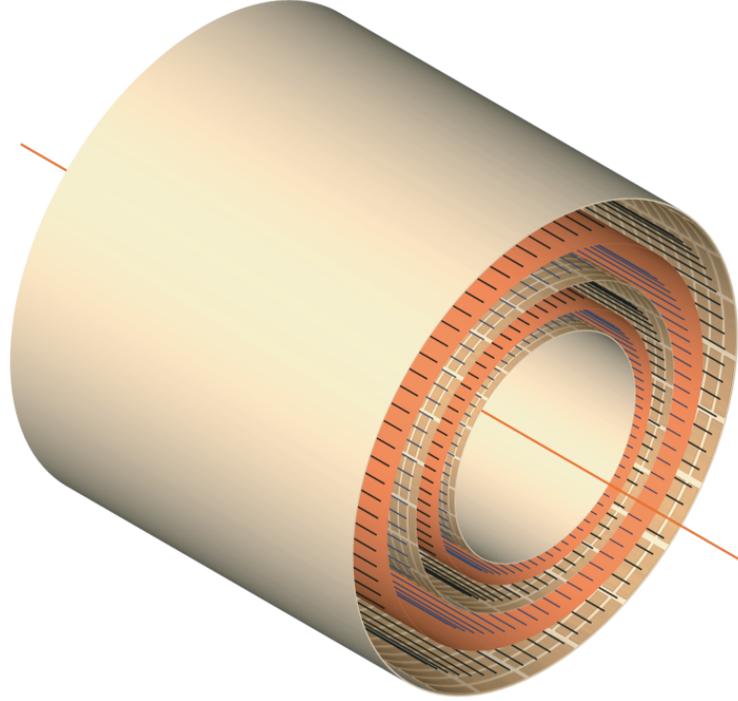
Figure 163: Cathode chamber view of two superlayers.

The accidental rate is proportional to the solid angle of the pads relative to background source times the time window. Compared to the present CLAS detector, we will have roughly the same number of channels per layer as Region 1; and a time window on the inner layer a factor of 10 smaller than Region 1. The major reduction in electromagnetic background comes from the solenoidal shielding scheme. Tests using a Helmholtz coil and cylindrical absorber showed that the dominant background was directed forward from the source (the mouth of the absorbing cylinder). We thus expect that the central tracker will be adequately shielded from any Møller background.

For B=3 Tesla, $P = 1$ GeV/c, 20 cm path and a 100 μm accuracy δS, we estimate that

$$\frac{\delta P_{perp}}{P_\perp} = 2.2\% \ .$$

The inner part of the central tracker consists of six layers of a silicon microstrip detector. In addition to providing tracking and vertex reconstruction (when combined with the gas chamber for polar angles from 40° to 135°), the microstrip detector will provide tracking information and vertex reconstruction for the polar angle from 5° to 40°.

Silicon Strip Detector The limited radial space available in the Central Detector region for particle detection forces the charge particle tracking detectors to be located very close to the target in order to retain acceptable momentum resolution. Use of a small microstrip detector near the target can provide excellent position resolution, which will provide both position measurements
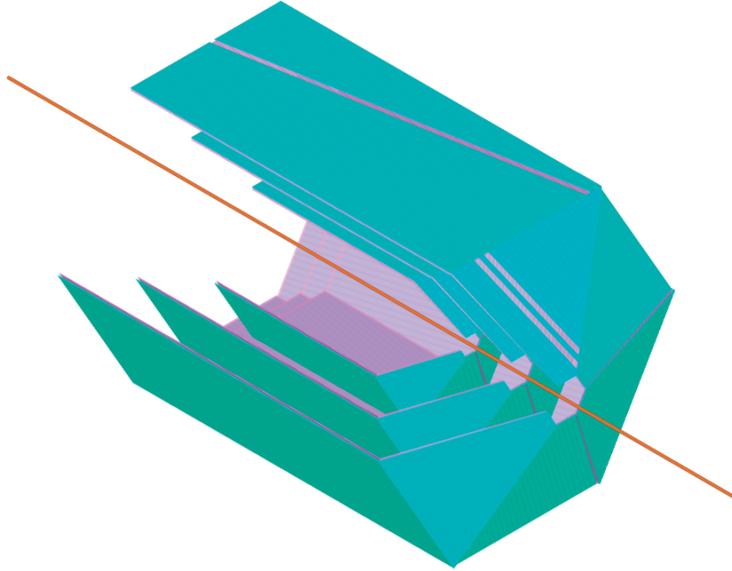
Figure 164: Concept of a Silicon Strip Detector covering the angular range from 5° to 135°. The orientation of the strips is indicated as well. We anticipate that the signal readout will be in the back. A total number of 50,000 readout channels are needed for full coverage. The signal readout will be at the back end.

close to the interaction point for excellent angle and vertex resolution, as well as providing good momentum determination for large angle tracks. These aspects are of particular importance in the detection of relatively low momentum protons and recoil hyperons, e.g. $\Lambda \to \pi^- p$, as well as in resolving the decays vertex of $K_s \to \pi\pi$. As mentioned earlier, the microstrip detector will also provide tracking at forward angles to aid in the reconstruction of high momentum tracks and in regions which are blocked by the torus coils. The track segments near the target can be linked up with tracks reconstructed in the forward angle tracking chambers to improve angle and momentum resolution. This is especially important for the CLAS^{++} configuration where the first tracking chamber is located at a distance of about 2 meter from the target.

Fig. 164 shows a possible conceptual layout of a silicon strip detector, arranged in 6 layers around the target. The six layers (only the 3 superlayers are shown, each contains two stereo layers) provide 3 space points (x, y, z) for a given track. Alternating layers have strips at different angles to provide stereo readout and resolve ambiguities. In the large angle region the strips can be arranged to provide $\pm 10^o$ readout. This will provide near optimal momentum resolution for tracks in the longitudinal solenoid field, while at the same time giving good polar angle resolution due to the excellent position resolution. In the forward region the strips are arranged to have a much larger crossing angle, giving excellent angle resolution for forward going tracks down to angles of 5°. The graph shows also a possible strip layout of the silicon wafers. A strip pitch of 300μm is assumed which is expected to result in a position resolution of better than 100μm. The first two layers may consist of 100μm thick silicon wavers, while the four outer layers, which are considerably larger could be as thick as $280\mu m$. Using thinner wafers for the inner layers would allow detection

of recoil protons down to lower momenta. To limit the effect of multiple scattering, we consider the possibility of having strips on either side of the wafer for the outer four layers, which would reduce the multiple scattering effect considerably, and improve the momentum resolution. However, such design considerations will have to be carefully balanced against complications in the detector construction, and the reduction of the readout signal for minimum ionizing particles, among others.

Instrumentation The readout chips, in die form are attached to a substrate that is attached to the SSD. The substrate provides a pitch transition from the detector (300 μm) to the readout chips (50 μm), allows mounting the chip close to the strip, allows a certain degree of thermal matching and mechanical support, provides the routing for bias voltages and control signals and serves as a support for the output cable/fiber assemblies.

The substrate(s) may be FR-4 or polyimide High Density Interconnect (HDI) (a.k.a. flex interconnect). Ceramic substrates (Al_2O_3, BeO, AIN) are attractive for their thermal performance. For example, AIN has a coefficient of thermal expansion very similar to silicon. On the other hand, BeO has very high thermal conductivity. The wire bond pads must be gold-plated for reliable bonding.

The strips are wire bonded to pads on the substrate. These pads are routed to the appropriate chips and wire bonded to the pads on the chips. All chips' pads are wire bonded and routed out through bonded HDI assemblies.

The logic signals on the HDI assemblies are routed away from the detector along the support structure and connect to optical fiber driver boards. Multiplexing may be implemented through high-speed optical links (5 GHz) or by use of Wavelength Division Multiplexing (WDM) and multimode optical fibers.

Prototyping Silicon strip technology has matured during the past decade and is now widely used in high energy and nuclear physics applications. Yet, detectors have often very specific applications in experiments, are usually custom made, and require some prototyping effort. We are planning to construct one segment of the proposed detector with the help of the Brookhaven National Laboratory Instrumentation Group [Zepc], which would then be tested in Hall B in conjunction with the solenoid magnet currently planned for the DVCS experiment. The prototype work is expected to commence in the fall of 2003.

Forward Detector

Overview The Forward Detector (FD) detects charged and neutral particles in the angular range between 5 and 40 degrees. The new detector is designed to provide extended particle iden-

tification, better charged particle tracking resolution, improved two-photon separation, nearly full azimuthal coverage for photon detection and greatly reduced sensitivity to background compared to the present CLAS. The FD consists of the following detector elements beginning with the one closest to the target:

- Forward angle part of the silicon microstrip detector (see Fig. 164)

- High threshold Čerenkov counter (HTCC)

- Coil calorimeter (coilEC)

- Tracking chambers (R1, R2, R3) with axial and stereo readout

- Low threshold Čerenkov counter (LTCC)

- Time-of-flight scintillator arrays (FTOF)

- Preshower electromagnetic calorimeter (preEC)

- CLAS forward electromagnetic calorimeter (FEC)

We give here a brief description of every element in the FD system. A more detailed description is provided in the sections following this overview.

High threshold Čerenkov detector The bulk of the FD provides active coverage in the azimuthal range not blocked by the main torus coils. Electron identification and pion rejection is accomplished using a new Čerenkov detector HTCC operated with a light radiator gas such as CO_2. This will provide pion rejection for momenta up to 4.9 GeV.

Coil electromagnetic calorimeter The coil electromagnetic calorimeter (coilEC) provides photon detection in the regions shadowed by the torus magnet coils. In conjunction with the microstrip detector it can discriminate photons from charged tracks.

Tracking chambers Forward tracking of charged particles is accomplished by three sets of chambers, analogous to the present CLAS drift chambers and named accordingly, Regions 1, 2 and 3 (R1, R2, R3). These chambers will cover less than one third the polar angular range of the present setup. By keeping the channel count constant, we are able to decrease the cell size and active time window by more than a factor of two, resulting in better spatial resolution and decreased sensitivity to backgrounds.

Low threshold Čerenkov counter The LTCC is the modified CLAS Čerenkov Detector operated with a higher density gas to allow pion identification for momenta above 3 GeV/c.

Forward time-of-flight detector The FTOF array consists of scintillator strips recycled from the existing CLAS TOF detector. The new array will consist of a double layer of 5cm thick

scintillator paddles each 5cm wide. This will provide a much improved timing resolution as the amount of light collected in the photomutipliers is increased by a factor of several.

Preshower electromagnetic calorimeter   The forward electromagnetic calorimeter (FEC) currently used in CLAS will be augmented by a more highly segmented pre-shower electromagnetic calorimeter (preEC) located immediately in front of the FEC. It will provide better spatial resolution; especially needed for the detection of the two photons from high-energy π^o decays. The FEC will be used as is.

Expected performance of the forward detector   The forward spectrometer will be able to detect all charged and neutral particles emitted in the polar angular range of 5 to 40 degrees; providing momentum resolutions of $\delta P/P = 0.005 + 0.001 * P$ for charged particles and energy resolutions of $\delta E/E \leq 9\%\sqrt{E(GeV)}$ for photons. Particle identification is accomplished using time-of-flight information, Čerenkov counters, and electromagnetic calorimetry. In addition, kinematical fitting can be applied in some cases. Electrons and π^- can be separated for momenta up to 5 GeV/c using gas threshold Čerenkov counters, and above 5 GeV in electromagnetic calorimeters. Kaons(protons) can be separated from pions for momenta up to 3(6) GeV using the upgraded time-of-flight arrays, and above 3 GeV using the low threshold Čerenkov counter as a veto for kaons. Only the direction of the momentum vector can be measured for charged particles headed for the main torus coils. All of the detectors can operate in the background environment expected at luminosities of $10^{35}s^{-1}\ cm^{-2}$.

In the following sections we describe the new detector components of the FD in more detail.

High Threshold Čerenkov Counter (HTCC)   The HTCC is the first active detector downstream of the microstrip tracker. Its main function is to aid in the identification of electrons and pions. A relatively light gas such as CO_2 will be used as radiator. This will provide a threshold for the detection of charged pions of 4.9 GeV/c. In combination with the CLAS FEC, this will provide highly efficient electron identification. A pion rejection factor of > 2000 can be achieved this way for the entire momentum range up to 4.9 GeV.

The HTCC will also be used in combination with the LTCC for charged pion identification in the critical momentum range from 2.9 - 4.9 GeV. In this momentum range the HTCC does not detect pions while the LTCC does, this way providing identification of both electrons and charged pions. The HTCC is located in front of the Torus magnet and the first forward tracking chamber. A conceptual view is shown in Fig. 165.

The very limited space available for the HTCC puts serious constraints on the optics and the performance of the mirror system and the photon detectors. Figure 166 illustrates the optics of the HTCC. To optimize the light collection light produced at scattering angles less than about 20 degree is reflected towards large angles in the same Torus sector, while light produced at scattering angle greater than 20 degree is reflected towards the opposite Torus sector. The expected response in
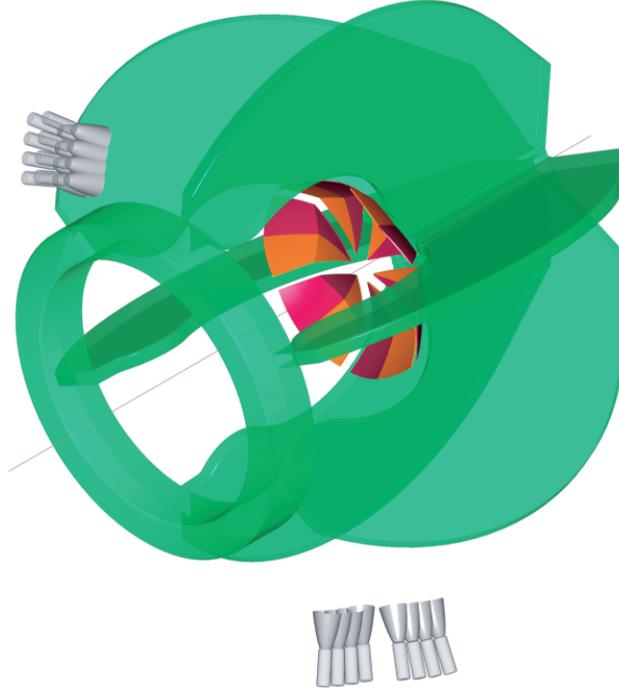
Figure 165: Concept of the High Threshold Čerenkov Detector located inside the Torus coil arrangement.

terms of the number of collected photoelectrons has been simulated using the measured properties of the mirror system in the CLAS Čerenkov counter, and photomultipliers with known photocathode sensitivities and quartz windows [5]. Figure 167 shows the projected distribution of the average numbers of photoelectrons (N_{pe}) across the $\phi - \theta$ plane. In the polar angle range from 6 to 35 degrees the N$_{pe}$ is between 11 and 15, slightly dependent on the polar angle due to the varying pathlength in the radiator gas. N$_{pe}$ is independent of the azimuthal angle ϕ. Influence of the magnetic field of the solenoid on the particle trajectories is neglected as for the high momentum electrons (1 GeV/c) the solenoid field in first approximation will only produce a change in azimuthal angle. The main effect is a smearing of the photon distribution in the detector plane.

Most photons will directly hit the photocathode area in the 5" photomultiplier tubes, those outside are collected in Winston cone mirrors around the PMTs. The PMTs are located in the fringe field of the Torus magnet and will be magnetically isolated with a multi-layer magnetic shield. Such magnetic shields have been used successfully in the CLAS Čerenkov detector.

Forward Tracking Chambers The forward tracking chambers measure charged tracks which have polar angles between $5°$ and $40°$. In order to use the missing mass technique effectively, the forward chambers must have excellent momentum resolution. The design we present here should allow momentum determination of $\delta p/p = \sqrt{(0.1\% * p)^2 + (0.2\%/\beta)^2}$. The spatial resolution

---

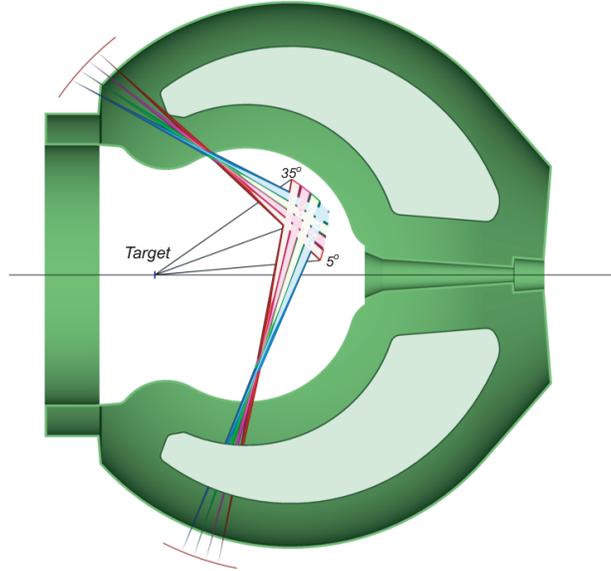[5]The characteristics of the Burle 8854 photomultiplier have been used

Figure 166: Optics of the High Threshold Čerenkov Detector. Čerenkov photons are generated in the gas volume beginning after the microstrip detector and the mirror system. The mirror system consists of 4 small angle segments which reflect the light towards the outside region of the torus magnet in the same sector. The 4 large angle mirrors reflect the light towards the PMTs located in the opposite sector. In order to avoid light obstruction due to the beam pipe the mirrors are tilted by about $\pm 15^o$ left and right of the beam pipe.

portion of $0.1\% * p$ is a factor of three better than the performance of the current CLAS tracking system. The chambers' intrinsic resolution is expected to improve from the present 330 μm to 200 μm, due to smaller cell size. We also expect to gain another factor of 1.5 by carefully controlling our knowledge of the B field and the chamber positions.

The forward tracking system consists of six microstrip layers, three sets of drift chambers: region 1, located immediately before the Torus magnet; region 2, located between the Torus coils, and region 3, just behind the Torus coils. The drift chamber arrangement is similar to the one currently used in CLAS, and optimizes the momentum resolution. The cell structure will be very similar to the current design, and will consist of a hexagonal cell geometry. Because the polar angular coverage will be much less than that of the current chambers, the cell size and hence the time window and the spatial resolution are expected to be roughly half that of the present chambers. The additional microstrip layers will provide much improved azimuthal angle information especially important at forward angles.

This design will provide precise measurements of the particle trajectory (100 μm accuracy per 12-layer chamber). They are also much less sensitive to background rates than the current chambers. The background rates for the R1 chambers will be reduced by an additional factor of two by using a special, high drift-velocity gas mixture such as $He - CF_4$.
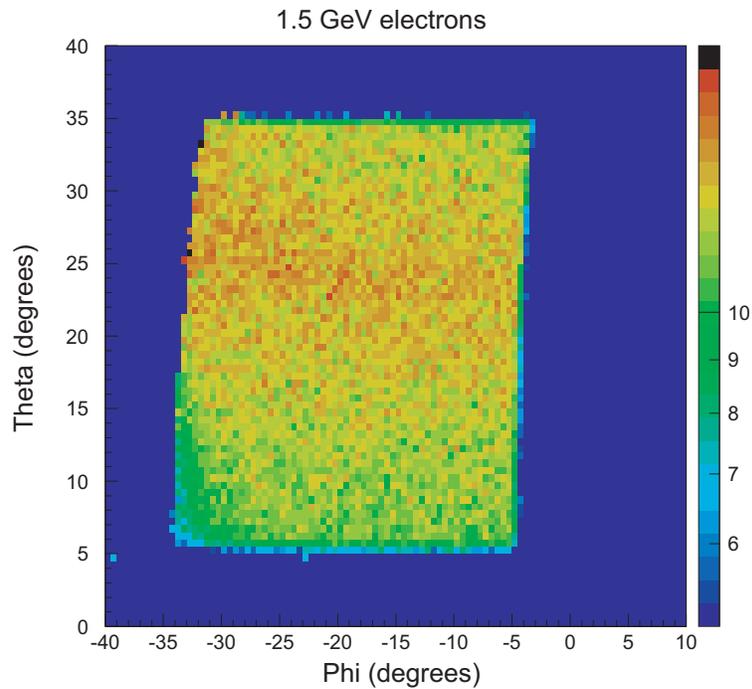
Figure 167: Left: Distribution of the number of photoelectrons N_{pe} for the HTCC in the $\phi - \theta$ plane. The simulation was done for electrons of 1.5 GeV/c momentum. The solenoidal field was included in the simulation at full strength of 5 Tesla central field. The phi motion of the electrons in the solenoid field leads to a slight broadening of the photon distribution at the Winston cones and PMTs. Right: Average N_{pe} versus the polar angle (projection of the graph on the left onto the θ axis). The θ-dependence in N_{pe} is due to the different radiator gas length for different polar angles.

Figure 168: Time differences between protons and pions, and between kaons and pions over the 500 cm path length expected for the outer TOF system.

Low Threshold Čerenkov Counter The Čerenkov counter installed in the existing CLAS detector will be re-used to provide electron/pion separation for momenta up to 2.7 GeV/c and to identify π^+ and π^- for momenta greater than 3 GeV/c. The radiator gas will be C_4F_{10} as in the current system. In CLAS the Čerenkov counter is exclusively used for electron/π^- separation. The mirror system in the CLAS Čerenkov counter was designed to be most efficient for inbending particles, while for outbending trajectories less than full efficiency for detection is obtained. At the higher energies after the upgrade the LTCC will be used to identify pions both inbending and outbending. In order to achieve full detection efficiency the optical system needs to be re-adjusted and the elliptical mirrors probably need to be replaced.

Outer TOF System The outer TOF system has the geometry of the existing CLAS detector [Ad02, Sm99a], but the detectors will be upgraded for improved timing resolution. The design goal is to achieve timing resolution of $\sigma =$50 ps for the shorter scintillators. This timing resolution allows separation of pions from kaons up to 3 GeV/c and pions from protons up to 6 GeV/c (Fig. 168). This assumes a "4σ" difference in time between the two particles and allows identification of a signal in the presence of other particles with ten times higher rates.

The resolution of the counters in the present CLAS TOF system can be summarized as follows: The attenuation length of the forward-angle counters (15-cm wide) can be approximated by $\lambda = 134$ cm $+ 0.36 \cdot L$, where L is the length of the counter in cm. The large-angle scintillators (22-cm wide) have an approximate attenuation length of 430 cm. The time resolution of each counter has
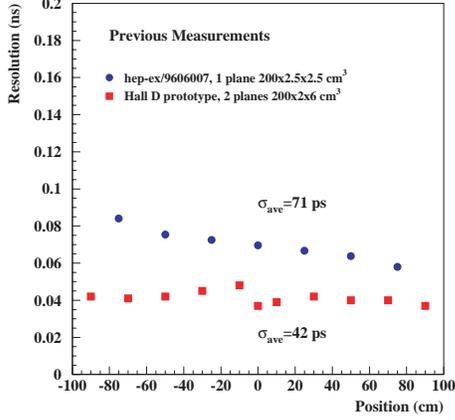
Figure 169: Previous measurements from two prototypes, 200 cm in length. The resolution of 50 ps is achieved using two scintillator planes which determine times with resolution of 70 ps.
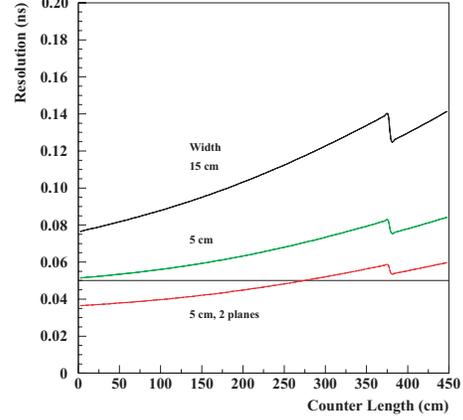
Figure 170: Expected resolution for the existing detectors (15 cm wide) with an intrinsic electronic resolution of $\sigma_0 = 40$ ps. Also shown are predictions for 5 cm wide counters and for two planes of 5 cm wide counters.

been measured with cosmic-rays; it can then be parameterized with the following formula:

$$\sigma_{TOF}(ns) \quad = \quad \sqrt{\sigma_0^2 + \frac{\sigma_1^2 + (\sigma_P \cdot L/2)^2}{N_{pe} \cdot \exp(-L/2\lambda)}} \tag{74}$$

where $\sigma_0 = 0.062$ ns represents the intrinsic resolution of the electronic measuring systems and other processes which are independent of light level, $\sigma_1 = 2.1$ ns is the combined single-photoelectron response of the scintillator and PMT, and $\sigma_P = 0.0118$ ns/cm corresponds to path length variations in the light collection.

Prototypes have achieved the desired resolution for counters 200 cm in length. Two examples are shown in Fig. 169 proving that a single plane of scintillators can achieve a resolution of 70 ps. The combined resolution of two measurements achieves the resolution of 50 ps. The prototypes used fast scintillator and XP2020 PMTS.

Electronics   As a guide to necessary improvements in the time resolution of the system, we scale the parameterization of the CLAS system to narrow counters. The intrinsic resolution of the electronics system (σ_0 in Eq. 74) must be reduced and we have measured it to be as small as 14 ps in various setups [Sm91]. There are many contributions to this term, and each electronic component will have to be selected carefully to insure that it mets our specifications. In order to achieve the rate capability at a luminosity of $10^{35} cm^{-2} s^{-1}$ (see Section on Central TOF system), a pipeline TDC will be used to readout these detectors. The Jefferson Lab Fast Electronics group is developing such a TDC based on the COMPASS F1 chip which satisfies our requirements. Therefore, we assume that $\sigma_0 = 40$ ps determined by the resolution of the TDC, which is 40 ps for the COMPASS F1 chip. The predicted resolution from Eq. 74 is 65 ps, assuming that the width of the counters is reduced to 5 cm, and is consistent with prototyping measurements of Fig. 169. The predictions are shown in Fig. 170.

Table 29: Rise time for various PMTs. The existing CLAS detector uses XP2262 PMTs.

PMT (2")	Rise Time (ns)
XP2262B	2.0
XP2020	1.5
XP2020/UR	1.4
R2083	0.7

Table 30: Properties of several scintillators. The existing CLAS detector utilizes BC-408 scintillator.

Scintillator	Bulk λ (cm)	τ (ns)
BC-408	380	2.1
BC-404	160	1.8
BC-418	100	1.4

Photomultiplier Tubes   The prototypes that have achieved the desired resolution have used XP2020 PMTs, which have faster rise times than our current CLAS detector. While detailed prototyping efforts should be performed to optimize the choice of components, we expect that a faster PMT will be required. In Table 29 we give the rise time of various common tubes. The XP2020 PMTs have 25% faster rise time than the XP2262 tubes used in the current detector which is achieved with improved transit time spread across the photocathode. Faster PMTs are available, but in practice should be matched to the decay times of the scintillator material for improved performance of the overall system.

Scintillator   This parameterization is used to study the possible improvements in resolution based on a tradeoff between the decay time of the scintillator (σ_1 in Eq. 74) and the number of photoelectrons arriving at the PMT which depends on the attenuation length λ. The bulk attenuation length and the scintillator decay times for three typical scintillators are listed in Table 30. In Fig. 171 the expected resolution is plotted as a function of counter length for the three scintillators listed in Table 30. For the figure we have used bulk attenuation lengths for BC-404 and BC-418, while we have used the measured values for BC-408. We have also plotted the resolution for BC-418 for half the bulk attenuation length. The plot indicates that, if the actual attenuation lengths approach the bulk attenuation of the material, the decay time dominates the performance for counters less than 200 cm in length. This is an option that should be explored experimentally for the shortest counters. Otherwise, we see that the existing material BC-408 is a good choice for scintillation material.
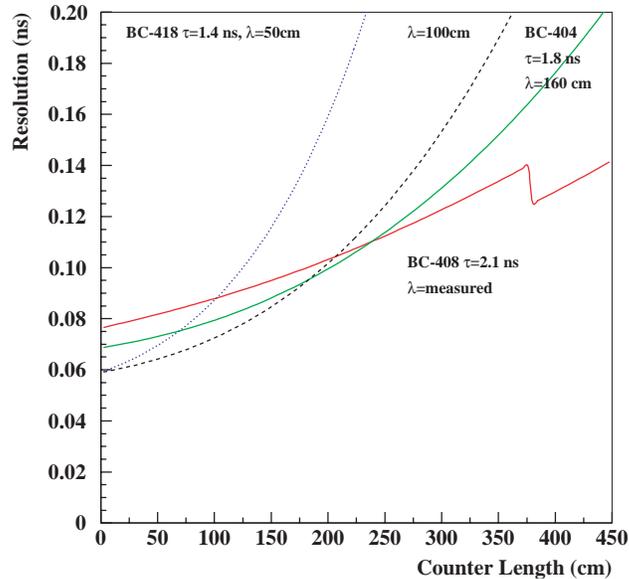
Figure 171: Resolution for various scintillators showing the tradeoff between attenuation length and scintillator decay time.

Inner Calorimeter In the present CLAS system, neutral particles heading for the coils are not detected. As is the case for charged particles, we would like to determine the direction and (to the extent possible) the energy of all photons. This requires coverage of the inside of the torus coils with photon detectors. Ideally, the detector should also give some information on charged particles, such as their energy deposition, range, etc.

The detector must be very compact since there is little space available in the angular range between 5° and 40° to complement the forward calorimeters. There is also a significant magnetic field in the region of the Torus coils that must be accommodated in the calorimeter design. A promising solution is to install short radiation length crystals. The currently most likely candidate is the scintillator crystal lead tungstate ($PbWO_4$). To avoid problems with the magnetic field interfering with photomultiplier readout, the crystal light can be collected with avalanche photodiodes (APD). The signal will be further amplified in low noise preamplifiers and in post amplifiers, before digitization.

This technique is currently planned for use in the DVCS experiment with CLAS. The DVCS experiment has requirements very similar to the requirements for the CLAS upgrade. In particular the experiment will use a superconducting solenoid for shielding the detectors from the Møller electron background.

A conceptual design of a $PbWO_4$ calorimeter for the Torus coil region is shown in Fig. 172
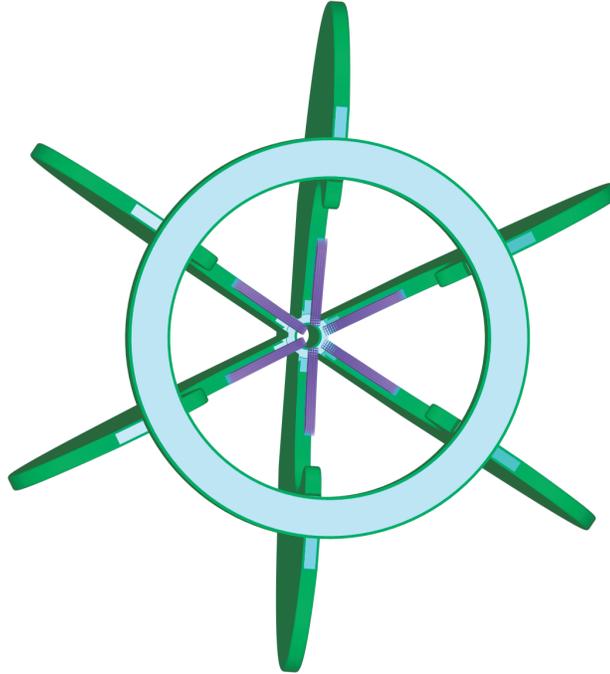
Figure 172: Arrangement of the Inner Calorimeter covering the regions of the torus magnet coils. The calorimeter consists of lead-tungstate crystals. The light is collected in Avalanche Photodiodes which are insensitive to magnetic fields. The APD signal is then amplified in low noise preamplifiers.

Forward Angle Calorimeter The CLAS forward electromagnetic calorimeter (FEC) will be reused in CLAS^{++} without any modifications. In conjunction with the two threshold Čerenkov detectors the FEC provides electron identification up to the highest particle momenta, and efficient pion rejection with a rejection factor of > 2000 at an electron detection efficency of $>99\%$. Above the pion threshold of the HTCC the FEC will continue to provide pion rejection, however with reduced rejection power (> 100 at $> 95\%$ electron detection efficiency).

Pre-shower calorimeter A major part of the physics program will require reliable detection of π^0s through their two-photon decays, in a wide range of momentum and angles. Forward-going photons in CLAS are detected in the forward electromagnetic calorimeter (FEC). FEC is a lead-scintillator sandwich with three stereo readout planes oriented at approximately 120° to each other. The transverse size of the readout module in a plane is about 10 cm. The energy of the photons is reconstructed using the fraction of the shower energy deposited in the scintillators. For the FEC this is about 30% of the total energy deposited in the calorimeter. The production angles of the photons are determined via the hit position on the FEC, reconstructed from three stereo readouts.

With 12 GeV beams π^0s will be produced with momenta up to 9 GeV/c. With increase of the pion energy the spatial distance between two photons at the calorimeter will decrease, Figure 173, and at pion momenta above 4 GeV/c the distance between two hits will be too small to allow
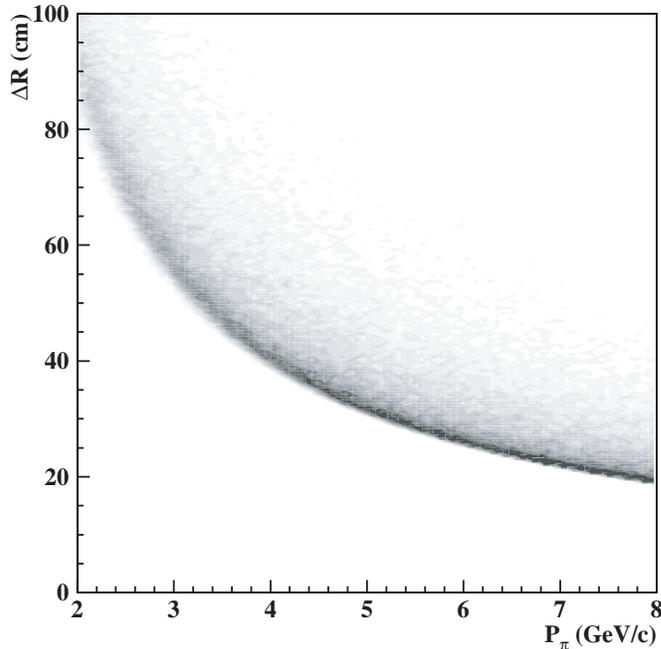
Figure 173: Distance between hit positions of the two photons from π^0 decay at the FEC plane as a function of the pion momentum. At a pion momentum of 8 GeV/c the minimum distance between the two photons is 20 cm which does not allow a reconstruction of the two photons in the existing CLAS FEC.

unambiguous reconstruction as two separate hits. Most of high energy pions will be reconstructed as a single hit and can be misidentified as a single high energy photon. In Figure 174 π^0 detection efficiency of as a single hit (triangles) or as two hits (squares) in the forward calorimeter is shown as a function of pion momentum. Open symbols represent GEANT simulations with existing geometry. As one can see with increase of pion momentum the efficiency for reconstruction of two hits rapidly decreases, and two photons are mostly reconstructed as a single hit.

Finer transverse granularity of the readout plane is needed to resolve two photons from high energy pions. This can be done with a finer segmented pre-shower located in front of each FEC module. The pre-shower will be used for a more precise determination of the hit position. Most of the shower energy will still be absorbed and reconstructed in the FEC. In Fig. 174 full symbols are simulations with higher transverse segmentation of the calorimeter. Having two hits spaced more than 3 readout segments in a view will permit the separation of 2 photons from π^0 decay up to 9 GeV/c.

The conceptual design for the pre-shower is similar to the existing FEC of CLAS. It is based on a lead-scintillator sandwich arrangement with the shape of an approximately equilateral triangle. Three stereo readout planes are oriented parallel to the sides of the triangle. There are 9 layers of scintillators, 3 alternating layers in each view. Each layer will consist of 3 cm wide and 0.5 cm thick scintillator strips. 2 mm thick lead sheets are interleaved between two scintillator layers.
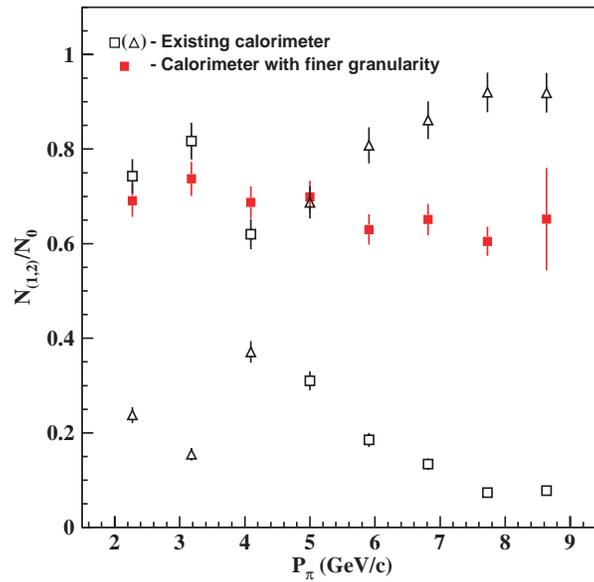
Figure 174: π^0 reconstruction efficiency from the reaction $ep \rightarrow ep\pi^o$ with beam energy of 11.5 GeV. Simulations are done with the CLAS FEC only. Open squares symbols indicate events when two hits are reconstructed, the invariant mass of the two photons is near the π^0 mass, and the energy sum is about the energy of the pion. Open triangles show the frequency of single hit reconstruction with the energy corresponding to the π^0 energy. For momenta of 4 GeV/c and higher most of the π^0 events are misidentified as single photons. The full red squares show the results of a simulation when the preshower detector is used in the reconstruction. Pions are reconstructed over the full momentum range in this case.

Figure 175: 3-d view of a corner of the pre-shower module. Three layers are shown only. Wavelength-shifting fibers are used to read out the light generated in the plastic scintillators. The scintillators and embedded fibers provide stereo information due to a geometry which is similar to the geometry of the CLAS FEC.

Light produced in the scintillator will be transported to the photo detector via four 1 mm radius waveshifting (WS) fibers embedded in the half-circular equally spaced grooves on the surface of the scintillator, as seen in Fig. 175. Photomultiplier tubes with $\sim 1''$ green sensitive photocathode will be used for light detection. Corresponding strips from 3 layers of the same view will be read out with a single PMT. From studies using a prototype model we expect about 15 photoelectrons for 1 MeV energy deposition in the scintillator. With a sampling ratio of 0.3 this corresponds to 5 photoelectrons per 1 MeV deposited in the full calorimeter.

Simulations of exclusive, $ep \rightarrow ep\pi^o$, and semi-inclusive, $ep \rightarrow e\pi^0$, reactions showed that pions with momenta $> 4~GeV$ are produced at angles $\theta < 25°$. Therefore, the pre-shower must provide coverage for straight tracks up to 25°. This corresponds to about half the size of the existing FEC. This implies that the height of the triangle, corresponding to the active area of pre-shower detector must be about 180 cm. The 64 scintillator strips in a layer with 3cm width cover the desired area. As described above, corresponding scintillator strips of the layers of a view are read out with a single PMT via four green WS fibers per strip, 12 fibers for each PMT. There will be 192 readout channels in each sector, making a total of 1152 channels for the entire system. Each read out channel will be furnished with trigger electronics, ADCs and TDCs.

3.B.4   Polarized Target Operation in CLAS^{++}

Longitudinally polarized Target in Solenoid Magnet   Part of the program for CLAS^{++} requires a polarized solid state target polarized parallel or anti-parallel to the electron beam. In

CLAS^{++} this can be accomplished by adding some correction coils to the superconducting solenoid to improve the field uniformity around the target. The correction coils are needed since the solenoid magnet alone may not produce a sufficiently uniform magnetic field in a large enough volume around the target to achieve highly polarized protons or deuterons (neutrons). With this option, the complete central detector could be used for polarized target experiments, allowing nearly full coverage for particle detection. This arrangement will allow measurement of multi-hadron final states in addition to the scattered electron. The target cryostat will have to be re-designed to allow for its operation in a warm bore magnetic field environment.

Transversely Polarized Target. At the higher energies achievable with the Upgrade there is a significant interest in semi-inclusive and exclusive processes involving transversely polarized targets. In the CLAS^{++} configuration, and if the central detector is removed, the polarized target cryostat can be inserted from the top in between the torus coils which are no longer instrumented with tracking chambers. This provides a straight forward way of rotating the magnet by 90° to provide a transverse (to the beamline) polarization. As the magnetic field will deflect the incident beam vertically a magnetic chicane will be needed to compensate for that deflection. The chicane is to be inserted into the beamline upstream of CLAS^{++}. The Helmholtz coil geometry will restrict the acceptance for particle detection to the forward region.

3.B.5 Beam Line

There are no major changes in the beamline necessary for the main 12 GeV operation. The bulk of the beamline equipment will operate as designed or better with an electron beam of higher energy and current. The items that should work without major upgrades include the three nA RF beam position and current monitors, beam profile harps, beam charge asymmetry monitors, beam halo monitors, beam viewers and beam raster magnets. One beamline element that is not-upgradable to 12GeV running is the tagger magnet. New beamline elements or existing equipment that needs modification for the upgrade are described in the following sections.

Faraday Cup The Faraday cup (FC) currently installed in the Hall B beamline contains no provision for water cooling. With the increase in beam energy by a factor of 2, and with the increase in luminosity by a factor 10, which will mostly come from an increase in beam current, the total power absorbed in the FC could increase by a factor of 20. This will either require the implementation of some cooling capability into the Faraday cup, or limit the duration during which the FC can be exposed to the beam. Another, though less desirable, possibility could be to limit use of the Faraday cup to short periods of time, e.g. for calibrating the upstream beam current monitors, and to move the FC out of the beam after the calibration is completed. This in turn would require installation of a low power beam dump located downstream of the FC that would dump the electron beam during routine operation.

Møller Polarimeter   The Hall-B Møller polarimeter consists of a magnetized permadur target followed by two magnetic quadrupole magnets that deflect the electrons into scintillating fiber bundles. The maximum beam energy of the present polarimeter is given by the maximum field of the quadrupole magnets. This maximum is ~ 8.5 GeV. In order to achieve operations with an 12 GeV beam energy the polarimeter will need to be reconfigured. A combination of increasing the distance separating the two magnets and relocating the detector bundles further from the magnets should be sufficient for 11 GeV operation. The determination of the optimum configuration for operation with any beam energy between 3 and 11 GeV is ongoing.

Magnetic Chicane   Additional modifications will be needed when operating a polarized target in CLAS^{++} when the magnetic field is oriented transverse to the beam line. A beam chicane[6] will be needed to compensate for the beam deflection of about $3.2°$ (at 12 GeV) in the polarized target field (~ 2 Tm integral). It will be inserted into the beam line upstream of CLAS^{++}.

Beam raster magnets   The installed beam raster system, which is used in conjunction with the polarized target, is dimensioned to allow full rastering over a polarized target a 1.5 cm diameter. The power supplies will be replaced with more powerful supplies.

3.B.6   Data Acquisition System and Trigger

The primary feature driving the redesign of the CLAS^{++} Data Acquisition (DAQ) and triggering system is the higher data rates associated with the approximate factor of 10 increase in instantaneous luminosity that will be delivered to the experiments in Hall B.

Design criteria for the system   The CLAS^{++} DAQ must handle level1 trigger rates up to 20kHz at 10kByte/event event size with ¡15% dead time. High data transfer rates over the network will be handled by using gigabit Ethernet. The proposed DAQ system must assemble the event data from many front-end buffers to the Event Recorder (ER). The system must provide sufficient computing resources for executing physics algorithms which can substantially reduce the expected input rates. It must also provide continuous monitoring of the detector so that malfunctions may be readily identified and corrective measures taken. These functions will be performed by using a high performance readout network to connect the sub-detector readout units (ROC) via multiple event builders (EB) to the event filtering units (EFU, possibly implemented in computer farms). The flow of event data will be controlled by the triggering and timing system (TTS).

---

[6]The chicane is not part of the equipment complement for the upgrade, however it is part of a proposal currently under development for an experiment at 6 GeV, and may therefore exist before the energy upgrade

System upgrade CLAS^{++} DAQ system design requirements are based on the rate estimates of the 12 GeV leading physics programs. The current system will be upgraded to meet the design requirements and to minimize the efforts, that will be invested to satisfy increased requirements of the 12 GeV physics programs. The following upgrade strategy will be used to achieve desired goal.

- Utilizing pipelined digitization hardware for the CLAS^{++} new detector components.

- Replace the CLAS existing detector components: ADCs and high resolution TDCs with the equivalent pipelined digitization hardware, ready to function in the free-running DAQ mode.

- Keep existing low resolution TDC (TDC1877/1877S) in the system.

The mentioned hardware upgrades, with conjunction of the fast and optimized readout system, will guarantee fulfillment of the CLAS^{++} DAQ design requirements. Using pipelined digitization hardware components in the system will provide most of the benefits, typical for the free-running DAQ systems. Gradual replacement of the remaining hardware (low resolution DC TDCs) with the pipelined equivalent will help us eventually implement full operational free-running DAQ system for future CLAS experiments.

Figure 176 shows possible data flow diagram of the CLAS^{++} DAQ system. Here is a possible scenario of implementing higher level triggering algorithms, which demonstrates flexibility of the proposed system. In order to optimize the data flow, the event filtering computer farm performs event selection in two stages. First, a level2 filtering decision is made on a subset of the data from a programmable set of the detector components. This will help us to avoid system bandwidth saturation by reading out large volumes of tracking data at high level1 rates. The remainder of the full event data are only transferred to the filtering farm on a level2 accept, and a final level3 algorithm is then applied to the complete event. This activity is controlled by the Filtering Supervisor (FS) system.

3.B.7 Event Reconstruction and Offline Computing

The expected online data rate of 100 to 200 MByte/s cannot efficiently be handled when using the same procedures adopted by CLAS in the past: an efficient online event reduction is required to keep the data transfer rates to the Jefferson Lab tape silo within the bandwidth limits. Furthermore, the online event reduction and event processing will allow for a comparatively fast access to processed data for further analysis. We consider establishing a "grid-based" cluster of analysis and simulation centers to optimize the data processing.

Data Reduction and Online Event Reconstruction Major parts of data reduction will have to be performed online. The first stage of data reduction (noise reduction) will be performed at
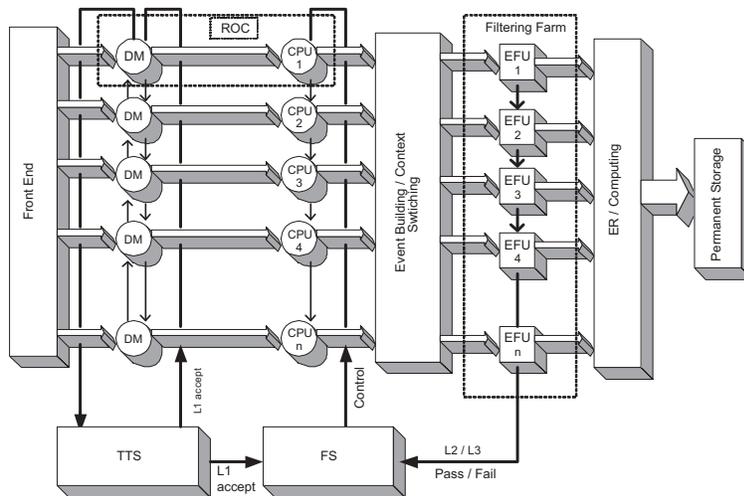
Figure 176: CLAS^{++} DAQ bloc diagram. DM - Digitization Module, TTS - Triggering and Timing System, FS - Filtering Supervisor, EFU - Event Filtering Unit, ER - Event Recorder.

the crate level, the second stage in form of fast event filtering and tagging of events (Level 3) which will remove data which are not of interest for further analysis.

A fast online reconstruction will provide sufficient information on data quality and first-pass analysis of basic reactions. Depending on the available CPU power it is possible to perform a full event reconstruction of all events: using an online farm in the Hall-B Counting House and/or part of the JLab CUE farms which requires either a second output stream or large pre-silo stage disks. Taking into consideration the current achievements (7-10 ms/event) and the projected increase of CPU speed over the next 6 years, a full event reconstruction can be performed within 3-4 ms despite the more complex detector setup of CLAS^{++}. The output will be written to disk in form of data summary files which contain all information required to perform a first-pass event analysis.

The (quasi-) online event reconstruction requires zero order calibration constants which have to come from analyses of previous run periods (and commissioning data) as well as the analysis of data taken during the first days in the specific run period. Additionally, small subsets of data will be selected for further analysis to perform a quasi-online calibration of all detector components. This continuous calibration process will provide a quick response to any changes in crucial detector parameters. In parallel, these subsets will be transferred to university-based analysis centers which will be responsible for a refinement of the online calibration.

The data summary files as well as the data subsets to be used for calibration purposes will be stored for several days on large RAID arrays to allow for fast access. We expect that the JLab Computer Center will provide the necessary infrastructure of fast network connections as well as short- and long-term storage media.

3.C Hall C and the Super High Momentum Spectrometer (SHMS)

3.C.1 Overview

Much of the physics outlined in Chapter 2 can be accessed only by a spectrometer system providing key features not available in the existing CEBAF facilities. It must have acceptance for very forward-going particles and analyzing power for particle momenta approaching that of the incoming beam. It must provide excellent particle identification even at these high energies. It must be capable of rapid, accurate changes to the kinematic settings with well understood acceptances allowing experiments to efficiently cover broad regions of phase space, enabling, for example, precise L/T separations. The basic design must be flexible so that specialized detector elements, such as polarimetry or additional particle ID, can be incorporated to satisfy the needs of particular experiments. And it must possess an efficient, highly time-resolved trigger system and a target and data-acquisition system suitable for running at high luminosity.

Our plan for meeting these needs consists of producing a new Super-High-Momentum Spectrometer (SHMS) and outfitting the existing HMS spectrometer with a compatible data-acquisition system. The SHMS will be capable of analyzing the higher energy particles produced by the upgraded CEBAF beam at scattering angles as low as 4.5° (central axis at 5.5°). It will be designed as a companion to the HMS so that, taken together, the system will provide full momentum range single-arm capabilities as well as double-arm coverage over the entire kinematic region of interest to the proposed experiments. Thus, the SHMS will not be a replacement for the HMS, but rather a complementary partner to it just as the SOS (Short Orbit Spectrometer) functions as a partner to the HMS.

We present our plan by first reviewing the characteristics of the existing HMS in section 3.C.2. The physics demands developed in Chapter 2 of this report drive the proposed improvements to the HMS and determine the needed specifications for the companion SHMS. A summary of those specifications and a design for the SHMS which provides what the physics demands is given in section 3.C.3.

3.C.2 The High-Momentum Spectrometer

The HMS is a focusing spectrometer which can be tuned for central momenta from 0.4 to 7.3 GeV/c and production angles from 10.5 to 90 degrees relative to the beam direction. Its momentum acceptance is ±10% and the angular coverage is ±32 mr in-plane by ±85 mr out-of-plane, achieved by the optical system consisting of three quadrupoles in a FDF arrangement followed by a dipole. The angular acceptance is defined by a collimator near the upstream end of the spectrometer.

The optical system is followed by a detector stack made up of two pairs of crossed scintillator hodoscopes, twelve planes of precision drift chambers, a gas Čerenkov counter which can operate
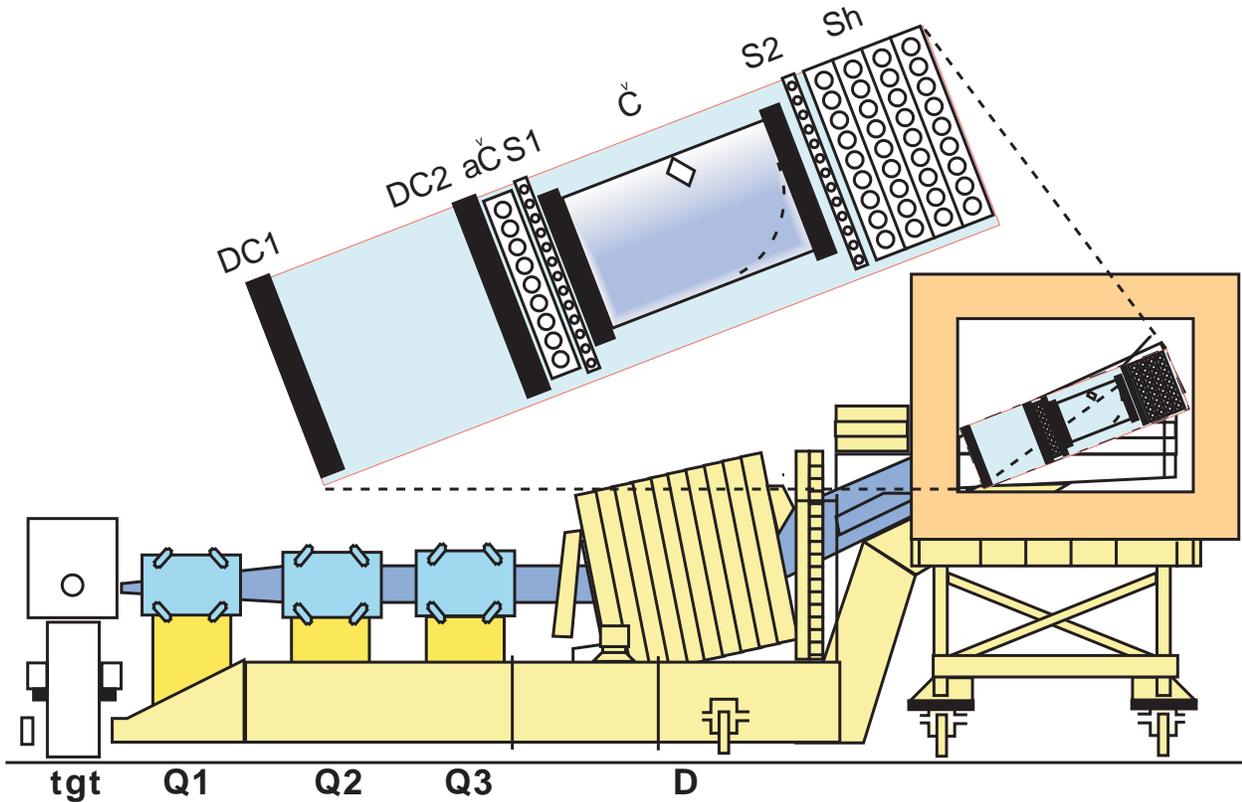
Figure 177: Sketch of the High-Momentum Spectrometer showing the Magnets, the Carriage, and an expanded block diagram of the Detector Stack.

from 0.3 to 2.5 atm., an aerogel Čerenkov counter, and a segmented lead-glass shower counter. A schematic diagram of the magnets and detector stack is shown in Fig. 177. The system is read out by a triggering and data-acquisition system providing full event readout of more than 2000 events/s with time-of-flight (TOF) and coincidence time resolution better than 200 ps.

Since the beginning of physics operation in Hall C, the HMS has provided precision tracking and particle identification for many experiments. Figure 178 shows some of the detector calibration results from these experiments which demonstrate its resolution and particle discrimination capabilities are summarized in Table 31.

Rotation of the whole spectrometer to the desired central scattering angle is accomplished remotely, without the need for access to the radiation enclosure, in about ten minutes. Angular setting accuracy is better than half a milliradian. Similarly, the central momentum may be adjusted remotely in about the same amount of time. These capabilities are crucial to experiments that must take data at a multitude of kinematic settings.
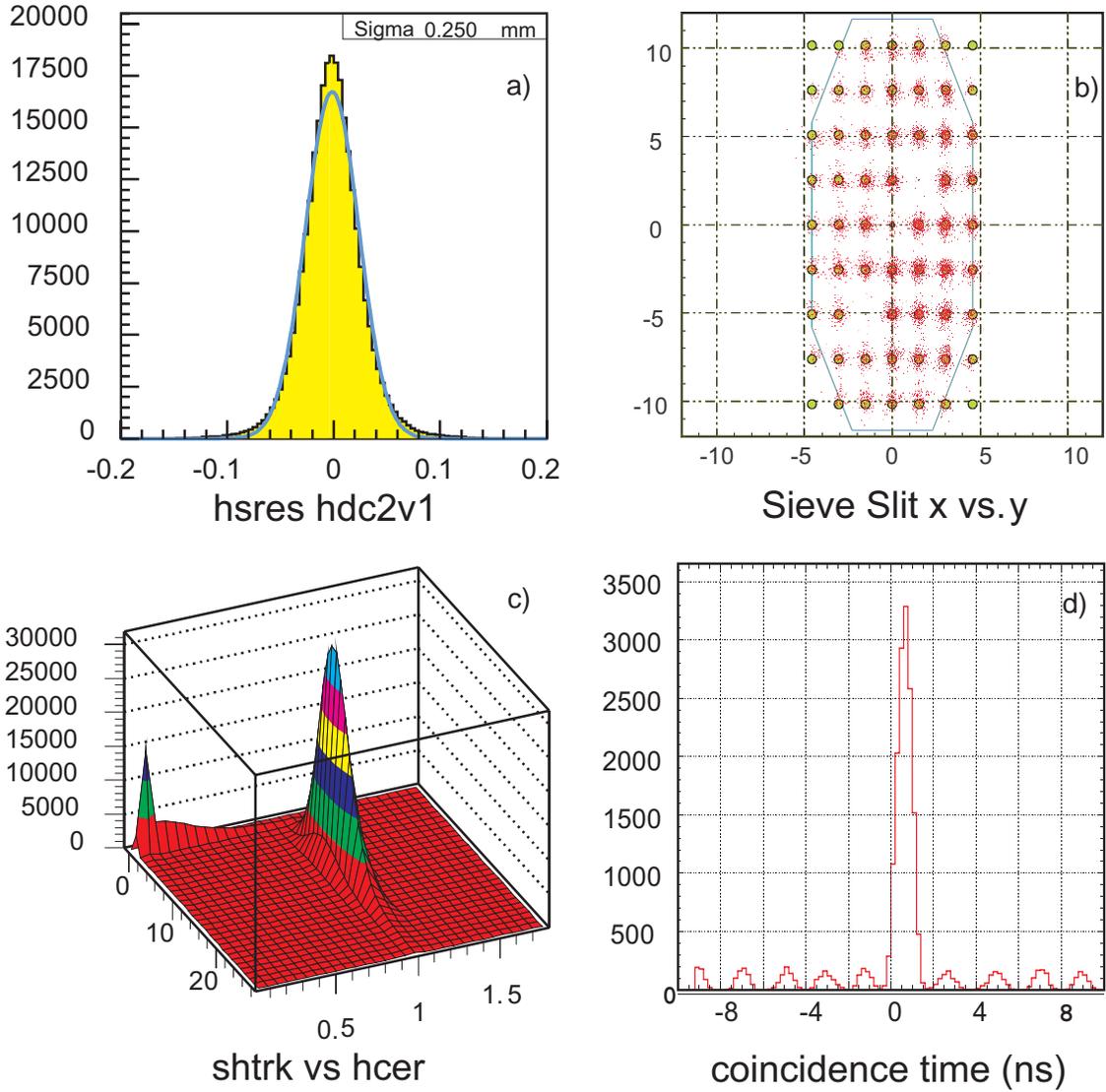
Figure 178: HMS Spectrometer Representative Data: Tracking capability is shown by a) Single-plane wire chamber resolution, and b) sieve slit reconstruction. Panel c) shows Shower Counter Energy vs. number of photons in the Čerenkov, demonstrating clear electron-hadron separation. Coincidence time resolution in the HMS–SOS hodoscope system is demonstrated in panel d) by the clear separation of particles from neighboring RF buckets.

Table 31: Summary of the HMS Performance and the Design Specifications for the SHMS.

Parameter	HMS Performance	SHMS Specification
Range of Central Momentum	0.4 to 7.3 GeV/c	2.5 to 11 GeV/c
Momentum Acceptance	±10%	-15% to +25%
Momentum Resolution	0.1% − 0.15%	< 0.2%
Scattering Angle Range	10.5 to 90 degrees	5.5 to 25 degrees
Target Length Accepted† at 90°	10 cm	50 cm
Horizontal Angle Acceptance	±32 mrad	±18 mrad
Vertical Angle Acceptance	±85 mrad	±50 mrad
Solid Angle Acceptance	8.1 msr	4 msr (LSA tune)
		2 msr (SSA tune)
Horizontal Angle Resolution (yptar)	0.8 mrad	2-4 mrad
Vertical Angle Resolution (xptar)	1.0 mrad	1-2 mrad
Vertex Reconstruction Resolution (ytar)	0.3 cm	0.2 - 0.6 cm
Maximum DAQ Event Rate	2,000 events/second	10,000 events/second
Maximum Flux within Acceptance	~ 5 MHz	~ 5 MHz
e/h Discrimination	>1000:1 at 98% efficiency	1000:1 at 98% efficiency
π/K Discrimination	100:1 at 95% efficiency	100:1 at 95% efficiency

† This length corresponds to what the spectrometer can "see" perpendicular to its optic axis.
  The acceptable target length at any accessible scattering angle is, to first order, the projection of this length.

3.C.3   The Super-High-Momentum Spectrometer

Overview   The Super-High-Momentum Spectrometer (SHMS) will play a vital role in the overall JLab physics program at 12 GeV. Short latency detector elements will minimize pileup and out-of-time events and, coupled with advanced data-acquisition components, will allow readout of 10,000 or more events per second. An inevitable consequence of relativistic kinematics is that much of the interesting physics at 12 GeV will only be accessible provided at least one of the spectrometers can achieve angles significantly below 10 degrees. The SHMS will achieve a minimum scattering angle of 5.5 degrees with acceptable solid angle and it will do so at high luminosity. The maximum momentum will be 11 GeV/c, well matched to the maximum beam energy available in Hall C. These three characteristics (high luminosity, small scattering angle, and high momentum) are essential for carrying out a program of electron-hadron coincidence experiments at large $z = E_h/\nu$, where ν is the electron energy loss. (For orientation, in the limit of $z \rightarrow 1$, one approaches the exclusive limit.) At large z (*i.e.* $z \approx 1$), sensitivity to the valence quark structure of the hadron is maximized and the reaction mechanism is simplified.

The HMS-SHMS spectrometer pair will be rigidly connected to a central pivot which permits both rapid, remote angle changes and reproducible rotation characteristics which simplify accurate measurements. From its inception, the SHMS momentum and target acceptances have been designed to be very flat, with performance similar to that of the HMS. This also simplifies making accurate measurements. These capabilities will facilitate experiments which rely on a large number of angle and momentum settings, such as L–T separations, for which accurate pointing as well as
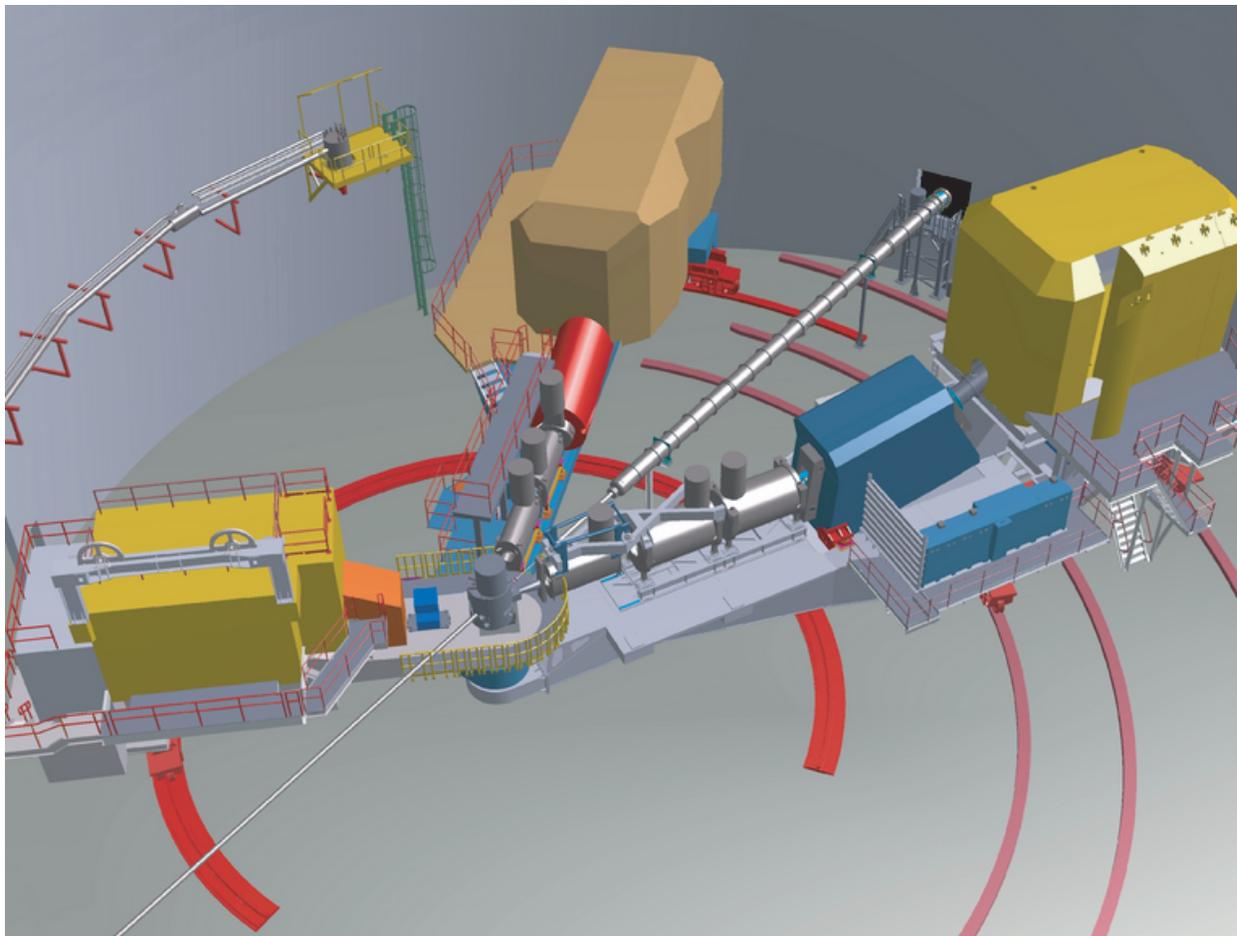
Figure 179: A CAD drawing of the new SHMS spectrometer installed in Hall C together with the existing HMS spectrometer (right) and the SOS spectrometer (left).

flat momentum and target acceptances are essential. Finally, for experiments which are willing to trade off small-angle performance for increased solid angle, this can be achieved by pulling the magnets and detectors forward and re-tuning the spectrometer. A CAD drawing of the new SHMS, together with the existing HMS and SOS spectrometers in Hall C, is shown in Fig. 179. In the remainder of this section we will address the design and performance details of the SHMS.

The SHMS Magnets and Structural Design

General   The SHMS is an 11 GeV/c superconducting spectrometer. The magnet system consists of two cold iron quadrupoles similar in design to the HMS Q1, and a combined-function warm bore magnet that is 5 m long. The cryogenics are proven systems using standard JLab components. The shield house is a composite of concrete, steel and lead. The magnets and the
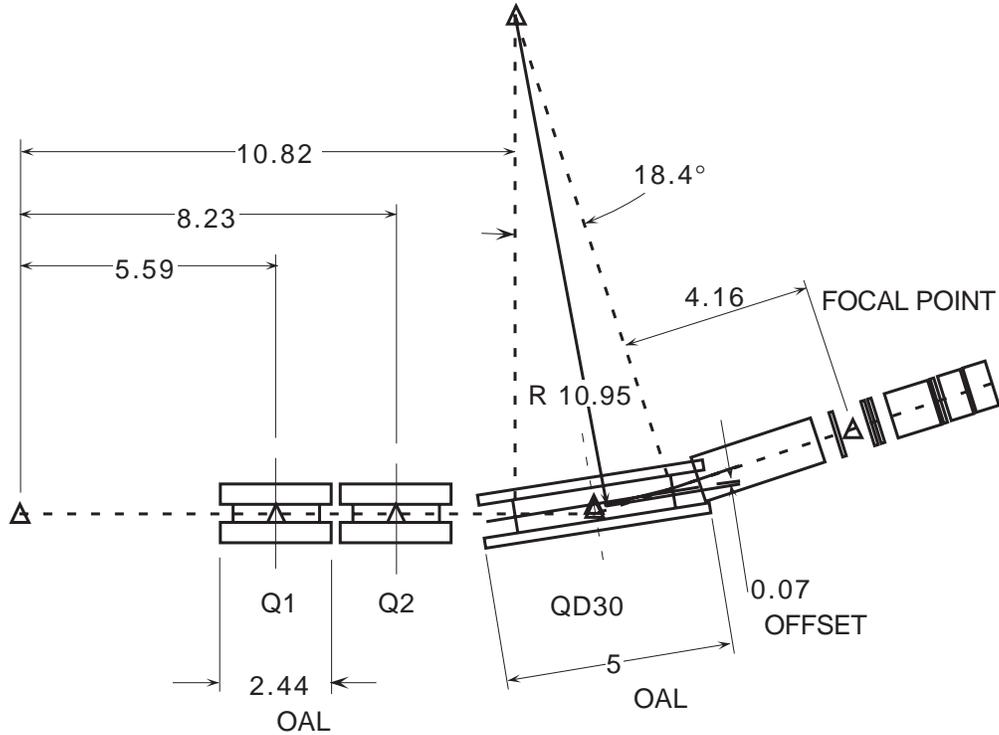
Figure 180: SHMS Spectrometer Key Dimensions (meters) showing the location of the two quadrupoles and the combined-function magnet relative to the target and the detector stack.

shield house are supported by a welded steel structure with steel drive wheels. Fig. 179 shows a perspective view of the spectrometer and Fig. 180 provides a line drawing of the layout.

Q1 at 8.6 T/m   The SHMS spectrometer requires two quadrupoles with a gradient of 8.6 T/m and 40-cm aperture. The requirement to reach the scattering angle of 5.5 degrees means that the quads must be narrow. The existing HMS spectrometer Q1 magnet can just reach the required gradient due to the built in margin in operating current. The Q1 and Q2 magnets were designed by Oxford Instruments with a considerable operating margin so that the required gradients for HMS could be reached given some uncertainty in the yoke packing factor and the performance of the then new design of the large cold iron quads. The power supplies, for example, were sized at 1250 A even though the gradient was predicted to be reached at ~1050 A. The cold iron quads worked as designed and the margin was never called into service. The margin in power supply current was matched by similar margins in the current leads, superconductor critical current, and force containment. Table 32 has the relevant Q1 parameters at the present maximum excitation and, for comparison, those required for SHMS. The forces at the 8.6-T/m gradient require further evaluation to determine if any internal structural modifications are required. The design margins in the present Q1 are very comfortable but much of this is lost at the higher excitation. Figures 181 and 182 show the gradient field quality and saturation at 8.6 T/m. Both are reasonable and meet the requirements.

Table 32: Q1 comparison between HMS at 1010 A and SHMS at 1291 A.

Parameter	HMS	SHMS	Change
Gradient (T/m)	7.11	8.59	20.8%
Current (A)	1010	1291	27.8%
Pole Tip Field (T)	1.78	2.15	20.8%
Field in Iron (T)	3.72	3.82	2.7%
Coil Forces[†]			
F_x (N)	28,571	44,062	54.2%
F_y (N)	7,465	-12,604	68.8%

[†]for Coil Stack 1

Figure 181: Comparison of the Q1 gradients along Z at 7.1 T/m and 8.6 T/m.

The project plan for SHMS is to procure, through competitive contracting, two Q1 magnet systems with a slightly thicker yoke shell to compensate for the ~50% force increase. This modification will add a few centimeters to the overall size of the yoke/shell combination. The SHMS power supply will be rated for 1350 A, an increase of ~10% over the present HMS Q1 supply. Similarly, the energy dump resistor will be designed to absorb a higher stored energy.

QD30 Superconducting Magnet for the SHMS   The spectrometer requires a combined-function superconducting magnet that can simultaneously produce a 4.0-T dipole field and a 3.0 T/m quadrupole field inside a warm bore of 30 cm. A magnetic design using TOSCA 3-D[TOSCA] has been performed to establish the basic magnetic requirements, provide 3-D field maps for optics analysis, and produce basic engineering information about the magnets. A four sector cosine theta current distribution and a two sector cosine two-theta quad design with warm bore and warm iron has been selected and analyzed. A cut-away drawing is shown in Fig. 183.
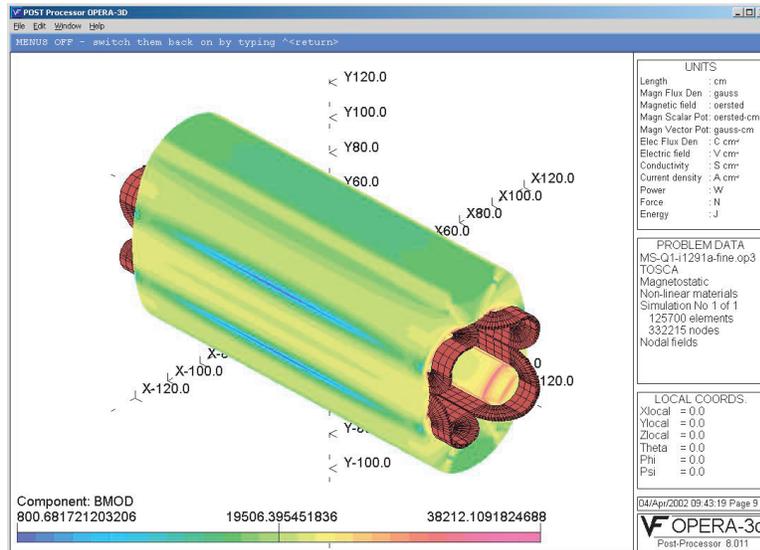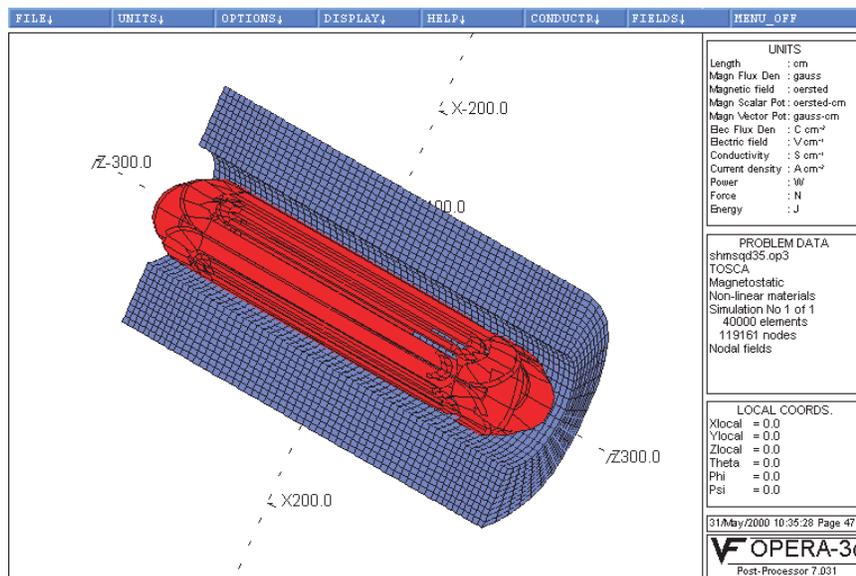
Figure 182: Magnetic Fields in Q1 at High Current.

Figure 183: Cut-Away View of QD30 Magnet with beam–left side of yoke removed. Orientation is with bend field horizontal. Perspective angle is such as to make the image appear approximately as installed.

The magnetic design uses TOSCA-generated cosine theta type coils with "constant perimeter ends". These coils closely approximate the ideal cosine geometry that would be a perfect generator of high purity fields. Practical considerations such as finite current distributions, a limited number of sectors, and TOSCA's internal approximations, all contribute to deviations from the ideal geometry and are the sources of higher order field errors in the design. The yoke is modeled as non-linear iron with the nominal properties of 1010 steel. It is 4.2 m long with an outer elliptical shape having radii 120 cm 100 cm and a 60-cm inner circular radius. The detailed shape of the yoke is not very important in a cosine type magnet as the design requires an unsaturated yoke for good internal fields. The high field region is either on top or on the bottom depending on the relative sign of the dipole and quadrupole coils, therefore an elliptical yoke represents an ideal solution.

The QD30 combined-function magnet produces a peak field of 4.3-T in the bore and 5.4 T in the windings (see Figs. 184 – 187). These fields are comparable to those achieved in large bore magnets produced 20 years ago for MHD research, particle spectroscopy and coal sulphur separation. There are significant differences between the present magnet design and these prototypes. For example, the stored energy of the QD30 is somewhat less even though the field volumes are comparable. This is due to the fact that the superposed quadrupole field produces significantly less stored energy for a given maximum field. The combined fields also produce a very asymmetric resultant field and force distribution. The fields add on the bottom of the magnet and subtract on the top, so the fields across the bore range from $\sim$0 to $\sim$5 T. Similarly the fields in the windings are highest where the fields add (5.4 T) and nearly –2 T where they subtract. Thus there is a net force between the yoke and coil that must be dealt with due to the asymmetry. The peak linear force densities are 40,000 pounds per inch for the dipole winding and 11,000 pounds per inch for the quadrupole winding. These forces add on one side and subtract on the other yielding peak pressures that range from 4680 psi to 2100 psi. Simple pressure vessel computations for 20-ksi material stress yields a 6.0-inch thickness for the cold mass force collar. Due to the large radial thickness of the windings (3.5 inches) and cryostat (11.8 inches), the required 6-inch pressure shell is easily accommodated without stressing the coil cold mass. Obviously in a real cold mass the stress will be distributed and the resulting stresses lowered. The large size of the cryostat will allow separate fluid pressure vessels in accordance with the ASME code. This will greatly simplify the final design and result in a much more conservative magnet. A fully clamped winding is planned for the final construction.

Cryogenic stability of the QD30 quadrupole and dipole has been evaluated against the Steckly criterion, α. The condition of stability is that α must be less than one, which means that the velocity of spread of a normal zone is negative. That is, a normal zone will always shrink. Analysis shows that α is 0.79 and 0.48 for the dipole and quadrupole coil designs, respectively.

Magnet DC Power and Energy Dump System   The DC power system for the SHMS magnets will consist of four independent power supplies. These supplies will be 12-pulse SCR supplies with a final stage transistor regulator providing stability of 10 ppm. They will be low-voltage high-current commercial units readily available from Danfysik and others. A DC current of
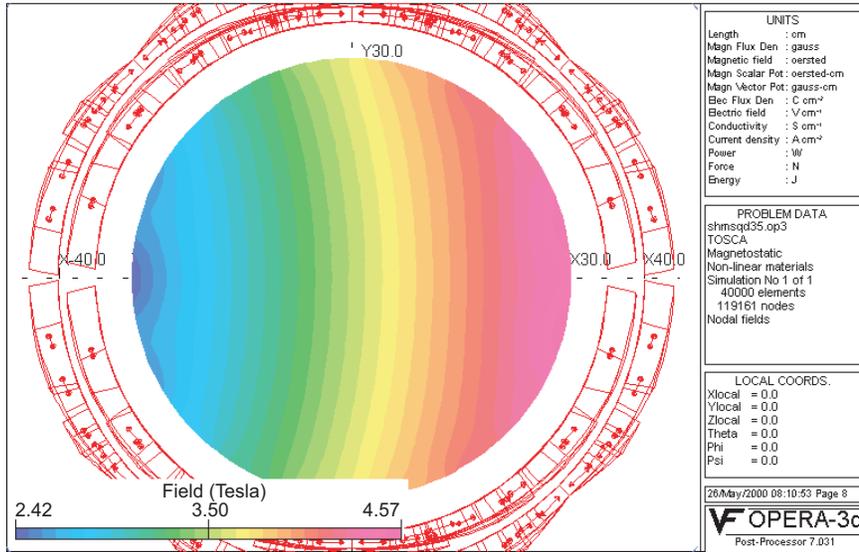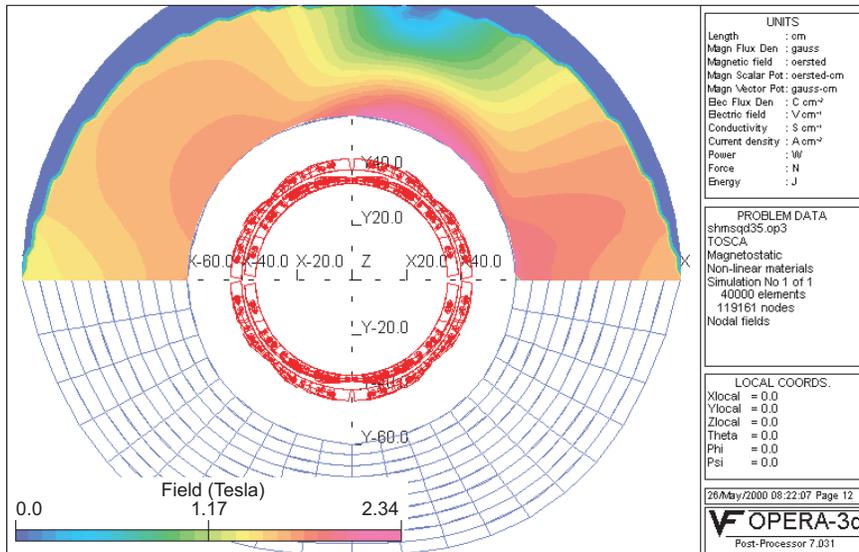
Figure 184: $|B|$ in QD30 Midplane (G).

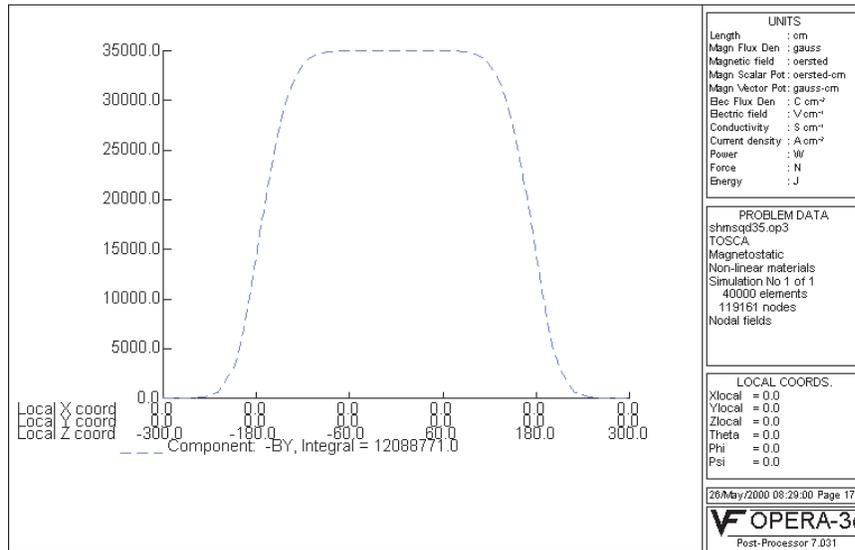Figure 185: QD30 Yoke Saturation- $|B|$ (G).

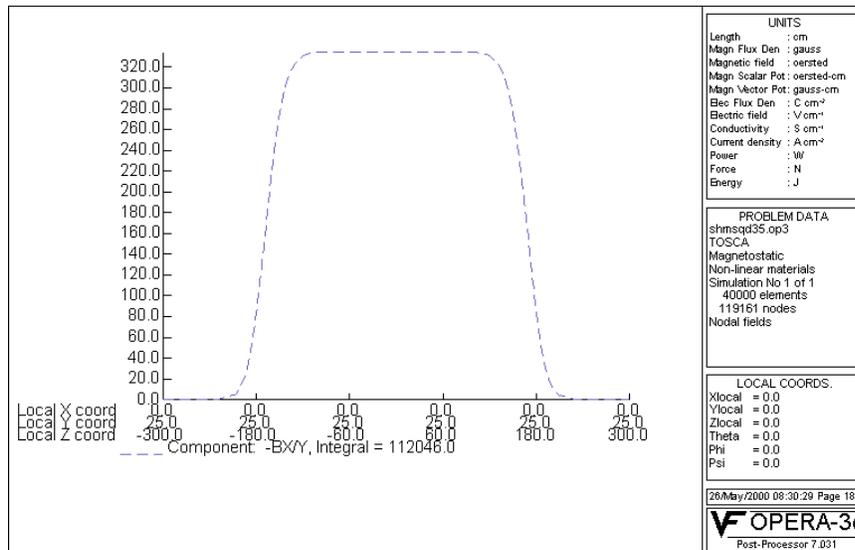Figure 186: QD30 Dipole Field (B_y) along the central axis $x = y = 0$.

Figure 187: QD30 Field Gradient $\partial B_x / \partial y$ along $x = 0, y = 25$.

Table 33: SHMS QD30 Magnet Parameters.

Function	Combined Quadrupole – Dipole	
Bore	30 cm Warm	
Overall Length	5.0 m	
Outer Diameter	3.2 m	
Yoke	240 kilopound (kip) warm 1010 steel. Length: 4.2 m.	
	Outer envelope: ellipse with half-axes 1.2 m × 1.0 m.	
	Inner envelope: 0.6 m radius circle.	
Coil and cryostat	40 kip St.Steel 5 m Long, 0.6 m (0.3 m) outer (inner) radius	
Stored Energy	13.0 MJ	
	Dipole	Quadrupole
Amp–Turns	3.3×10^6	1.8×10^6
Current Density	$5600 A/cm^2$	$5040 A/cm^2$
Coil Sectors	4	2
Winding	$\cosine(\theta)$	$\cosine(2\theta)$
Magnetic Strength	12.50 Tm	11.48 (T/m)m
Central	Field 3.58 T	Gradient: 3.63 T/m
Effective Length	3.45 m	3.4 m
Uniformity	dB/B $\sim 1 \times 10^{-3}$	dG/G $\sim 1 \times 10^{-3}$
Peak force density	40 kip/in	11 kip/in
Peak pressure	3390 psi	1290 psi

5000 A at 10 V would be a reasonable choice for SHMS dipole due to the relatively low inductance (0.72 H), and would provide a charge time under 30 minutes. The Quad power supplies will be identical to those in use on HMSQ1 and the QD30 magnet supply will be similar to the new HMS dipole power supply. All of the supplies will provide $\sim$ 10 V for ramp-up or ramp-down, have polarity reversal switches, and the possibility of NMR control for the dipole coils.

The energy dump systems will consist of a 10 V ramp-down, a slow dump and a fast dump resistor. The fast dump for the Quads will provide 450 V while the fast dumps for the QD30 magnet will apply a voltage of 150 V to the dipole coils and 250 V to the quad coils. These voltages may increase as the design progresses to maintain a reasonable final coil temperature near 80 K. The large cold mass and moderate current densities ensure that sufficient material is available to absorb a large fraction of the stored energy at a low final temperature during a quench discharge. The QD30 magnet circuits will have dump resistances such that the time constants are equal so that both coils will discharge at the same rate. The design is such that in the event of a discharge of one coil set, the second set will see a voltage which mimics a quench and a discharge of the second coil will be initiated. The possibility of a real second coil quench is also likely due to eddy current heating in the stabilizer material.

Magnet Control System   The SHMS magnets will have a control system that is self contained and able to be operated remotely by EPICS. The magnets' internal controls will take care of interlocks, operating valves by PID, and converting information from the magnet into

engineering units. The EPICS system will allow operation from remote screens, archival data logging and graphic display. A dual processor PLC designed for critical fail safe process control will be used. Such PLCs can switch the process control from primary to secondary in ∼50 ms in the event that the primary processor fails. They can also be switched manually or by software for routine maintenance. The use of dual processor PLCs can reduce if not eliminate the nuisance of radiation induced local processor lockup. The PLC will use a combination of commercial electronics and PLC I/O modules for signal acquisition. Liquid level control and cryogenic thermometry is straightforward to provide using commercially available units. Readouts of magnet voltages, pressures, strain gauges and valve position LVDTs will be performed by standard PLC plug–ins.

Support Structure   The SHMS support structure will be a welded steel frame riding on steel wheels and a center bearing. The structure will be built from prefabricated sections that must be welded together in the Hall. The steel structure will have a main beam section that will carry the entire spectrometer. The entire beam and spectrometer will ride on large hinged steel wheel bogies and floor mounted rails to allow precise scattering angle changes. This system is similar to that used in the HMS and SOS spectrometers. The steel fabrications will be hollow welded structures similar to ship hull sections. As such they will have internal access to permit complete welding of all seams and joints. The wheel sections will be driven by motors and reducers with variable frequency drives. The wheels are planned to be conical sections that are machined at the proper angle to control the radius of rotation. The use of the successful "Bertozzi" hinges on the wheel assemblies to eliminate the large radial forces that arise from even small misalignments is incorporated in the design.

Spectrometer Motion System   The SHMS spectrometer has a required range of motion from 5.5 degrees to 25 degrees. These two orientations are shown in Fig. 190. Proximity detectors will ensure that the system always moves in a safe angular range and that obstacles are avoided. Positioning accuracy consists of three components: angular measurement, pointing control, and distance from pivot. The scattering angle positioning tolerance will be 0.01 degrees, the pointing tolerance will be ±0.5 mm, and the distance off the pivot will be constant to within ±1 mm. While it may be possible to measure these quantities more accurately, these are the spectrometer setting tolerances. Note that this is similar to what has been obtained with the HMS. The scattering angle will be measured by a shaft encoder that can detect an angle change of 0.003 degrees. A scale etched into the floor at the radius of the rear drive wheels and viewed by a video camera with a graticule lens will confirm the scattering angle setting. Pointing and distance from pivot will be controlled by a large central crossed roller bearing. The accuracy of such bearings is a few thousandths of an inch. A view of the pivot showing simultaneous connection of the SHMS, and SOS, and the HMS, is provided in Fig. 189.

The motion of the SHMS spectrometer will be coordinated by a stand-alone PLC that integrates the drive wheel motion, angle read-back, proximity sensors, and obstacle detection. The
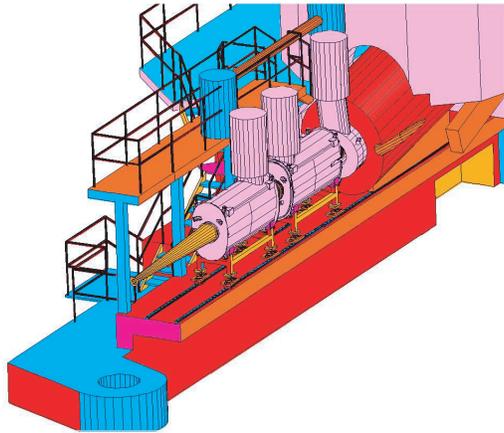
291

Figure 188: SHMS Pivot with Slider.

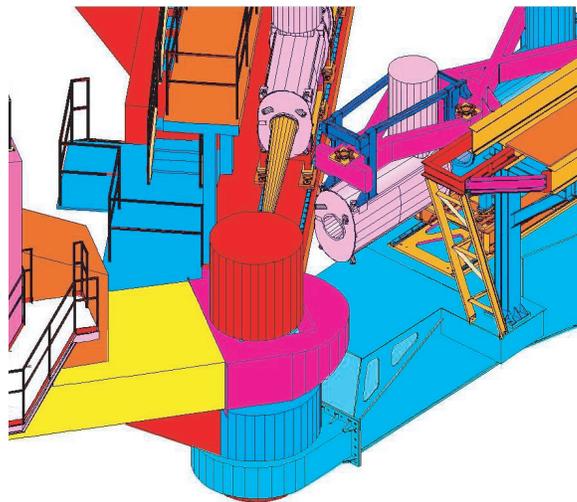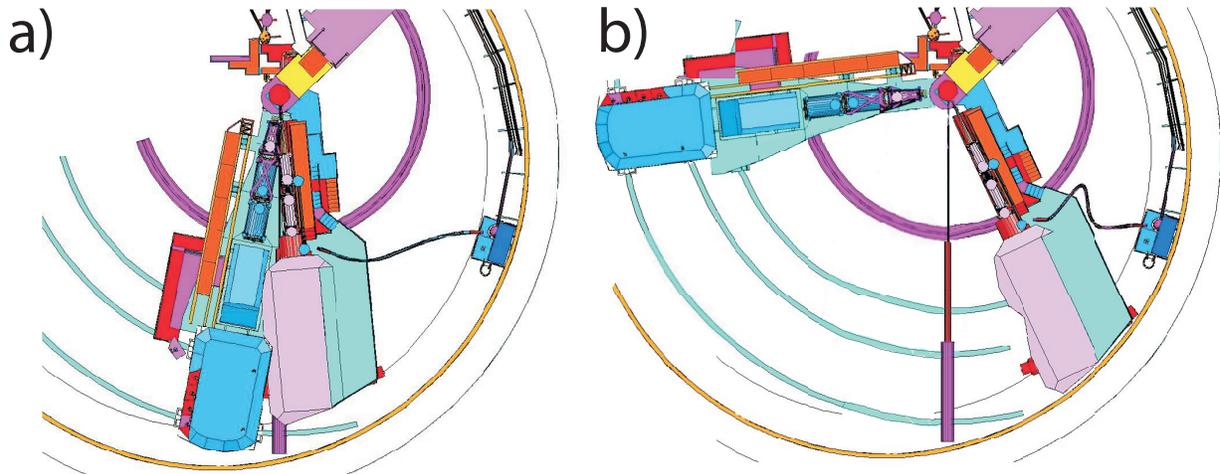Figure 189: Hall C Pivot with (from left) SOS, SHMS, and HMS Attached.

Figure 190: The SHMS-HMS spectrometer pair in two extreme configurations: a)the SHMS at 5.5°
and the HMS at 10.5° ; and b) the SHMS at 25° and HMS at 85°.

rotation motion will be limited to a preprogrammed range set in EPROM in the PLC and by the
proximity detection. This design is similar to the HMS rotation control system.

Shield House   The SHMS spectrometer shield house will be a reinforced cast concrete
structure that is built on the steel carriage. The concrete thickness will be 100 cm on all sides
except toward the pivot where it will be 200 cm. The concrete is formed and poured in place. A
conventional concrete mix will be used with added borate to absorb thermal neutrons. The interior
walls, floor and ceiling will have a minimum 2-inch thick lead lining except for the front wall which
will have 3 inches of lead. The lead will be covered and constrained by a system of aluminum
plates and C channels. The SHMS detectors will be mounted on a transverse rail system so that
the detectors may be easily removed for servicing and relocated accurately. The shield house will
be accessed by a door that is hinged to open outward on the side away from the beam, and a
removable block wall. There will be a limited amount of space inside the shield to allow a corridor
access on both sides of the detector stack.

SHMS Cryogenic System

Description   The SHMS magnets will be designed with a cryogenic interface similar to the
existing HMS magnets. Internally the magnets will have thermal siphon circulation from helium
and nitrogen reservoirs. The reservoirs will contain dual relief devices: an ASME coded mechanical
relief and a rupture disc set at a 25% higher pressure. Exhaust lines for relief which are separate
from the cool-down lines will be used so that there will be no chance of a contamination blockage
in these pressure relief paths. Temperature sensors, liquid level sensors, and voltage taps will be
within the reservoirs. The magnets will have liquid level control and valves to permit independent

warm up or cool down using a local heat exchanger. The cryogenic valving will allow for top-fill and bottom-fill of helium and nitrogen for steady operation and for cool-down, respectively. Cold return and warm return shutoff valves will be included to allow a smooth transition from cool-down to regular closed cycle operation. The cryogenic supply will use the existing Hall C G0 transfer line including the G0 flex line, vacuum jacketed return lines, flex gas lines and cool-down heat exchanger. The SHMS cryogenic system will use a new cryogenic distribution box mounted on the back of SHMS and a flexible transfer line similar to that constructed for the G0 experiment. The magnets will be connected by JLab standard U-tubes similar to those used on HMS/HRS quads. A set of gas manifolds installed on the back of the SHMS will collect and return cryogenic gases to the existing Hall C cryogenics system. A stand and a platform are required for support of equipment and for personnel access. The system is completed by automated cool-down valves and actuators identical to those used on HMS.

Operating modes During normal operation the SHMS magnets will be fed helium gas at 4.5 K and 3 atm. This gas gets JT expanded at each magnet by a valve that is controlled by the SHMS magnet control system to maintain liquid level. Boil off gas and JT flash will be returned to the local refrigerator at 1.2 atm. and 4.2 K. Nitrogen will be fed to the SHMS at $\sim$85 K and 4 atm. where it is expanded into the N_2 reservoir by a valve under local control. Boil off N_2 will be vented outside. Vapor cooled current leads will be controlled by valves that servo on the SHMS magnet current and adjust the helium gas flow accordingly. Separate flow control and measurement for each current lead is a normal part of this design. Non burn-out current leads are specified. The helium gas from the leads will be returned warm to the End Station Refrigerator compressor suction. The cool-down gas return and N_2 gas return lines will be vacuum jacketed to prevent ice and water from accumulating near the magnets.

Internally the SHMS magnets use thermal siphon circulation. An insulated supply line will feed helium to the bottom of the magnet cryostat and a return line will collect the slightly less dense fluid at the top of the cryostat and return it to the helium reservoir through a stand-pipe. The magnet heat leak will provide the energy to drive the circulation. The pipes are sized for 10 times the design heat load to ensure stable thermal siphon flow under all conceivable conditions. The LN_2 system design is similar.

During cool down and warm up, 4-atm. helium gas at 300 K will be blended with a pre-cooled 80-K helium stream on the SHMS in a "cool-down heat exchanger" (CDHXR). This variable temperature source will be controlled by the SHMS magnet control system to provide a 70-K differential temperature for either warming or cooling, and will maintain an internal temperature difference in the SHMS magnet of no more than 50 K. This CDHXR will provide a precise method of warming and cooling the SHMS magnets independently in a manner which minimizes thermal stress due to relative contraction. This technique will also provide increased cryogenic efficiency.

SHMS Vacuum Systems   The SHMS spectrometer will have three vacuum systems dedicated to the operation of a) the QD30 superconducting magnet, b) the SHMS spectrometer vacuum, and c) the Čerenkov detector. The SHMS cryogenic system is presumed to be made leak tight and cryo-pumping so a dedicated vacuum system is not included in the design. The QD30 magnet will also be leak tight, but a vacuum system tailored to leak testing, commissioning and biannual vacuum servicing will be included as a dedicated system. It can be used to commission and service the cryogenic system as needed. It will be portable, self contained, and fully instrumented. The spectrometer and Čerenkov vacuum systems will be dedicated to those devices and will be permanently installed on the SHMS.

The pumping system for the QD30 magnet will consist of a turbo pump backed by a direct drive roughing pump. A 1000 liter per second turbo pump with a full port gate valve, roughing bypass manifold and leak testing manifold will be required. The wheeled pump station will have a mechanical $30 - 0 - 30$ vacuum gauge, high range and low-range thermocouple gauges, and a cold cathode ion gauge. A dedicated RGA for system commissioning will be needed. A large full port cold trap that can be piped in for system startup and mounted on a separate wheeled cart is included in the specification. Appropriate auxiliary vacuum hoses, valves and flanges to facilitate connecting to all the SHMS vacuum systems will be provided as well.

The SHMS will have thin aluminum entrance and exit windows. The windows will be hydroformed spherical shapes similar to those in use on the HMS. The spectrometer vacuum between these windows will be maintained by a large mechanical pump and roots blower as a roughing system, and a 1000 l/s turbo pump.

The Čerenkov vacuum and gas system design is similar to the above but includes the capability of introducing other gases besides helium. This system will be dedicated to providing the correct Čerenkov atmosphere and will have differential pressure relief valves to limit the operating pressure range. Appropriate monitoring equipment to verify that the correct index has been achieved will be necessary. An arc cell system and a hygrometer will be used for quality control of the process. The Čerenkov system operates first with a nitrogen purge to dry the system, then the nitrogen is displaced with the detection gas. A small volume purge of the detection gas may be maintained to permit monitoring of gas quality.

SHMS Optics and Monte Carlo

SHMS Optics Design   The goal of the SHMS design was a compact, general purpose spectrometer similar in properties to the HMS, but with a higher maximum momentum setting for experiments that will use the 11 GeV beam available in Hall C from the CEBAF upgrade. The SHMS needs to be compact in order to fit into the forward-angle space now used by the SOS spectrometer, with angular range from 5.5 to 25 degrees, and a minimum angle with respect to the

HMS of 16 degrees. The design process also sought to minimize the cost. A summary of the design parameters is given in Table 31.

To achieve these goals, the SHMS was designed as a vertical bend, QQ(QD) spectrometer. Two quadrupole magnets are followed by a combined-function magnet that includes both quadrupole and dipole elements. This is similar to the HMS optical layout, except that the last quad and the dipole have been superimposed to make the spectrometer compact.

The first two quads are copies of the HMS Q1 magnet. Re-use of this design helps keep costs low, and the performance of these magnets is well known. The QD is a new design, the engineering details of which may be found in section 3.C.3. Because of the large fields required to bend 11 GeV electrons in a compact spectrometer, the QD must be superconducting, without iron pole-faces. The coils are enclosed in a cylindrical shell of iron, which serves as a flux return yoke. This configuration is very compact, and relatively inexpensive to build. However, it is not a true QD magnet. That would require a toroidal iron shell, and similarly curved coils. A true QD magnet would be very expensive to build, and the performance of the SHMS with a cylindrical QD is adequate.

The SHMS design is very flexible. The coils in the QD are separately excited, and the magnets and detectors will have adjustable positions, making many tunes possible. We consider two here: the original Small Solid Angle (SSA) tune used to design the spectrometer, and a Large Solid Angle (LSA) tune, with all magnets and detectors moved forward 2.32 meters as a rigid body.

Several tools were used in designing the SSA tune. The first of these is TOSCA[TOSCA], a finite-element, 3-D magnetostatics program. The results discussed here come from the 'QD30' TOSCA model of June 5, 2000. TOSCA calculated the field values on a 3-D grid inside the magnet, and a model was fit to the horizontal, or y field component on the $y = 0$ plane (the vertical mid-plane, or symmetry plane of the magnet.) A ray-tracing program was then used to numerically integrate the equations of motion for an electron in the model's field. This determines the trajectory of the central ray in the spectrometer.

Early in the design process, the total bend angle was fixed at 18.4 degrees. This is essentially the maximum that can be allowed without limiting the acceptance through the QD magnet. An important point to realize is that the quadrupole fields in the QD bend the central ray. Optimizing the spectrometer performance involved tuning the Q/D ratio, and this required compensatory changes in the dipole strength in order to preserve the correct bend angle.

It should also be noted that the central ray has to be offset from the exact center of the QD to avoid cutting off the acceptance by the magnet entrance and exit. Monte Carlo simulations showed that an offset of 7 cm in the center of the magnet combined with a beam-pipe transition at 200 cm from the QD center would optimize the acceptance. This layout is shown in Fig. 180. A complex transition pipe will join the QD to the neighboring quad magnet.

With a central trajectory specified through the QD, the optics of the spectrometer as a whole could be studied. The optics are defined by map functions that transform the trajectory of a particle at one location to its trajectory at a different location. We used the COSY [COSY] program to calculate 5th order Taylor series polynomial expansions of both the global map from target to detectors, and the individual sequential maps that transform from one significant aperture in the spectrometer to the next. The COSY calculations are based on a model of the spectrometer magnets that we describe below. Concurrent with the map calculations, COSY would track an ensemble of test rays through the spectrometer, and adjust the strength of the first two quads to produce the sharpest focus at the detectors. This process was iterated with manual adjustment of other parameters, such as focal plane position, to optimize the performance. The end result was the standard tune. Parameters of the standard tune are given in table 34, and the tracks of 27 test rays are shown in Fig. 191.

COSY magnet model   Standard COSY quadrupole elements were used for the two quad magnets, as was done in the HMS optics model. There are no COSY standard elements corresponding to the QD magnet, and it had to be modeled using the general field-map element. Past experience has shown that this requires extremely smooth field-map data, such that the TOSCA field-maps could not be directly used. Instead, field values were calculated from a model fit to the data. The use of a model also allows changes to be made in the fields to simulate small changes in the dipole and quadrupole coil excitations for tuning purposes. This model was also used in the central-ray integrations mentioned above. The form of the model is:

$$B_y(x, z) = \sum_{i=0}^{6} C_i(z) \, (x/r_0)^i \tag{75}$$

in which (x, y, z) are right-handed Cartesian coordinates with z the axis of the magnet pointing downstream, y is horizontal, and x is in the vertical plane, pointing upwards, with origin the center of the magnet; B_y is the y-component of the magnetic field in the plane $y = 0$; and $r_0 = 30$ cm is the radius of the beam-pipe. For each discrete z_j in the TOSCA data, polynomial coefficients C_{ij}^T were fit to the data using the method of singular value decomposition. Gaussian interpolation was then used to calculate coefficients at arbitrary z:

$$C_i(z) = \sum_j C_{ij}^T \, \exp(-[(z - z_j)/(s \, \Delta z)]^2)/(s \, \sqrt{\pi}) \tag{76}$$

where Δz is the 2-cm grid spacing. $S = 2.5$ gives smooth results that accurately reproduce the TOSCA data.

As mentioned above, both the dipole and quadrupole coil excitations needed to be adjusted by small amounts to fine tune the bend angle and optimize the focus. In principle, this could be done by re-running the TOSCA model, but this was not practical. Instead, we use symmetry arguments
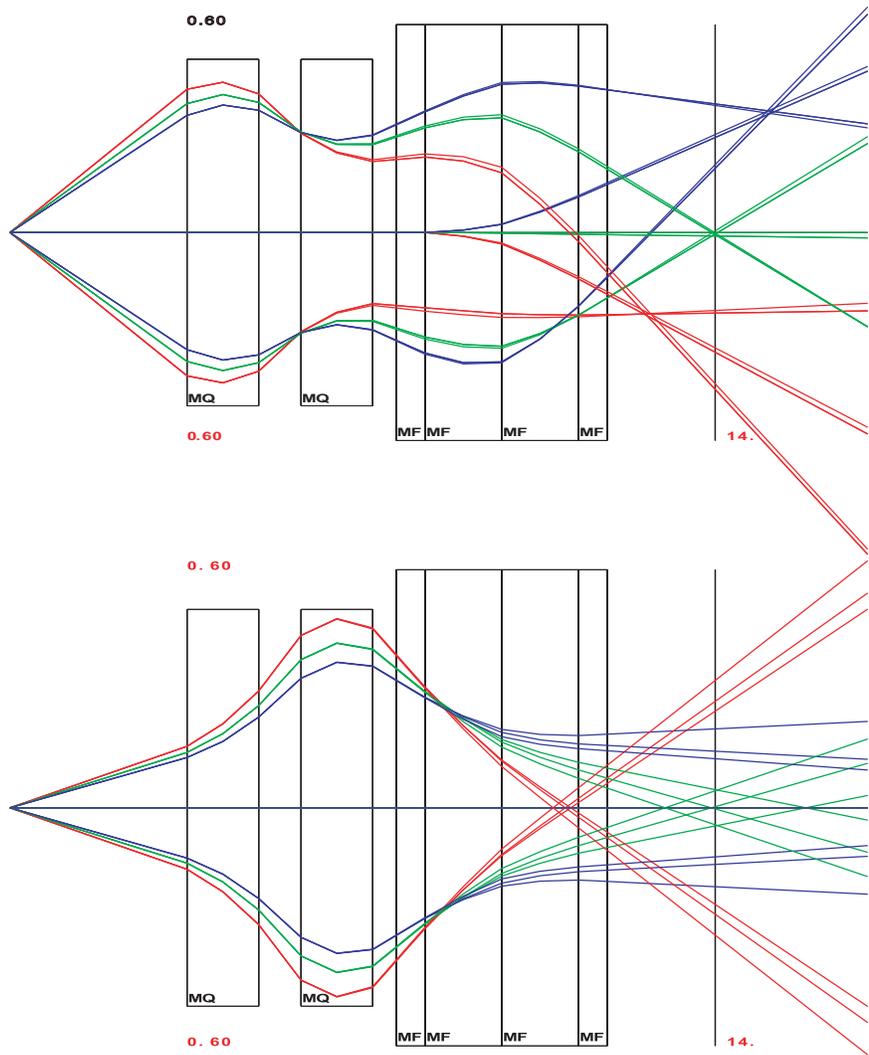
Figure 191: Rays Tracked through the SHMS by COSY for the SSA Tune. The top panel is the bend-plane projection (COSY (x, z) coordinates), while on the bottom is the transverse projection (COSY (y, z) coordinates). 27 rays are plotted for all combinations of 3 values of total momenta ($\Delta p/p_0 = 0.1$ [blue], 0 [green], -0.1 [red]), 3 values of p_x/p_0 (0.4, 0, -0.4), and 3 values of p_y/p_0 (0.15, 0, -0.15).
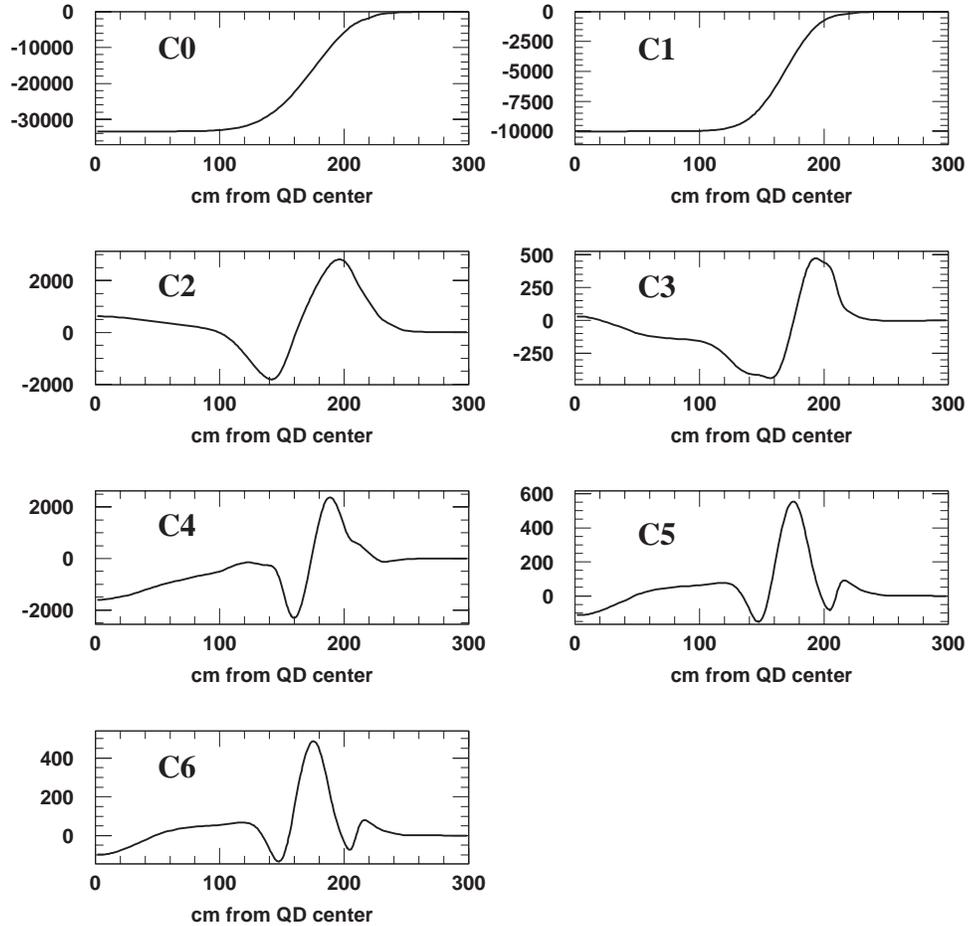
Figure 192: Polynomial Coefficients in the QD Magnetic Field Model as a function of z, the axial distance from the magnet center. (The functions are symmetric about $z = 0$.) $C0$ is the dipole component, $C1$ the quadrupole component, and the others are higher order contributions. The vertical axes are the contribution to B_y at $x = 30$ cm, in gauss.

to treat all the terms in the model that are even-order in x as harmonics of the dipole coils, and the others as harmonics of the quad coils. Thus, we adjusted the dipole excitation in the model by simply scaling the even-order coefficients, and similarly adjust the quadrupole excitation by scaling the odd-order ones. This approximation neglects non-linear saturation effects in the iron and thus is only good for small corrections. The adjusted coefficients are plotted as a function of z in Fig. 192. One can see that there are significant higher order terms beyond about $z = 120$ cm, with the C_2 component dominant. Once the final tune is determined by this approximation, a full TOSCA calculation based on the tune values may be performed to verify the results.

LSA tune The LSA tune is closely related to the SSA tune. It is produced by sliding all the magnets and detectors forward by 2.32 m. The QD is operated with the same fields, so that the central ray follows the same path through the QD and the detectors. The fields in the two

Table 34: SHMS Optics Parameters for SSA and LSA Tunes. Coordinates are given as (horiz,vert) distance from nominal target center.

Parameter	SSA tune	LSA tune
Q1, Q2 mechanical length	189.0 cm	189.0 cm
Q1, Q2 magnetic length	187.9 cm	187.9 cm
Q1, Q2 pole-tip radius	25.0 cm	25.0 cm
Q1, Q2 beam-pipe inner radius	20.5 cm	20.5 cm
Length from target center to Q1 center	558.5 cm	326.5 cm
Length from target center to Q2 center	857.5 cm	625.5 cm
Q1 field gradient for 11 GeV	-7.7069 T/m	-10.7436 T/m*
Q2 field gradient for 11 GeV	8.6041 T/m	9.3790 T/m*
QD beam-pipe inner radius	30.0 cm	30.0 cm
Central ray path-length to middle of QD	1290.0 cm	1058.0 cm
Coordinates of QD center	(1288.2 cm, 20.8 cm)	(1056.2 cm, 20.8 cm)
QD rotation	9.200°	9.200°
Total bend angle	18.400°	18.400°
Layout bend radius	1079.8 cm	1079.8 cm
Coordinates of layout bend center	(1116.6 cm, 1079.8 cm)	(884.6 cm, 1079.8 cm)
Total length of central ray	1850.0 cm	1718.0 cm
Central ray coordinates at focal plane	(1824.3 cm, 177.3 cm)	(1687.2 cm, 208.8 cm)
Field at QD center for 11 GeV	3.3416 T	3.3416 T
Quad component at QD center, 11 GeV	3.3416 T/m	3.3416 T/m
Minimum spectrometer angle	5.5°	10°
Maximum spectrometer angle	25°	25°
Minimum separation from HMS	16°	25°

* Maximum achievable quad gradient of 8.6 T/m limits central momentum to 8.8 GeV

quadrupoles were re-optimized by COSY in order to produce a good focus at the focal plane, which was shifted 1 meter farther back from the QD, as measured along the central ray, to avoid tipping the focal plane to too shallow an angle. By having the quads closer to the target, the solid angle acceptance is increased, as is evident from Fig. 193, in which we track the 27 standard test rays. However, this tune requires substantially higher quadrupole fields, as listed in Table 34. The values listed, corresponding to a central momentum of 11 GeV/c, exceed the capability of these magnets. The maximum central momentum that can be reached in this mode of operation is 8.8 GeV/c, for which Q1 operates at its maximum gradient of 8.6 T/m. Note that with a central momentum of 8.8 GeV/c the SHMS still accepts full energy (11 GeV/c) particles, albeit with somewhat poorer resolution. With the quads moved forward the minimum scattering angle becomes 10°.

SHMS model in the 'physics' Monte Carlo   The field maps generated by COSY have been incorporated into a model of the spectrometer so that detailed simulations can be made of the SHMS acceptance, resolution, and distributions of events at the detectors. COSY-generated transformations are used to propagate particles from the target to each of the important apertures in the spectrometer. In addition, the particle trajectories can be evaluated at each detector package
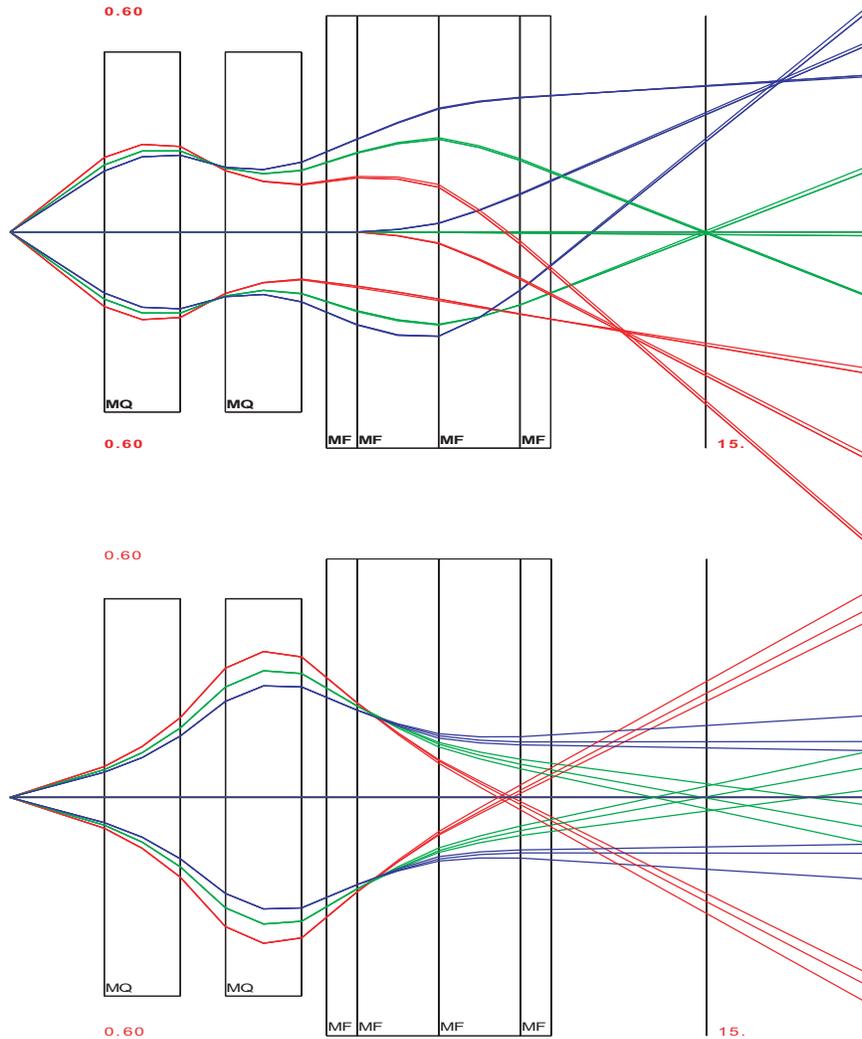
Figure 193: Rays Tracked through the SHMS by COSY for the LSA Tune. The top panel is the bend-plane projection (COSY (x, z) coordinates), while on the bottom is the transverse projection (COSY (y, z) coordinates). 27 rays are plotted for all combinations of 3 values of total momenta ($\Delta p/p_0 = 0.1$ [blue], 0 [green], -0.1 [red]), 3 values of p_x/p_0 (0.4, 0, -0.4), and 3 values of p_y/p_0 (0.15, 0, -0.15).

in order to determine the active region needed for each detector.

The SHMS model is of the same format as the existing HMS and SOS models, and so has been added to 'SIMC', the physics Monte Carlo used extensively in Hall C. This allows generation of various physics processes, taking into account the cross sections and event distributions, as well as multiple scattering and energy loss in target, spectrometer, and detector materials, and any relevant particle decays. The SHMS model includes the same level of detail as the models for the existing spectrometer, and so the simulation can be used for detailed and extremely realistic studies under a variety of conditions. In particular, it can be used to determine the acceptance and resolution as functions of target length, collimation scheme, and detector configuration.

SHMS Performance (Resolution/Acceptance)

A stand-alone Monte Carlo has been used to investigate the properties of the SHMS design as developed in the previous section. The Monte Carlo was run with the spectrometer at $90°$ and a target length of 70 cm. Electrons were generated uniformly over the phase space and sent through the SHMS spectrometer with the central momentum (p_{cent}) set at 7.5 GeV/c. Events were generated over the $\delta = (p - p_{\text{cent}})/p_{\text{cent}}$ range of -40% to 40%, horizontal angle ($y' = dy/dz$) range of ± 100 mr and vertical angle ($x' = dx/dz$) range of ± 100 mr relative to the spectrometer axis. Studies were done with the large solid angle (LSA) tune (spectrometer moved forward by 2.32 m) and the small solid angle (SSA) tune.

Plots of the δ, Y_{tar}, y' and x' acceptance are shown in Fig. 194 for the large solid angle (LSA) tune (solid black line) and the small solid angle (SSA) tune (solid red line). Both tunes have a large acceptance in δ and Y_{tar}, the horizontal position. Both tunes have a flat acceptance in Y_{tar}. For the LSA tune, the δ acceptance is flat for negative δ and gradually decreases with increasing positive δ. The SSA tune has a fairly flat acceptance with a drop-off above $\delta = 10\%$. Both tunes have a sharp drop off below $\delta = $ -20%. In designing the size of the detectors, cuts of $-15 < \delta < 25$ % and $-25 < Y_{tar} < 25$ cm were used. The plots of y' and x' acceptance in Fig. 194 include these cuts. The LSA tune has about twice the x' acceptance of the SSA tune.

The beam envelope at z=0 in the detector hut is plotted in Fig. 195 for the LSA tune with cuts of $-15 < \delta < 25$ % for target lengths of 0.5, 4, 30 and 50 cm. (Note that a 30 (50) cm target viewed at $90°$ roughly corresponds to a ≥ 70 (120) cm target at $\leq 25°$.) We use the TRANSPORT[Br80a] coordinate system in which +X is down and +Y is beam left. For the 0.5-cm target, one can see the expected hourglass shape of the X versus Y distribution and with increasing target length the waist of the hourglass expands. The bottom plots in Fig. 195 (for target lengths of 30 and 50 cm) show that the detectors have to be increased by 1.4 times in the horizontal dimension to accommodate an increase of the target length by 1.7 times . The detectors will be built for $-25 < Y_{tar} < 25$ cm, but, where appropriate, will initially only be instrumented for the 30-cm target. The beam envelope for the LSA tune is plotted in Fig. 196 at key points within the detector stack.

The effective solid angle was calculated by generating 100K events over a range of horizontal angle of $\Delta x' = \pm 0.1$, vertical angle of $\Delta y' = \pm 0.1$, $-15 < \delta < 25$ % and $-25 < Y_{tar} < 25$ cm. The effective solid angle, Ω, was calculated as $\Delta x' \cdot \Delta y' \cdot \frac{\# \text{ accepted}}{\# \text{ thrown}}$. The LSA tune has $\Omega \approx 4.0$ msr, while the SSA tune has $\Omega \approx 2.0$ msr.

The resolutions for the target quantities δ, Y_{tar}, y' and x' for 7.5 GeV/c electrons are plotted as functions of δ in Fig. 197 for the SSA tune. For these calculations, the assumption was that the pipe which could contain the gas and mirror for the first gas Čerenkov detector will be at vacuum. This Čerenkov detector is primarily intended for experiments in which high resolutions are not needed. The solid blue curve has no multiple scattering nor wire chamber resolution in the Monte Carlo and indicates the limitations of the optics matrix used in the model of the SHMS. The blue line is nearly at zero except near the edges of the δ range, confirming that the optics matrix is adequate. The red dashed curve shows the effect of including wire chamber resolutions in the Monte Carlo. The solid black curve adds the effect of multiple scattering. For the Monte Carlo, the hydrogen target cell was a cylinder with radius 3.37 cm and a wall thickness of 0.005 inches. The combination of the scattering chamber window, air, and spectrometer entrance window was 0.6% radiation lengths. In the detector hut the material was the spectrometer's exit window (taken as Mylar/Kevlar material of 0.020 inches thickness in the simulation), air, and the material of the drift chambers. The resolutions in y' and x' are relatively independent of δ. The contribution to the resolution in y' and x' from wire chamber resolution and multiple scattering are about equal, while the Y_{tar} and δ resolutions are dominated by wire chamber resolution with multiple scattering having almost no effect at this momentum. The Y_{tar} resolution has a fairly dramatic parabolic dependence on δ. For the SSA tune, the δ resolution is seen to have a slightly asymmetric parabolic dependence on δ with a minimum at $\delta \approx$ -1%. For the LSA tune (not shown here) the δ resolution has an asymmetric parabolic dependence with a minimum at $\delta \approx$ -6%. The average resolutions for δ, Y_{tar}, y' and x' are about 0.05 %, 0.20 cm, 0.8 mr, 0.8 mr for both the SSA and LSA tunes, meeting or exceeding the requirements given in Table 31.

SHMS Detector Systems As the momentum range of a spectrometer changes, so also do the demands on the particle detector elements. At higher momenta, the degradation of angle and momentum resolution due to multiple scattering are reduced, and one can consider incorporating a low-mass detector in the upstream regions of the detector stack. The times-of-flight (TOF) of different particle species differ less, making trigger timing somewhat easier, but also making particle identification by TOF a less viable option. Particle identification using the Čerenkov effect also depends upon the relative speeds of particles, which means that Čerenkov counters must be more thoughtfully designed than at lower momenta, and that other identification techniques should be considered. Higher energy leads to larger fluctuations of the energy deposited in a total-absorption calorimeter, as there is a higher probability that some of the energy leaks out the back; this necessitates considering a thicker shower counter for the SHMS than is used in the HMS.

The above considerations lead us to a SHMS detector system design which would essentially be
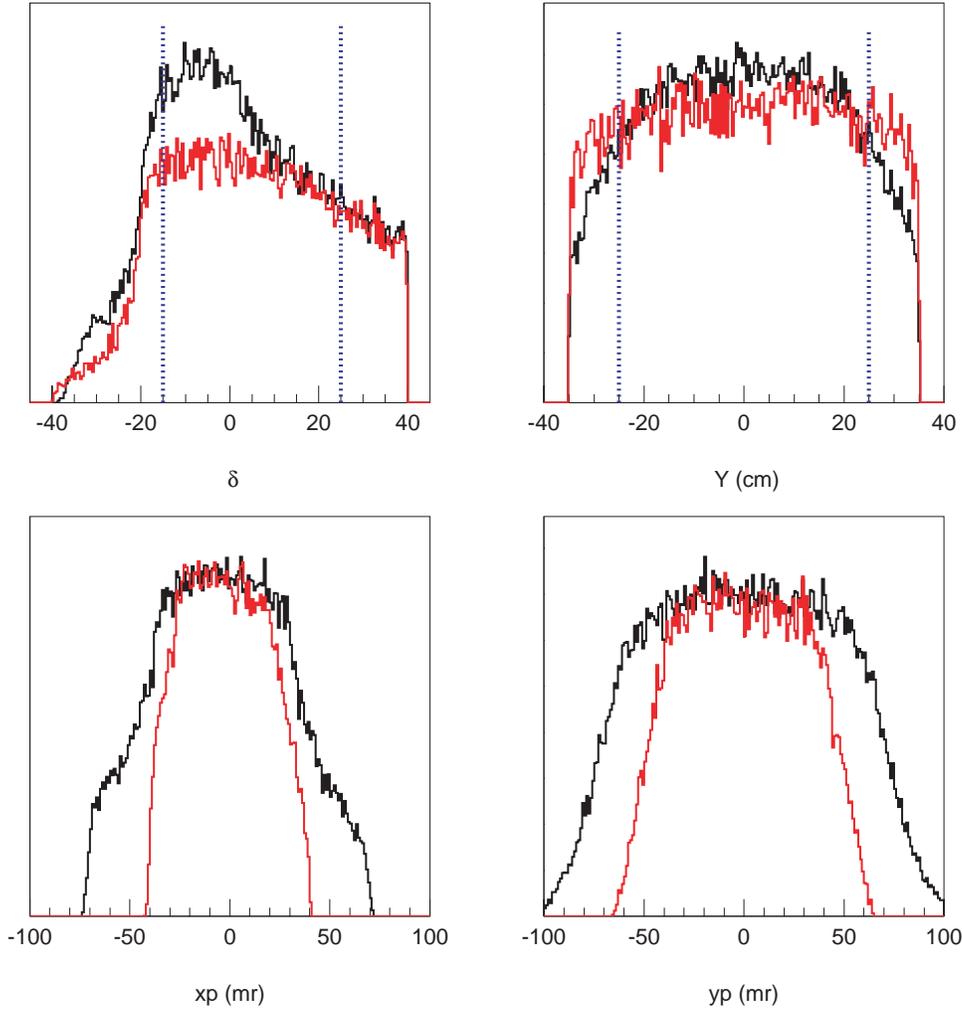
Figure 194: The Phase Space Acceptance plotted as function of δ, Y_{tar}, y' and x' for the large solid angle (LSA) tune (black solid line) and the small solid angle (SSA) tune (red solid line). The y-axis is yield in arbitrary units and the LSA and SSA yields have been scaled to match each other at the maximum. The blue dotted lines indicate the limits of $-15 < \delta < 25$ % and $-25 < Y_{tar} < 25$ cm which were used in determining the detector size. The plots of y' and x' include the cuts of $-15 < \delta < 25$ % and $-25 < Y_{tar} < 25$ cm.

Figure 195: Plots of the Vertical (X) versus the Horizontal (Y) position at z=0 cm in the detector hut for target lengths of 0.5 cm, 4 cm, 30 cm and 50 cm. Spectrometer set for large solid angle tune with a cut of $-15 < \delta < 25$ %.
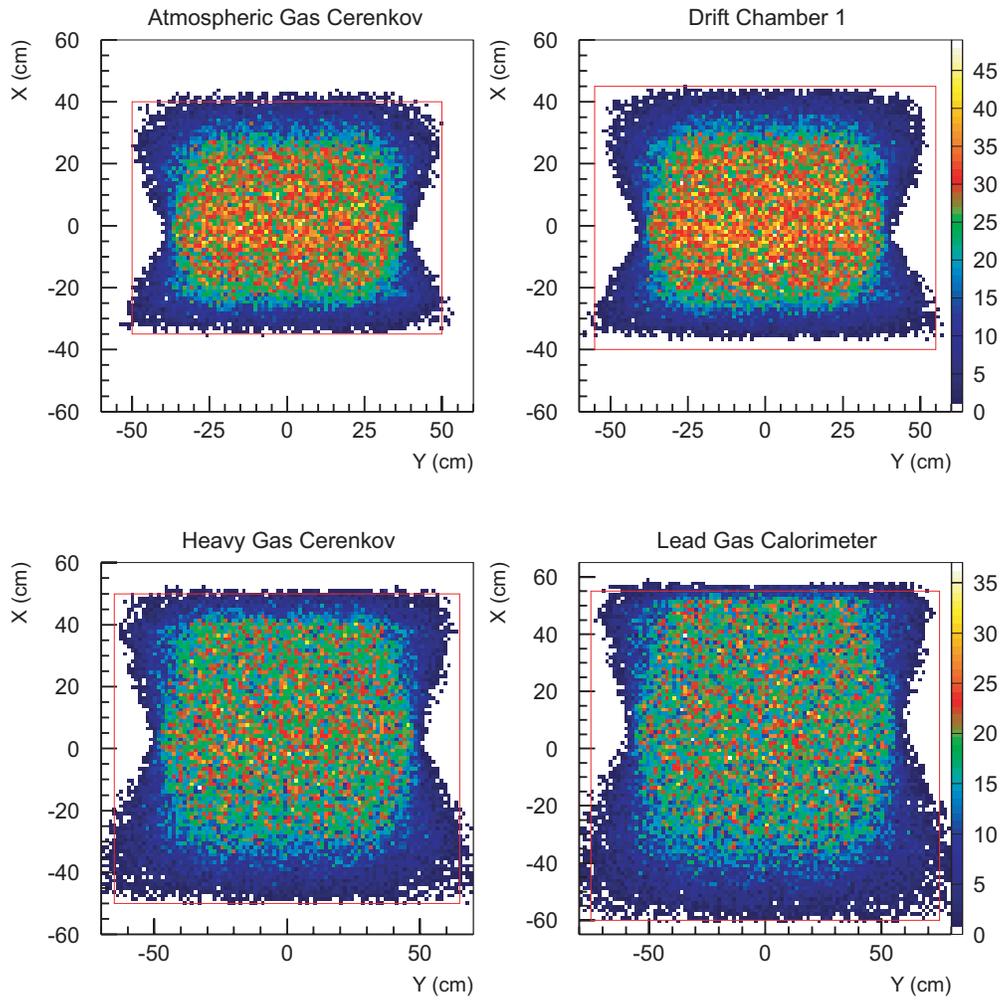
Figure 196: Plots of the vertical X versus the horizontal Y position at z=-60 cm (*Atmospheric Čerenkov*), z=-40 cm (*Drift Chamber 1*), z=160 cm (*Heavy Gas Čerenkov*) and z=320 cm (*Lead Glass Calorimeter.*) Spectrometer set for large solid angle tune with cuts of $-15 < \delta < 25$ % and $-25 < Y_{tar} < 25$ cm.
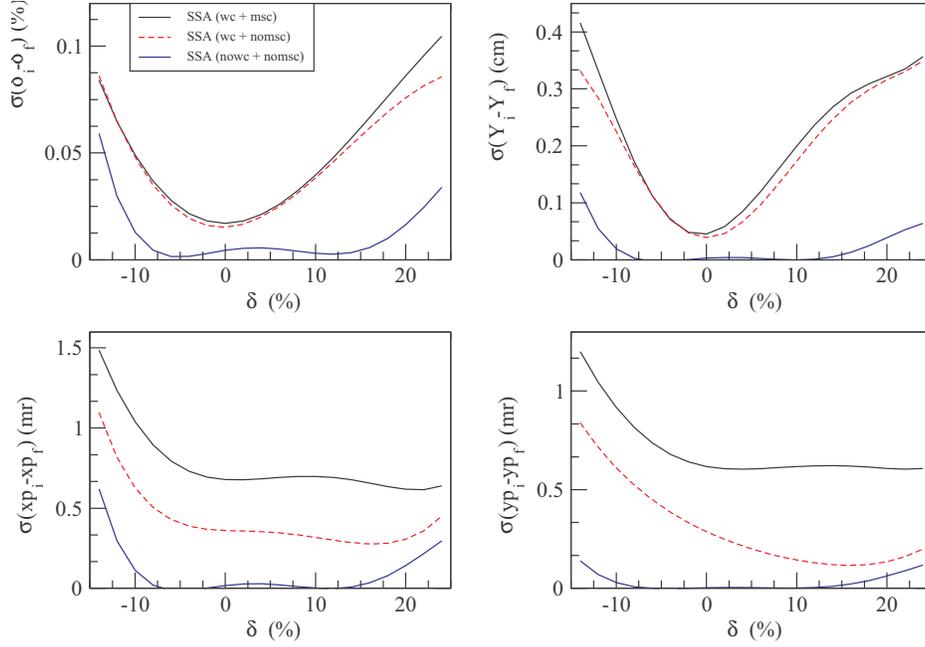
Figure 197: For the small solid angle (SSA) tune, plots of the resolutions in the target quantities δ, Y_{tar}, y' and x' as a function of δ for 7.5 GeV/c electrons. The solid black curve is the best estimate of real-world resolutions. Other curves explained in the text. The subscripts f and i refer to the reconstructed and originally generated variables.

a HMS stack modified for higher energies. However, new physics initiatives demand the inclusion of new capabilities. Measurement of the polarization of final state particles would require the inclusion of a polarimeter in the SHMS detector stack, for example. Experiments at higher rates or with low signal-to-background would benefit from improved electron/hadron discrimination, such as that provided by the addition of a transition radiation detector (TRD). Pion/kaon separation, primarily achieved by gas and aerogel Čerenkov counters, can be enhanced by recording dE/dx information in the tracking chambers and the TRD. Below, we describe an integrated system of detector components which are optimally matched to one-another and to the physics to be done in Hall C. A block diagram of the proposed detector system is shown in Fig. 198. The overall specifications for the spectrometer, developed for the physics, were summarized in Table 31.

The magnetic optics described above provides good resolution over a large acceptance. It also allows the possibility of performing experiments with a projected target length as large as 50 cm without giving up good resolution. To detect and measure this full acceptance will require that the detectors cover a large area. The required detector sensitive areas are given in Table 35. Our plan is to build the mechanical components of the detectors large enough to achieve full coverage of the 50-cm (projected) target over a 40% momentum bite (-15% < δ < +25%). However, until such time as the full acceptance is actually needed by an experiment, only the central regions of the detectors (covering a 30-cm projected target) will be instrumented.
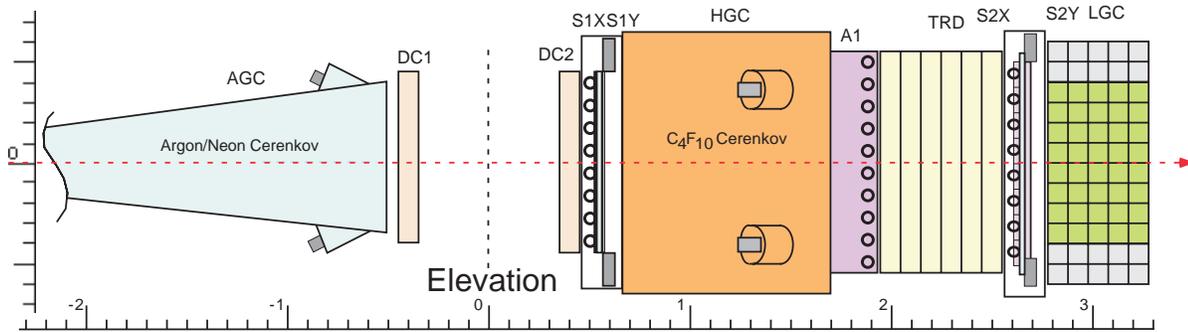
Figure 198: Block Diagram of SHMS Detector Arrangement.

Table 35: Sensitive Areas of the Detectors for Momentum Range -15% $< \delta < +25\%$, for both 30-cm long and 50-cm long targets.

Detector	30-cm Target		50-cm Target	
	X size	Y size	X size	Y size
Atm. Gas Č	75	80	75	100
Drift Chambers	85	80	85	110
Scint. Hodo 1	90	90	90	110
Heavy Gas Č	100	95	100	130
Aerogel Č	110	100	110	140
TRD	110	100	110	140
Scint. Hodo 2	110	100	110	140
Shower Counter	115	120	115	150

Wire Chambers   The SHMS tracking system will provide the only measurement of particle momentum and production angle in the spectrometer. Given an adequate description of the magnetic optics, the momentum and production angles are determined by measuring enough of the track to generate a track vector at the reference plane, then projecting it back to the target.

Although Multiple Coulomb Scattering is reduced at higher momentum, it is still a significant effect limiting momentum and angular resolution, even at 11 GeV/c. We have considered several alternatives to wire chambers for tracking in the SHMS, but conclude that gas drift chambers remain the best choice to simultaneously provide the necessary position resolution while keeping the detector mass low.

The particular design we have chosen is based upon the successful SOS drift chambers, with only minor modifications suggested by the different SHMS optical parameters and lessons learned from the original design. These chambers provide better than 180-μm single-plane resolution and operate at rates of at least 1 MHz per wire, while placing only about 0.002 radiation lengths of material in the path of particles for a stack of six sense planes. The excellent performance of the SOS drift chambers is demonstrated by the distributions of track residuals shown in Fig. 199.

A simplified diagram of the chamber design is shown in Fig. 200. These chambers are constructed using the "open plane" technique, in which individual wire and cathode (foil) planes are fabricated on a work bench, then stacked up on a rigid frame to make the chamber assembly. This method of construction is relatively simple and robust, lending itself nicely to fabrication in a modest workspace.

As a baseline, we plan to use commercially available readout electronics of the same design as presently in use in the SOS, the HMS, and other wire chambers at JLab. However, we note that there is the possibility of enhancing the particle identification power of the SHMS spectrometer if we measure the energy loss distribution of particles traversing the wire chambers. To do so would require modified electronics at the chamber and the addition of analog readout for groups of wires. A study of the feasibility and usefulness of performing a maximum likelihood analysis of these Landau distributed dE/dx samples is ongoing. Figure 201 shows the results of a simulation of such a dE/dx system for identifying kaons and pions.

Quartz Čerenkov Hodoscope   The existing scintillating hodoscopes in Hall C are used for a surprising number of essential functions: to provide a trigger which is approximately 100% efficient for minimum ionizing particles[7], to reject accidental coincidences in multi-arm experiments, to help measure the efficiency of the tracking system, and to provide Particle Identification (PID) by time-of-flight (TOF).

While the first three functions listed above will still be critical for the SHMS, the PID function

---

[7]For common detector materials, this corresponds to $\beta\gamma \simeq$ 3-4, so a "realistic worst case scenario" is the detection of protons of momenta 3-4 GeV/c.
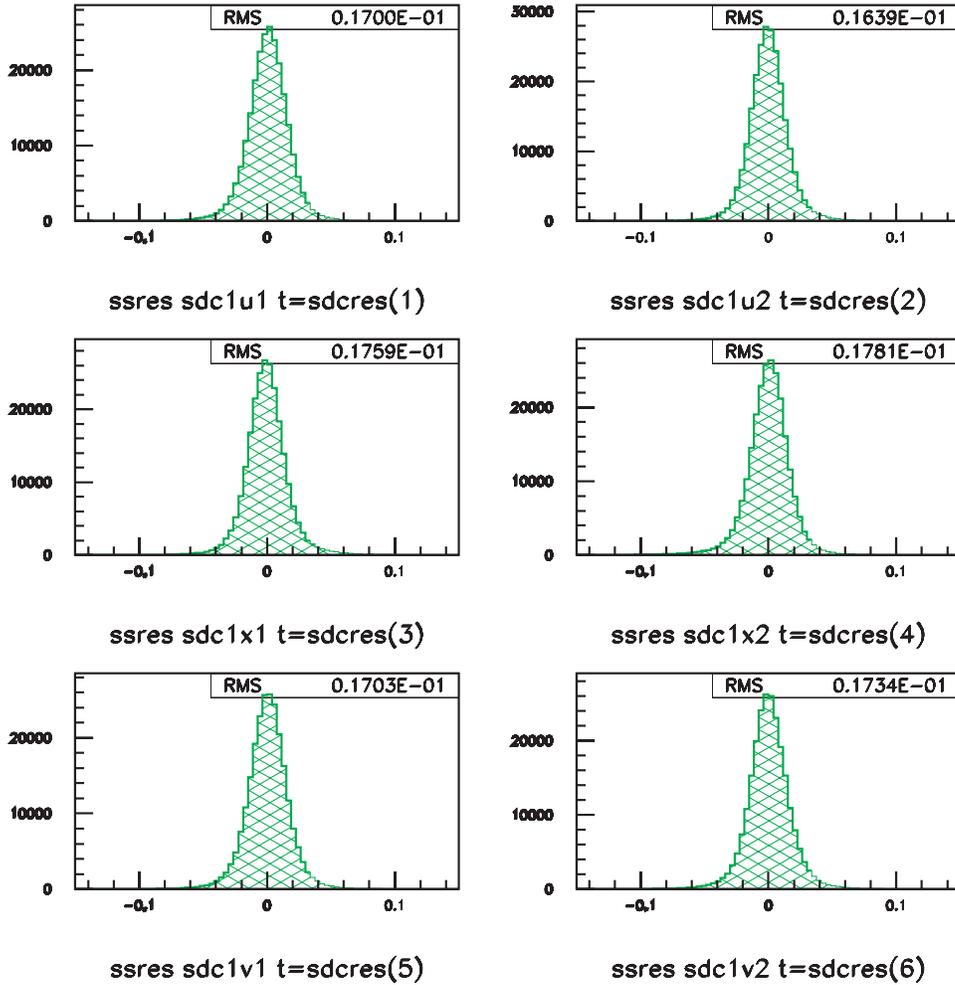
Figure 199: Measured Residual Distributions in the SOS Wire Chambers. The figures show the deviations (in centimeters) between measured hit locations in each wire chamber plane and the projected position of the associated fitted track as it passes through the wire plane. In each case track fits were performed without using the measurement from the wire plane under study. Typical residual widths are 170 microns (RMS).
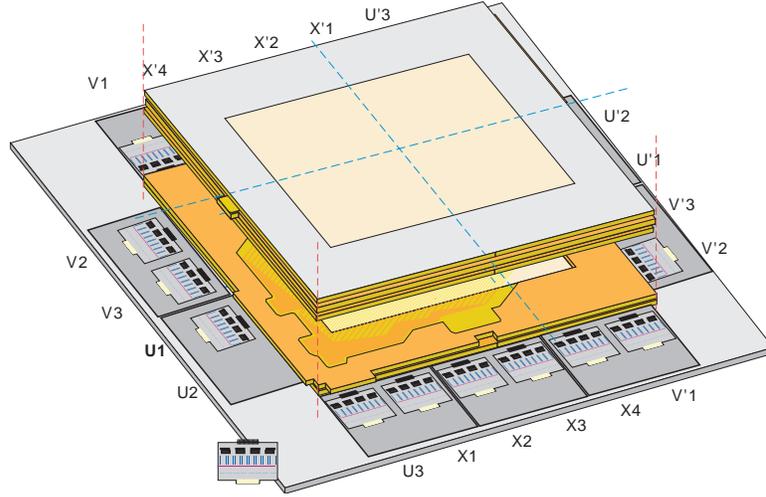
Figure 200: Block diagram of the SHMS Wire Chamber Assembly. The chamber is built by stacking individual wire and foil planes, each of which is fabricated separately using precision tooling.
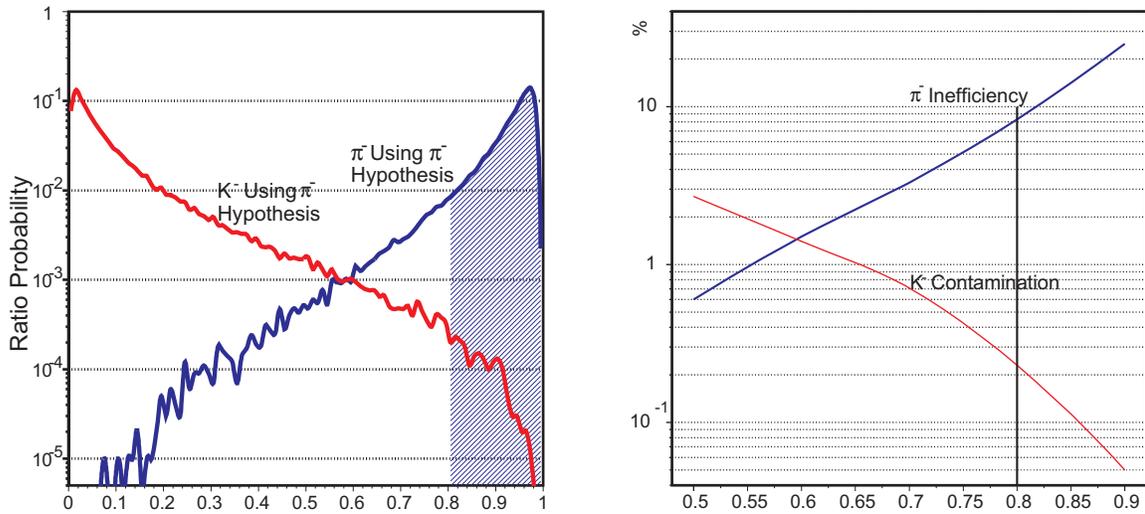

Figure 201: Pion/Kaon Discrimination using a Likelihood function applied to simulated energy loss distributions for 7 GeV/c particles in 12 wire chamber planes. For the (pion/kaon) hypothesis, only the eight (highest/lowest) measured energies are used. Left: the distribution of pion likelihood ratios $R = \frac{L_\pi}{L_\pi + L_K}$ when the incident particle is a kaon or a pion. Right: the pion inefficiency and the kaon contamination as a function of the choice of cut, when equal numbers of pions and kaons are passed through the system.
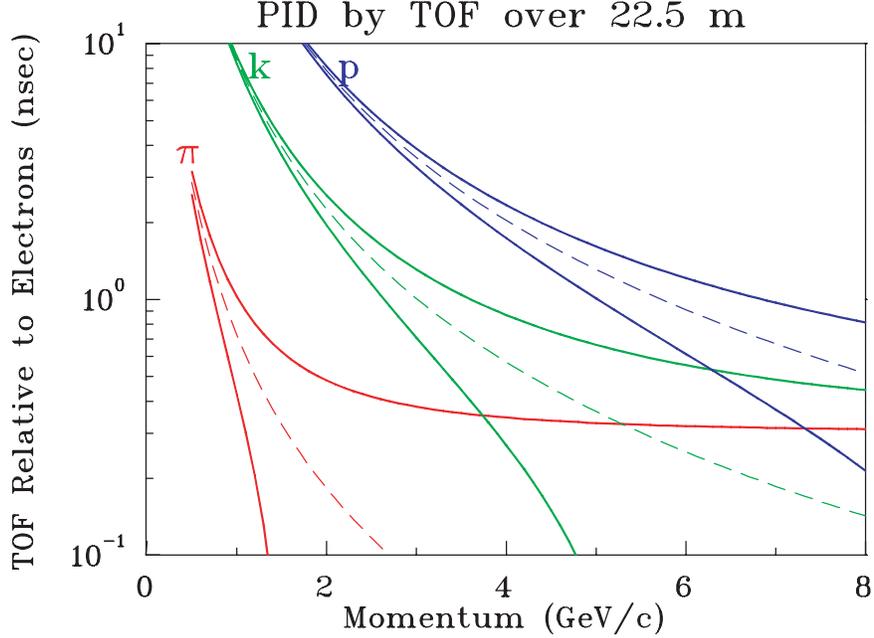
Figure 202: The dashed lines represent the time-of-flight (relative to electrons) versus momentum. The vase-shaped envelopes in solid lines demonstrate the limitations due to finite timing resolution ($\pm\,1.5\sigma$ with $\sigma = 200$ ps assumed). At the points where the solid lines first intersect, the separation is only 3σ.

by TOF over the short $\simeq$ 2.2-m baseline inside the SHMS hut will be of little use at the higher average energies of the upgrade. Figure 202 shows that, even over a 22.5-m distance from the target to the detector stack, particle identification by TOF is of limited use. Generally speaking, efficient, high-confidence PID will require extensive use of other technologies such as Čerenkov detectors, and that the time resolution requirement for the hodoscope system may therefore be relaxed. This means that the front hodoscope array can be made thinner (5mm versus the present 10mm in the HMS and SOS) which will help reduce the production of knock-on electrons which would otherwise deteriorate the performance of downstream Čerenkov detectors. Meanwhile, the rear hodoscope array can be made quite thick (10mm-25.4mm) since it will be the last element before the electromagnetic calorimeter.

Taking into account the essential functions, and folding in our experience with the Hall C scintillating hodoscopes, we arrive at the following specifications for the SHMS hodoscopes:

- Trigger: Because it is the heart of the SHMS trigger, the hodoscope must have $\geq$ 99.9% trigger efficiency for minimum ionizing particles. To help ensure high efficiency, the pulse
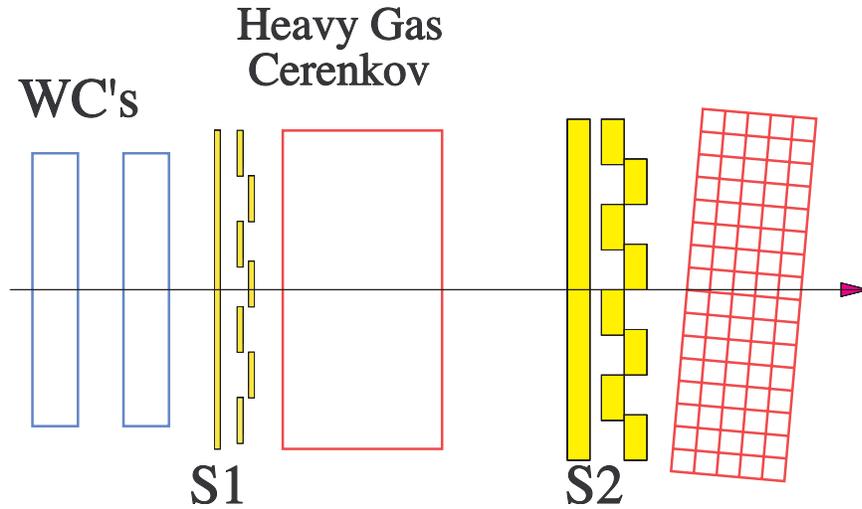
Figure 203: The thin S1 X and Y arrays will be located immediately after the wire chambers. The thicker S2 arrays will be located just before the electromagnetic calorimeter. (Drawing not to scale.)

height variation across an element should be less than 10%. There must also be sufficient redundancy such that an $S_1 \cdot S_2$ coincidence is robust with respect to the inefficiency (or even loss) of a few channels. The detector should also be insensitive to background.

- Rejection of Accidentals: The mean-time resolution of the SHMS focal plane must be at least 100 ps (rms). This will easily permit a coincidence time resolution of 200 ps (rms) so that ± 1-ns cut (single beam bucket) on coincidence time would remove only the tails of the good event distribution beyond 5σ.

- Wire Chamber Tracking Efficiency: The segmentation of the hodoscope X and Y elements has to be sufficiently fine to define a beam of particles which pass through the active region of the wire chambers.

- The hodoscope should have minimal adverse impact on downstream detectors.

- The hodoscope should have a 10-year lifetime before major overhaul.

The solution which meets all of the above specifications is two pairs of X-Y hodoscopes (Fig. 203), named S_1 and S_2, similar to those currently installed in the HMS and SOS. The two arrays would be separated by roughly 2 m, with S1 following the Wire Chambers and S2 just before the Calorimeter. The new features which we would like to emphasize are that

i. S1 will be made of "thin" (*e.g.* 5mm), scintillator elements with long attenuation length BC408,

ii. S2 will consist of a relatively "thick" (*e.g.* 2cm-3cm) quartz Čerenkov radiator elements, and

313

Table 36: Nominal dimensions for the hodoscope elements of each of the four arrays. There are eight elements per plane.

Element	Material	Width	Length
S1X	5 mm BC408	11.3 cm	110 cm
S1Y	5 mm BC408	14 cm	90 cm
S2X	2.5 cm Quartz[9]	14 cm	140 cm
S2Y	2.5 cm Quartz	18 cm	110 cm

iii. standard 12-stage PMTs like the XP2262B will be employed, operated at low anode currents for extended lifetime.

Since the existing Hall C hodoscopes are made of scintillator, the most dramatic change listed above would be the use of a quartz Čerenkov for the S2 arrays. Simulations by Simicevic[Si01] for the $Q_{weak}(proton)$ experiment indicate that it is reasonable to expect several hundred photoelectrons (p.e.) for a 1-meter length quartz radiator with a moderately good surface reflectivity. A quartz Čerenkov detector operated at a threshold of 100 p.e. could be essentially 100% efficient and blind to low-energy backgrounds, resulting in a much cleaner $S_1 \cdot S_2$ trigger. This capability is critical for the clean detection (and accurate tracking efficiency determination) of protons in extremely low cross section measurements[8] at a CW facility.

Each of the four arrays will have eight rectangular bars of scintillator or Čerenkov radiator. The active area of the arrays is designed to have $\simeq 100\%$ acceptance of the beam envelope for the full momentum bite and target acceptance of the large solid angle tune. The SHMS beam envelope simulations can be found in Section 3.C.3. A summary of the nominal hodoscope dimensions is given in Table 36. Finally, with one PMT on each end of a scintillator or Čerenkov radiator paddle, the total number of SHMS hodoscope channels will be 64.

Particle Identification

Overview Hadron identification for momenta up to 11 GeV/c will be fundamentally different from that of the HMS-SOS detector systems. With increasing momentum it becomes more and more difficult to distinguish hadrons by time-of-flight measurements. With the 2.2-m flight path in the detector hut, kaon-pion separation by time-of-flight becomes infeasible at roughly 2 GeV/c. At 3.5 GeV/c also proton-kaon separation will no longer work. Coincidence timing with a hadron flight path in the SHMS of 22.5 m and a reconstructed coincidence time resolution of roughly 200 ps extends this to 4 GeV and 7 GeV, respectively. Note however, that particle identification by means of coincidence timing will in general not distinguish particles from accidental coincidences and therefore will lead to an irreducible background that must be subtracted. Therefore, at high

---

[8] *e.g.*, $d(\gamma,p)n$ at high s and $A(e,e'p)A-1$ at high Q^2.

momenta one must rely on other means of particle identification, *e.g.* Čerenkov detectors, dE/dx measurements, and Transition Radiation Detectors (TRD).

As described in detail below, the Super-High Momentum-Spectrometer will draw upon a variety of techniques to achieve particle identification over its entire momentum range. A global outline of the scheme is shown graphically in Fig. 204, where the discrimination power is shown as the significance of the measurements (number of standard deviations) in the various PID detectors versus the particle momentum.

Electron identification can always be accomplished by use of energy measurements in the electromagnetic calorimeter, and optionally improved upon with a TRD. Over the SHMS momentum range, electrons will always radiate in Čerenkov counters, so these devices will also contribute to electron tagging. For extreme cases at high momentum and low signal to background, such as measurements at $x > 1$, we envision adding another Čerenkov counter in place of the last section of vacuum pipe just upstream of the first wire chamber. This device, using a Ne-Ar mixture at atmospheric pressure, can have its index of refraction tuned to enhance either electron-pion or pion-kaon discrimination at high momentum.

For hadron identification the following PID strategy can be employed:

~ 1 **to** ~ 3 **GeV/c:** Kaon-pion separation can be achieved with the appropriate choice of one aerogel Čerenkov. A time of flight path of 2.2 m with a TOF resolution of 200 ps still allows one to distinguish protons from kaons at the 3σ level up to 2 GeV/c. At the high end of this range, proton PID can be improved with the use of an additional aerogel counter with n=1.02.

~ 3 **to** ~ 5.5 **GeV/c:** Pions will trigger a C_4F_{10} gas Čerenkov. The C_4F_{10} pressure will be adjusted such that kaons do not radiate. Kaons will trigger an $n = 1.015$ aerogel Čerenkov.

~ 5.5 **to** **11 GeV/c:** Pions will still trigger the C_4F_{10} gas Čerenkov. An atmospheric pressure gas Čerenkov counter will be inserted upstream of the first wire chamber and filled with an Ar-Ne mixture to provide a pion tag or an additional electron tag. At these higher momenta the multiple scattering in this added detector will be tolerable.

Thus, an appropriate choice of combinations of detectors and techniques will allow the SHMS to provide useful particle identification over its entire momentum range. The remainder of this section will describe each of these detectors.

Shower Counter The SHMS magnetic spectrometer is aimed to cover small forward angles and higher momentum settings not available so far in Hall C[WP01]. When identifying electrons at these settings, good particle identification is needed to suppress high hadron background. Lead glass electromagnetic calorimeters are well suited to this purpose.
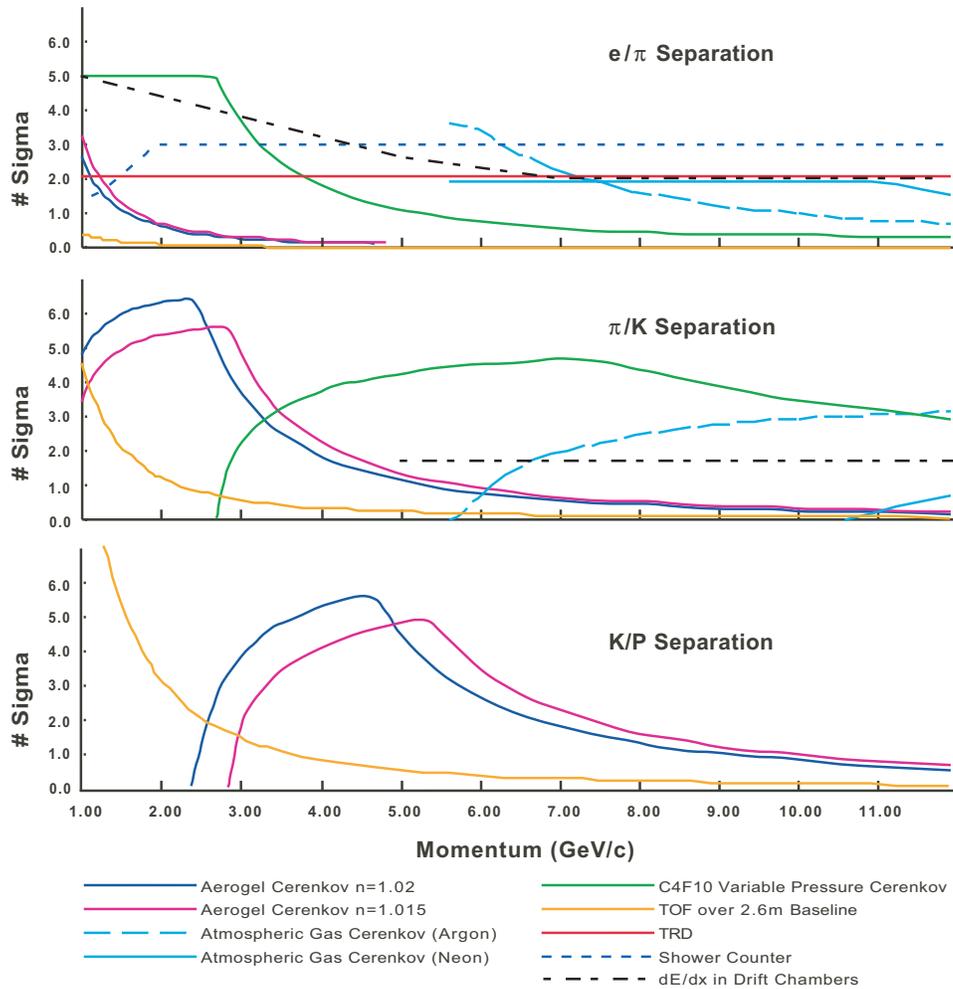
Figure 204: Particle Identification Resolving Power over the SHMS Momentum Range. The vertical scale in each graph is number of standard deviations which separate the two particle types shown, calculated for all of the relevant detectors in the system.
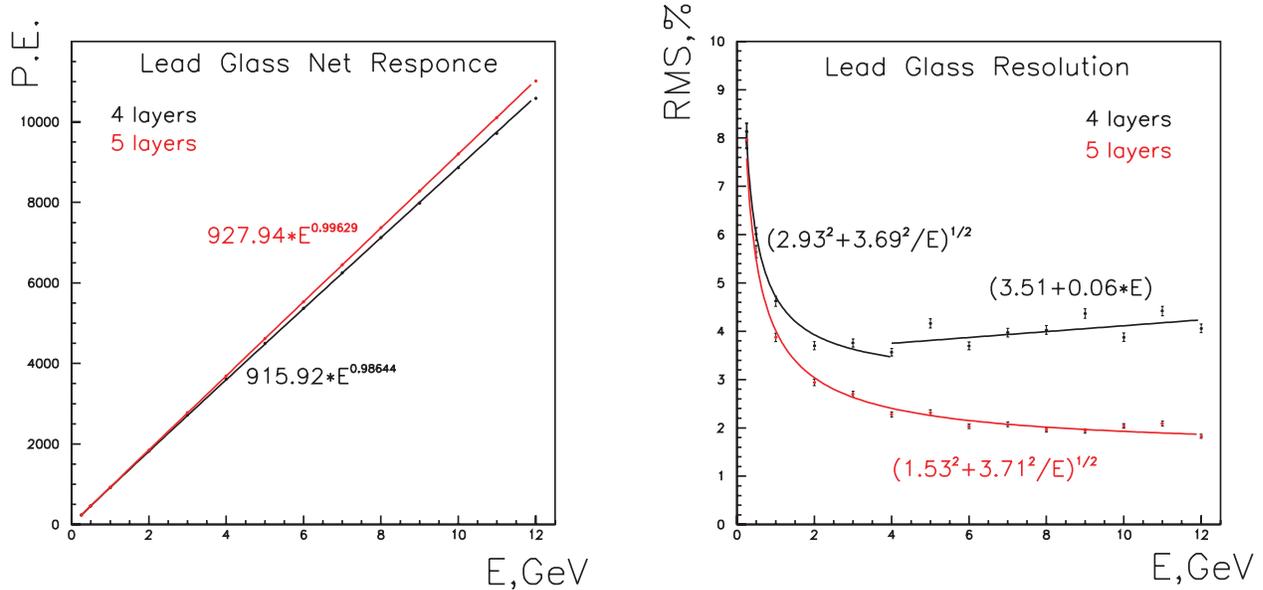
Figure 205: EGS4 Monte Carlo simulation of the linearity (left panel) and resolution (right panel) of a TF-1 Lead Glass modular calorimeter. The calibration, coordinate correction and electronic effects are not included.

The design of the SHMS electromagnetic calorimeter is similar to the existing HMS and SOS calorimeters in many respects. The HMS calorimeter consists of $10 \times 10 \times 70 \ cm^3$ TF-1 Lead Glass rectangular blocks wrapped in thin aluminized mylar and in tedlar film for optical tightness. The characteristics of the TF-1 lead glass are: density $\rho = 3.86$ g/cm^3, refractive index n=1.65, radiation length $R_L = 2.74$ cm. The blocks are arranged in four layers for a total thickness of 40 cm (14.6 radiation lengths). Photomultiplier tubes (Philips XP34462B) are mounted at both ends of each block in the first two layers and at one end for the remaining layers. The modules are equipped with ST–type fiber adapters for the gain monitoring system.

Figure 205 shows the results of a Monte Carlo simulation for the lead glass calorimeter. As can be seen from the left panel, the calorimeter is linear within 3.5% up to electron energies of 12 GeV. The energy resolution of the HMS calorimeter (PMTs mounted on one end of each block) measured in the energy range 0.5–4.0 GeV is given by

$$\frac{\Delta E}{E}(\%) = \frac{6.1}{\sqrt{E(GeV)}} + 0.3 \tag{77}$$

and is comparable to the resolution of similar devices[PDB]. The SOS calorimeter is somewhat better in this respect[Ar98]. More details on the HMS and SOS calorimeter construction and performance can be found in Ref. [Ar98]. The performance of the calorimeters has not deteriorated significantly in the 7 years since they were first installed.

The observed π^-/e^- rejection factor of the HMS calorimeter is better than $(1-5) \times 10^{-2}$ in the momentum range 0.5 to 2.0 GeV/c, with electron detection efficiency $\geq 99\%$. At these low momenta, pion rejection can be improved at the cost of electron efficiency by using a tighter cut
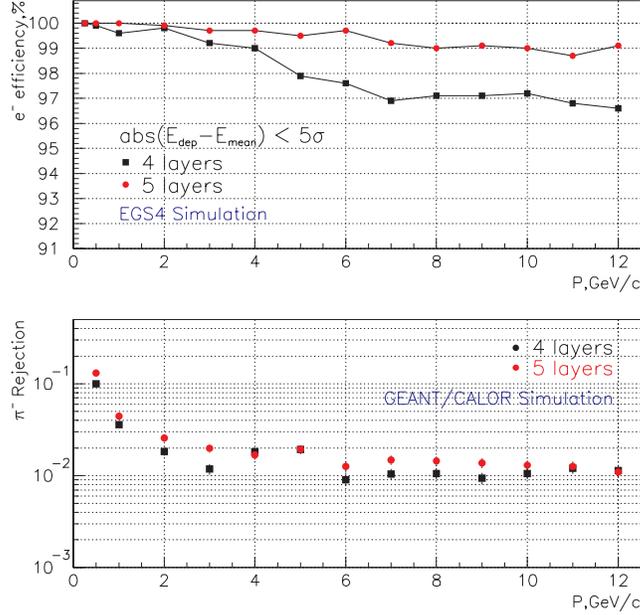
Figure 206: Electron detection efficiency (top panel) and pion rejection (bottom panel) obtained from the Monte Carlo simulation of the TF-1 Lead Glass Calorimeter. The calibration, coordinate correction and electronic effects are not included.

on the calorimeter energy. At higher momenta, the pion rejection is not significantly improved by a tighter cut.

The energy dependence of the resolution of the calorimeters indicates almost complete absorption of electromagnetic showers up to energies of ~ 4 GeV. However, at higher energies the Monte Carlo simulation predicts a slow rise of the resolution, which is a clear indication of leakage (see Fig. 205, right panel). Adding an additional layer restores full absorption, hence improving both the resolution and linearity. Adding a fifth layer also improves the electron detection efficiency (see Fig. 206, top panel), but it does not change the pion rejection (Fig. 206, bottom panel). Exploiting the transverse and longitudinal spread of the deposited energy will improve pion rejection, and the contribution of a fifth layer may be valuable in this case.

Two side by side stacks of 12 blocks are needed to cover the whole acceptance of the spectrometer (see Fig. 196) and thus 120 modules would be required. As adjacent blocks will be optically decoupled, the light will be collected with PMTs on both ends of the calorimeter blocks. The calorimeter will be deflected by small amounts in both vertical and horizontal directions to avoid cracks in between the modules.

Alternatively one can construct a lower cost, 4–layer calorimeter using only 96 modules. It will still contain most of the electromagnetic shower and hence have hadron/electron rejection capability. The leakage of energy will not significantly affect the hadron rejection, but will hurt the electron efficiency (or the electron rejection when measuring pions).

318

Another low-cost alternative is an assembly of 132 short modules oriented along the beam direction. A preshower wall of 24 long modules before this assembly may be helpful for the separation of minimum ionizing hadrons from just developed electromagnetic showers. The deepness of the calorimeter should be optimized to get good rejection across the SHMS momentum range.

Atmospheric Pressure Čerenkov One of the typical uses of the SHMS will be to detect highly inelastic scattered electrons. At such kinematics the pion background can be significant, so a reliable method of electron identification is required. Threshold Čerenkov detectors are excellent tools to use when the particle velocity β is greater than phase velocity of light in the medium c/n. The minimum momentum at which a particle will exceed the phase velocity of light in the medium is given by:

$$P_{min} \cdot c = \frac{M \cdot c^2}{\sqrt{n^2 - 1}} \tag{78}$$

Thus, if we require 10 GeV/c pion to be under threshold, then $n - 1$ must be 0.0001 or smaller, which can be achieved either by choosing low-pressure gases, or certain noble gases at STP. For example $n - 1 = 0.000067$ for Ne, $n - 1 = 0.000033$ for He.

The main characteristic of threshold Čerenkov detectors is the number of detected photons. For very low refractive-index gases the number of emitted photons is extremely small. At $p > 9.0$ GeV/c a gas Čerenkov for electron-pion discrimination should be over 2.5-3 m long in order to have an adequate number of photoelectrons. A $\beta=1$ particle traversing a 3 m long Ne radiator will produce about 30 photons in the visible light range (300-700nm). Most PMTs are not very sensitive below 300 nm. Since the production has a λ^{-2} dependence, and $n(\lambda)$ goes to unity at short wavelengths, the Čerenkov light produced will be peaked in the ultraviolet (100-300nm). Using these photons will double the number of photoelectrons from the photocathode [Ar98, So99]. PMT windows coated with p-terphenyl, which absorbs UV light and retransmits it in the range of 390 nm, increase the PMT response by about 90% compared to the uncoated tubes[So99]. The expected number of photoelectrons will be $\simeq 10 - 12$.

The solution to adjust the refractive index by using the noble gases at STP appears more attractive than the use of a low-pressure tank. The low-pressure approach requires a 3 m long vacuum sealed volume. Having this volume under-pressurized tends to gradually take in O_2 and H_2O which can change not only the threshold condition, but also absorb the ultraviolet part of the Čerenkov radiation. Further, using Ne and Ar at STP allows the windows of the Čerenkov tank to be made very thin (possibly from tedlar). This will aid in minimizing multiple scattering in front of the drift chambers.

The atmospheric Čerenkov tank we propose would replace the final 3 m of the vacuum pipe as it enters the SHMS detector hut. The diameter needs to be only about 60 cm at the upstream end, and cover 75×100 cm² at the downstream end. A vacuum window with the same scattering properties as the standard one would be installed upstream of the Čerenkov counter. The Čerenkov windows and mirrors and their supports will be made lightweight so as to keep multiple scattering
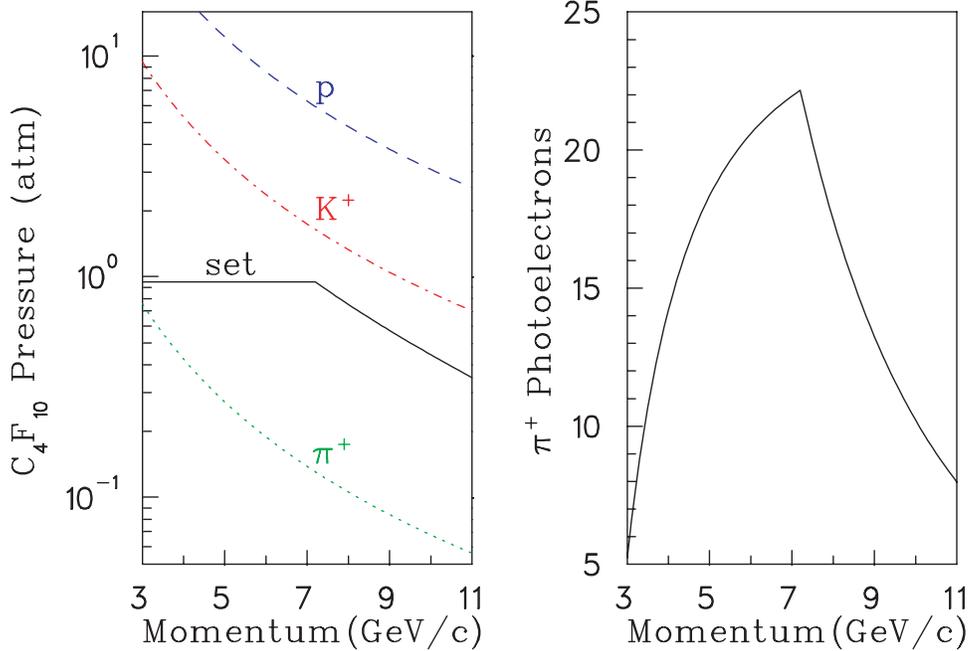
319

Figure 207: (Left) Threshold C_4F_{10} pressure required for Čerenkov light generation from the particles indicated. The solid curve indicates the operating pressure planned for the detector. (Right): Number of photoelectrons anticipated for the detector, taking into account the transmittance, reflectivity, and quantum efficiency functions of the detector components.

at a minimum. Even then, the detector would only be compatible at the high end of the SHMS momentum range.

Heavy Gas Čerenkov Above ~ 3 GeV/c, hadron species cannot be reliably distinguished by time of flight over the 2.2-m baseline planned for the SHMS detector stack, and so information from Čerenkov detectors becomes increasingly relevant. An aerogel Čerenkov detector with $n = 1.02$ will provide $\pi^{\pm}/K^{\pm}$ discrimination only up to 2.4 GeV/c. Beyond this momentum, a gaseous Čerenkov detector is required. Based on the excellent operational experience at JLab and elsewhere, we propose to construct a threshold Čerenkov using the heavy perfluorocarbon (PFC) gas C_4F_{10} as a radiator. This gas has an index of refraction of 1.00143 at standard temperature and pressure, and so can be used here over a wide range of incident particle momenta.

The solid curve in the left panel of Fig. 207 indicates the gas pressure we propose to use at each SHMS central momentum setting. It is expected that the detector gas pressure will be remotely controlled from the counting room as the spectrometer momentum is changed. We assume 0.95 atm. pressure from 3.4 GeV/c to 7.0 GeV/c, and sub-atmospheric pressure at higher momenta. The gap between the 'set' and 'K^{+}' curves above 7 GeV/c takes into account the +25%/-15% momentum bite of the SHMS, and a possible 0.1-atm error in the setting of the gas pressure regulator. We do not anticipate the detector being used for π^{+}/K^{+} separation at momenta below 3.4 GeV/c.

Figure 208 shows a schematic design for the heavy gas Čerenkov. The enclosure is a cylinder
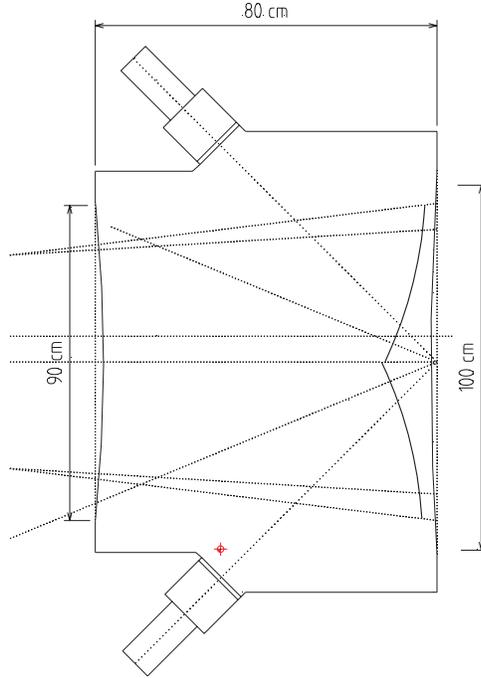
Figure 208: Schematic Design for the SHMS Heavy Gas Čerenkov Detector.

of nonmagnetic stainless steel, with the PMTs located outside, viewing through a 1-cm thick UV-grade fused silica window. This allows for better isolation of the pressurized cavity, and allows one to maintain proper PMT-mirror optical alignment should the PMT require servicing. Four mirrors and photomultipliers are required to cover the SHMS beam envelope; they should be of the highest possible quality. As a reference design, we have selected the Photonis[PHOT] XP4508B 5" photomultiplier tube. This is similar to the PMT currently used in Hall B, except that it has a flat face of fused silica, which allows for flush mating with the quartz window. A custom-design voltage divider with boosted voltage between the photocathode and the first dynode will be used to provide optimum focusing of the photoelectrons, and so minimize losses within the dynode chain. To minimize abberations, the mirrors should be thin glass, which can be structurally reinforced outside of the beam envelope. Protected aluminum mirror coatings with $> 90\%$ reflectivity down to 200 nm are commercially available[LAM10]. We propose to use $0.020''$ titanium for the particle entrance and exit windows, which is the same material used on the G0 spectrometer [Be02c].

C_4F_{10} is very expensive, and so a recovery system is required. C_4F_{10} has excellent UV transmission characteristics (97%@170 nm) provided it is kept pure. A filter and cold trap may be desirable additions to the gas recovery system, to maintain the required gas purity. Both oxygen and water absorb strongly below 200 nm, and should be kept below 0.1%. Residual nitrogen has an effect on the refractive index, and should be kept constant and below $< 1\%$.

The right panel of Fig. 207 indicates the number of detected photoelectrons expected from a π^+ for a 70-cm radiator length. The C_4F_{10} transmission, mirror reflectivity, quartz transmittance,

and PMT spectral characteristics, as well as possible optical misalignment, were all taken into account. The resulting π^+ detection inefficiency, assuming that an off-line cut is placed at < 1.5 photoelectrons to eliminate knock-on events, is less than 0.1% for all momenta between 3.4 and 10.3 GeV/c, and rises to a modest 0.3% at 11.0 GeV/c.

In conclusion, a heavy gas Čerenkov detector, utilizing a C_4F_{10} radiator with variable pressure between 0.4 and 0.95 atm., appears to be a practical way to obtain reliable π^+/K^+ separation within the SHMS.

Transition Radiation Detector The purpose of the transition radiation detector (TRD) is to separate electrons from pions. This is possible because ultra relativistic charged particles emit *transition radiation* (TR) in the form of x-rays when they traverse a dielectric boundary[Gi46]. TRDs are composed of multiple modules stacked together where a single module contains a radiator and x-ray detector (*i.e.* multiwire proportional chamber). Each radiator is made up of many dielectric interfaces of low-Z material to increase the TR yield. TRDs typically have a threshold of $\gamma = 1000$, hence only electrons will produce TR photons in the momentum range of the SHMS. In general, particle identification is accomplished either by examining the total energy deposited in the detector or by cutting on the number of high energy clusters (typically above 5–7 keV) deposited along the track. It has been shown that there is improvement in the particle separation if cluster counting is performed[Lu81a, Fa81]. This is because the number of clusters obeys a Poisson distribution while the total energy has a long Landau distributed tail. The pion rejection factor (PRF), which is inversely related to the pion efficiency, is largely dependent upon the length of the detector, as shown in Fig. 209 with smaller effects coming from the type of radiator, chamber, electronics and particle identification method[PDB].

The detector will be located between the heavy gas Čerenkov and the back hodoscope planes and will be about 60 cm long. To maximize the PRF, uniformly spaced foils of polyethylene would be close to ideal (lithium foils being ideal), but due to the relatively large active area of the detector (110×140 cm^2), carbon fibers or polyethylene foam will be considered. Using a fiber or foam radiator decreases the PRF by a factor of about 2 when compared to foils. The radiator will be 50 mm thick with a mean foil thickness of about 17 μm and a mean gap or pore size of about 200 μm. This corresponds on average to 230 foils per radiator which will produce about one detected TR x-ray per module. The x-ray detector will be a xenon filled longitudinal drift proportional chamber to facilitate cluster counting. Since xenon gas is expensive, the chamber gas will be recirculated and filtered. Figure 210 shows a sketch of a single TRD module and the pulse distribution. The longitudinal drift will be 20 mm and, if a 90% Xe/10% CO_2 gas mixture is used (drift velocity ~ 25 mm/μs for $\mathcal{E} = 3$ kV/cm), the maximum drift times will be about 0.80 μs. The proportional region will be 8×5 mm^2 (anode wires spaced by 5 mm). Monte Carlo simulations which include hadronic showers and δ-ray production will be needed to determine if this segmentation is sufficient. Special attention must be paid to the exit cathode plane to reduce bulging due to pressure changes and the "hydrostatic" pressure inside the chamber. The electronics
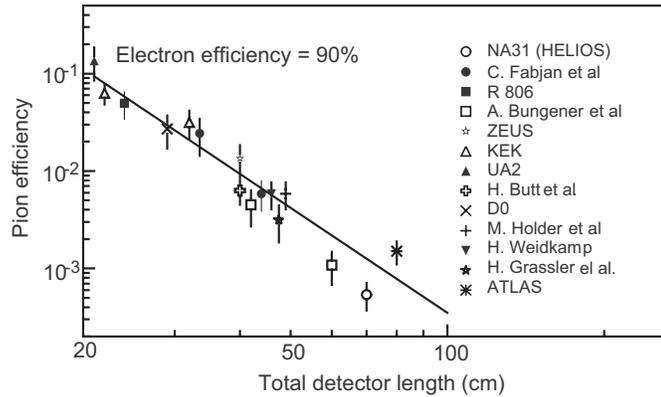
Figure 209: Pion Efficiency Measured (or Predicted) for different TRDs as a function of the detector length for an electron efficiency of 90%. (Figure from Ref. [PDB])
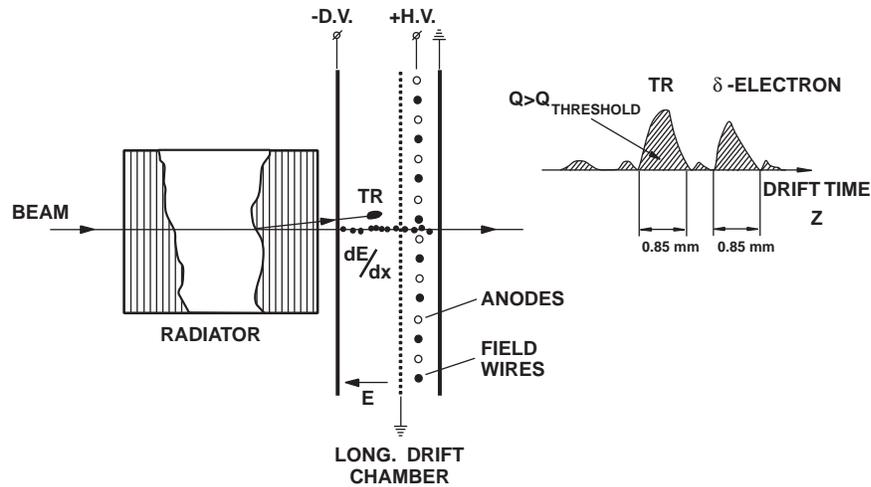

Figure 210: Single module with time expansion chamber (TEC) which includes a drift region and a proportional region. The output signals will consist of uniform dE/dx ionization with localized TR clusters and δ-ray clusters.

on each anode wire will consist of a preamplifier, a shaping amplifier and an 8-bit flash ADC.

At least six modules will be used for the TRD with a total length of about 60 cm. At 90% electron efficiency, this will result in a PRF of about 200 - 300. At 95% electron efficiency, the PRF will reduce by a factor of 3 or 4, but if a higher rejection factor is needed, additional modules could be used and/or a foil radiator could be used. Off-line analysis which includes more sophisticated statistical methods (*i.e.* likelihood) and an intelligent cluster threshold will also improve the PRF. This intelligent threshold will vary the threshold with drift time, thus taking advantage of the energy dependence of the photon's range in the chamber. Since the TR yield tends to saturate at $\gamma \sim 8000$, the PRF will be flat over the SHMS momentum range. The combination of the TRD, shower counter and a Čerenkov will be more than adequate to suppress any hadronic background encountered in the SHMS. Additionally, having three particle identification detectors will provide a better mechanism for systematic studies of the detector efficiencies.

Aerogel Čerenkov Counter The aerogel detectors will be standard diffusion box type detectors consisting of a layer of silica aerogel in a diffuse reflective box, read out at the sides by large 5-inch PMTs. For the SHMS, a detector with a minimum active area of 110×140 cm^2 is needed for full coverage of the beam envelope at the anticipated detector location, 2.3 m downstream from the focal plane (see Fig. 196 and Ref. [WP01]). Thus, a detector could be 110 cm in x (bending or vertical) with 5 PMTs on each side and 140 cm in y (horizontal). Allowing for an up to 10 cm thick aerogel layer the entire box will be roughly 30 cm deep (in z direction).

The technology of aerogel detectors with a diffusion box and PMTs as light collectors is well established at Jefferson Lab. The Hall C detector with $n = 1.034$ yielded 19.3 photoelectrons for $\beta = 1$ particles [Mo99a]. The two Hall A detectors, A1 with $n = 1.015$ (9 cm) and A2 with $n = 1.055$ (5 cm), yielded 8 and 30 photoelectrons, respectively [Zh01a]. The significantly better performance of A2 is certainly due in part to the higher index of refraction. Additionally, it is believed to benefit from a higher photoelectron yield of the Photonis tubes used in this detector as opposed to the Burle tubes used in the A1.

Two more detectors are currently under design, one for the HMS and another for the hyper-nuclear spectrometer (HKS). The HKS detector explores the possibility of segmenting the detector along the focal plane and thus increasing the rate capability. This should also be considered for the SHMS detector, *i.e.* to ensure reliable performance at the very forward angle settings possible with this spectrometer. The design with 5 PMTs on each side would allow for 5 optically separated segments. Limiting individual segment rates to 1 MHz would result in a total rate capability of 5 MHz for particles above the Čerenkov threshold. To compensate for the dead areas introduced by segmentation, a second plane with the segments offset by half a segment width would be required.

As aerogel the materials SP15, SP30 and SP50 from Matsushita Electric Works is recommended. Matsushita's aerogel has a waterproof coating that makes it hydrophobic. This removes the need for baking (in fact baking will destroy the coating) and also increases transparency. A
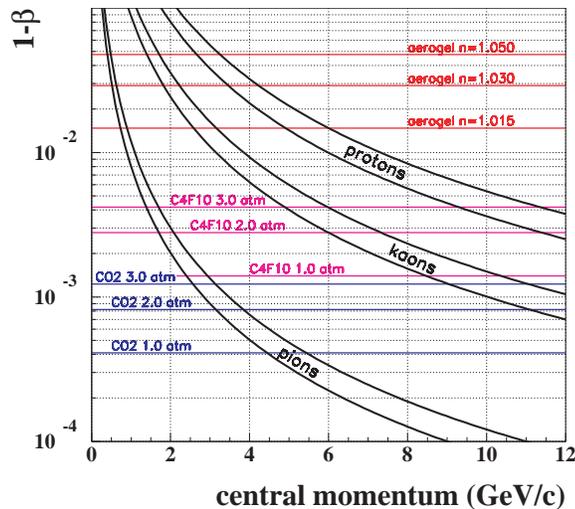
Figure 211: Hadron Velocity $1 - \beta$ as a Function of Momentum. For each particle a band is shown corresponding to a momentum acceptance of $\pm 10\%$. The horizontal lines show thresholds for different Čerenkov radiators.

low-cost 5-inch PMT (Photonis XP4572) has been successfully employed in the Hall A A2 detector and should also be considered for the detector proposed here. Figure 211 shows the thresholds for these materials as a function of momentum.

The performance of the detector has been simulated with D. Higinbotham's Monte Carlo code [Hi98]. With the standard parameters and $n = 1.015$ one gets 6 photoelectrons. This results in a detection efficiency of $> 99\%$ for a 1 p.e. cut and 88% for left-right coincidence of $\geq$ 1p.e. The experience with the Hall A A2 and the HKS prototype suggest that this simulation is a lower estimate. Therefore, it is expected that we will actually see closer to 10 photoelectrons and achieve a left-right coincidence efficiency close to 98%.

Focal Plane Polarimeter   To measure the ratio of proton electric to magnetic form factor at $Q^2 > 12\,\mathrm{GeV}^2$ using the recoil polarization technique, the focal plane polarimeter (FPP) which is being built for the HMS will have to be moved to the SHMS. The FPP is in effect two polarimeters in series, so there is a CH_2 analyzer followed by drift chambers and then an additional CH_2 analyzer followed by drift chambers. A drawing of where the FPP would fit into the SHMS detector package is shown in Fig. 212. The 2nd Čerenkov and aerogel/TRD would have to be removed.

Trigger, Data Acquisition, and On-line Computing

Trigger The focal plane trigger electronics used for the HMS and SOS has been designed to be flexible, fast and efficient at detecting particles. These triggers consist of requiring hits in a majority of the hodoscope planes combined with options to require or veto on signals from the various particle ID capable detectors in the focal plane hut. The SHMS trigger electronics will be
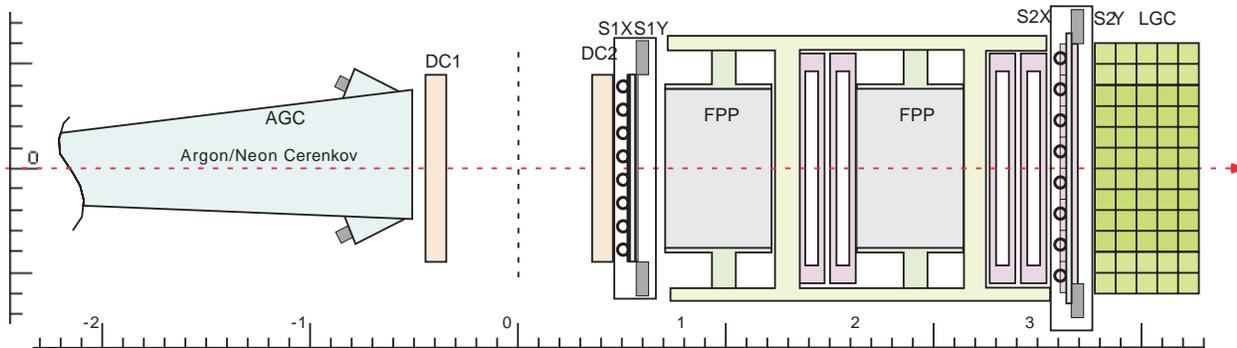
Figure 212: A Schematic of where the Focal Plane Polarimeter could fit into the SHMS Detector Package. There are two CH_2 analyzers, each followed by a set of drift chambers.

similar to the HMS and SOS logic but there will be opportunities for increased sophistication in the trigger.

The design of the HMS and SOS triggers was in part driven by the desire to minimize the time to form the trigger, thus minimizing the amount of delay required for the TDC and ADC inputs from each PMT. With the use of common stop TDCs and ADCs such as those described below, triggers will not need to be formed as quickly. This will allow for the possibility of more sophisticated triggers and the use of computer controllable logic modules.

DAQ Electronics The fine resolution (0.5 ns) TDCs used for the Hall C drift chambers are multihit common-stop models that do not require long cables to delay the signals until a trigger arrives. The absence of delay cables greatly simplifies the physical layout of the experimental apparatus and electronics and also simplifies the commissioning of experiments. Such common-stop devices have not been available at the higher resolutions required for PMT based detectors, and no similar devices have been affordable for charge digitization. For PMT digitizers the inputs must be delayed by approximately 400 ns to wait for the formation of focal plane triggers and a coincidence between spectrometers. Recent advances, however, make it clear that multihit, buffered, common stop TDCs and ADCs of sufficient resolution will be available for the SHMS.

The JLab Physics Electronics Group is developing a 64/32 channel TDC based on the F1 chip [Br99a]. When used in the 32 channel mode this TDC will have a least count of 60ps, yielding sufficient time resolution for any PMT based detector. The effort to develop this TDC is already well advanced and it is expected that the VME module being developed will be used by some experiments at JLab within the next few years. The per-channel cost of this TDC is expected to be comparable to that of common-start high-resolution TDCs used now.

Standard ADCs operate by integrating the current on an input while a gate is present. Since this gate is generated by a trigger which can take many hundreds of nanoseconds to form, each ADC input must be delayed with long coaxial cables. The use of analog delay can be avoided by using a Flash ADC to continuously digitize the input and saving the data in memory while waiting

for the gate. When the gate arrives, the appropriate samples can be summed to produce a digital integration of the input. While this technique has been used, it is not in common use for situations with PMT pulses only a few tens of nanoseconds in width.

While affordable commercial Flash ADC modules are not available, indications are that either affordable modules will be available before the upgrade or that building suitable modules at JLab will be feasible. Flash ADC modules suitable for particle physics use, such as the Struck SIS3300, are available now. This 8 channel module which digitizes at 100MHz with a 12 bit Flash ADC would work well with detectors with wide PMT pulse shapes. However, the cost per channel is several times that of conventional ADCs, so the module would only be appropriate for prototyping and specialized applications.

As part of R&D efforts for the Hall D GlueX experiment, a single channel ADC prototype that uses a 250MHz 8bit Flash ADC chip has been designed. The key components of this design are inexpensive, so overall costs should be comparable to those of conventional ADC modules. Even though the 8 bit resolution is less than the 10 to 14 bits typically used in nuclear physics spectrometers, some resolution is recovered by the fact that a PMT pulse a few tens of nanoseconds wide will be sampled several times yielding better precision. An ADC based on this existing design is already good enough for the majority of the charge digitization required for the SHMS, but we note that higher resolution flash ADCs may be affordable at the time of the upgrade. The JLab electronics group is currently exploring development of a general purpose ADC module based on the GlueX flash ADC prototype.

A side-benefit of flash ADCs is that not only do they record pulse shape, but also pulse timing. Although it is unlikely that a flash ADC can obtain time resolutions as good as the 60ps of the F1TDC, sub nanosecond timing is feasible. This will allow moderate time resolution to be obtained for detectors such as Gas Čerenkov, Aerogel, TRD, and Lead Glass shower counters without additional discriminators or TDC modules.

Data Acquisition and On-line Software The philosophy of the data-acquisition system for Hall C with the SHMS is that the DAQ should not be the limiting factor in the event rates that can be handled. Experience in Hall C has shown that factors other than DAQ, such as accidentals rates or singles rates on individual detectors, generally limit overall trigger rates to less than 10K events/s. With the front end TDC and ADC electronics discussed above, a DAQ system can be constructed that can handle event rates in excess of 10K/s with minimal deadtime. Other than the front end electronics, no technology advances are required in order to obtain these data rates. Future improvements in the speed and cost of networking, CPUs, and disk drives will only help to simplify the design of the DAQ system.

Data acquisition will continue to be managed by CODA[CODA]. CODA development over the next few years will include an emphasis on an on-line analysis farm as a part of CODA. With the upgrade we plan to add a moderate analysis farm. This will have two uses:

1. Real-time accumulation of diagnostic histograms

2. Data compression (background filtering, sparsification)

Stand-Alone (Third-Arm) Calorimeter　　A large lead-glass calorimeter is planned to be used in experiments in Hall C with the present CEBAF 6 GeV machine. An approved experiment, GEP-III, will use the calorimeter to detect the scattered electron from the elastic $\vec{e}p$ reaction. This experiment will measure the ratio of proton electric to magnetic form factor at $Q^2 = 9$ GeV^2 by measuring the ratio of the transverse to longitudinal polarization of the outgoing proton in the elastic $\vec{e}p$ reaction. To cleanly identify elastic events, the scattered electron will be detected in a lead-glass calorimeter. This calorimeter is being constructed and is expected to be ready for the GEP-III experiment in 2005. The new calorimeter can be used in experiments to measure the ratio of proton electric and magnetic form factors at $Q^2 = 9$–14 GeV^2, and to perform $\gamma - \pi°$ production experiments. This new calorimeter is also planned to be used in real Compton scattering (RCS) experiments with 11 GeV beam energy which are extensions of experiments done with 6 GeV beam.

The calorimeter will consist of 1600-1700 lead-glass blocks. Two sizes of lead glass are used in the calorimeter. One set (which was used in the RCS experiment which ran in Hall A) has a frontal area 3.8x3.8 cm with length of 45 cm. The other set has a frontal area of 4.0x4.0 cm with length of 40 cm. The expected position resolution is 3-5 mm. The lead-glass calorimeter will have a frontal area of 2.7 m^2 and an aspect ratio of 2:1. The infrastructure for the calorimeter, such as platforms, cabling, and electronics, is planned to be usable for the experiments with 12 GeV beam. The electronics readout will be flexible. It will use active splitters for amplitude digitization of each channel and timing of the sums of 8 channels. The splitters will be designed to allow the full formation of a calorimeter trigger for experiments that need it, such as the RCS experiments.

3.D　Hall D and the GlueX Experiment

3.D.1　Introduction

The goal of the GlueX experiment is to search for gluonic excitations of $q\bar{q}$ pairs with masses up to 2.5 GeV/c^2. The identification of such states requires knowledge of their production mechanism, identification of their quantum numbers, J^{PC}, and measurement of their decay modes. These in turn require a partial wave analysis of exclusive final states. The decay products of produced mesons must be identified and measured with good resolution and with full acceptance in decay angles. In many cases, the decays of mesons involve a chain of particle decays. The GlueX detector must therefore be hermetic (effective 4π coverage) and have the capability of measuring directions and energies of neutral particles (γ, π^0, η) and four-momenta of charged particles with good resolution. Clearly, particle identification is also required.

The partial wave analysis technique depends on high statistics and, in the case of incident photons, also requires linear polarization. The latter is needed to identify the production mechanism. The linear polarization is achieved by the coherent bremsstrahlung technique. The degree of linear polarization and flux of photons in the coherent peak fall dramatically as the photon energy approaches the endpoint energy. On the other hand, it is desirable to have photon energies high enough to produce the required masses with sufficient cross–section and with sufficient forward–boost for good acceptance. For a fixed incident momentum and a fixed resonance mass, it is also desirable to have a fairly constant $\mid t \mid_{min}$ over the natural width of the resonance. This requirement demands a higher incident photon energy than expected by simple threshold production.

An operating photon energy of $9.0 \, \text{GeV}$ produced from a $12.0 \, \text{GeV}$ electron beam represents an optimization of beam flux, cross–section and degree of polarization. The GLUEX detector is optimized for this energy range. Extensive Monte Carlo simulations has been performed to optimize the detector's ability to reconstruct exclusive final states. Acceptances are nearly 90% for many complicated channels, and the detector resolutions have been balanced to facilitate excellent reconstruction of the events. This will allow kinematic fitting to reduce background contamination of events. Such backgrounds are known complications in partial wave analysis.

3.D.2   The Photon Beam and Polarization

Linearly polarized photons can be produced in the desired energy range by using the technique of coherent bremsstrahlung. A horizontal plan view of the photon beam line is shown in Fig. 213 with the major components labeled. The electron beam enters the figure from below ground at the left and is bent into the horizontal plane to enter the tagger building. There it passes through two small dipoles to impinge upon the bremsstrahlung radiator.

The Photon Tagger and Beam Collimation   After its exit from the radiator, the electron beam passes into the tagger magnet where the primary beam is bent in the direction of the electron beam dump. The radiator crystal is thin enough that most of the electrons lose less energy in traversing the radiator than the intrinsic energy spread of the incident beam. Those electrons which lose a significant fraction of their initial energy inside the radiator do so by emitting a single bremsstrahlung photon. These degraded electrons are bent out of the primary beam inside the tagger magnet and exit the vacuum through a thin window, passing through air for a short distance to strike the focal plane of the spectrometer. The primary electron beam is contained inside vacuum all the way to the dump.

The tagging system used in the GLUEX experiment will consist of a dipole magnet spectrometer with two sets of plastic scintillation counters in the focal plane to tag photon energies: a precision set with 0.1% energy resolution and a broad-band set with a coarser energy resolution of 0.5%. The precision system will be composed of 64 narrow counters and will nominally tag photons from 70%
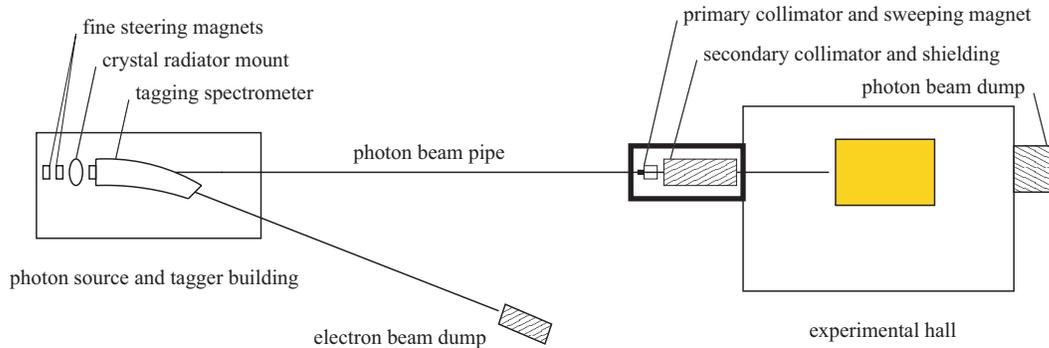
Figure 213: A schematic plan view of HALL D photon beam line for the GLUEX experiment, (shown in the horizontal plane as viewed from above). The objects in this figure are not drawn to scale.

to 75% of the electron beam, but will be movable allowing precision tagging of other energy bytes as well. The broad-band tagging system will tag photons between 25% and 92% of the electron beam energy using 128 fixed scintillation counters. The second system will be crucial for alignment of the radiator crystal and could also be used by other experiments that might be run in HALL D.

The tagger magnet will be similar to the existing tagger in Hall B of Jefferson Lab. The higher energy needed in GLUEX is largely compensated for by going to smaller bend angles, so the sizes of the magnets are comparable, although the HALL D system will bend in the horizontal rather than in the vertical plane.

The photons that are produced in the radiator pass through a small hole bored in the return yoke of the tagger magnet and exit the vacuum through a thin window in the forward direction. They then pass into a transfer pipe, which may either be evacuated or filled with helium to reduce photon beam degradation due to interactions, and travel to the experimental hall. Just before entering the hall the photon beam passes through a system of collimators and sweeping magnets. In Fig. 213 they are shown in a separate enclosure for shielding purposes. The primary collimator is first. It selects the part of the photon beam that is allowed to reach the target. Debris from interactions along the inside surface of the collimator bore forms a halo around the photon beam that exits the collimator. The charged component of the halo is deflected away from the beam axis by a dipole "sweeping" magnet just downstream of the collimator. A secondary collimator follows the sweeping magnet to stop the deflected shower particles and block the halo of secondary photons generated by the first collimator. This collimator is of a larger diameter than the primary and so sees a reduced rate of secondary interactions on the inner surface of the hole. Any new showers that are generated there are cleaned up by a second sweeping magnet. The beam then passes through a final collimating aperture into the experimental hall. This triple-collimation system was copied from the setup developed at SLAC [Ka75].

The collimated photon beam, now only a few mm in diameter, is delivered to the experimental target. After traversing the target (3% radiation lengths), the photon beam passes through the
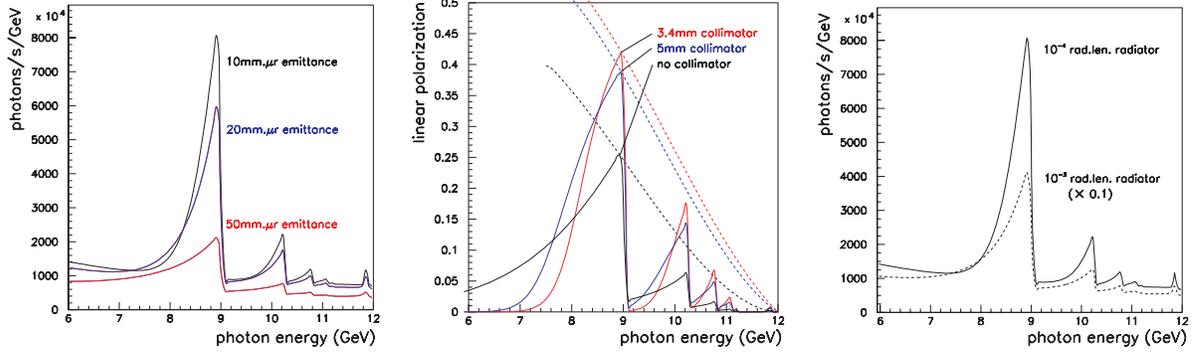
330

Figure 214: Left: The effect of collimation on the coherent bremsstrahlung spectrum, (various collimation diameters are given with the optimum value being 3.4 mm). Center: Plane polarization of the coherent bremsstrahlung. The dashed lines indicate the trajectory of the peak polarization. Right: Collimated coherent bremsstrahlung spectrum for 2 crystal radiator thicknesses.

detector and into the photon beam dump at the back of the HALL D building. Based upon a design upper limit of $60\,kW$ ($5\,\mu$A at $12\,$GeV) being delivered to the electron beam dump, the total power in the photon beam is at most $1.5\,W$ in the experimental Hall And at most $15\,W$ in the collimator enclosure. The safety issues of such a beam have been reviewed by Jefferson Lab's RadCon group. As an additional safety constraint, permanent magnets will be installed in the photon beam down stream from the tagger building to prevent an accidental loss of the electron beam into HALL D. These magnets have been obtained as surplus from Fermilab.

Polarization via Coherent Bremsstrahlung   The net polarization of the beam under different collimation conditions is shown in Fig. 214 (center panel). The dashed curves show how the maximum polarization in the peak varies as the peak energy is changed by rotating the crystal. The polarization in all cases is zero at the endpoint, but its dependence on the electron beam energy E and photon energy k is different. Without collimation it rises as $(k - E)^2$, one power coming from the intensity of the coherent peak relative to the incoherent component and goes linearly to zero at the endpoint, and the other from the intrinsic polarization of the coherent photons that also behave like $(k - E)$ near the endpoint. Collimation allows one to essentially isolate the coherent component, so that the polarization available to the experiment rises from zero at the endpoint in a linear fashion. The dashed curves in Fig. 214 demonstrate this point.

In order to obtain the full polarization enhancement from collimation, it is necessary to have a distance between the radiator and collimator of about $80\,m$. This distance scale is set by the requirement that the collimator aperture must be large compared to the size of the electron beam spot on the collimator, but small compared to the actual photon spot size. Figure 215 shows the maximum polarization as a function of radiator-collimator distance for a coherent peak at $9\,$GeV. The collimator diameter was adjusted in this calculation to keep the collimation half-angle at $0.5\,m_e/E$. At zero distance the collimator has no effect except to attenuate the beam, and so the uncollimated polarization from coherent bremsstrahlung is obtained. At $100\,m$ separation distance
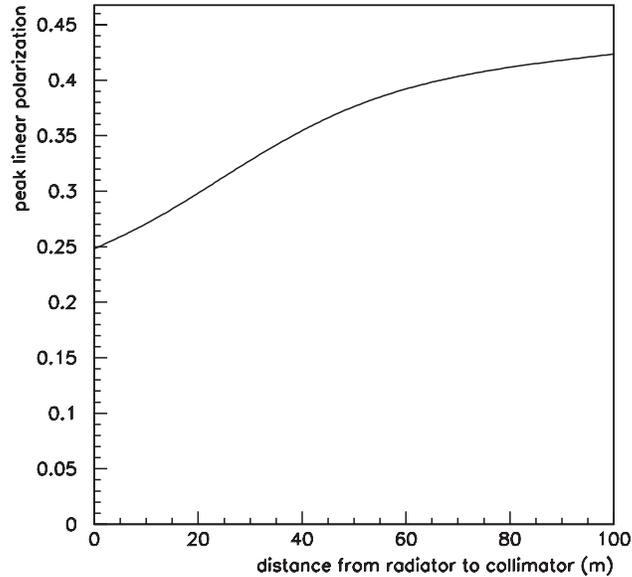
Figure 215: Maximum polarization *vs* radiator-collimator distance for a coherent peak at 9 GeV. The collimator diameter was held fixed in this calculation to keep a constant ratio between the sizes of the virtual electron spot and the collimator.

the polarization enhancement has saturated. The design for HALL D calls for a radiator-collimator distance of 80 m with a collimator diameter is 3.4 mm.

The range of permissible thicknesses for a crystal radiator is bounded from above by multiple scattering of the electron beam as it passes through the radiator; this causes the beam divergence to grow, thereby enlarging the photon beam spot on the collimator face and reducing the ability of collimation to discriminate the coherent component relative to the incoherent part. The minimum thickness is determined by the thickness necessary to achieve the full coherent gain. For a 12 GeV beam energy and a 6 GeV coherent photon the coherence length is 18 nm. The coherence length does not impose a practical limit on how thin the radiator should be. The effects of multiple scattering are best presented by showing the calculated spectra for various radiator thicknesses. The photon spectrum for a 20 μm (10^{-4}) and a 100 μm (10^{-3}) radiator is shown in Fig. 214 to demonstrate the effect. The 100 μm spectrum is scaled down by a factor of 5 to facilitate the comparison, but it is clear that for a significant coherent gain, the crystal thickness must be near 20 μm.

Synthetic diamonds are made using either vapor deposition (CVD) or high pressure high temperature (HPHT) techniques. CVD diamonds have an extensive mosaic and are unsuitable for coherent bremsstrahlung, but HPHT synthetics look very promising. The Glasgow group recently acquired a 5 mm $\times$5 mm synthetic diamond less than 18μm thick which has a [100] orientation. This diamond yielded a very good coherent bremsstrahlung spectrum and X-ray measurements showed rocking curve widths of less than 10μr, quite close to the ideal value for diamond.

A 30- cm-long liquid hydrogen target will be used. It will be contained in the same vacuum
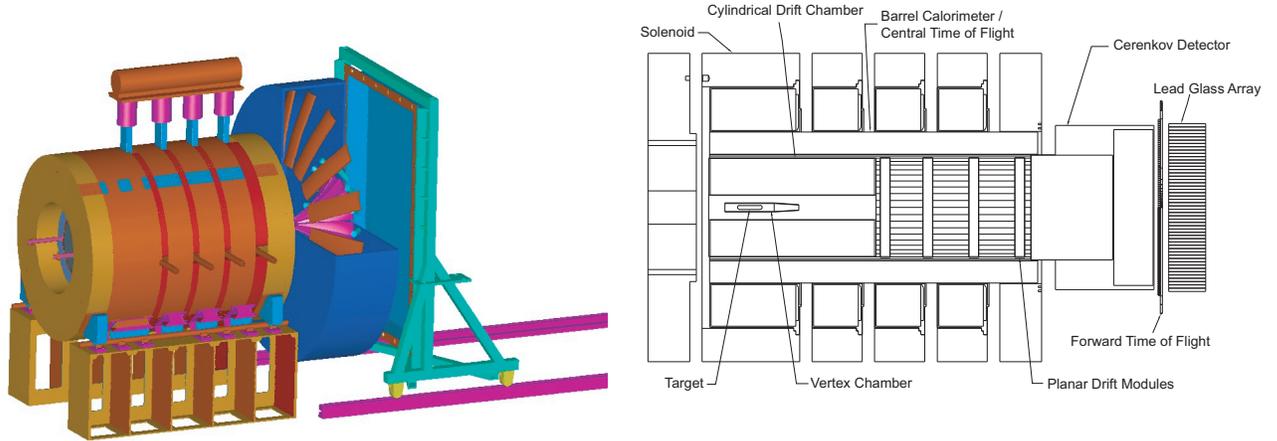
332

Figure 216: A 3D cutaway view of the GLUEX detector (left) and schematic diagram of its major subsystems (right)

jacket as the photon tagger radiator and will be constructed of low mass materials. The collimated photon beam will be contained within a radius of 2.5 cm from the beam axis. This will allow adequate space between the hydrogen vessel and the innermost detector element for insulation, a vacuum pipe and any plumbing and wiring required to instrument the target.

3.D.3   The GlueX Detector

The GLUEX detector has been optimized to provide nearly hermetic acceptance for both charged particles and photons. In addition, a combination of particle identification systems will allow very good K-π separation. Design optimization will allow the detector to fully reconstruct exclusive many-body final states. In conjunction with high statistics, this will allow excellent partial wave analysis of many final states. Figure 216 is a schematic representation of the proposed detector with the individual subsystems discussed briefly below. A more detailed description can be found in the GLUEX Design Report [GX02].

The Super-conducting Solenoid   Momentum analysis in GLUEX will be provided by a nominal 2 Tesla superconducting solenoid magnet. This solenoid was built at SLAC ca. 1970 for the LASS spectrometer [As87] and subsequently moved to LAMPF in 1985 for inclusion in the MEGA spectrometer. The MEGA Experiment and the solenoid were decommissioned in place in 1995. The MEGA experiment has since been removed from the solenoid and arrangements are underway to ship the solenoid from LANL to the Indiana University Cyclotron Facility (IUCF) for refurbishment and testing. This magnet was designed and built using standards that today would be considered ultra-conservative. The magnet employs a cryostatically stable design and uses cryostats that were designed to be easily opened for service with hand tools. A recent inspection [ML00] of the magnet at LANL revealed that it is still in excellent condition and worthy of the time and cost involved in

relocation and refurbishment. Nevertheless, the magnet support systems are now 30 years out of date so even though the magnet is in excellent condition it requires some maintenance, updating, and modifications for use as part of the GLUEX experiment.

The LASS/MEGA solenoid was inspected in April 2000 by a team from the GLUEX collaboration, JLab staff and two of the original designers of the magnet. This team met at Los Alamos with the MEGA staff and inspected the magnet installation and the fourth coil. Except for two small mechanical vacuum pumps the system was completely intact. The committee concluded that "the condition of the magnet is excellent and if cooled down in place would in all likelihood work!" Subsequently, Jefferson Lab formally transferred the solenoid system from Los Alamos to JLab as of October 2001. A Memorandum of Understanding (MOU) was negotiated with LANL to cover all disassembly aspects of the MEGA experiment. This work, performed by a JLab crew, began in November 2001 and was completed in February 2002. The solenoid is now at IUCF where testing and repairs are underway under the auspices of a MOU between JLab and IUCF. A detailed description of the work needed to bring the magnet systems up to date and have the magnet operational in the GLUEX experiment can be found in reference [GX02].

Particle Tracking and Particle Identification   The system of tracking chambers in the GLUEX detector must cover as close to a 4π solid angle as possible over a wide range of particle momenta, and have sufficient momentum resolution to be able to identify missing particles. In the solenoid region, the chambers are inside the barrel calorimeter. The location of the target, very near the entrance to the solenoid, coupled with the energies involved which force the reaction products into forward angles, result in an effective 4π coverage in the center-of-mass of the produced particles, even though the geometrical coverage around the target is less than that. The chambers also must extend as close to the beam line as possible. Near the target, this will provide very accurate vertex information which will be important in identifying decaying particles (e.g. K_S, Λ, Σ, ...). In the forward region, this is needed to reconstruct very fast particles ejected at small angles (down to nearly 0°). Finally, at large angles, the tracking must be able to separate π's and K's up to momenta of about $0.5\,\mathrm{GeV/c}$ — a regime where dE/dx measurements will work. To satisfy the tracking requirements, a starting point based on the LASS detector [As87] was used. A series of three different tracking elements will be implemented as shown in Fig. 216, with each element optimized for a particular region in the detector.

The Vertex Detector   The Vertex System (VTX) surrounds the target and has several purposes. First it will be used to provide accurate tracking information very close to the target. These track elements must be sufficiently well defined to be connected to the other tracking chambers. Secondly, the VTX must provide a fast signal (start signal for the event) which can be used in the level -1 trigger of the experiment. Finally, it is a critical element of all time-of-flight systems. The vertex detector will consist of two detector packages. One will be optimized for timing purposes and the other one will provide fast tracking information (see Fig. 217).
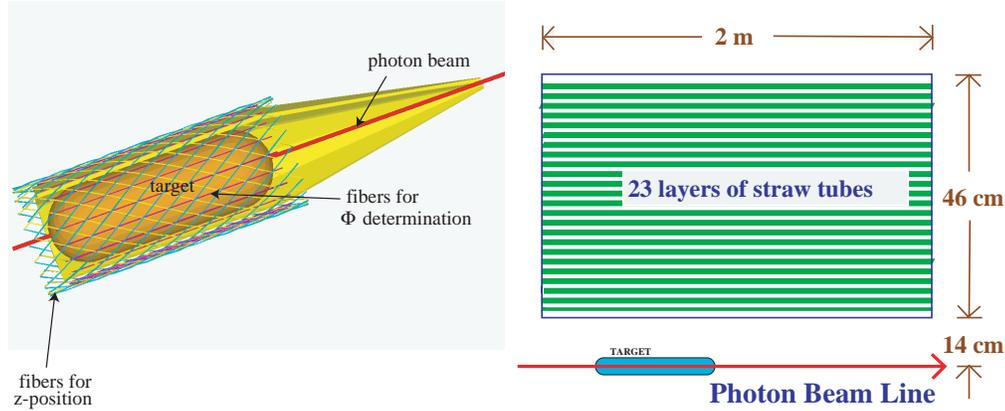
Figure 217: Left: The start counter/vertex chamber. Right: The straw tube chamber.

The timing detector will consist of a cylindrical array of 10 scintillator paddles covering scattering angles between 1° and 90° for the full length of the target. The scintillators have a thickness of 5 mm which reduces to 2 mm in the forward direction. This will provide good light output and therefore a good timing signal. Using Bicron BC-404 scintillating material in combination with fast photo multipliers should result in an overall timing resolution better than 120 ps.

The fast tracking detector will consist of three super–layers of fibers, each containing two layers to minimize dead space. The central layer will be arranged around the target and parallel to the beam, and will determine the azimuthal angle. The z position is deduced from the two outer layers. They will be wound in two opposite helices around the first layer. In order to function in the high magnetic field, we are studying the possibility using Visible Light Photon Counters (VLPC) developed by Rockwell in collaboration with Fermilab [Pe89]. The spectral sensitivity of the VLPCs require us to use SCSF-3HF multi clad scintillating fibers from Kuraray which have a long attenuation length of 5.5 m and are also the least susceptible to radiation damage. One of the main advantages of using VLPCs is their large quantum efficiency of approximately 80% [Wa97] for the light produced by the fibers together with a very high rate capability of 10^8 single photoelectrons per second. The design of this detector system will closely follow the prototype system developed by the D0 collaboration at FNAL [Ba96]. The expected position resolution will be less than 1 mm.

The Cylindrical Drift Chamber   The Cylindrical Drift Chamber (CDC) surrounds the VTX and provides very good $r - \phi$ information and moderate-to-good z information. This chamber also provides dE/dx information for tracks which do not reach any time-of-flight detectors. The CDC is used to accurately track particles between polar angles of 20° and 170°. To minimize material in the forward end plate of the chamber, the chamber must be self–supporting. This leads to a straw chamber, where the straw walls support much of the wire tension. The disadvantage of this design is the difficulty of making dE/dx measurements in a circular straw tube, which requires careful primary path-length corrections.

The straw-tube chamber will contain 3349 straws, each of which is 1.6 cm in diameter. They are arranged in 23 layers. Eight of the 23 layers will be stereo tilted by $\pm 6°$ from the straight tubes. Figure 217 schematically shows the arrangement of the tubes in the chamber. The tubes are assumed to have an $r - \phi$ resolution of 200 μm, while resolution along the wire length will be obtained using the stereo layers. This will nominally yield a resolution along the length of the wire of about 200 μm$/\sin(6°)$ or about 1 mm. The chamber end plates are 0.95 cm thick, and constructed as eight separate *pie-shaped* pieces. The chamber plates extend between an inside radius of 14 cm and an outer radius of 60 cm. Current plans call for no inner shell, and an $8\,mm$ thick outer fiberglass shell. The straw tubes consist of $100\,\mu m$ thick aluminized kapton, and have 20 μm diameter gold–plated tungsten wires in them. In order to study the behavior of straw tube chambers, a 2 m long chamber with 2 cm diameter tubes has been acquired from the EVA experiment at Brookhaven.

In the construction of the straw-tube chamber, the most technically difficult to construct are the stereo tubes. A 1/3-scale model of the chamber has been built with the specific purpose of understanding the construction difficulties of the stereo layers, and has demonstrated the importance is the transition region from straight to stereo layers. A prototype of the end plate is currently being built to determine how accurately the plate can be built.

The choice of gas also plays a significant role in the chamber's performance due to the $2.25\,T$ magnetic field in the detector. In order to study this, the GARFIELD program [Ga84] has been used to compute electrostatic properties of the straw tubes, both with and without the magnetic field. The chamber will require a *slow* gas in order to minimize the *Lorentz angle*. Calculations indicate that the maximum drift time will be on the order of $500\,ns$ in such a mixture. Investigations are currently underway with mixtures containing larger fractions of CO_2, a slow gas known to work well in high magnetic fields.

The Forward Drift Chambers   The Forward Drift Chambers (FDC) are disk-shaped drift chambers. The basic drift package is a plane of wires with 150 μm spatial resolution between two planes of cathode strips. The strips are arranged in a u and v geometry with respect to the wires, allowing the reconstruction of a 3–D space point from each hit. The chambers are arranged in packages of six, which results in a small track segment, so as to facilitate a later linking of the tracks. Given the number of spiraling tracks, it is critical that these chamber packages not only provide good spatial resolution, but also reasonable directional information. The basic chamber element is a disk with an outer radius of 60.0 cm and the wires strung as chords across the chamber. With a 1.0 cm wire spacing, each chamber will contain 119 wires. In addition, there will be an equal number of cathode strips on each face. These are arranged in a u–v pattern with respect to the wires. The wires that cross through the beam line will be deadened out to a radius of about 3.5 cm by placing material such as Styrofoam in the chambers.

Monte Carlo studies show that the combined tracking system provides very good momentum

resolution for the event topologies in GLUEX. The system is sufficient to identify undetected particles by missing mass cuts. In particular, a missing neutron can be separated from a completely missing recoil Δ for most kinematic regions. Detailed information on resolutions can be found in reference [GX02].

Electromagnetic Calorimetry   The goal of the GLUEX calorimetry is to detect and measure photons from the decays of π°'s and η's, which, in turn, can come from the decays of produced mesons, or from an excited baryon (N^* or Δ). The positions and energies of the photons must be of sufficient accuracy to allow for a complete kinematic reconstruction of the event. Finally, for events with only charged particles, it is essential to be able to veto on neutral missing energy. Thus, nearly hermetic coverage is critical. For selected triggers, neutral energy requirements (or vetoes) are relatively easy to implement.

Calorimetry in the GLUEX experiment will be handled by three different detector systems. In the forward region ($\theta > 14°$), a circular array of lead-glass (Pb-Glass) crystals will be used. In the central region ($14° < \theta < 138°$), a lead-scintillating-fiber matrix calorimeter will be deployed, and in the backward region ($\theta > 138°$) an iron-scintillator photon veto detector will be the likely choice. In the forward and central region, it is necessary to be able to accurately reconstruct the photon energy and direction for physics event, whereas, photons in the backward direction can only result from background events and only a veto system is necessary.

The Forward Calorimeter   The Forward Calorimeter in the GLUEX experiment is a circular lead glass array (see Fig. 218). The crystals have been salvaged from an existing detector, the Brookhaven National Laboratory E852 lead glass calorimeter [Cr98], and are currently in storage at JLab. In order to be used in the GLUEX experiment, a new support structure will need to be constructed. This will allow the crystals to be stacked in a circular arrangement and the detector package to move in and out of the GLUEX detector region. Moreover, new Cockroft-Walton base similar to those used in the JLab Radϕ experiment will be used. Finally, the gated ADCs used in E852 will be replaced with 8 bit, 250 MHz FADCs to eliminate dead time and allow digital pipeline triggers.

The calorimeter has a measured resolution, σ_E/E in percent which can be parameterized as $a + b/\sqrt{E\,[\,GeV]}$ where $a = 1$ to 2 and $b = 5$. The average spatial resolution is 2 to 4 mm and decays with up to eight photons are routinely reconstructed.

Operating an electromagnetic calorimeter, like the LGD, near a high-intensity (a few $\times 10^7$ photons per second) photon beam line could be a concern given the backgrounds one might expect with a tagged bremsstrahlung photon beam. For this reason, the experience with the LGD used in the Radphi experiment in the Hall B photon beam is of particular relevance. Because of the high quality of the photon beam, beam-associated backgrounds were manageable, even when operating
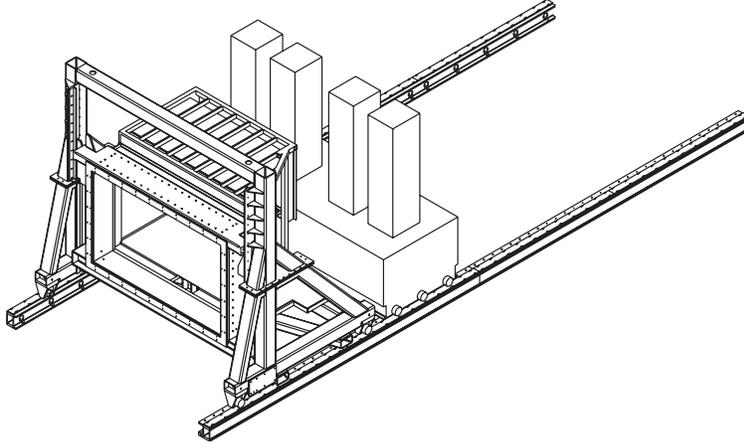
Figure 218: A sketch of the Pb–glass array as modified for the GLUEX detector. The glass is stacked in a circular arrangement to match the solenoid.

at an endpoint energy of 4 GeV. At higher energies the beam spot size will be even smaller and the LGD energy resolution will improve.

The Barrel Calorimeter The Barrel Calorimeter, shown schematically in Fig. 219, will utilize scintillating fibers embedded in a lead matrix to make a relatively high–resolution sampling calorimeter. Advantages include speed, cost, ease of readout, and the fact that it is based on a proven technology. This technology has been used in calorimeter design and operation for more than a decade. The ratio of the active scintillator to the passive high-Z material, as well as the diameter of the fibers can be tuned to enhance resolution, to determine the radiation length, and to achieve uniformity in the electromagnetic to hadronic response (the e/h ratio). For high-resolution EM performance, the JetSet detector developed at Illinois [He90] was the first designed specifically to optimize EM resolution. The recipe produced a detector comparable to lead glass at a considerably lower cost and with approximately half the radiation length. Our design for GLUEX follows this concept but would be a full 12.5-15 X_0 thick at normal incidence and considerably longer. Realization of these changes fortunately can be based on the KLOE calorimeter at DAΦNE, a device of the same length as the barrel calorimeter but with an even larger inner diameter [An96]. The KLOE detector has achieved an excellent energy resolution parameterization of $\sigma/E \approx 4.4\%/\sqrt{E}$ in a half–length prototype, using 1 mm-diameter scintillating fibers, and 0.5 mm-thick lead sheets.

For GLUEX, we will build 54 modules each 4.5 m in length and 20–25 cm deep, using the same diameter of fibers and thickness of lead sheets as for the KLOE detector, (see Fig. 219). The readout scheme takes advantage of the fact that all fibers run parallel to the axis of symmetry of the solenoid and therefore all light piped to the ends of the modules retains its azimuthal and radial information. Since this device is located near the central region of the solenoid, where the magnetic field is ∼ 2 Tesla, field-resistant readout must be employed. The most promising candidate is the hybrid photo diode devices developed for CERN applications. They have a very fast rise time (6 ns
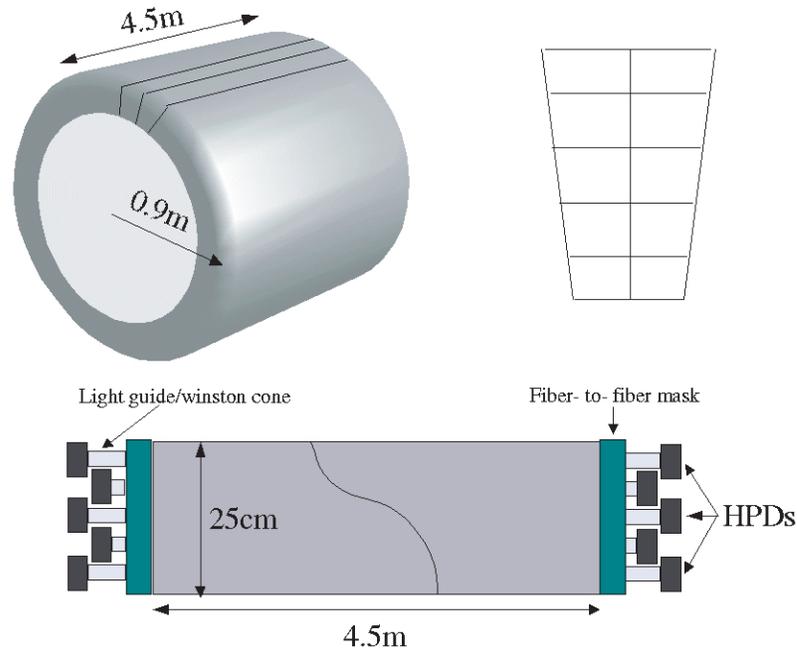
338

Figure 219: Sketch of the Barrel Calorimeter made from bars of Pb/SciFi material. Upper left: perspective view; upper right: close up of end with suggested readout segmentation for one of the 54 bars; Lower: side view showing approximate locations of the PMTs.

or less), a fast fall time (less than 10 ns), and excellent energy resolution. They are immune to magnetic fields up to 2 T and their power supplies are very compact due to the fact that they draw virtually no current even under maximum bias. The polished ends of the lead, scintillating fiber matrix will be coupled to multiple independent light guides or to a fiber-to-fiber mask.

An important feature of these detectors is the signal rise-time and overall duration. Because fast plastic scintillator is used, integrated signal time can be kept below 100 ns with shorter times possible if deemed necessary for rate considerations. At the expected maximum luminosity no problems are anticipated. With short rise-times, very good timing can be expected for each of the PMTs involved in collecting the light from a shower. Time differences from the two ends produces the z coordinate of the hit. The mean light collection time of the two readout ends can be used to determine the particle time-of-flight (TOF). TOF coupled with the track length and momentum then yields particle mass. In the KLOE design, timing of $\approx$ 250 ps (RMS) was achieved, and improvements are possible.

In order to construct 4.5 m long modules, we have been studying the KLOE tooling development. Several visits of HALL D physicists to Frascati and Pisa have already taken place and their training in the use of the KLOE 15 cm-wide lead swagging machine is nearly complete. In May 2002, we successfully swagged 0.5 mm thick lead sheets, and glued 10 layers of lead and 1 mm optical fibers together, producing the first Pb/SciFi test module with dimensions 100 cm x 15 cm x 1.25

cm. This swaging machine is now located at Regina on loan from Frascati, were the construction of larger modules is well under way.

We have conducted several static tests at Regina and in-beam test at TRIUMF of several makes of single– and multi–clad SciFi strands have also been conducted, from Kuraray and Pol.Hi.Tech. The main features of the results were in close agreement with benchmark tests from KLOE. The Kuraray fibers showed a consistently superior performance as per the light attenuation coefficient. They also exhibited a better timing resolution. However, the Pol.Hi.Tech. multi–clad fibers performed better in terms of light yield, based simply on the observation that for the same bias and gain the mean of the ADC spectra for these fibers was higher. For this reason, multi–clad fibers have been ordered and their testing is in progress.

Finally, considerable R&D has gone into the investigation of the performance of the hybrid PMTs as well as toward the development of a suitable pre-amplifier electronic circuit. In our tests we used the DEP PP0350G hybrid PMT and its PP0100Z HV power supply. This device is powered by a HV supply which is typically set to -8 to -9 kV, and a bias of -60 to -80 V is applied across the diode. The gain response of the hybrid PMT at -8 kV is around 1600, which necessitates the use of a preamplifier. For our initial evaluation, we have used a Cremat[10] CR-101D charge sensitive pre-amplifier. Its rise time is 13 ns, its input capacitance is 20 pF and its power dissipation is 150 mW. These tests have pointed to the great care which must be exercised so as to electrically isolate the circuits. Much effort was expended in the avoidance of current (ground) loops in the circuit and in the shielding of the circuits from RF noise. Many parameters of the circuit were studied, such as rise time, signal amplitude, ADC response and photo-cathode positional sensitivity. All measurements were very promising and we are confident that we are close to a production design.

The Upstream Photon Veto   The Upstream Photon Veto is needed to be able to detect and veto on photons traveling in the backward direction. Detailed Monte Carlo studies have shown that events in which a baryon resonance is recoiling against the meson system can produce photons, from the baryon decay, which are traveling in the backward direction. The detector is a soft-steel scintillator sandwich device located directly upstream of the target and in place of the solenoid's original field shaping mirror plate. In the current design, the mirror plate is modified by removing all of the soft iron within the inner solenoid radius. This modification effectively removes the upstream mirror plate leaving only a soft iron annulus the size of the magnet coils and has several benefits: it allows the addition of an upstream photon veto, and upstream access to the target region, cylindrical drift chamber, and the upstream end of the barrel calorimeter.

The photon veto consists of 18 layers of 1 cm thick scintillator alternating with first 12 layers 0.635 cm ($0.36X_o$) thick steel sheets then 6 layers of 1.270 cm ($0.72X_o$) thick steel sheets (see Fig. 220). Each scintillator layer consists of seven 34 cm× 238 cm paddles forming a plane. The central paddle has a hole to allow for the passage of the beam and the target support and cryogenic

---

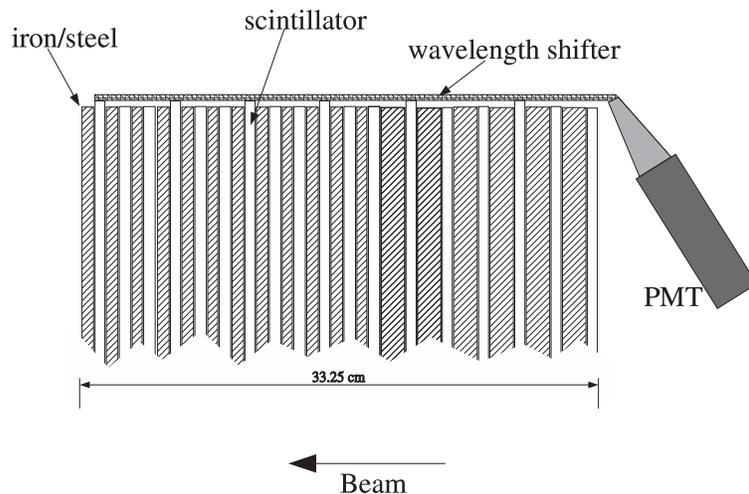[10]Cremat Inc., 45 Union Street, Watertown, MA 02472, USA.

Figure 220: Sketch of a upstream photon veto segment. The 18 scintillator layers are arranged into three alternating orientations: x, u, and v. Shown is the light collection for one such orientation. The light collecting ends of the scintillators are joined together via a wavelength shifter which is oriented perpendicular to the scintillators. The wavelength shifter is used to redirect the light through 90° and out the upstream end of the solenoid to photomultiplier tubes (PMT).

system. The effective area of each plane is approximately 238 cm$\times$ 238 cm. The total counter thickness is 33.25 cm (8.91X$_o$). The layers are arranged into three alternating orientations: x, u, and v (± 45 deg, respectively).

Charged Particle Identification   Charged particle identification (PID) separates $\pi^\pm$ from $K^\pm$ from p (and the occasional $\bar{p}$). (We do not consider $e^\pm$ nor $\mu^\pm$ identification explicitly, but they can be separated from hadrons at some level using the electromagnetic calorimeters.) Two detector systems will be constructed explicitly for this purpose, namely the time-of-flight hodoscope and the Čerenkov detector. Both of these address PID in the forward region, where velocities are close to c and the separation is the most difficult. In the solenoid, we expect to make use of dE/dx in the drift chambers and timing in the barrel calorimeter. Furthermore, constrained fitting is a generally useful tool for identifying the event topology as a whole.

If the particle momentum is not too high, time-of-flight is useful for PID in the forward region. For TOF scintillators that are 2 m long, RMS time resolutions on the order of 100-200 ps are typically achievable using well established techniques [Mo79, Be82]. With improvements in photomultiplier design, however, one can achieve 50 ps RMS for detectors with long, narrow geometry. Superior time resolution has also been achieved with mesh PMTs which will work well in a high magnetic field. In Fig. 221 shows range of relevant momenta for particle identification for both the time-of-flight system and the Čerenkov counter. Beam tests of prototype time-of-flight designs have been carried out and the results indicate we are well on track to achieving time resolutions below 100 ps.
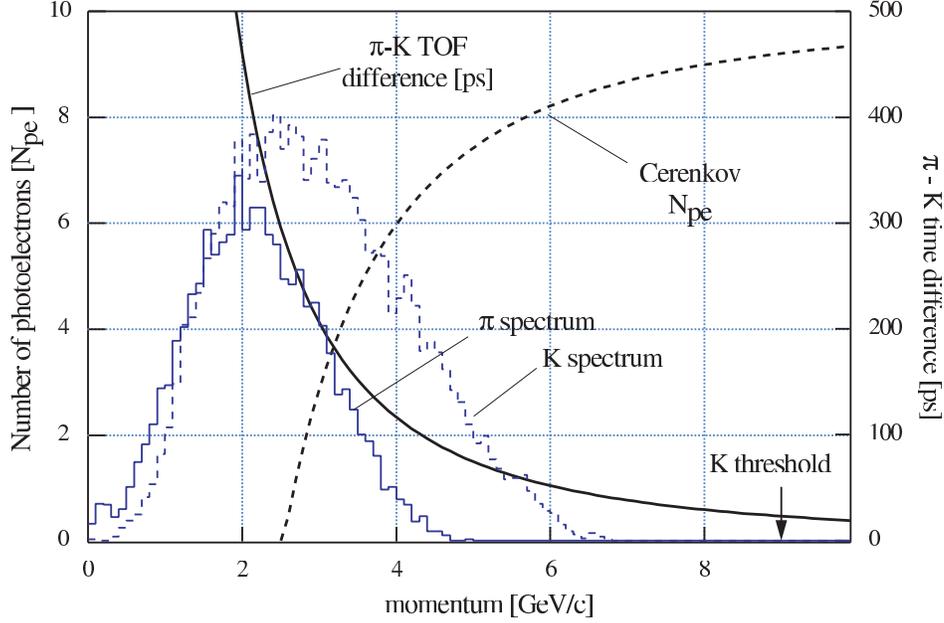
341

Figure 221: The time of flight difference between π and K mesons and the number of photoelectrons from the Čerenkov counter as a function of momentum. Also shown are expected π and K momentum spectra for $K^*\bar{K}^*$ final states.

The Time-of-Flight System   In the forward region the TOF system will consist of two walls of scintillation counters oriented perpendicular to each other and located downstream of the Čerenkov counter and just upstream of the lead glass detector (LGD). The scintillator bars need to be 2 m long to cover the active regions of the Čerenkov counter and LGD. The bars will be read out at both ends with photomultipliers. The width of the bars is set by the requirement that the overlap of charged particles from the same event at the TOF in any one bar be acceptably small ($< 2\%$).

Extensive prototype studies have been carried out to optimize the TOF system design [De01]. Data on scintillation bars of various dimensions and manufacture and various phototubes were collected using a cosmic ray test facility at Indiana University and using hadron beams at the Institute for High Energy Physics (IHEP) in Protvino, Russia, . The first data run at IHEP was used to test 2-m long counters with square cross sections of 2.5×2.5 cm^2 and 5.0×5.0 cm^2. The scintillator material was type EJ-200, produced by the Eljen Corporation. This scintillator has a decay time of 2.1 ns, a bulk attenuation length of 4 m, an index of refraction of 1.58, a peak in the emission spectrum at 425 nm, and a light output equal to 64% of that of Anthracene. The average time resolution measured for various combinations of scintillation bars was in the range of 100-180 ps for the 2.5 cm bars and sub-100 ps for the 5.0 cm bars, depending on the PMTs used. In a later data run 2 m-long bars of cross sections 2.5×6.0 cm^2 were tested using a 5 GeV/c beam. Using constant fraction discriminators the time resolution for two bars was measured to be less than 40 and 60 ps when particle cross 6.0 cm and 2.5 cm of scintillator respectively. Based on the results presented above, we have chosen the 2.5 cm thick, 6 cm wide bar for the TOF wall.
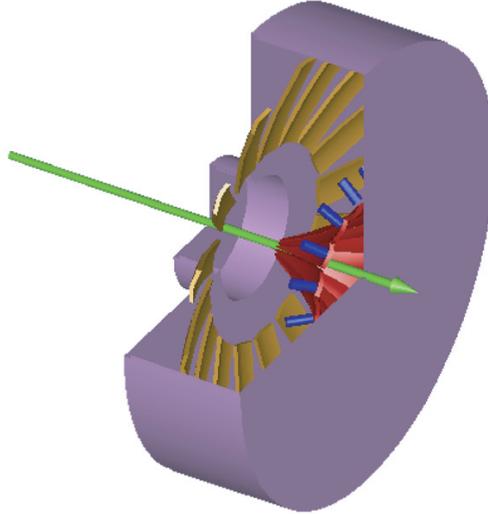
Figure 222: A schematic drawing of the GLUEX Čerenkov detector system. The beam direction is indicated with an arrow. The Čerenkov light is focused by ellipsoidal mirrors (red and orange) into phototube assemblies at the downstream side (blue cylinders).

The Čerenkov Detector   The primary function of this detector is to signal the presence of pions over a large part of the expected momentum range. The Čerenkov Detector is planned to be a gas filled threshold detector running at atmospheric pressure. Current studies suggest that a C_4F_{10} filled Čerenkov detector ($n = 1.0014$) will be a good match to the kinematics of GLUEX reactions. For individual tracks, the results of the Čerenkov detector coupled with the time-of-flight system are shown in Fig. 221.

The detector will be segmented into sixteen azimuthal regions, each housing a single mirror that focuses light onto its own photomultiplier tube. Light emitted into the region within 10 cm of the beam axis will not be collected in order to suppress accidental coincidences in the detector. The optical design of the detector (two ellipsoidal mirrors) was chosen to produce a strong focus at the photomultiplier tubes. This produces small linear magnification and allows good light collection from the wide range of particle trajectories exiting the solenoid. Prototype mirrors were constructed and tested for their focal properties. These were found to be mechanically and optically stable after being cut to shape. Having two mirrors in the design also offers flexibility as to the placement of the photomultipliers. This freedom will be used to place the axis of the tubes perpendicularly to the ambient magnetic field, in order to optimize the effectiveness of the passive magnetic shields surrounding the photomultipliers. A schematic drawing of the Čerenkov is shown in Fig. 222.

Because the GLUEX experiment will be reconstructing exclusive final states, perfect K-π separation for all tracks is not necessary. Detailed Monte Carlo studies using the detector parameters and imposing additional constraints such as the total strangeness in an event and kinematic fitting have been performed. We find that combining all available information will make for a very efficient particle identification system for GLUEX events.

Sub-system Installation and Integration The assembly and integration of each of the detector subsystems into the GLUEX detector requires careful coordination and attention to many diverse issues.

The magnetic field configuration outside the magnet dictates the location and orientation of standard PMTs and/or use of hybrid PMTs. The field distribution can be affected by magnetic materials used for support structures such as iron and, therefore, care must be taken in choosing common materials for the various support systems.

The detectors in the forward direction (Čerenkov, TOF and LGD) are relatively isolated mechanically and operate independently of other systems. The detectors inside the magnet, however, are in close proximity and mounted on the same mechanical frames that are anchored either on the BCAL or the solenoid. Therefore, cabling, power consumption, and access for maintenance must be coordinated carefully. In general, care must be exercised in the design of the electrical circuits, so as to avoid ground loops and RF interference.

The mounting and assembly of detectors must allow for the delivery of services required for their operation, including cryogenics, electrical power, ventilation, gas connections for the Čerenkov and drift chambers, as well as high voltage and signal cables for all detectors. During installation and servicing, careful surveying must be carried out to ensure a precise (better than 100 μm) knowledge of the relative tracking element location. Moreover, access to each sub-system must be facilitated for purposes of maintenance or repair.

3.D.4 Rates, Electronics, Trigger and Data Acquisition

The goal of the GLUEX readout electronics system is to digitize and read out the detector signals for level 1 trigger rates of up to 200 kHz without incurring dead time. A pipelined approach is required. The digitized information will be stored for several μs while the level 1 trigger is formed. Multiple events must be buffered within the digitizer modules and read while the front ends continue to acquire new events.

Two basic types of readout electronics will be used in GLUEX, FADCs and TDCs. Detectors which measure energy will be continuously sampled with flash ADCs while detectors which require precise time measurements will use a multi-hit TDC. No currently available commercial solutions exist. These boards will be designed by our collaboration. Prototypes have been constructed, and are being tested.

The number of channels in the GLUEX detector is not large enough to justify the financially risky development of custom integrated circuits. Programmable logic devices are fast enough and available at reasonable cost. Programmable logic also allows for optimization of the data path without redesigning a printed circuit. ICs developed for other experiments could also be used.
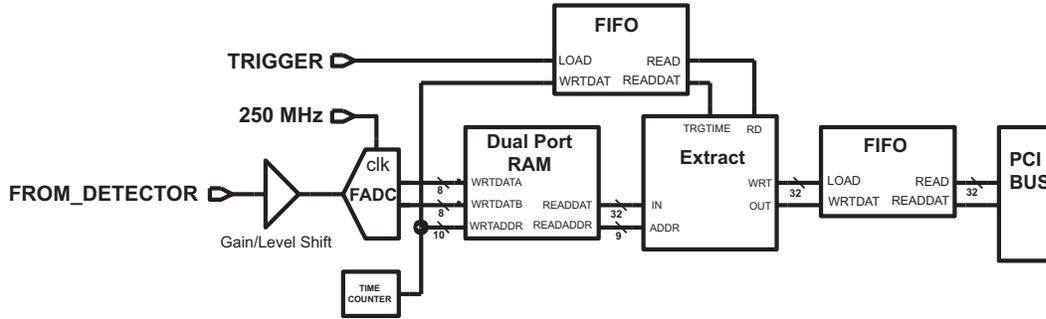
Figure 223: Block diagram of prototype FADC board.

Electronics technology is constantly evolving, and the optimum solution for the GLUEX detector depends on when funding becomes available and the construction schedule.

A single channel prototype of the calorimeter FADC has been designed and built at Indiana University. A block diagram is shown in Fig. 223. A differential amplifier inverts the negative PMT signal and shifts the voltage levels to match the input range of the digitizer integrated circuit. The digitization is performed by an SPT7721 integrated circuit manufactured by Signal Processing Technologies [Spt]. This IC costs about US$25 each in small quantities. An 8-bit value is produced internally every 4 ns; two samples are output every 8 ns (125 MHz).

All digital functions are performed in a Xilinx [Xiln] XC2S50 programmable gate array. This IC costs about US$15 each in small quantities. A dual port RAM configured as a circular buffer stores the data for 8 microseconds. Upon receipt of a trigger signal the data from the time window of interest is copied to an output FIFO which can buffer the data from multiple events. This FIFO is interfaced to a 32 bit, 33 MHz PCI bus. More information on this prototype is available [Sm02].

The Photon Tagger, Start Counter, Vertex Tracker, Forward Drift Chamber anodes, Čerenkov Detector, Barrel Calorimeter, and Time of Flight Wall will all be read out using multi-hit TDCs. Such a high resolution pipeline TDC module has been developed for use at Jefferson Lab, and is designed to meet the requirements of current experiments, as well as to serve as a prototype for future experiments, including GLUEX. The design is implemented as a VME-64x module. This bus standard was chosen because it is already in use at Jefferson Lab, has good (and evolving) data transfer capabilities, and reasonable channel densities are possible. A block diagram is shown in Fig. 224. The module is built around the TDC-F1 integrated circuit from Acam-Messelectronic Gmbh [Acam], originally designed for the COMPASS experiment at CERN [Co99].

The prototype was outfitted with a single F1 chip. All channels were found to be operational and tested for performance. Timing signals were generated with a measured jitter of approximately 30 ps. The time calibration at low resolution was found to be 115.1 ps/count (120 ps/count nominal) and 57.5 ps/count in high resolution (60 ps/count nominal). Subtracting the contribution from the time generator we obtain 62 ps and 51 ps for the prototype performance in both the low
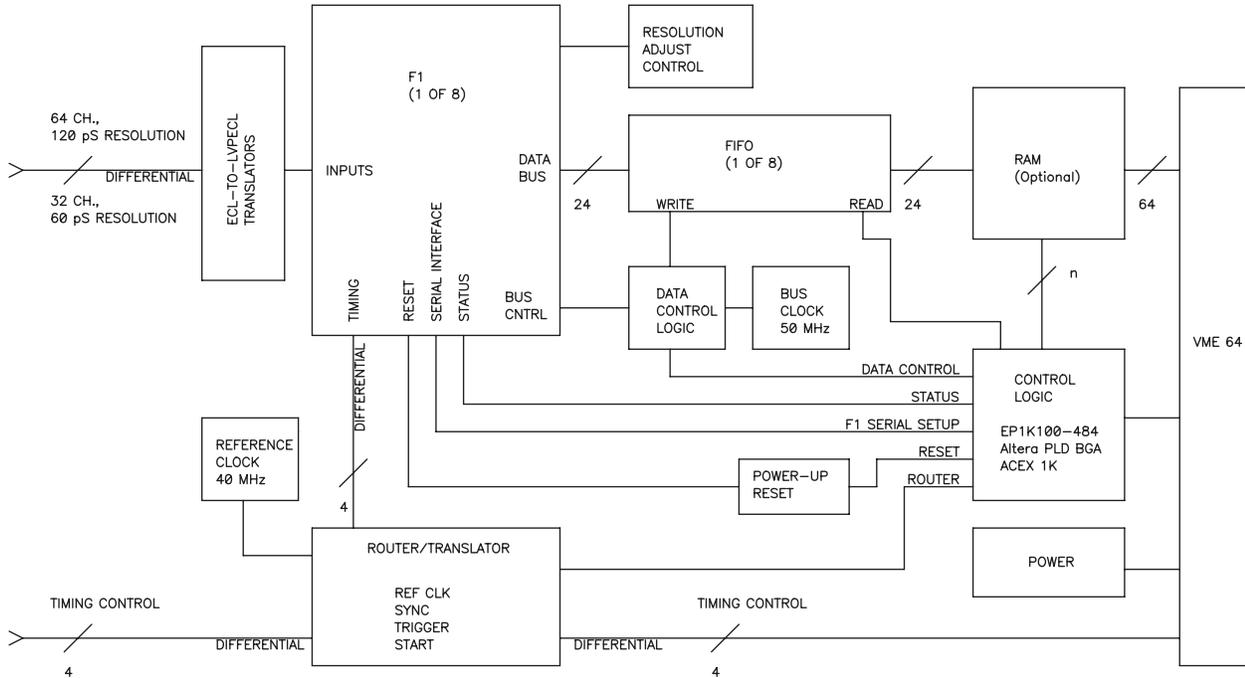
Figure 224: Block diagram of prototype TDC board.

and high resolution respectively. This is to be compared with the quoted rms resolution of the F1 chip of 40 ps.

Table 37 gives the total hadronic rate as well as the tagged hadronic rate for fixed electron beam conditions for various energies of the coherent peak. For $E_\gamma = 9\,\mathrm{GeV}$ and $10^8\,\gamma/s$ in the peak, the experiment will have a total hadronic rate of $365\,\mathrm{KHz}$ and a tagged hadronic rate of $14\,\mathrm{KHz}$. Initial operating conditions will be at about 10% of these values, $(10^7\,\gamma/s)$, but as the trigger improves, and the detector is better understood, rates will be pushed up toward the 10^8 number.

In order to achieve the roughly 20-1 reduction in event rate, GLUEX will use a two-stage trigger, combining a hardware-based level 1 trigger with a software (reconstruction) based level 3 trigger. An essential feature of the GLUEX design is to build pipelining into the entire trigger, digitizer, and data acquisition systems at the outset. This has the twin virtues of allowing adequate time for the level 1 trigger to do its job, while eliminating signal degradation involved in delaying the signals while the trigger operates. Pipelining in this way also allows us to upgrade from initial photon fluxes of 10^7 photons/sec to eventual fluxes of 10^8 photons/sec without any significant changes to the trigger/DAQ architecture. Eliminating conversion dead times will allow us to acquire events which occur very close together in time.

The data acquisition goal for GLUEX is to accept the level 1 trigger rate without incurring any DAQ system dead-time. The high rate of level 1 triggers (70-180 kHz) drives the design of the trigger, the front-end electronics, and the DAQ system. When the level 1 trigger is asserted, a time

346

Table 37: Operating parameters for an experiment using the coherent bremsstrahlung beam. The calculation assumes a 12 GeV electron beam energy and a 3.4 mm collimator 80 m downstream from a radiator of thickness 10^{-4} radiation lengths. The electron beam current is taken to be 3 μA. The rates in the detector (last two rows) are calculate for a 30 cm hydrogen target and an open hadronic trigger.

E of peak	8 GeV	9 GeV	10 GeV	11 GeV
N_γ in peak	185 M/s	100 M/s	45 M/s	15 M/s
peak polarization	0.54	0.41	0.27	0.11
(f.w.h.m.)	(1140 MeV)	(900 MeV)	(600 MeV)	(240 MeV)
peak tagging efficiency	0.55	0.50	0.45	0.29
(f.w.h.m.)	(720 MeV)	(600 MeV)	(420 MeV)	(300 MeV)
power on collimator	5.3 W	4.7 W	4.2 W	3.8 W
power on target	810 mW	690 mW	600 mW	540 mW
total hadronic rate	385 K/s	365 K/s	350 K/s	345 K/s
tagged hadronic rate	26 K/s	14 K/s	6.3 K/s	2.1 K/s

slice of each ring buffer will be copied, compressed and stored. Buffering will occur in groups of at least 10 event fragments on each electronic board and then transferred first across a backplane to be built into crate-event fragments and then to a computer farm to be built into complete events. The farm will perform a quick analysis to reduce the event rate by approximately a factor of ten before recording to mass storage media. This design allows GLUEX to start running with a modest tagged photon rate and then to scale-up by an order of magnitude.

The goal of the level 3 trigger is to reduce the event rate given by the level 1 trigger to an acceptable on tape rate. In low intensity running (10^7 tagged photons/s) the level 1 trigger rate is expected to be 15 kHz. Since the DAQ system is being designed to handle this rate to tape, the level 3 trigger farm will not have to cut any events, although it may be used to reduce the event rate somewhat. In high intensity mode where the level 1 rate is 70 to 180 kHz, the level 3 trigger must be able to reduce the event rate by a factor of ten.

Most of these unwanted events result from an untagged (mostly lower energy) photon interacting in coincidence with a tagged photon. Rejecting these events means that level 3 must be able to calculate, with reasonable accuracy, the energy of the photon which produced the event. This involves accurately reconstructing tracks, matching them with the calorimeter information, and adding additional energy deposited by neutral particles in the calorimeters.

Because of the accuracy requirements and the demands of linking information from different detectors, we have decided to use a processor farm architecture for level 3 instead of building a dedicated hardware processor. All events passing the level 1 trigger will be read into the level 3 processor farm where they will be reconstructed; events passing the cuts applied will then be written to tape. This approach allows for algorithmic flexibility and improvements, and the ability to cost-effectively adjust to higher rates, but it does put pressure on the DAQ system.

Table 38: Rates, sizes, and processing requirements for the level 3 trigger.

	Low Rate	High Rate
Event Size	5 kB	5 kB
Event Rate to Farm	20 KHz	200 KHz
Data Rate to Farm	100 Mbytes/s	1000 Mbytes/s
Num Links to Farm	1	10
Data Rate per Link	100 Mbytes/s	100 Mbytes/s
Link Technology	Gigabit Ethernet	Gigabit Ethernet
Events/s per Link	20000	20000
SPECints/ev for L3	0.1	0.1
Num SPECint/link	2000 SPECint	2000 SPECint
Num SPECint/link x 2	4000 SPECint	4000 SPECint
Num 200 SPECint processors/link	20	20
Total Num 200 SPECint processors	20	200

We estimate the processing power required as follows. The Hall B on line hit-based event reconstruction system obtains 3% momentum resolution using $\sim$ 5 ms of CPU time on a 20 SPECint processor (about 0.1 SPECint/event); full reconstruction with better than 1% resolution takes about 45 ms. Assuming the same for GlueX gives 20000 SPECint total for the full level 3 farm at 200 KHz event rate. Assuming 50% processor utilization (due to I/O overhead, etc.), approximately 40000 SPECint (200 processor boxes at 200 SPECint each) are needed. 150 SPECint boxes are currently running in the JLab farm system, and, depending on the improvement in CPU performance over the next few years, it is likely that far fewer boxes will be required, perhaps 1/4 as many.

3.D.5 Computing and Partial Wave Analysis

GlueX will be the first Jefferson Laboratory experiment to generate petabyte scale data sets on an annual basis (One petabyte $= 1\ PB = 10^{15}$ Bytes). In addition, the need to generate physics results in a timely fashion has been identified as a primary goal of our collaboration since its inception. For these reasons, a well-designed, modern, and efficient computing environment will clearly be crucial to the success of the experiment.

Currently, there are a number of particle physics projects world wide which also will produce very large data sets, and which will function with large dispersed collaborations. It seems quite reasonable to expect that over the coming years many new tools will be developed that will aid in effectively processing and managing these large volumes of data. As a collaboration, we will undoubtedly make effective use of these tools, which will include such things as grid middle ware,

distributed file systems, database management tools, visualization software, and collaborative tools.

Nonetheless, it also is clear that the GLUEX collaboration will need to develop a suite of tools which are dedicated to this experiment. This will include data acquisition and trigger software, experiment monitoring and control software, data reduction tools, physics analysis software, and tools dedicated to the partial wave analysis (PWA) effort.

The primary goal of GLUEX is the systematic identification and categorization of short-lived meson states, unraveled from the raw, multi-particle reaction data using the techniques of PWA. Achieving this goal requires simultaneous access to two large and independent data sets, namely the actual reduced experimental data and the simulated Monte Carlo data, each sorted for the particular multi-particle reaction(s) under consideration. It is quite probable that these data sets will be distributed physically over multiple locations, and that the access will be from other separated sites, associated with the group which has undertaken that particular analysis.

This not only impacts the structure of the data grid, but also implies that new analysis tools need to be developed. This especially includes visualization tools, as one searches for the appropriate combination of partial waves which best describe the reaction. That is, as one fits the parameters associated with a certain set of partial waves, some visual inspection mechanism is needed to evaluate how well the fit reproduces distributions in angles and invariant mass, for the many possible combinations. A universal set of tools is important in order to come to a more or less standard set of measures that would be applied by the analysis groups.

In order to identify the J^{PC} quantum numbers of a meson, it is necessary to perform a PWA. In the simplest terms, a partial wave analysis is an attempt to determine production amplitudes by fitting decay angular distributions. The fit may include information on the polarization of the beam and target, the spin and parity of the resonance, the spin and parity of any daughter resonances and any relative orbital angular momenta. The analysis seeks to establish both the production strengths and the relative phase motion between various production amplitudes. Phase motion is critical in determining if resonance production is present.

While the implementation of a PWA is in principle straight forward, there are both empirical and intrinsic difficulties. Empirically, instrumentation effects, such as detector acceptance and resolution, can conspire to make one distribution look like another. These similar distributions can lead to *leakage* from one wave into the other in the PWA. Here, cropping, smearing, or incorrect acceptance corrections of two physically different distributions may lead to distributions which are apparently indistinguishable. There is also the related problem of background in PWA. Backgrounds involve a different final state accidentally reconstructing as the channel under study. Either a particle is missed by the detector, or when putting the final state back together, multiple interpretations are possible. Both of these effects limit one's ability to measure phase motion, and can be particularly severe in a region of dense overlapping resonances. These difficulties can be minimized by properly designing the experiment. Full angular coverage in the distributions can be

achieved by using a nearly 4π detector with excellent resolution. In addition, high statistics are critical to be able to accurately separate these partial waves. A thorough PWA requires nearly 4π coverage, excellent resolution, high statistics and a very good understanding of the detector.

The PWA method is subject to intrinsic mathematical ambiguities for certain final states. Two or more different choices of amplitudes lead to identical observables. Here there are at least two approaches. The first assumes some a priori physics knowledge that allows one to choose one solution over another. The second, and cleaner approach is to simultaneously examine several final states to which the resonance can decay. While the distributions may be confused in one final state, such as $\eta\pi$, they are likely to be absent or different in a second such as $\rho\pi$. This latter approach assumes that the detector has been optimized for many different final states, and that relative normalizations between these are understood.

This latter approach of looking at multiple final states not only allows the separation of different waves, but also yields key information about the relative decay rates of mesons. This information is critical to understanding the underlying wave functions of the mesons — their content, and mixing with other states. The ability to measure many final states accurately, and to perform a simultaneous PWA is a key feature of the GLUEX spectrometer for doing excellent spectroscopy.

The use of photon polarization will allow us to both simplify the analysis parameterization, as well as access additional information on the production of mesons. It will also provide key checks on the stability of the analysis itself. While circularly polarized light may yield some information in a few special cases, the true gain comes from linear polarization. Linear polarization defines a *new spatial direction* beyond the photon direction, while for circular polarization, the polarization and the momentum are in the same direction. Secondly, linearly polarized light is a coherent sum of circularly polarized light, which leads to new interference terms.

As part of the GLUEX design studies, the group has carried out a double-blind partial wave analysis on simulated data for the reaction:

$$\gamma p \rightarrow \pi^+\pi^+\pi^- n,$$

for $8.5\,\mathrm{GeV}$ photons. Studies have been done with photon polarizations ranging from 0% up to 100%. The simulated data correspond to a mix of seven waves including the a_1, a_2, π_2 and the $J^{PC} = 1^{-+}$ π_1, all of which decay via $\rho^\circ\pi^+$ to the 3π final state. The data are assumed to proceed via purely one–pion exchange. Two different packages for partial wave analysis have been used, each using a different formalism for fitting the data. The results between the two agree. The use of more than one analysis package on real data will allow us to better access the systematics associated with the fitting of the data. The data used in these fits corresponds to a couple percent of one year's reconstructed sample using 10^7 photons per second. It should be noted that this channel has a large photoproduction cross section, while the goal of the experiment is to simultaneously study channels with much smaller cross sections.
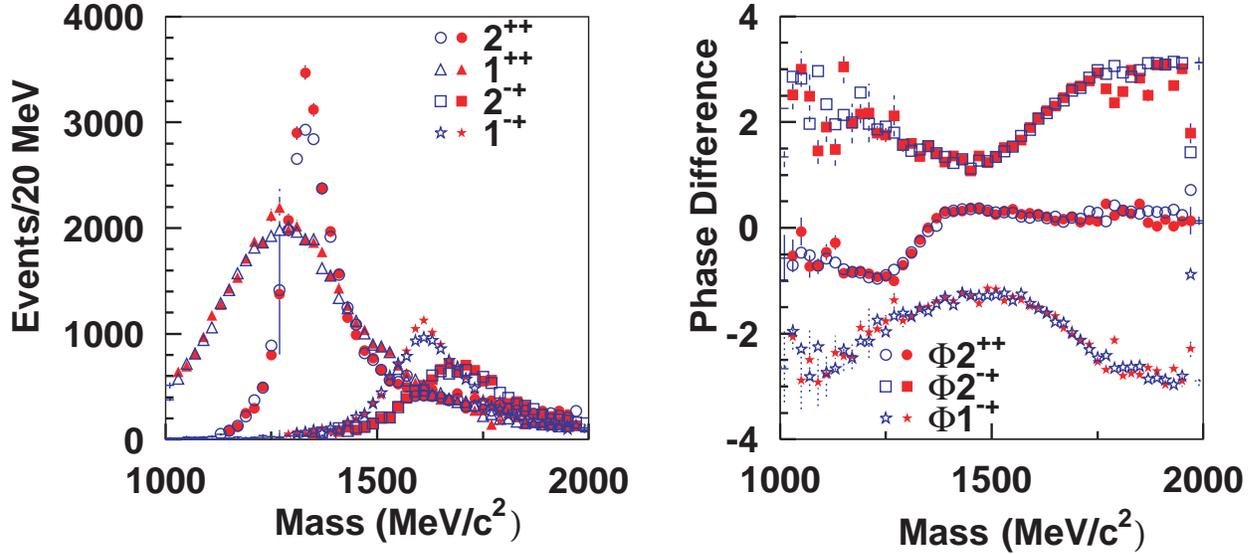
Figure 225: Partial Wave Analysis results for simulated 3π data. The solid points correspond to generated data, while the open points correspond to events which have been run through the GLUEX Monte Carlo program. The left hand figure shows the intensities of several waves, while the right hand figure shows the phase difference from the 1^{++} wave.

Figure 225 shows the results of fits to the simulated data. The solid figures correspond to simple generated data, while the open figures are for data which has been run through the GLUEX Monte Carlo program to simulate both acceptance and resolution effects. The small differences between the two curves are due mostly to resolution, particularly for the fast π's in the events. It should be noted that the 3π channel while one of the stronger photo production channels, is also one of the more difficult as far as resolution goes. The four curves correspond to the $a_2(1320)$, ($J^{PC} = 2^{++}$), the $a_1(1260)$, (1^{++}), the $\pi_2(1670)$, 2^{-+} and an exotic $\pi_1(1600)$, (1^{-+}). The phase differences are plotted with respect to the $a_1(1260)$ wave. A second PWA exercise was performed to assess the ability to extract an small exotic signal from mix of various non-exotic waves, (this latter study used simple 4-vector smearing and cuts rather than the fast Monte Carlo). Figure 226 shows the results of this second study where the exotic wave was about 2.5 % of the total sample. The statistics shown correspond to several days of running and it is clear that one can easily extract this small signal from the data, and accurately reproduce the original resonance

Similarly, a study on the effect of linear polarization in determining the production mechanism has been undertaken. To do this, a second event generator was built that produced the same 3π final states via ρ exchange, rather than π exchange. The naturality of these two exchange particles are opposite from each other, and in the absence of linear polarization, only the sum of the two intensities can be determined. With the addition of linear polarization, it is possible to disentangle the two contributions. Figure 227 shows this by examining the exotic 1^{-+} wave produced via both these mechanisms. The upper curves in the figures correspond to fits to the sum of the two intensities, and are well fit for all polarizations. The lower curves correspond to fits to the
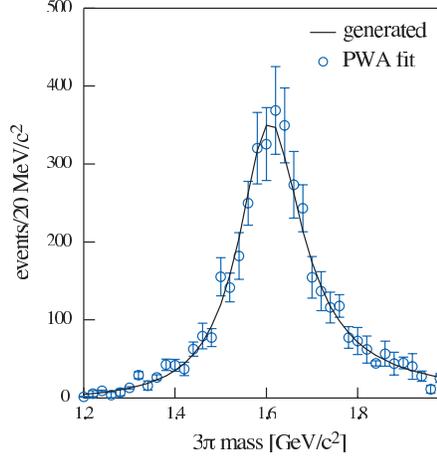
Figure 226: The results of a double-blind Monte Carlo exercise showing the $J^{PC} = 1^{-+}$ exotic wave after fitting (open circles) and the exotic wave input (curve) into the mix of $\gamma p \to \pi^+ \pi^+ \pi^- n$ events that were generated in this study. Details are given in the text.

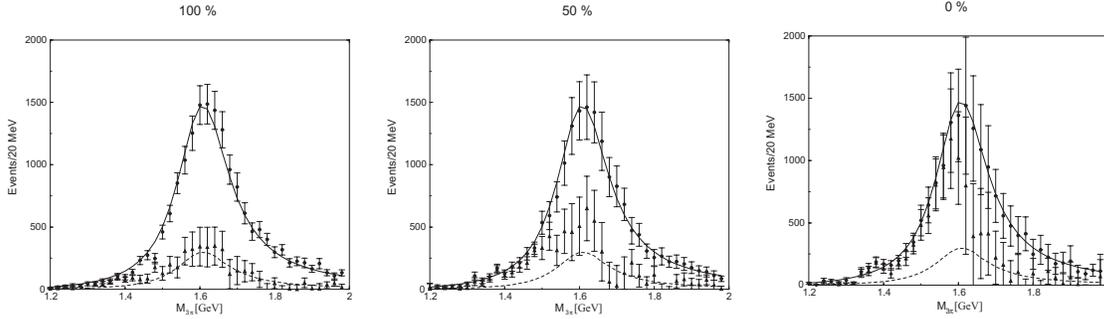Figure 227: Partial Wave Analysis results for simulated 3π data generated with a combination of natural and unnatural parity exchanges with 100%, 50% and 0% linearly polarized photons. The upper curves correspond to the sum of the two intensities, while the lower curves correspond to the differences between the two intensities.

differences between the two intensities. This is completely undetermined for the unpolarized data set, while it is separated for the polarized samples.

A detailed *leakage* study has also been performed using the PWA tools [Za01]. In doing this, the geometry in the detector simulation for producing physics events and the detector simulation for performing the PWA were varied by several σ in the resolution parameters for the GLUEX detectors. A search was then made for signals that leaked into the exotic waves with the results that with the current detector geometry, it is extremely difficult to produce leakage into the exotic waves.

The GLUEX collaboration has organized a collaborative program with the CLEO-c experiment to develop advanced tools for PWA that would be useful for both groups. The initial efforts by GLUEX members have been to begin work on parallelizing existing PWA codes, and using these to analyze large existing data sets collected by the E852 collaboration. A sample of approximately

35-million 3π events is being analyzed using the large computer facilities available at Indiana University. These efforts have made possible the PWA analysis of the largest data set ever.

In order to continue and expand these efforts, members of both the GLUEX collaboration and the CLEO-c collaboration submitted an NSF ITR proposal in February of 2003. This proposal would support a 4-year multi-pronged development and implementation of the next generation of PWA tool. Under this proposal, the CLEO-c contingent will develop data caching tools and interfaces to allow transparent access to large data sets. The GLUEX collaboration will work on visualization tools, parallelization of PWA code and improvements in minimization algorithms. In parallel with this, improvements in theory will be explored and implemented into the PWA tools. The tools will initially be applied to existing E852 data sets. Once CLEO-c spectroscopy data becomes available, they will be analyzed. At the end of the 4 year proposal, the goal is to have a robust set of tools that can be used to handle the GLUEX data.

3.D.6 Summary

The GLUEX beam and detector have been optimized to facilitate a robust PWA of mesons and baryons produced with an 8 to 9 GeV linearly polarized photon beam. Even with rates of only $10^7\,\gamma/s$, the experiment will collect at least an order of magnitude more data than existing π beam experiments during its first year of running. Such an increase in statistics coupled with a new production mechanism will not only allow us to map out the gluonic excitations, but to measure their decay properties and production mechanisms as well.

3.E Experiment-Specific Equipment

3.E.1 Properties of Light Pseudoscalar Mesons via the Primakoff Effect

In addition to the 12 GeV upgrade to the CEBAF accelerator, the proposed program to perform high precision measurements of the electromagnetic properties of the light pseudoscalar mesons would require a high energy photon tagging system and a multichannel calorimeter to detect photons from the meson decays. While the calorimeter is common to both the photo- and electroproduction measurements, the transition form factor measurements involve electroproduction, and would be performed with the same setup as the radiative width measurements but with the bremsstrahlung radiator removed and the photon tagger turned off. In such a configuration, the calorimeter would simultaneously detect both the two photons from the meson decay as well as the scattered electron.

The construction of a new tagging system is necessitated by the fact that the existing Hall B tagger is designed for a maximum energy of 6 GeV and at present and there are no known plans to bring it to the capability to tag higher energy photons. While a high energy photon tagging system has been proposed by the Hall D Collaboration[HallD], its design is optimized to provide
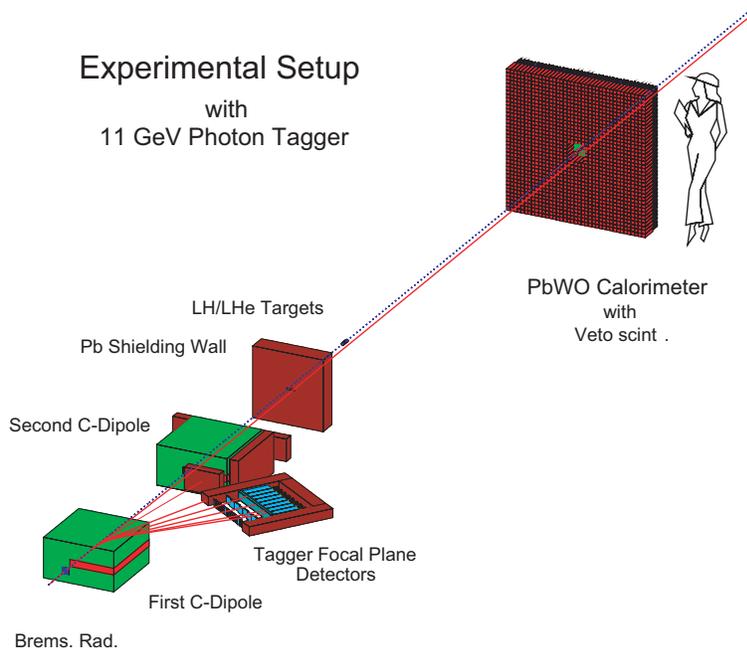
Figure 228: Side view of the experimental setup for η and η' two–gamma decay width measurements. It includes (1) a photon tagging system, and (2) a 1.5 m$\times$ 1.5 m multichannel calorimeter.

linearly polarized photon beams with high collimation of the bremsstrahlung photons. This requires a relatively long distance (approximately 90 meters) for photons from the bremsstrahlung radiator to the collimators, thus making this part of the photon beam line inaccessible. The experimental program proposed here simultaneously requires high precision in both photon flux control (at the 1% level) and angular resolution for forward meson production ($\sim$0.3 mrad). This angular resolution requires the photon beam spot at the Primakoff production target to be minimized to about one millimeter. The optimal configuration for these measurements is thus one in which the physics target is relatively close to the bremsstrahlung converter and the photon beam is uncollimated. As such, the proposed Hall D tagging system will not simultaneously satisfy these two criteria.

We are proposing the construction of a photon tagging system based on a new approach involving parallel transport of both the photon and primary electron beams through the beam line to the beam dump. Two identical 'C-type' dipole magnets will displace the initial electron beam and make it parallel to the photon beam, which is produced in the bremsstrahlung radiator just upstream of the first dipole (see figure 228). The displacement is determined by two parameters – the integrated field in the dipole magnets and the distance between them.

The following requirements for the design of this tagging system have been imposed. First, it should be a functional, relatively low cost system. Second, its size and design should allow flexibility to potentially incorporate it into any of several upgraded Halls currently being proposed at Jefferson Laboratory. Two standard C-dipole magnets (see Fig. 228) with a $\int Bdl = 5$ kG meter placed 2 meters apart will provide a 5 cm parallel displacement of the electron and photon beams. Three
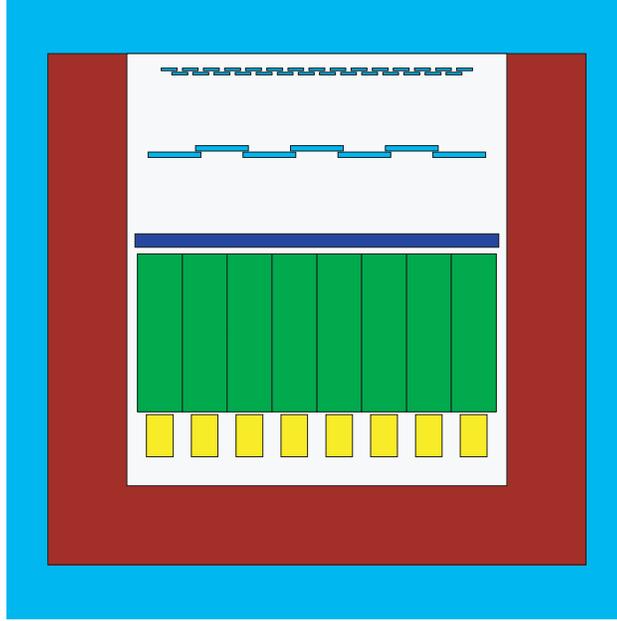
Figure 229: Focal plane detectors for the proposed high energy tagging system including two rows of segmented scintillators (top) and lead glass detectors (bottom). In the figure, the post-bremsstrahlung electrons enter from the top.

centimeter diameter, 10 cm long liquid hydrogen and helium-4 targets will be placed downstream of the second dipole. To minimize beam backgrounds, a set of lead shielding walls (20 radiation lengths thick) surrounding the second dipole and one with a narrow hole (8 cm width, 2 cm in height) in the middle of a wall will be placed one meter downstream of the second dipole and just upstream of the physics targets. The post-bremsstrahlung electrons will be deflected in the first C-dipole and detected by the tagger focal plane detectors (see Fig. 229). Three layers of detectors are proposed. The first will be highly segmented scintillating detectors for energy definition of the post-bremsstrahlung electrons. The second plane of seven scintillators will provide fast timing for the tagger, while eight lead glass detectors ($\sim 8.5 \times 8.5 \times 35$ cm^3) in the third plane will significantly improve background suppression. A 2.5 cm thick aluminum absorber plate in front of the lead glass detectors will cut down the low energy charged particle background produced in the shower counters. This design emphasizes the tagging of high energy photons only, with a focal plane of length approximately 60 cm providing tagged photons of energy $E_\gamma = 10.0 - 10.5$ GeV.

The decay particles from the forward produced neutral mesons will be detected in a high resolution electromagnetic calorimeter. We are proposing to upgrade the HYCAL detector, currently under construction for the Jefferson Lab PrimEx experiment, such that it is composed entirely of lead tungstate ($PbWO_4$) modules with a total overall size of $1.5 \times 1.5m^2$. This will consist of a 75×75 matrix of crystals, with a central 12×12 cm^2 hole (6×6 crystals removed) in the middle for the passage of the beams. This calorimeter will be placed at a variable distance (five to ten meters) downstream from the production targets to provide optimal acceptance for each experiment.
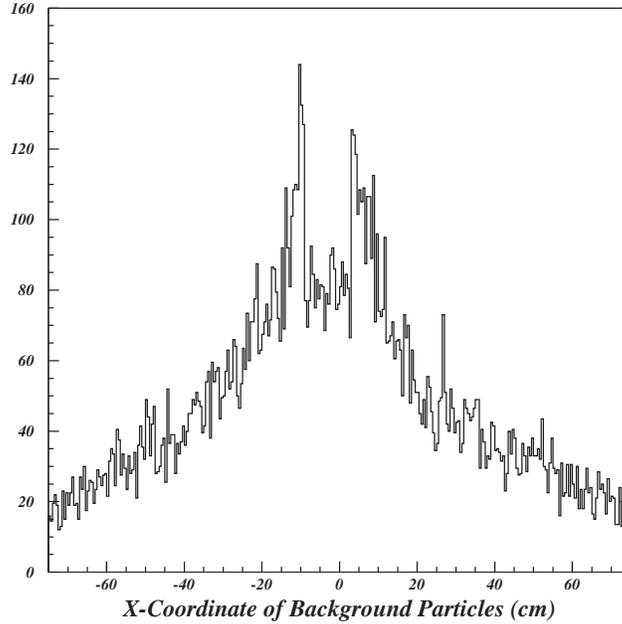
Figure 230: Background events in the calorimeter projected to the horizontal (dispersive) plane for a photon tagging (photoproduction) run.

As is typical of all conventional tagging experiments, the beam backgrounds for the decay width measurements will be dominated by the post bremsstrahlung electrons which lose relatively little energy in the bremsstrahlung radiator and hit the tagger structure. Conventional taggers also have an additional source of background from the electron beam dump. Since in the high energy tagging system proposed here the electron beam will be dumped together with the photon beam far from the tagger, this setup should be largely free of this second type of background. Nevertheless, in this geometry a significant number of electrons will hit the shielding structure close to the beam line. The forward electromagnetic calorimeter will be centered on the beam line downstream of the production target. As such, it will be very sensitive to the tagging setup configuration. There are two basic approaches to the geometrical design of the calorimeter. One is to remove a 6×6 matrix of crystal modules from the center of the calorimeter for the beam to pass through. This maximizes the geometrical acceptance and simplifies its determination. The next option is to remove all the modules from several rows of the calorimeter in the dispersive plane of the electron beam (the horizontal plane for this design). Here we propose the first option, removal of a central hole in the calorimeter, for the reasons mentioned above.

To estimate the background levels and to optimize the experimental setup, we have performed a Monte Carlo simulation based on the GEANT package. The photoproduction experiments will typically run with an electron beam current of 75 nAmps, which will produce 5×10^7 equivalent γ's/sec on a 10^{-4} radiation length thick gold radiator. We have simulated a total of 10^8 beam electrons through the setup with a 10 centimeter long liquid helium-4 target in the photon beam. This would be equivalent to approximately 200 microseconds of beam time in an experiment. The
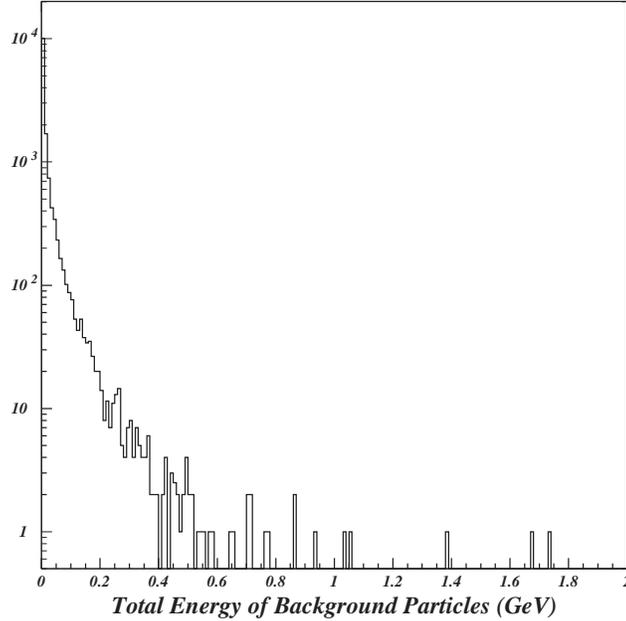
Figure 231: Energy distribution in calorimeter corresponding to the events in Fig. 230 (photon run).

resulting distribution of background events on the calorimeter is shown in Fig. 230, projected onto the horizontal axis. The energy distribution of these events is shown in Fig. 231. Based on these simulations, the electromagnetic calorimeter will have a rate of approximately 200 kHz of particles with energy bigger than 0.5 GeV. The expected rate per detector module is 0.4 kHz on average. These numbers are quite favorable for the proposed tagging system.

A similar experimental setup will be used for the transition form factor measurements. For these experiments, the bremsstrahlung radiator will be removed and there will be no magnetic field in the tagger dipoles. We have simulated 2×10^7 electrons through this setup, which is equivalent to 300 microseconds of running with an electron beam current of 100 nAmp. With a 0.5 GeV threshold, the total rate in the calorimeter is expected to be 80 MHz. The high segmentation of the calorimeter (5625 $PbWO_4$ modules) will bring this rate down to the level of 10 kHz per module, which is also quite favorable.

Photons resulting from η and η' decay, as well as scattered electrons in the transition form factor measurements will be detected in the highly segmented array of the shower calorimeter located downstream of the target. Currently, the PrimEx Collaboration is constructing a hybrid shower calorimeter for the π^o life time experiment in Hall B. This will be ready for commissioning in the Fall of 2003. We propose to use a somewhat larger version of this detector for these experiments. It will be 150×150 cm^2 in the dimensions transverse to the beam. The calorimeter is designed to measure both the position and the energy of electromagnetic showers using a two dimensional matrix of radiators ($PbWO_4$ crystals). This will be accomplished by choosing the cross section of the individual counters to be small enough so that the energy leakage into adjacent counters can

be used to determine the position of the shower axis.

The Primakoff cross section peaks at extremely small angles ($\theta_\eta = 0.1^o$ at $E_\gamma = 10\ GeV$) and therefore the experimental setup must have sufficient resolution for the η production angle in order to identify and extract the Primakoff amplitude. This resolution depends strongly on the decay photon energy and position resolutions of the calorimeter. As such, this detector will be constructed from lead tungstate crystals of size $2\times2\times18cm^3$. In our beam tests at Jefferson Lab in 2001 and 2002, crystal energy resolutions of $\frac{\sigma_E}{E} = 1.2\%$ and position resolutions of $\sigma_X = 1.2mm$ were obtained for 4 GeV electrons[Ga00], where the quoted value for position resolution is at the boundary between two lead tungstate crystal detectors. These results are consistent with those reported by the Mainz group for similar crystals operated at a stabilized temperature (8°C) where they attained:

$$\frac{\sigma_E}{E}(\%) = \frac{1.54}{\sqrt{E}} + 0.3, \tag{79}$$

with E given in GeV[Me00]. As compared to lead glass, use of these crystals will significantly improve the radiation hardness of the detector near the beam line where radiation doses can be high. Furthermore, a central $12 \times 12cm^2$ hole will be left open to enable the photon beam to pass through. The modules contiguous with this region on the beam axis as well as the two outermost layers of modules will be excluded from the fiducial volume of the detector to control coordinate resolution and detection efficiency near the boundaries of the detector. To monitor and correct possible gain changes due to temperature and aging, a light monitoring system similar to that of the PrimEx experiment will be used.

In these experiments, the Primakoff amplitude will be extracted from the differential cross section measurements for forward angle meson production. As mentioned earlier, the different angular dependences will enable identification of the Primakoff amplitude from the background nuclear coherent and interference contributions. We propose to perform a high precision measurement of the differential cross sections on two different nuclei, ^1H and ^4He, over a range of angles $(0-5°)$ as determined by the electromagnetic calorimeter. The $1.5 \times 1.5m^2$ calorimeter placed at a distance of $\sim 6m$ from the 10 cm long liquid helium target will provide a high geometrical acceptance for the two decay photons, yielding detection efficiencies of about 70%. The expected experimental angular distribution from a Monte Carlo simulation of $\eta \to \gamma\gamma$ events for a 30 day run is shown in Fig. 232. In this simulation, the experimental resolutions and all efficiencies of the setup are taken into account. The $\eta \to \gamma\gamma$ rate for a 10 cm long liquid ^4He target and 75 nAmp electron beam incident on a 10^{-4} radiation length thick gold bremsstrahlung target is $\sim 23,300 events/60 days$. Here, we have taken the upper 1 GeV energy range of the tagged photon beam only. The estimated experimental uncertainties for $\Gamma(\eta \to \gamma\gamma)$ are listed in table 39. The total error for the $\eta \to \gamma\gamma$ decay width has been estimated to be on the level of 3.1%, which includes 1.0% statistical error (for 60 days of beam time), and the estimated systematic errors are added in quadrature as is shown in the table.

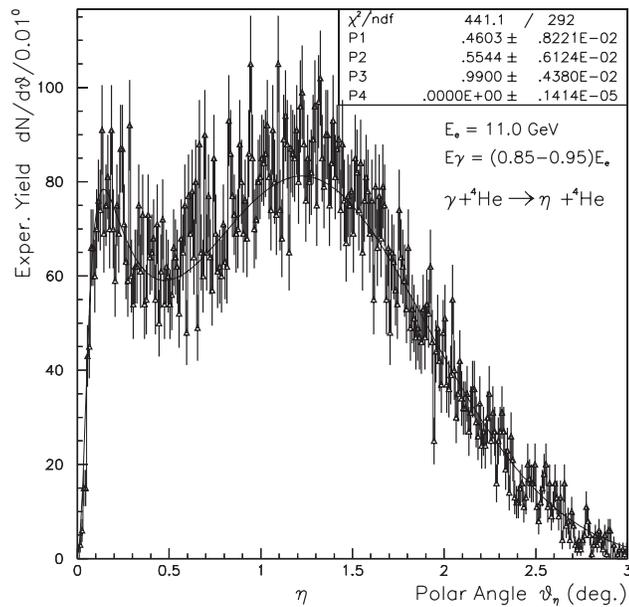The $\eta' \to \gamma\gamma$ experiment has two major difficulties as compared with the η decay width

Figure 232: Monte Carlo simulation of expected yield as a function of angle for $\eta\gamma\gamma$ events on ^4He.

Table 39: Estimation of the experimental uncertainties for $\Gamma(\eta \to \gamma\gamma)$ measurement.

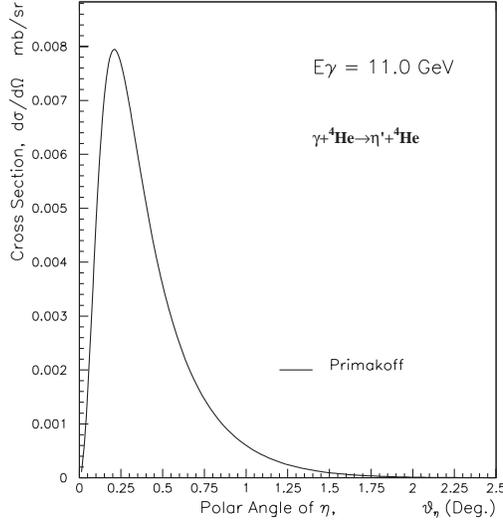| Error Source	Estimate (%)
statistical	1.0% (60 days)
photon flux	2.0%
target thickness	1.5%
acceptance, misalignment	0.5%
Physics background	0.4%
beam energy	0.2%
nuclear coherent contrib.	1.0%
distorted form factor	0.3%
branching ratio	0.8% (PDB)
Total	3.1%

Figure 233: Coulomb photoproduction of the η' as a function of angle.

experiment. The first and most important one is that the $\eta' \to \gamma\gamma$ branching ratio is relatively small and poorly known. ($2.12 \pm 0.14\%$[PDB]). The branching ratio directly effects the number of events in the experiment, necessitating more beam time for this measurement. The current experimental error on the branching ratio ($\pm 6.6\%$) sets a lower limit on the total error of any new experiment. We expect this situation to be improved by the time we perform the η' measurements. If this is not the case, we plan to run a dedicated experiment with a similar setup but with an additional low momentum recoil detector. At the forward production angles, the kinetic energy of the recoiling ^4He is in the range of 10-70 MeV, and the produced η''s will be identified by recoil detection through missing mass reconstruction. At the same time, the decay photons will be detected by the downstream electromagnetic calorimeter. A preliminary conceptual design of the recoil detector includes a cylindrical multi-layer proportional chamber under ~ 5 atm ^4He gas pressure. The differential cross section at the forward angles for the η' meson is shown in Fig. 233. Only the Primakoff contribution is shown here, since there are no experimental data for the η' done with the fixed target technique. Our estimation is that with 90 days of beam time and using a 15 cm long liquid ^4He target, we can reach a 3.0% statistical error for the η' decay width measurement. The systematic errors are basically the same as those for the η experiment shown in table 1, except for the branching ratio. Assuming that one can attain a $\sim 3.0\%$ error in the knowledge of the branching ratio, we estimate the total error in the determination of the $\eta' \to \gamma\gamma$ decay width to be on the level of 5%.

In summary, the proposed instrumentation to be constructed for this program, a highly segmented electromagnetic calorimeter and a high energy photon tagger, will provide a new and powerful experimental window on QCD at Jefferson Lab. Furthermore, one can fully expect such instrumentation to be of general use for future high precision experiments.